

Development of a novel, energy efficient process for the gas-phase electrolysis of hydrogen chloride to chlorine

Dissertation

zur Erlangung des akademischen Grades

Doktoringenieur

(Dr.-Ing.)

von M.Sc. Simon Bechtel

geb. am 26.04.1992 in Worms

genehmigt durch die Fakultät für Verfahrens- und Systemtechnik der Otto-von-Guericke-Universität Magdeburg

Promotionskommission: Prof. Dr. rer. nat. Helmut Weiß (Vorsitz)

Prof. Dr.-Ing. Kai Sundmacher (Gutachter)

Prof. Dr.-Ing. Thomas Turek (Gutachter)

Prof. Dr.-Ing. Karel Bouzek (Gutachter)

eingereicht am: 25.09.2020

Promotionskolloquium am: 18.01.2021

Abstract

The overarching goal of this work is to further develop the gas-phase electrolysis of HCl to Cl₂ employing an oxygen depolarized cathode on its path from a pure reactor concept towards an industrially feasible process. This is motivated by the fact that the production of Cl₂ is responsible for the highest GHG emissions and energy consumption of all base chemicals. Recent studies indicated an energetic advantage of the novel gas-phase electrolyzer over the currently industrially employed liquid-phase reactor, which employs hydrochloric acid as a feed stock. Hence, the gas-phase electrolysis of HCl to chlorine, if proven to be feasible, has the potential to significantly contribute to a more energy efficient chemical industry. To reach this goal, the work focuses on the following two aspects.

The first goal is to determine, whether this efficiency advantage of the gas-phase reactor can be maintained on the overall process level, taking account all necessary separation and product purification steps. Secondly, three main phenomena observed in earlier experimental investigations of the gas-phase reactor with a significant impact on its performance are not yet understood. These three phenomena are a limiting behavior observed in previous half-cell investigations of the HCl oxidation as well as in investigations of the full-cell combining the HCl oxidation with an oxygen depolarized cathode, and, lastly, severe performance losses in the oxygen reduction reaction itself. Hence, the second goal is the detailed understanding of the origin of these phenomena and the proposal of first systematic strategies for further increasing the reactor efficiency and its suitability for an industrial application of the process.

The first part of this work hence focuses on the development of novel separation strategies enabled by the different physical state of the now gaseous reactant HCl by means of flow sheet simulations and a rigorous exergy analysis. Three novel process variants, each based on the gas-phase reactor and a different separation strategy are proposed and benchmarked versus the industrial state-of-the-art process, showing that the exergy advantage of the gas-phase reactor can not only be maintained, but even be extended on the overall process level. Furthermore, it is shown that already intermediate single pass and overall conversions of HCl are exergetically feasible, reducing the complexity of the reactor design and operation. Since all three process variants exhibit a comparable exergy efficiency, various individual advantages and disadvantages are discussed,

facilitating a site-specific selection process of one of the three variants for an industrial application. Lastly, it is shown that the electrochemical reactor makes up for 88-95% of the overall exergy demand in the three process variants, motivating the dedication of the second part of this work to a detailed investigation of the electrochemical reactor.

Hence, a mathematical reactor model of the HCl gas-phase electrolyzer with a focus on the HCl oxidation kinetics, mass transfer, HCl and Cl₂ crossover and the water household is developed and complemented by the design of an experimental setup. Employing a combined experimental and theoretical approach, the HCl oxidation reaction and the oxygen reduction reaction are first investigated separately and finally, in combination.

Based on this approach, the first phenomenon, the limiting behavior in the HCl oxidation, is shown to be a pure reaction limitation. Consequently, reaction kinetics of the HCl oxidation reaction are proposed, which are so far the only kinetics published in the scientific literature that are able to emulate this limiting behavior. Secondly, the HCl and Cl₂ crossover investigations suggest that under relevant process conditions especially HCl crosses over in significant amounts. This leads to poisoning of the platinum cathode catalyst employed in previous studies and hence impedes the oxygen reduction reaction, explaining the before mentioned performance losses. Thirdly, the subsequent analysis of the full-cell combining the HCl oxidation and oxygen reduction indicate that the observed imitating behavior in this case is caused by either flooding of the cathode catalyst layer or membrane dehydration. Which one of these mechanisms dominates is shown to strongly depend on the thermal and water management of the cell, due to the significant overpotentials and exothermic dissociation of HCl in water, so that already slight changes in the operating conditions are able to provoke a change from flooding to membrane dehydration. Adjusting operating and geometrical parameters in the reactor model based on these insights leads to a simulated increase in the limiting current density by more than 90%.

These insights on all three phenomena are furthermore validated by own experiments and motivate the first application of a rhodium sulfide based cathode catalyst in the HCl gas-phase reactor, leading to significantly lower activation overpotentials. Based on the learnings from the mathematical reactor model, industrially feasible current densities of more than 5000 A/m² are experimentally achieved for the first time, while also maintaining a feasible cell potential of

1.09 V. This is a further significant step towards an industrial realization of the process as an energy efficient alternative to the state-of-the-art liquid-phase electrolysis.

Zusammenfassung

Das Ziel der Arbeit ist die weitere Entwicklung der elektrochemischen Gasphasenoxidation von HCl zu Chlor in Kombination mit einer Sauerstoffverzehrkathode von einem reinen Reaktorkonzept hin zu einem industriell anwendbaren Prozess. Dies ist motiviert durch die Tatsache, dass die Produktion von Chlor im Vergleich zu allen anderen Grundchemikalien mit den höchsten Treibhausgasemissionen und dem höchsten Energieverbrauch verbunden ist. Frühere Studien haben einen signifikant niedrigeren Energieverbrauch des Gasphasenreaktors gegenüber dem industriellen state-of-the-art Flüssigphasenreaktor, bei dem wässrige Salzsäure als Edukt eingesetzt wird, festgestellt. Die HCl Gasphasenelektrolyse, falls sie sich als industriell anwendbar herausstellt, hat daher das Potential, einen signifikanten Beitrag zur Energieeffizienzsteigerung der chemischen Industrie zu leisten. Um dieses Ziel zu erreichen, fokussiert sich die Arbeit auf die folgenden zwei Aspekte

Das erste Teilziel der Arbeit ist daher zu untersuchen, ob dieser Effizienzvorteil auf der Reaktorebene auch auf der Prozessebene unter Berücksichtigung aller notwendigen Trennungs- und Aufreinigungsschritte aufrechterhalten werden kann. Zweitens wurde in früheren experimentellen Untersuchungen des elektrochemischen Reaktors drei Phänomene beobachtet, die bisher noch nicht verstanden wurden, aber einen signifikanten Einfluss auf die Effizienz des Reaktors nehmen. Bei diesen Phänomenen handelt es sich um ein limitierendes Verhalten, das sowohl bei Halbzellenuntersuchungen der HCl-Oxidation, als auch bei Untersuchungen der HCl-Oxidation in Kombination mit einer Sauerstoffverzehrkathode beobachtet wurde, sowie um signifikante Kathodenüberspannungen der Sauerstoffreduktion. Das zweite Teilziel der Arbeit ist daher die Analyse dieser drei Phänomene und basierend darauf die Entwicklung erster systematischer Optimierungsstrategien mit dem Ziel einer weiteren Energieeffizienz- und Leistungssteigerung, die die Chancen für eine industrielle Anwendung der HCl Gasphasenelektrolyse erhöhen.

Der erste Abschnitt der Dissertation befasst sich deshalb mit der Entwicklung neuer Strategien für die Trennung des nun gasförmigen, nicht umgesetzten HCl von dem Produkt Chlor mit der Hilfe von Prozesssimulationen und einer Exergieanalyse. Es werden drei neue Prozessvarianten

vorgeschlagen, alle basierend auf dem Gasphasenreaktor und drei verschiedenen Separationsstrategien, und mit dem industriellen state-of-the-art Prozess verglichen. Es zeigt sich, dass der Exergievorteil des Gasphasenreaktors auf der gesamten Prozessebene nicht nur beibehalten, sondern sogar gesteigert werden kann, und dass selbst geringere HCl Gesamtumsätze von nur 60 % die Effizienz nicht maßgeblich beeinträchtigen, was die spätere Auslegung und den Betrieb des Reaktors vereinfacht. Da die drei neuen Prozessvarianten einen vergleichbaren Exergieverbrauch aufweisen, werden deren individuelle Vor- und Nachteile diskutiert, um den Auswahlprozess bei der industriellen Anwendung einer der drei Prozessvarianten nach produktionsstandortspezifischen Kriterien zu unterstützen. Die Untersuchungen zeigen weiterhin, dass der Reaktor für 88-95% des Exergieverbrauchs des gesamten Prozesses verantwortlich ist, sodass der zweite Anteil der Arbeit der Untersuchungen des elektrochemischen Reaktors selbst gewidmet ist.

Zu diesem Zweck wird ein mathematisches Reaktormodell mit besonderem Fokus auf die HCl-Oxidationskinetik, den Massentransport, die Permeation von HCl und Cl₂ durch die Nafion Membran und den Wasserhaushalt des Reaktors entwickelt und durch den Aufbau eines experimentellen Versuchsstandes komplementiert. Basierend auf dem Modell und dem Versuchsaufbau werden die Chlorwasserstoffoxidation und die Sauerstoffreduktion zunächst separat und abschließend in Kombination erforscht.

Es wird gezeigt, dass das erste Phänomen, das limitierende Verhalten der HCl-Oxidation, rein kinetisch bedingt ist. Basierend darauf wird die erste in der wissenschaftlichen Literatur publizierte Reaktionskinetik entwickelt, die in der Lage ist, dieses limitierende Verhalten wiederzugeben. Weiterhin wird gezeigt, dass die geringe Effizienz der Sauerstoffverzehrkathode bei der HCl Gasphasenelektrolyse vor allem durch Permeation von HCl und darauffolgende Vergiftung des Platinkatalysators bedingt ist. Bei der Analyse des gesamten Reaktors inklusive der anodischen Chlorwasserstoffoxidation und kathodischen Sauerstoffreduktion stellt sich heraus, dass das limitierende Verhalten in diesem Fall durch die Flutung der Sauerstoffverzehrkathode oder durch die Dehydrierung der Membran verursacht wird. Welcher dieser beiden Mechanismen dominiert, wird vor allem durch die Reaktortemperatur und den Wasserhaushalt beeinflusst. Infolge der stark exothermen Dissoziation von HCl in Wasser sowie der hohen Überspannung können bereits marginale Änderungen in der Reaktoroperation einen Wechsel zwischen Flutung und

Dehydrierung hervorrufen. Basierend auf diesen Erkenntnissen kann die limitierende Stromdichte in den Simulationen durch Anpassung von strukturellen- und Betriebsparametern um 90% gesteigert werden.

Die auf Basis von Modellsimulationen gewonnenen Einsichten in die drei oben diskutierten Phänomene werden experimentell validiert. Inspiriert durch die Permeationsanalyse wird erstmals ein Rhodiumsulfid basierter Katalysator eingesetzt, der zu signifikant niedrigeren Überspannungen führt. Inspiriert von den Erkenntnissen aus den Reaktorsimulationen werden erstmals Stromdichten von mehr als 5000 A/m^2 experimentell realisiert, bei weiterhin niedrigen Zellspannungen von 1.09 V. Dies stellt einen weiteren wichtigen Schritt in Richtung einer industriellen Anwendung des Prozesses dar.

Table of contents

Abstract	i
Zusammenfassung	iv
Acknowledgement	Error! Bookmark not defined.
Table of contents	vii
Notation	x
Abbreviations	xvii
1 Introduction	1
1.1 The role of HCl oxidation within the chemical industry in the light of climate change.....	1
1.2 Developments in the industrial oxidation of HCl to Cl ₂	4
1.3 Working principle of the HCl gas-phase electrolysis employing an ODC	8
1.4 State-of-the-art and open questions.....	10
1.5 Scope and outline of the work.....	13
2 Development of an overall process for the gas-phase electrolysis of HCl	16
2.1 Flowsheet simulations, assumptions and process constraints	17
2.2 Exergy analysis	20
2.3 Modeling of the state-of-the-art process	23
2.4 Modelling of the three novel processes based on the gas-phase reactor.....	27
2.4.1 ELECTRA-DIST process.....	28
2.4.2 ELECTRA-ABS process.....	30
2.4.3 ELECTRA-IL process.....	35
2.5 Results of the exergy analysis	41
2.5.1 Contribution of different process units to the overall exergy demand.....	44
2.5.2 Efficiency of the investigated separation strategies.....	45
2.5.3 Further characteristics of the three proposed separation strategies.....	47
2.5.4 Impact of the gas-phase reactor on the overall exergy demand of the process.....	50
2.5.5 Influence of the conversion on the specific exergy demand.....	52
2.6 Summary of the investigations on novel processes for the HCl gas-phase electrolysis	54
3 Development of a numerical reactor model of the HCl gas-phase electrolyzer	56
3.1 Review of the relevant history of PEM fuel cell modeling.....	56

3.2 1D nonisothermal two-phase agglomerate model.....	61
3.2.1 Energy balance	65
3.2.2 Gas-phase mass transport	68
3.2.3 Two-phase modeling of water	70
3.2.4 Membrane.....	74
3.2.5 Catalyst layer and reaction kinetics.....	78
3.2.5.1 Kinetics of the HClOR and ORR	78
3.2.5.2 Modeling of the catalyst layer	80
3.2.6 Half-cell model.....	83
3.2.7 Numerical methods and parameters	83
3.2.8 Reactor model summary.....	89
3.3 Numerical model for investigating the crossover of HCl and chlorine	89
3.4 Novel method for the precise determination of transport coefficients.....	94
3.4.1 Modeling of transport coefficients based on the kinetic gas theory.....	94
3.4.2 Shortcomings in the classical approach of determining LJ parameters and motivation of a new methodology	96
3.4.3 Framework of the proposed methodology	101
3.4.4 Evaluation of the accuracy of the novel parameter set.....	107
3.4.5 Summary of the investigations on the modeling of transport coefficients.....	117
4 Experimental setup for investigating the gas-phase electrolysis of HCl.....	119
4.1 Half-cell setup	119
4.2 Full-cell setup.....	122
4.3 Catalyst, membrane and gas diffusion media	124
4.4 Operation and electrochemical measurements.....	126
5 Results of the theoretical and experimental investigations of the HCl gas-phase electrolysis.....	128
5.1 Investigations of the HClOR.....	128
5.1.1 Role of reaction kinetics in the limiting behavior of the HClOR.....	128
5.1.2 Role of mass transfer in the GDL.....	133
5.1.3 Mass transfer and catalyst utilization within the agglomerates.....	134
5.1.4 Role of membrane hydration.....	136

5.1.5 Deriving reactor optimization strategies	137
5.1.6 Experimental validation	139
5.1.7 Summary of the new insights on the HClOR	146
5.2 Crossover of HCl and chlorine and its influence on the ORR	147
5.2.1 HCl and chlorine crossover in a liquid-phase reactor employing an ODC	149
5.2.2 HCl and chlorine crossover in the gas-phase reactor employing an ODC	156
5.2.3 Summary of the crossover investigations.....	160
5.3 Investigations of the full-cell setup employing an ODC.....	160
5.3.1 Simulated polarization data and model-based investigation of the limiting behavior	161
5.3.2 The role of thermal management	165
5.3.3 Outlook on reactor optimization strategies	170
5.3.4 Experimental investigations of the HCl gas-phase electrolysis employing an ODC.....	181
5.3.5 Summary of the full-cell investigations	185
6 Conclusions	188
7 Outlook	192
Appendix	197
List of Figures	215
List of Tables	219
References	220
Publications	238
Curriculum Vitae	238

Notation

Greek symbols

α	Charge transfer coefficient cathode	-
α	Polarizability	m^3
α_{red}	Reduced polarizability	-
β	Symmetry factor	-
β_L, β_G	Exponents for the liquid and gas-phase permeability	-
γ_i	Activity coefficient of species i	-
δ	Factor accounting for polarity	-
δ	Characteristic length equivalent to the thickness of the gas diffusion layer and catalyst layer	m
ε	Potential depth	K
ε_i	Porosity of layer i	-
ζ	correction factor diffusion coefficients	-
η	Overpotential	V
η_A, η_C	Anode and cathode overpotential	V
$\eta_{j,i}$	Dynamic viscosity of species i in phase j	Pa s
θ	Surface coverage of Pt-Cl species	-
κ_M	Ionic conductivity membrane	$\frac{\text{S}}{\text{m}}$
λ	Membrane water content	-
λ_i	Thermal conductivity of species or part i	$\frac{\text{W}}{\text{mK}}$

μ	Reduced mass of two gas molecules	-
μ_i	Dipole moment of species i	A s m
$\mu_{red,i,j}$	Reduced dipole moment of species i and j	-
ν_i	Stoichiometric coefficient	-
ξ	Drag coefficient membrane	-
ξ_{exp}	Experimental uncertainty	-
ρ_i	Density of species i	$\frac{\text{kg}}{\text{m}^3}$
σ	Collision diameter	m
τ	Tortuosity	-
ϕ_M	Potential loss in membrane	V
ϕ_{Nafion}	Ionomer volume fraction in CL	-
ϕ_{ORR}	Thiele modulus in the agglomerates for ORR	-
ϕ_{RI}	Potential loss within the CL, GDL and plate on both sides	V
χ	Scaling coefficient	-
Ω	Collision integral	-

Latin symbols

A	Electrode area	m^2
a	Eucken correction factor	$\frac{1}{\text{K}}$
a	Internal area	$\frac{\text{m}_{\text{active}}^2}{\text{m}^3}$
a^μ	Specific internal area of the agglomerates (microscale)	$\frac{\text{m}_{\text{active}}^2}{\text{m}_{\text{agg}}^3}$
a_i^μ	Activity of species within agglomerates	$\frac{\text{mol}}{\text{m}^3}$
b	Eucken correction factor	-
\dot{B}	Exergy flow	$\frac{\text{J}}{\text{s}}$
\dot{B}_{chem}	Chemical exergy flow	$\frac{\text{J}}{\text{s}}$
b_{chem}	Molar chemical exergy	$\frac{\text{J}}{\text{mol}}$
\dot{B}_{phys}	Physical exergy flow	$\frac{\text{J}}{\text{s}}$
b_{spec}	Specific exergy	$\frac{\text{J}}{\text{kg}}$
C	Absorption capacity ionic liquid	$\frac{\text{mol}}{\text{Pa m}^3}$
C_{DL}	Double layer capacity	$\frac{\text{F}}{\text{m}^2}$
c_i	Concentration of species i	$\frac{\text{mol}}{\text{m}^3}$
c_i^∞	Concentration of species i in bulk solution	$\frac{\text{mol}}{\text{m}^3}$
$c_{O_2,ref}$	Oxygen reference concentration at 1 bar partial pressure and 333 K	$\frac{\text{mol}}{\text{m}^3}$
c_P	Heat capacity	$\frac{\text{J}}{\text{kg K}}$
$\overline{c_P}$	Mass weighted average heat capacity of mixture	$\frac{\text{J}}{\text{kg K}}$
D	Ability for desorbing a species dissolved in the ionic liquid	-

d_i	Thickness of part i	m
$D_i^{w,\infty}$	Diffusion coefficient of species i in bulk water	$\frac{\text{m}^2}{\text{s}}$
D_i^w	Diffusion coefficient of species i in the aqueous solution-filled pores of the membrane	$\frac{\text{m}^2}{\text{s}}$
$D_i^{\mu,eff}$	Effective Diffusion coefficient of species i in the agglomerates	$\frac{\text{m}^2}{\text{s}}$
D_{ij}^{eff}	Stefan-Maxwell diffusion coefficients	$\frac{\text{m}^2}{\text{s}}$
$\overline{D_{ij}^{eff}}$	Diffusion coefficients in the inverted solutions of the Stefan-Maxwell equations	$\frac{\text{m}^2}{\text{s}}$
D_{iM}^{eff}	Knudsen diffusion coefficient of species i	$\frac{\text{m}^2}{\text{s}}$
D_W	Diffusion coefficient of water in Nafion	$\frac{\text{m}^2}{\text{s}}$
D_W^0	Pre-factor, diffusion coefficient of water in Nafion	$\frac{\text{m}^2}{\text{s}}$
E_c^{rev}	Activation energy ORR at reversible cell potential	$\frac{\text{J}}{\text{mol}}$
E_{cell}	Cell potential vs reversible hydrogen electrode	V
E_{OC}	Open circuit potential	V
E_{ORR}, E_{HClOR}	Effectiveness factor in the agglomerates for the ORR and HClOR	-
E_c^{rev}	Activation energy ORR at reversible cell potential	$\frac{\text{J}}{\text{mol}}$
EW	Equivalent weight of membrane	$\frac{\text{kg}}{\text{mol}}$
F	Faraday's constant	$\frac{\text{A s}}{\text{mol}}$
f	Water volume fraction membrane	-
f_{int}	Internal degrees of freedom	-
f_{trans}	Translational degrees of freedom	-
$\Delta_R G^\circ$	Standard Gibbs free energy of reaction	J

$\Delta_R g^\circ$	Molar standard Gibbs free energy of reaction	$\frac{\text{J}}{\text{mol}}$
$g_{(\theta_1, \theta_2, \varphi)}$	Angular dependent parameter	-
$\Delta_R H$	Reaction enthalpy	J
H_i	Henry constant of species i	$\frac{\text{Pa m}^3}{\text{mol}}$
h_v	Interstitial heat transfer coefficient	$\frac{\text{W}}{\text{m}^3 \text{ K}}$
i	Electric current	A
j	Current density	$\frac{\text{A}}{\text{m}^2}$
$j_{o,s}$	Exchange current density ORR	$\frac{\text{A}}{\text{m}^2}$
$j_{o,s}^*$	Prefactor of the ORR exchange current density	$\frac{\text{A}}{\text{m}^2}$
J_i	Diffusive flux of species	$\frac{\text{mol}}{\text{m}^2 \text{ s}}$
j_{limit}	Limiting current density	$\frac{\text{A}}{\text{m}^2}$
K'	Equilibrium constant for chloride adsorption/desorption	$\frac{\text{m}^3}{\text{mol}}$
K_0	Potential independent prefactor of equilibrium constant K'	$\frac{\text{m}^3}{\text{mol}}$
K_0^*	Potential and temperature independent prefactor of equilibrium constant K'	$\frac{\text{m}^3}{\text{mol}}$
k_A	Rate constant of Tafel step for the HClOR	$\frac{\text{mol}}{\text{m}^3 \text{ s}}$
k_G^{eff}, k_L^{eff}	Effective gas and liquid-phase permeability	m^2
$K_{M,i}$	Partitioning coefficient of species i between the bulk solution and the membrane	-
K_{LLE}	Partitioning coefficient of chlorine between the aqueous and the organic phase	-
$k_{ORR}^{\mu,0}$	Standard reaction rate ORR	$\frac{1}{\text{s}}$
$k_{r,G}, k_{r,L}$	Relative gas- and liquid-phase permeability	-

k_{sat}	Saturated permeability	m^2
L	Cathode catalyst (Pt) loading	$\frac{g}{m^2}$
M	Molar Mass	$\frac{kg}{mol}$
m	Mass of one molecule	kg
$M', M_\eta, M_{D_{ij}}, M_\lambda$	Subsets of Lennard-Jones parameters	-
N_i	Molar flux of species i	$\frac{mol}{m^2 s}$
\dot{n}_i	Molar flow rate of species i	$\frac{mol}{s}$
p_c	Capillary pressure	Pa
P_{el}	electrical power input of the electrochemical reactor	W
p_i^j	Pressure of species i in layer j	Pa
p_L	Liquid-phase pressure	Pa
P_{sat}	Saturation pressure of water	Pa
p_{tot}	Total gas pressure	Pa
\dot{Q}	Heat flow	$\frac{J}{s}$
R	Universal gas constant	$\frac{J}{mol K}$
R	Total thermal resistance	$\frac{K}{W}$
r	Distance	m
R_{agg}	Agglomerate radius	m
r^μ	Reaction rate on the microscale	$\frac{mol}{s m^3}$
S	Entropy	$\frac{J}{K}$

S	Selectivity ionic liquid	-
S_L	Liquid-phase saturation	-
$S_{L,irr}$	Irreversible liquid-phase saturation	-
T	Temperature	K
T^*	Reference temperature ORR	K
T_a	Reference temperature for the exergy analysis	K
T_{in}, T_{wall}	Feed and wall temperature	K
t_i^w	Transference number of species i in the aqueous solution-filled membrane pores	-
V	Gas channel volume	m^3
V_0	Molar volume of liquid water	$\frac{m^3}{mol}$
v_d	Pore velocity	$\frac{m}{s}$
v_{H_2O}	Water crossover through membrane	$\frac{mol}{s}$
V_M	Molar volume of dry membrane	$\frac{m^3}{mol}$
\dot{V}	Volumetric flow rate	$\frac{m^3}{s}$
w_i	Weight fraction of species i	-
X	Conversion of HCl	-
x_i	Mole fraction of species i in the liquid phase	-
y_i	Mole fraction of species i in the gas phase	-
z_i	Charge number of species i	-

Abbreviations

aCL, cCL	Anode and cathode catalyst layer
aGC, cGC	Anode and cathode gas channel
aGDL, cGDL	Anode and cathode gas diffusion layer
CE	Chapman Enskog
CE	Counter electrode
ECSA	Electrochemically active surface area
EW	Equivalent weight
GC	Gas channel
GDE	Gas diffusion electrode
GHG	Greenhouse gas
HClOR	HCl oxidation reaction
HDL	Hydrodynamic diffusion layer
HER	Hydrogen evolution reaction
IL	Ionic liquid
IUPAC	International Union of Pure and Applied Chemistry
LJ	Lennard-Jones
MDI	Methylene diphenyl diisocyanate
MEA	Membrane electrode assembly
OCV	Open-circuit voltage
ODC	Oxygen depolarized cathode
ODE	Ordinary differential equation
OER	Oxygen evolution reaction
ORR	Oxygen reduction reaction
PEM	Polymer electrolyte membrane
RH	Relative humidity
RHE	Reversible hydrogen electrode
RT	Room temperature
TDI	Toluene diisocyanate
VLE	Vapor-liquid equilibrium

WE Working electrode

1 Introduction

1.1 The role of HCl oxidation within the chemical industry in the light of climate change

In the light of climate change and the global goal to limit the average temperature increase to 2 °C compared to pre-industrial levels, the European Union has set the goal of reducing greenhouse gas emissions to 80 - 95% below the levels of 1990 (Boulamanti 2017). Since the chemical and petrochemical industry is the third largest industrial greenhouse gas (GHG) emitter and responsible for 19.5% of the overall European industrial energy consumption, the European Commission published a report, in which technological advancements for this sector are proposed. The advancements are projected to save 72.5 Mt CO₂ equivalents of GHG emissions as well as 225 PJ of energy, which corresponds to a 36% and 4% reduction compared to the business-as-usual (BAU) scenario (Boulamanti 2017), respectively.

The majority in energy savings are predicted to come from reduced electricity and fuel consumption and only 14% of it from cutting down the demand in feedstocks, underlining the importance of developing more energy efficient chemical processes. These advancements discussed in (Boulamanti 2017) focus on the production processes of 26 base chemicals that make up for the vast majority of the overall energy demand and GHG emissions of the sector. According to this report and a similar study by Dechema (Bazzanella 2017), Cl₂ is the base chemical, whose production is responsible for not only the highest GHG emissions, more than 80 Million tons CO₂ equivalents in 2015 (Bazzanella 2017), but also the highest energy utilization with 35 TWh of electrical energy consumed in 2010, which corresponds to 17% of the total electricity consumption of the chemical industry in Europe (Boulamanti 2017). Cl₂ is widely used for the production of organic solvents, monomers and chemicals for water treatment and has a capacity of 66 million tons of Cl₂ worldwide in 2014, mainly produced by brine electrolysis (Rohan 2015, Boulamanti 2017).

However, the brine electrolysis is not the only source of chlorine. One third of all substances produced with the aid of chlorine do not contain Cl₂ themselves and 50% of the employed Cl₂ is being discharged in form of side products like HCl or chloride salts (Pérez-Ramírez 2011). A great example process with a further growing industrial relevance is the isocyanate production (Pérez-

Ramírez 2011). The most important isocyanate is methylene diphenyl diisocyanate (MDI) with a production capacity of 4.6 million tons in 2011 and a growth rate of 5%, followed by toluene diisocyanate (TDI) with a production volume of 3 million tons in 2013 (Sonnenschein 2015, Thyssenkrupp 2012, Merchant Research 2015). Both, MDI and TDI are mostly used in the production of polyurethanes. In their production, phosgene, which is synthesized from Cl_2 and carbon monoxide, is employed as a reactant. Therefore, for each mole of TDI and MDI, two moles of Cl_2 are consumed and four moles of HCl emerge as a byproduct. Since processes that potentially consume HCl, like the production of PVC, are growing at a much slower rate, the market for this byproduct is over-saturated (Pérez-Ramírez 2011, Martínez 2015). The most feasible and sustainable solution to this is the electrochemical or heterogeneously catalyzed oxidation of HCl to Cl_2 , which is then recycled back into the above-mentioned processes (Ooms 2010). The oxidation of HCl hence poses another important source of Cl_2 in the chemical industry (Clements 2010).

While the brine electrolysis still makes up for most of the chlorine production, the HCl emerging from the above-mentioned isocyanate production alone, not even taking into account the synthesis of halogenated solvents and other chlorine-consuming processes, allows for the production of ca. 5 Million tons of Cl_2 from gaseous HCl per year. This is equivalent to 8% of the overall chlorine production volume and becomes of relevance when looking at the energy consumption of the brine electrolysis compared to the electrochemical oxidation of HCl. The up to now most efficient industrially employed electrochemical process for the latter one is the Bayer-UHDENORA process, employing hydrochloric acid as feedstock. The electrical energy demand of the liquid-phase reactor of this process is $1070 \text{ kWh/t}_{\text{Cl}_2}$, which is 40% less than the electricity consumption of a membrane-based brine-electrolysis reactor, even when employing an oxygen depolarized cathode (ODC) (Bazzanella 2017, Thyssenkrupp 2012, Paidar 2016). In recent years the concept of a gas-phase reactor, directly oxidizing gaseous hydrogen chloride, has been investigated (Martínez 2015, Kuwertz 2013). With an electrical energy demand of $730 \text{ kWh/t}_{\text{Cl}_2}$ (Kuwertz 2013, Martínez 2015), this reactor allows for another 31% savings in the electrical energy consumption compared to the Bayer UHDENORA variant, which is equivalent to a 60% lower electricity consumption per ton of Cl_2 compared to the most efficient variant of the brine electrolysis. Whether the above mentioned 5 million tons of Cl_2 would be produced via the HCl

gas-phase electrolysis or the classical brine electrolysis would hence change the electricity consumption of the overall chlorine sector by 5%. Considering that various industrial brine electrolysis plants are not yet equipped with the energy efficient membrane + ODC technology and that the isocyanate production is only one of various Cl_2 consuming processes with HCl as a byproduct, the possible impact is likely even higher. Please note however, that these estimations are only based on the electricity consumption of the reactor. In chapter 2.5 the influence of subsequent separation steps on the energy savings are discussed in more detail.

Due to the technological maturity of the brine electrolysis, the European Commission (Boulamanti 2017) sees only a moderate potential for the Cl_2 production to impact the overall GHG emissions and energy consumption of the chemical industry sector and most of this potential is predicted to come from a decarbonization of the electricity employed in the brine electrolysis (Bazzanella 2017). However, considering the significant differences in the electricity consumption between the gas-phase electrolysis of HCl and the classical brine electrolysis as well as the size and growth rate of the polyurethane and related markets, the gas-phase electrolysis of HCl harbors the potential for major and so far unexpected reductions of the energy consumption and GHG emissions in the chlorine sector.

The gas-phase electrolysis is therefore not only an economically and energetically more feasible option for HCl recycling within an isocyanate production site compared to the state-of-the-art Bayer UHDENORA process, but can also play an important role in reaching the European and worldwide climate goals, when viewed as an integral part of the overall chlorine industry. However, currently the HCl gas-phase electrolysis has only been investigated on a laboratory scale and no (published) attempts have been made to further investigate the industrial applicability of this technology. For this very reason, the present work focuses on the development of a novel, energy efficient and industrially applicable process for the gas-phase electrolysis of HCl.

To allow for a better understanding of this technology in the overall historical context of the industrial HCl oxidation, a brief introduction of these historical developments is given in the following before going into more detail about the technology itself.

1.2 Developments in the industrial oxidation of HCl to Cl₂

While the present work focuses on the electrochemical oxidation of HCl, it should be noted that there is a heterogeneously catalyzed alternative, the Deacon-like processes, which were described in detail by Ramirez *et al.* (2011). In general, the heterogeneously catalyzed variants have the advantage of a significantly lower energy demand and therefore lower production costs. The energy consumption of the Sumitomo process (by Sumitomo chemical Co., Ltd.) for example is 85 % lower than that of the Bayer UHDENORA process (Iwanaga 2004, Seitsonen 2010). This is due to the fact that the electrochemical reactors require a significant amount of electrical energy in order to reach industrially relevant current densities of 5000 A/m² (Pérez-Ramírez 2011, Kuwertz 2013). However, the investment costs for the electrochemical process are markedly lower. Furthermore, the modularity of the electrochemical variant offers a flexible production capacity and ease of scalability which makes it very attractive in small scale plants or volatile economic settings (Pérez-Ramírez 2011, Kuwertz 2013). Especially in the context of the current transition from fossil fuels to renewable energy sources, the electrolysis of HCl allows for employing the electricity stemming from these renewable sources for a more green and sustainable production of Cl₂ as shown in Figure 1.1. This fits well into the findings of the above discussed report of the European Commission suggesting the stronger integration of electricity generated by renewable resources into the production processes of the chemical industry (Boulamanti 2017).

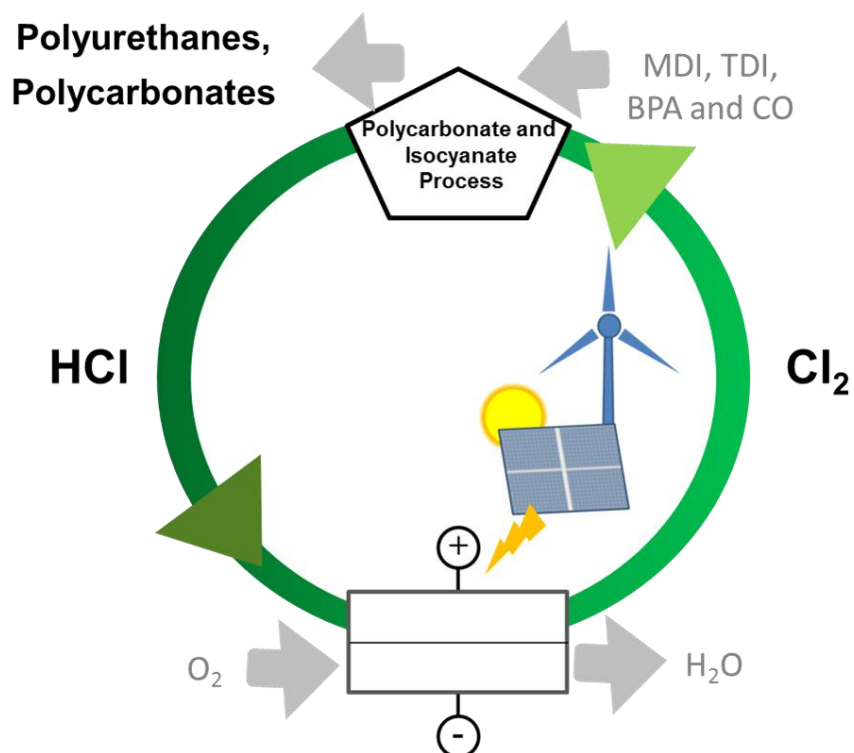
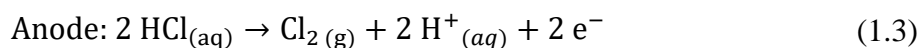
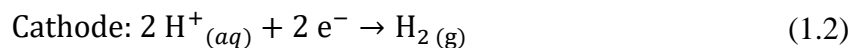
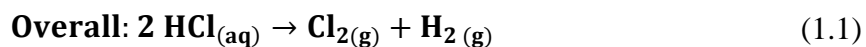


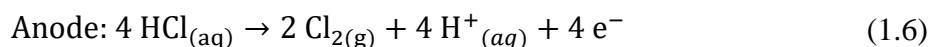
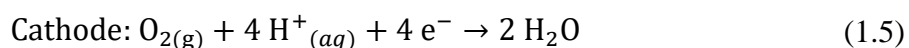
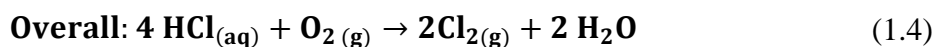
Fig. 1.1, Scheme for the utilization of renewable energy sources for recycling HCl to Cl₂, which then again enters into main industrial processes like the polyurethane production. Adopted from (Bechtel 2018a) with permission from John Wiley and Sons.

The electrochemical recycling of Cl₂ from HCl was developed in 1948 and has been industrially employed from the 1960s on in the form of the Bayer-Uhde-Höchst process, which is based on the diaphragm electrolyzer technology (Jörissen 2014) utilizing aqueous hydrochloric acid as a reactor feed. In the cathode chamber, hydrogen is produced, following the overall stoichiometry depicted in (eq. 1):



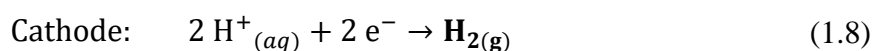
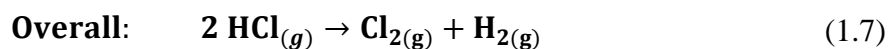
A more recent process variant based on a patent by Bayer (now Covestro), from now on referred to as the Bayer UHDENORA process (R. Weber 2006), is offered by thyssenkrupp Uhde Chlorine Engineers, which is a joint venture between thyssenkrupp Industrial Solutions and Industrie De Nora uniting the electrolysis plant businesses of the formerly separated entities thyssenkrupp

Electrolysis, UHDENORA and Chlorine Engineers. This process is based on the membrane electrolyzer technology employing an oxygen depolarized cathode (ODC), which reduces the energy consumption of the electrochemical reactor by 30% compared to the Bayer-Uhde-Höchst process. Hence the overall stoichiometry reads as follows:



The Bayer UHDENORA process is also based on a liquid-phase reactor utilizing hydrochloric acid as a feed and is the up to now most efficient industrially employed electrochemical variant. A more detailed discussion of this process follows in chapter 2. Please note that in the present work, the term liquid-phase reactor refers to a reactor with a liquid electrolyte being fed into the anode chamber.

In addition to the liquid-phase electrolysis of hydrochloric acid, there have been several attempts to directly oxidize gaseous HCl. The first gas-phase reactor that was realized in a pilot scale plant, was developed and patented by Dupont in 1993 (Trainham 1993). While gaseous hydrogen chloride is converted to chlorine in the anode compartment of the cell, the protons diffusing through the proton exchange membrane are reduced forming hydrogen at the cathode, following the stoichiometric scheme



However, this process has never been industrially commercialized. Recently, Kuwertz *et al.* (2013) and Martínez (2015) developed a gas-phase reactor in which the anode reaction is equivalent to the one proposed by Dupont, on the cathode side however, an ODC is employed. Hence, oxygen and the protons permeating through the membrane are forming water at the cathode catalyst. The stoichiometry is identical to equation 1.4 with the exception that gaseous and not aqueous HCl is oxidized. The use of an ODC greatly reduces the cell potential (Thyssenkrupp 2012). A disadvantage however, consists in the more sluggish oxygen reduction reaction (ORR) in

comparison to the hydrogen evolution reaction (HER) (J. L. Zhang 2006) as well as a more difficult water management, which so far restricted the practical operation to lower current densities of 4000 A/m² at most (Kuwertz 2013). In comparison, the Bayer UHDENORA reactor operates at 5000 A/m² (Thyssenkrupp 2012). The cell potential of the reactor developed by Kuwertz *et al.* (2013) is -0.97 V at a current density of 4000 A/m² and a temperature of 313 K compared to values ranging from -1.4 to -1.7 V for the Dupont reactor at the same current density (Trainham 1993), depending on the catalyst and operating conditions, and ca. -1.4 V for the Bayer UHDENORA process at 5000 A/m² (Martínez 2015, Thyssenkrupp 2012). This makes the gas-phase reactor employing an ODC the most energy efficient variant by far.

Please note that Zhao *et al.* (2017a,b) proposed two alternative cathode reactions employing a Fe³⁺/Fe²⁺ and I₃⁻/I⁻ redox mediation system. The respective ion being reduced through the electrochemical reaction is oxidized by feeding gaseous oxygen into the catholyte tank and thereby regenerated to again take part in the electrochemical reaction. The advantage of this mediation system is a low cell potential of -0.64 V for the Fe³⁺/Fe²⁺ pair and -0.94 V for the I₃⁻/I⁻ pair at 4000 A/m². Additionally, no expensive catalyst is needed. However, a major disadvantage turned out to be the significant performance decay rate. After an operation time of 80 h in the Fe³⁺/Fe²⁺ case (Y. G. Zhao 2017a) and only 17 h in the I₃⁻/I⁻ case (Y. G. Zhao 2017b), the cell potential rose to almost 1.2 V. The prominent decay is most likely caused by the presence of cations which strongly reduce the proton conductivity of the membrane. Even in the I₃⁻/I⁻ system, it can be assumed that the decay is a consequence of the counter ion K⁺, as Hongsirikarn *et al.* (2010) showed that not only iron cations but also Na⁺ significantly reduces the membrane conductivity. This substantial decay rate makes both reactor variants proposed by Zhao *et al.* (2017a,b) inapplicable for an industrially scaled process in their current state. All three variants of the gas-phase reactor are visualized in Figure 1.2.

The HCl entering the anode compartment of the cell diffuses through the anode gas diffusion layer (aGDL) towards the anode catalyst layer (aCL) where it is converted to chlorine. In the opposite direction, the product Cl_2 itself diffuses through the aGDL and leaves the reactor together with unconverted HCl. In a similar manner, the oxygen entering the cathode compartment of the cell diffuses towards the cathode catalyst layer (cCL), where it is being reduced forming water with the protons that are emerging from the HCl oxidation reaction (HClOR) on the anode side and are permeating through the ionomer membrane in-between the two catalyst layers. Ideally, the membrane is only permeable for protons and water. The latter one is transported by means of a hydraulic flux, a diffusive flux and an electroosmotic flux caused by the migration of protons through the membrane. The concentration gradient of water is caused by the humidification of the oxygen stream entering the cathode compartment as well as the water emerging in the cCL as a consequence of the ORR. Please note that depending on the occurrence of temperature or pressure gradients and the condensation/evaporation of water, further driving forces can become relevant in the transport of reactants and products, which are discussed in detail in the course of this work, but are left out at this stage to better visualize the overall working principle of the electrolyzer.

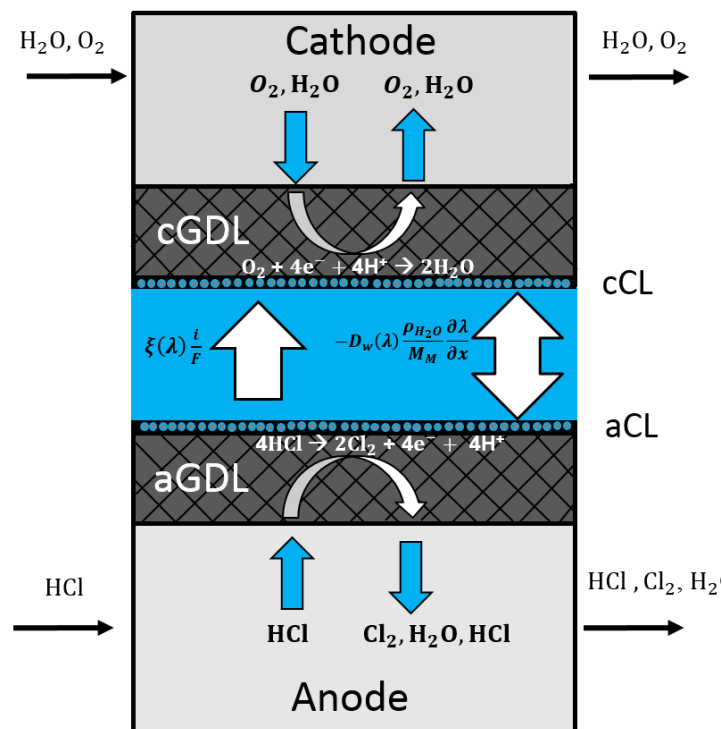


Fig. 1.3, Working principle and components of the gas-phase reactor adopted from (Bechtel 2020a).

1.4 State-of-the-art and open questions

Kuwertz *et al.* (2013) and Martínez (2015) showed that the energy demand of the gas-phase reactor is significantly lower than the one of liquid-phase reactor employed in the Bayer UHDENORA process. However, the implications of the gas-phase reactor on the efficiency of the overall electrolysis process, taking into account all necessary separation and purification steps, have not been investigated so far. Since the absence of significant amounts of water in the anode outlet stream of the gas-phase reactor leads to a different separation problem compared to the Bayer UHDENORA process, an important, not yet answered question is, whether the efficiency advantage of the electrochemical gas-phase reactor can be maintained on the overall process level.

In addition to the full-cell setup by Kuwertz *et al.* (2013) employing an ODC, Martínez *et al.* (2013, 2014, 2015) developed a half-cell reactor focusing on both half-cell reactions separately, the HClOR with H₂ emerging on the cathode side, similarly to earlier experiments by Trainham *et al.* (1993) and Eames and Newman (1995), as well as the ORR. This half-cell reactor served the purpose of a more detailed investigation of both half-cell reactions and is hence not to be seen as an alternative reactor concept for an industrial application of the HCl gas-phase electrolysis. The experiments of both authors delivered important first information about the feasibility of the gas-phase electrolysis and the influence of different process parameters on the performance of the reactor. However, various phenomena observable in their experimental polarization data and the influence of process conditions and structural parameters of the reactor on these phenomena are not yet understood. In the following, the phenomena and open questions with the most significant impact on the industrial applicability as well as efficiency of the HCl gas-phase electrolysis are introduced.

In the reactor setup of Kuwertz *et al.* (2013) employing an ODC, a limiting behavior can be observed at current densities of more than 4000 A/m². Hence, a stable operation at a current density of 5000 A/m², like in the Bayer UHDENORA process, has not yet been achieved but is highly relevant for the feasibility of this process in an industrial application (Thyssenkrupp 2012). Such a limiting behavior can also be noticed in the half-cell measurements of Martínez *et al.* (2013, 2014, 2015), albeit at current densities of 5000 to 9500 A/m², depending on the reactor temperature

and catalyst. The origin of the limiting behavior in both cases is not yet understood. Due to its significant importance, relevant literature discussing this phenomenon is briefly evaluated in the following, first for the HClOR and subsequently for the full-cell setup employing an ODC.

A similar limiting behavior as in the half-cell measurements by Martínez *et al.* (2013, 2014, 2015), was already observed in the first investigation of the gas-phase HClOR by Trainham *et al.* (1993), who however did not offer an explanation. The first attempt in this direction was made by Eames *et al.* (1995), who developed a simplified numerical reactor model for the HClOR. They predicted the experimentally observed limiting behavior to be due to a dehydration of the membrane adjacent to the aCL and the corresponding strong increase in its ohmic resistance. However, this does not explain why the experimental investigations of Martínez *et al.* (2013, 2014, 2015) with online ohmic drop correction still show the above-mentioned limiting behavior. These authors attributed this effect to mass-transfer limitations on the anode side. However, their supposedly mass transfer-limited current densities vary significantly depending on the catalyst system and loading, raising the question, if rather kinetic effects play an important role.

In regards to the reaction kinetics, Martínez (2015) discussed two possible microkinetic mechanisms, a Heyrovsky-Volmer and Heyrovsky-Tafel mechanism, as known from literature on the brine electrolysis (Conway 1979, Gileadi 1993). For both mechanisms, the authors assumed the latter step (the Volmer or Tafel step) to be rate determining, while the adsorption and desorption of species on the catalyst surface in the Heyrovsky step was assumed to be fast and hence quasi-stationary. While Martínez (2015) concluded the Heyrovsky-Tafel mechanism to be the valid one, the Tafel slope at high surface coverages as well as the potential dependent reaction orders expected for this mechanism did not match with their experimentally determined values. Hence, the reaction pathway of the gas-phase HClOR and its impact on the observed limiting behavior cannot yet be determined with sufficient certainty. Certainly, Kuwertz *et al.* (2016a) showed that the overpotential of the ORR contributes more significantly to the overall cell potential in their full-cell reactor than the HClOR at intermediate current densities of up to 4000 A/m^2 . However, especially at higher, yet still technically relevant current densities, the limiting behavior of the HClOR has the potential to significantly impede the performance of the electrolyzer and a detailed understanding of its origins is therefore critical for the further development of this process.

As mentioned above, a limiting behavior was also observed in the experiments of Kuwertz *et al.* (2013) employing an ODC. However, since these limiting current densities are markedly lower and exhibit a different temperature dependence than the ones observed in the HClOR experiments of Martínez (2015), the cause is likely to be different. Kuwertz *et al.* (2016b) suggested flooding in the cathode chamber, hindering the transport of oxygen to the active catalyst sites, as a possible explanation. In classical hydrogen PEM fuel cells, another widely discussed cause for such a limiting behavior is dehydration of the membrane and adjacent catalyst layers, especially when the anode feed stream is not humidified as in the setup of Kuwertz *et al.* (2013). Based on the currently available data, a precise determination of which physical mechanism, flooding, dehydration or possibly the limiting behavior of the HClOR, is causing the observed limiting current densities in the experiments of Kuwertz *et al.* (2013, 2016a,b,c), is not possible.

A last distinct phenomenon in the polarization data obtained with the full-cell setup is the significantly increased open-circuit voltage (OCV) of the ORR as well as a markedly higher activation overpotential. Kuwertz *et al.* (2016a) experimentally determined the OCV of the ORR half-cell reaction to be between 680 and 750 mV at a temperature of 313 K, while in classical hydrogen PEM fuel cells, OCVs of 1 V and higher can be achieved at the same temperature (J. Zhang 2006). In the work of Kuwertz *et al.* (2013, 2016a,b,c) and Martínez (2015), platinum dispersed on carbon was employed as the anode and cathode catalyst. It is well known that the ORR on platinum-based catalysts is severely impeded by both the presence of HCl in the oxygen feed stream (Baturina 2011) or, in the case of measurements in a liquid electrolyte, chloride anions in solution (Schmidt 2001).

A possible explanation for the reduced performance of the ORR in the experiments of Kuwertz *et al.* (2013) is hence the crossover of HCl or Cl₂ from the anode to the cathode and consequent poisoning of the platinum-based catalyst. Motupally *et al.* (2002) concluded by means of measuring the decrease of the pH in the cathode chamber of a reactor similar to the half-cell investigated by Martínez (2015) that up to 0.1% of the HCl fed into the reactor crosses over to the cathode side. Since liquid water is fed into the cathode chamber of this reactor type (please see Figure 1.2), the water household of the cell, and hence the transport of species through the membrane, differs significantly from the one in the reactor type proposed by Kuwertz *et al.* (2013) employing an ODC. Furthermore, it is not yet clear whether mainly the crossover of HCl or Cl₂

caused the decrease in the pH in the cathode chamber in the experiments of Motupally *et al.* (2002). Due to the significant impact on the performance of the ORR, the extent to which HCl and Cl₂ are crossing over under realistic process conditions of the gas-phase electrolysis and the quantitative impact of this crossover on the performance of the ORR as well as the dynamics of this catalyst poisoning process, pose another important open question. Lastly, this emphasizes the importance of future investigations on alternative catalyst materials, as they are already used in the liquid-phase reactor of the Bayer UHDENORA process, and the influence of the catalyst on the energy efficiency and longevity of the gas-phase electrolyzer.

Building on these open questions concerning the overall feasibility and efficiency of the gas-phase electrolysis on the process level as well as the interplay and relevance of various physicochemical processes within the reactor cumulating into the above discussed phenomena like the limiting behaviors or performance losses, the scope of the present work is defined in the following chapter.

1.5 Scope and outline of the work

A major disadvantage of the electrolysis of HCl compared to its heterogeneously catalyzed oxidation has so far been the significantly higher energy demand. The goal of this work is hence to propose a novel, energy efficient and industrially feasible process for the electrolysis of gaseous HCl as a contribution to reducing the energy demand and GHG emissions of the chemical industry, more particularly the chlorine sector. This includes the development and evaluation of new separation strategies tailored to the gas-phase reactor and benchmarking the overall process versus the current state-of-the-art, the Bayer UHDENORA process, in order to transform the gas-phase electrolysis of HCl from the current stage of a reactor concept to an industrially feasible process. The second major focus of this thesis is the investigation of the most relevant physicochemical processes taking place within this gas-phase reactor as well as their impact on the reactor performance. Based on these insights, first systematic optimization strategies are to be developed in order to further increase the efficiency and industrial feasibility of this process.

The work is structured into the three following main parts. In the first part, addressed in chapter 2, three novel strategies for the separation of gaseous HCl and Cl₂ are proposed and flowsheet

simulations of the three novel processes, consisting of the gas-phase reactor and these three separation sequences, as well as of the Bayer UHDENORA process are carried out. Subsequently, a detailed exergy analysis is performed in order to evaluate whether the significant efficiency advantage of the gas-phase reactor over the liquid-phase reactor can be maintained on the overall process level. Additionally, the influence of process and reactor specific parameters like the single pass and overall conversion of HCl on the efficiency of the novel process variants is evaluated to lay a first foundation for determining feasible operation windows in an industrial application.

In the second part of the work, addressed in chapter 3 and 4, the development and validation of a mathematical reactor model resembling the half-cell experiment of Martínez (2015) and the full-cell setup of Kuwertz *et al.* (2013), as well as the design of an own complementary experimental setup is discussed. The numerical 1D non-isothermal two-phase agglomerate model focuses on a detailed description of the HCl oxidation reaction kinetics, a rigorous modeling of the mass transfer of all species as well as on the water household and thermal management of the reactor to enable an in-depth analysis of the phenomena discussed in chapter 1.4. Furthermore, to allow for an accurate modeling of mass transfer effects, a new method for the precise determination of diffusion coefficients, thermal conductivities and viscosities of gases based on the kinetic gas theory is developed and implemented into the numerical reactor model. Please note that while the reactor model is validated with the experimental data of Martínez (2015) and Kuwertz *et al.* (2013), the major focus of the model is not a quantitative reproduction of their experimental results but rather to understand the above-mentioned physicochemical processes and phenomena, how they are being influenced by various operating and geometrical parameters, and finally to determine their impact on the cell performance. Lastly, a mathematical model for the investigation of HCl and Cl₂ crossover in the gas-phase electrolyzer and in a liquid-phase reactor, as employed in the Bayer UHDENORA process, is developed.

The experimental setup introduced in chapter 4 allows for half-cell and full-cell investigations similar to the ones by Martínez (2015) and Kuwertz *et al.* (2013). It serves the purpose of validating the reactor model and especially the optimization strategies derived from it. Furthermore, a novel reactor concept, the alkaline electrolysis of HCl, is developed, aiming to mitigate the effects of catalyst poisoning as well as water household and thermal management challenges in the classical setup.

Lastly, in the third part, addressed in chapter 5, the combined insights from the reactor simulations and experiments are discussed. A new rate expression for the HClOR is proposed and validated and the interplay of both mass transfer and reaction kinetics as well as their influence on the limiting behavior observed in the experiments of Martínez (2015) are investigated. In regards to the full-cell setup, the thermal management and water household of the reactor are analyzed to investigate flooding as well as membrane dehydration and how both effects impact the performance of the reactor, especially the experimentally observed limiting behavior. Furthermore, various structural and operating parameters like the feed gas and coolant temperature, the catalyst loading and the thickness of both the membrane and the GDL, are systematically analyzed in regards to their impact on the above discussed phenomena. Moreover, the crossover of HCl and Cl₂ and its influence on the ORR is investigated, employing the mathematical model presented in chapter 3 and the half-cell setup introduced in chapter 4, which finally motivates the experimental investigations of alternative catalyst materials at the end of chapter 5.

Lastly, these insights are used to propose first systematic reactor optimization strategies aiming at enabling higher current densities while maintaining or further reducing the cell potential, which is an important step in making the HCl gas-phase electrolysis industrially feasible.

2 Development of an overall process for the gas-phase electrolysis of HCl

As delineated in chapter 1, the production of Cl_2 significantly contributes to the overall energy demand and GHG emissions of the European and worldwide chemical industry (Boulamanti 2017), indicating that improvements in the efficiency of producing this base chemical would be a noteworthy contribution to achieving the 2050 climate goals. While it was shown that the gas-phase reactor proposed by Kuwertz *et al.* (2013) has a significantly lower energy demand compared to the state-of-the-art liquid-phase reactor employed in the Bayer UHDENORA process, the objective of this chapter is to assess the exergy efficiency of the gas-phase electrolysis on the overall process level, taking all necessary separation and purification steps into account. Please note that major parts of this chapter are extracted from Bechtel *et al.* (2017, 2018a, 2018b, 2019a).

The anode outlet stream of the electrochemical gas-phase reactor investigated by Kuwertz *et al.* (2013) and Martínez (2015) consists mostly of Cl_2 and unreacted HCl, while the fraction of H_2O is significantly lower than in the anode outlet stream of the Bayer UHDENORA reactor, allowing for the development of new separation strategies. Consequently, three strategies are proposed to separate Cl_2 from the unreacted HCl and flowsheet simulations and a rigorous exergy analysis is carried out for these three processes as well as for the Bayer UHDENORA variant, in order to quantitatively compare their performance. The advantage of an exergy analysis versus a simple energy balance is the evaluation of all energy and work streams in regards to the maximum portion of useful work that can be gained from them, which allows for a more realistic comparison of the process efficiencies.

Before going into detail about the various processes, the general framework of the performed flowsheet simulations including necessary assumptions and process constraints as well as the theoretical concepts of the exergy analysis are explained.

2.1 Flowsheet simulations, assumptions and process constraints

In the present work, the sequential modular approach (Marquardt 1996) of the process simulation software Aspen Plus V. 8.8 is used to model first the state-of-the-art process based on literature data, as discussed in more detail in chapter 2.3, and secondly, the three novel processes ELECTRA-DIST, ELECTRA-ABS and ELECTRA-IL. These three processes are all employing the gas-phase reactor differing only in regards to the subsequent separation strategies.

All simulated processes are designed based on an MDI production site of BASF in Antwerp with a capacity of 650 kt/a (BASF 2017) and an assumed uptime of 8000 h/a, which is equivalent to 375 kt/a $\text{HCl}_{(g)}$ emerging as a byproduct that can be converted to Cl_2 by means of the here investigated electrolysis processes. The O_2 feed stream into the electrolyzer is chosen to be 82.9 kt/a, which is approximately the stoichiometrically necessary amount for converting all HCl. Please note that any amount of excess oxygen due to incomplete conversion does not impact the exergetic efficiency of the processes in the here presented analysis, as it can be recycled. The minimum purity of the obtained Cl_2 was set to 99.5 wt% equivalent to the grade 2.5 product sold by Linde (now Messer). The maximum amount of water in the Cl_2 product stream is limited to 100 ppm (mg kg^{-1}) (Ooms 2010). For both the liquid and gas-phase reactor, isobaric operation at 1.103 bar is assumed. The temperature of the gas-phase reactor is set to 313 K, at which Kuwertz *et al.* (2013) measured the lowest cell potential, and the temperature of the liquid-phase reactor is set to 328 K (R. Weber 2006, Ooms 2010).

Since the exergy demand of the processes strongly depends on the amount of converted HCl, the overall conversion must be identical in all simulations to ensure comparability and is hence set to 80%. This value is similar to the maximum conversion of Deacon-like processes and hence allows for comparability between both technologies (Hagemeyer 2018). The 20% of hydrogen chloride that are not converted, are dissolved in water, forming concentrated hydrochloric acid (37 wt%) with a purity of 99.9 wt% in all processes. This is supposed to reproduce an economically realistic scenario where a significant fraction of the employed HCl is converted to Cl_2 and the rest is either used within the Verbund in the form of concentrated acid or sold. Self-evidently, this ratio of 80:20 should and can be adjusted to the specific economic situation, which is dependent on a variety of criteria, like the market price of HCl, the geographical location of the site or the Verbund-internal

demand of hydrochloric acid (Ooms 2010). Hence, in chapter 2.5.5 the influence of the conversion on the exergy demand is systematically investigated for two of the three novel process variants to generate a first basis for such a site-specific decision process and to estimate the range of feasible conversions.

A further advantage of choosing a fixed overall conversion for the exergetic evaluation of all process variants is that all the inlet and outlet streams, with exception for waste streams and auxiliary substances, are essentially identical in all four process variants. Furthermore fixing the temperature and pressure of all streams entering and leaving the process to 298 K and 1.013 bar, if necessary by means of heat exchangers and compressors/valves, leads to identical exergies for the respective streams in all four processes. Hence, under the condition that waste and auxiliary streams are negligibly small, only the exergy of the supplied and discharged heat and electricity is relevant for comparing the exergy demand of all processes. This significantly reduces the complexity of the analysis. The exergy of the waste streams, and as a consequence also the exergy of the auxiliary substances fed into the processes, is indeed negligibly small so that the above assumption is justified.

In addition to the overall conversion, the single pass conversion for the electrochemical reactor has to be fixed. For the Bayer UHDENORA process, this value is set to 22.9% based on literature data of the actual process (Thyssenkrupp 2012, Ooms 2010). For the gas-phase electrolyzer employing an ODC, the maximum feasible single pass conversion has not yet been experimentally determined. Simulations based on the numerical reactor model presented in chapter 5.3, indicate that conversions of up to 80% are possible but require a sophisticated thermal management. Also for the DuPont pilot scale reactor (Trainham 1993), no information on the feasible single pass conversion is available. However, stable operation at current densities of 10 kA/m² was reported (Motupally 1998). Based on the underlying reason for the low single pass conversion of the liquid-phase reactor discussed in chapter 2.3, it seems reasonable that the gas-phase reactor should indeed be able to achieve significantly higher single pass conversions than the liquid-phase reactor, as predicted by the numerical model (please see chapter 5.3).

Therefore, the novel process variants were simulated at a single pass conversion of 80%. For the two process variants ELECTRA-DIST and ELECTRA-ABS, additional simulations at a single pass conversion of 60% were carried out to evaluate whether the novel processes are also feasible

at intermediate conversion levels. Please note that a constant cell potential of 1 V corresponding to an energy consumption of 730 kWh per ton of chlorine is chosen for the gas-phase reactor in this analysis. This value is based on the experimentally determined potential of ca 0.98 V at a current density of 4000 A/m² at 313 K in the work of Kuwertz *et al.* (2013). However, the HCl conversion in these experiments never exceeded 30%, so that in future investigations, the cell potential at higher conversions should be determined and substituted into the here presented exergy analysis. Since oxygen can be fed in excess and the experimentally determined overpotential of the HClOR constitutes only ca. 10 - 15% of the overall overpotential of the cell (Kuwertz 2016a), the increased HCl conversion is not expected to drastically affect the cell potential. In fact, Martínez (2015) proved in his half-cell investigations of the HClOR that reducing the concentration of hydrogen chloride in the feed stream to 40% leads to an overpotential increase of less than 0.07 V at a current density of 4000 A/m². This indicates that a conversion of 60% and more in the gas-phase reactor is possible with only a relatively small increase in the cell potential, so that the simplifying assumption of a conversion independent cell potential seems reasonable.

While the Bayer UHDENORA reactor operates at a current density of 5000 A/m², Kuwertz *et al.* (2013) only reached 4000 A/m² before the onset of a limiting behavior. However, in own experiments presented in chapter 5.3.4, it is shown that 5000 A/m² can also be achieved with the gas-phase reactor employing an ODC under optimized operating conditions at a comparable cell potential as in Kuwertz *et al.* (2013), so that the differences in the operating current densities between both processes can be neglected in this exergy analysis. All parameters discussed above are summarized in table 2.1.

Table 2.1, Conditions for the flowsheet simulations and exergy analysis.

Parameter	Value
HCl feed	375 kt/a
Purity Cl ₂	99.5% and < 100 ppm water
Purity hydrochloric acid (byproduct)	99.9%
Overall conversion	80%
Single pass conversion	22.9% liquid-phase reactor, 60 and 80% gas-phase reactor
Reactor temperature	313 K gas-phase reactor
Energy demand of the reactor	1070 kWh/t _{chlorine} liquid-phase reactor at 5000 A/m ² , 730 kWh/t _{chlorine} gas-phase reactor at 4000 A/m ² , but > 5000 A/m ² shown to be feasible in chapter 5.3.4

2.2 Exergy analysis

As stated in the chapter 2.1, the difference in the exergy input and output of all processes can be calculated by only considering all work and heat streams entering and leaving the overall system envelope. While the electrical energy needed for the compressors or the electrochemical reactor consists of pure exergy, the heat streams entering and leaving the process contain an energetic part as well. The exergy flow \dot{B} of a heat stream at constant temperature can be calculated based on equation 2.1 (Abdollahi-Demneha 2011, Querol 2013):

$$\dot{B} = \dot{Q} \left(1 - \frac{T_a}{T} \right) \quad (2.1)$$

Hereby, \dot{Q} is the heat stream, T is the temperature at which the heat is transferred and T_a is the reference temperature, which is chosen to be 298.15 K in this work. At operating temperatures below the ambient temperature the direction of the flow of exergy is opposite to the direction of

the heat flow. If the temperature is not constant, like in heat exchangers, the exergy is calculated according to equation 2.2 assuming that the operating pressure is constant:

$$\dot{B} = \int \left(1 - \frac{T_a}{T}\right) d\dot{Q} = c_p \int_{T_a}^T \left(1 - \frac{T_a}{T}\right) dT \quad (2.2)$$

with c_p being the isobaric heat capacity. As in most electrochemical processes, the electricity needed to operate the reactor contributes significantly to the overall exergy demand of the process. In addition to the electrical power demand of the reactor, the reaction heat has to be considered. Normally, the simulator Aspen Plus calculates the reaction heat and therefore the heat duty of a reactor. However, there is no electrochemical reactor unit available in Aspen Plus, so that the reaction was modeled with a homogeneous, stoichiometric reactor assuming mixing of all reactants. To account for the falsely included mixing enthalpy of the anode and cathode components the heat duty of a subsequent ideal separator in which water and oxygen are separated from HCl and chlorine is added to the heat duty of the stoichiometric reactor.

From the flowrates of oxygen and water in the cathode reactor outlet stream as well as the saturation pressure of water at 313 K of 7400 Pa, it can be deduced that most of the water exiting the reactor would be liquid, based on the simplified assumption that all water leaves the reactor through the cathode outlet. In chapter 5.3 however, polytropic operation of the reactor is investigated, which, in addition to the effect of water crossover, results in all water leaving the reactor in its gaseous state. Hence, the theoretical reaction heat $\dot{Q}_{reactor}$ is calculated for the two scenarios of all water leaving the reactor in either its gaseous or liquid state according to equation 2.3 in order to determine whether the physical state of water has a significant impact on the exergy demand of the novel processes.

$$\dot{Q}_{reactor} = \Delta_R \dot{H}^\circ X + \bar{c}_p \dot{m} \Delta T + P_{el} \quad (2.3)$$

In this equation, \bar{c}_p stands for the heat capacity of the product mixture calculated as a mass weighted mean value of the heat capacities of all involved pure substances, \dot{m} is the mass flow through the reactor, X the conversion, $\Delta_R \dot{H}^\circ$ the reaction enthalpy under standard conditions and P_{el} the electrical power input. The heat capacities and the standard enthalpies of formation are obtained from (Linstrom 2017). Please note that throughout the work, standard conditions are

defined as 298 K and 1.013 bar. Since the overall conversion of all processes is the same, the product $\Delta_R \dot{H}^0 X$ does not depend on the single pass conversion, contrary to the term $\overline{c_p} \dot{m} \Delta T$ which is a function of both the single pass and overall conversion due to the variations in the composition and mass flow.

Independently of the phase of water, oxygen is assumed to be only present in the gas phase since the mole fraction of oxygen dissolved in water at 313 K is only 0.0000187 (Wilhelm 1977). As explained above, the chemical and physical exergies of the process streams are not required for comparing the exergy demand of the considered process configurations. However, in chapter 2.5.5 of this work, the specific exergy demand per kg of produced Cl_2 , including the chemical exergies of all input and output material streams, is evaluated. Additionally, in order to analyze the exergy flows within the process and to identify the unit operations with the highest exergy loss, the chemical and physical exergy flow \dot{B}_{chem} and \dot{B}_{phys} of not only the in- and output but of all material streams are visualized in the form of a Sankey diagram exemplary in chapter 2.5.4 (Abdollahi-Demneha 2011, Querol 2013). Hence, for this specific part of the process analysis, the physical and chemical exergy of each substance stream is determined as follows.

$$\dot{B}_{phys} = \dot{H}(T, p) - \dot{H}(T_a, p_a) - T_a \left(\dot{S}(T, p) - \dot{S}(T_a, p_a) \right) \quad (2.4)$$

The chemical exergy $B_{chem,i}$ of substances present in the environment, e.g. the atmosphere or oceans, is calculated based on their concentrations within the stream in comparison to their concentrations in the environment. For substances that are not a part of the environment it is determined by generating these substances i from reactions of substances j that are existing in the environment

$$B_{chem,i} = \sum_j -\nu_j B_{j,chem}(environment) + \Delta_R G^\circ \quad (2.5)$$

where $\Delta_R G^\circ$ is the standard Gibbs free energy of reaction (Querol 2013). If a stream contains more than one substance, the mixing entropy has to be considered, leading to equation 2.6, with x_i being the molar fraction of substance i and γ_i being its activity coefficient (Abdollahi-Demneha 2011, Querol 2013). However, if the entropy term in equation 2.4 already includes the mixing entropy, it must not again be considered within the calculation of the chemical exergy:

$$B_{chem,mixture} = \sum x_i B_{i,chem} + RT_a \sum x_i \ln(\gamma_i x_i) \quad (2.6)$$

The chemical exergy of octane is extracted from (Moran 2010) and the ones for Cl₂, O₂, HCl and H₂O stem from Szargut (Szargut 2005). The chemical exergy of hydrochloric acid is a complex function of its concentration, which is indicated by the strong dependence of the chloride ion activity coefficient on the acid concentration. Hydrochloric acid with a concentration of 37 wt% as present in the discussed processes consists of 3.44 mole H₂O_(l) per mole HCl. Therefore, the chemical exergy can be determined according to equation 2.7.

$$B_{chem,37\% HCl_{aq}} = \dot{n}_{HCl} \left(b_{chem,HCl} + 3.44 b_{chem,H_2O_{(l)}} + \Delta_R g^\circ \right) \quad (2.7)$$

Here, b stands for the molar exergy of a substance and \dot{n}_{HCl} is the molar feed flow rate of hydrogen chloride. The value of $\Delta_R g^\circ$ was obtained by simulating the absorption of 1 mole HCl in 3.44 mole H₂O_(l) at standard conditions with Aspen Plus.

Please note that the here presented exergy analysis gives insights about the exergetic portion, and hence the maximum work that can be gained from every substance, heat and work stream going into and out of the process. However, whether for example such a heat stream is practically utilized in an industrial application by means of integration into the heat exchanger network also depends on site specific and financial decision factors and the heat exchanger network of the entire production process or even Verbund-site, in which the HCl electrolysis is incorporated. For this reason, no heat integration is performed in the present work, as this is only feasible under consideration of the whole production process of for example MDI or TDI.

2.3 Modeling of the state-of-the-art process

This process was modeled based on two patents by Covestro (former Bayer) (R. Weber 2006, Ooms 2010), product information by Thyssenkrupp (2012) and the work of Ramirez *et al.* (2011). All essential data is listed in Table 2.2 and the flowsheet is presented in Figure 2.1.

Table 2.2, Technical data and process conditions of the Bayer UHDENORA process according to (Thyssenkrupp 2012, R. Weber 2006, Ooms 2010).

Parameter	Value
Reactor temperature	328 K
Hydrochloric acid reactor feed concentration	14 wt%
Hydrochloric acid reactor outlet concentration	11 wt%
Temperature hydrogen chloride absorber	308 K
Concentration of hydrochloric acid product stream	37 wt%

According to Thyssenkrupp (2012) and R. Weber *et al.* (2006), the concentration of hydrochloric acid in the inlet stream of the reactor is 14%. Since the outlet concentration is not specified by the Thyssenkrupp source, the lower limit of 11% stated in the work of Ooms *et al.* (2010) and Weber *et al.* (2012) was chosen. The inlet concentration is limited by the conductivity of Nafion as a function hydrochloric acid concentration, which reaches a maximum at 10 wt% but decreases sharply at higher concentrations (Yeao 1979, Vidaković-Koch 2012). On the other side, the outlet concentration cannot be too low in order to avoid oxygen evolution, which explains the tight concentration interval at which the Bayer UHDENORA process can be operated, leading to a maximum achievable single pass conversion of 22.9% (Ooms 2010). In order to reduce the size of the recycle streams, which should have a positive impact on the energy demand and capital costs, this maximum value of 22.9% was chosen for the simulation. While it seems that the dechlorination takes part after the newly incoming hydrochloric acid is mixed with the reactor outlet stream in the basic flowsheet by Thyssenkrupp (2012), Ooms *et al.* (2010) describe the dechlorination to follow directly after the reactor outlet, which would be more efficient and was hence adapted in this simulation. There is no information available on how exactly the dechlorination is carried out, just that the obtained Cl_2 is subsequently dried, e.g with sulfuric acid or molecular sieves (Weber 2010). One possibility would be the physical separation of the gas phase in the $\text{Cl}_2/\text{HCl}_{(\text{aq})}$ mixture leaving the electrochemical reactor and subsequently drying the chlorine-rich gas phase (R. Weber 2006, Ooms 2010). Alternatively, the Cl_2 product could be

separated from the hydrochloric acid by means of distillation, either in combination with a subsequent drying step, or the distillation column could be designed to already yield sufficiently pure Cl_2 without the need of a drying step.

From a methodological viewpoint, both strategies are very similar, relying on the separation of chlorine as a result of differences in fugacities with the distillation variant leading to a higher purity due to the repeated equilibration of both phases on each theoretical stage of the column. In the present work, separation by distillation, adjusting the specifications of the column so that the chlorine product stream contains less than 100 ppm (mg kg^{-1}) water, was chosen for the following reasons. Firstly, due to the non-negligible solubility of Cl_2 in hydrochloric acid, simply separating the gas phase of the reactor outlet stream would leave 15% of the emerging Cl_2 absorbed in the liquid hydrochloric acid phase, based on solubility data by Alkan *et al.* (2005) at the reactor temperature of 313.15 K. Hence, this fraction of Cl_2 would be recycled with the diluted acid stream and would be prone to be released in the case of pressure or temperature changes in pumps or heat exchangers. This would not only pose a safety risk, but would also to some extent lead to a loss of valuable product (Ooms 2010). Increasing the temperature of the chlorine containing hydrochloric acid stream to 343.15 K would decrease the fraction of dissolved Cl_2 to 3% (Alkan 2005), but also lead to a significantly higher energy demand. While it is well possible that the method of drying the Cl_2 rich gas phase with sulfuric acid nonetheless displays a lower energy demand than the here proposed distillation, the temperature levels in the column for re-concentrating the sulfuric acid would be significantly higher, increasing the exergetic portion of the needed heat supply. Furthermore, an additional unit and substance stream would be introduced to the process in this case, impacting the capital and operating expenses. Lastly, designing the separation of Cl_2 in the state-of-the-art process as well as in the novel processes to yield a sufficient purity in regards to HCl and water traces without the introduction of more auxiliary substances like sulfuric acid allows for a well-defined comparison of the exergetic efficiency between all processes. However, if desired, both scenarios can be included in the exergy analysis in future investigations following the same method explained in this chapter.

Fig. 2.1 shows the process flow diagram for the state-of-the-art process. The split marked in red divides the dilute hydrochloric acid stream into two sub-streams that are used for the absorption of the incoming HCl and the dilution of the generated concentrated hydrochloric acid towards the

reactor inlet concentration. From the chloride ion mass balance follows that a split fraction of 9.88% of the incoming mass flow is directed towards the absorption step. The absorption of incoming HCl into the diluted acid stream takes place at a temperature of 308 K according to Thyssenkrupp (2012).

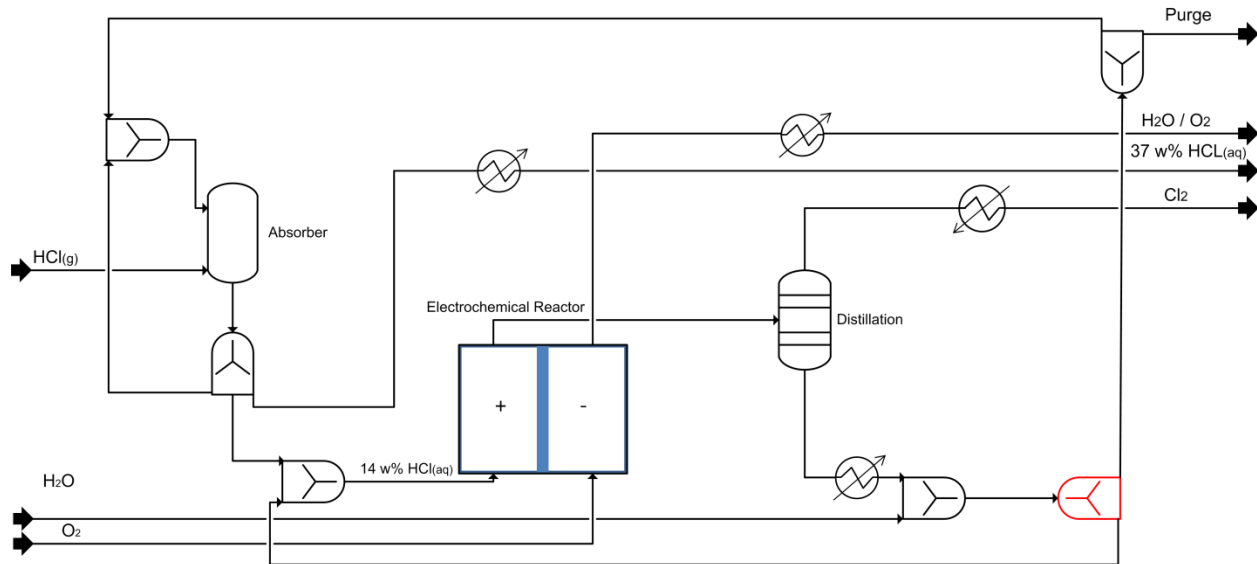


Fig. 2.1, Process flow scheme of the Bayer UHDENORA state-of-the-art process. Adopted from Bechtel *et al.* (2018a) with permission from John Wiley and Sons.

Model settings

The ENRTL-RK method, an ELECNRTL successor, was selected as a property model for the simulation of the state-of-the-art process, due to the presence of electrolyte species. This method employs an asymmetric reference state, meaning that infinite dilution of the aqueous phase is chosen as a reference state, and it collapses into the NRTL-RK method when no electrolytes are present (Tremblay 2012). Outside of the reactor, only the dissociation of HCl in water and the auto-dissociation of water are included as possible reactions in the chemistry settings. Cl₂ however, is not defined as a reactive species due to the fact that the equilibrium constant for its dissociation in water, forming hypochlorous acid and hydrochloric acid, is only about $4 \cdot 10^{-4} \frac{l^2}{mol^2}$ at 390 K (Morris 1946). Considering that the concentration of hydrochloric acid leaving the electrochemical

reactor is approximately 11 wt%, the equilibrium for the dissociation of Cl_2 is even further shifted towards molecular Cl_2 , justifying the omission of the dissociation reaction.

Both gases, HCl and Cl_2 , were defined as components obeying Henry's law. This is especially important in the case of HCl due to its low critical temperature of 325 K, which makes it non-condensable at conditions present in the distillation column (Linstrom 2018). At those temperatures, gas solubilities should be calculated by defining the gas as a Henry component or, at high pressures above 10 bar, employing an equation of state model is recommended (Aspen 2001, Carlson 1996).

2.4 Modelling of the three novel processes based on the gas-phase reactor

In the following chapters, the three newly developed processes based on the gas-phase reactor and three different methods for separating Cl_2 from unreacted HCl are discussed. In the ELECTRA-DIST process, the separation of these gases is carried out by means of a low-temperature distillation unit utilizing differences in the fugacities of both gases. The second process, ELECTRA-ABS, utilizes the difference in the solubilities of HCl and Cl_2 in a non-polar organic solvent. Subsequently, the remaining HCl residues are removed from the solvent by means of extraction with water. Finally, the ELECTRA-IL process is based on the absorption and subsequent desorption of HCl in an ionic liquid (IL), leaving essentially pure gaseous Cl_2 . Please note that while the process units are optimized within the flowsheeting software Aspen Plus in regards to their energy demand under the purity constraints discussed in chapter 2.1, the overall processes are not rigorously optimized. Since the purpose of this work is the development of an overall process for the gas-phase electrolysis of HCl as well as an assessment of its feasibility in comparison to the current state-of-the-art, a detailed optimization of the proposed processes is out of scope. However, in future investigations such an optimization is certainly of interest, which is why the following chapters not only present the final process design but also discuss important physicochemical trends and observations that led to the here presented processes and operating conditions and that serve as a basis for future rigorous optimization attempts.

2.4.1 ELECTRA-DIST process

In the classical Deacon process and its advanced successors like the Shell or UTC process, a gas mixture of Cl_2 , residues of HCl and O_2 remains after separating H_2O and most of the HCl from the reactor outlet stream. This gas mixture can be separated by compressing and cooling and thereby liquefying the Cl_2 in order to separate it from O_2 and traces of the other remaining components (Freire 1993). A similar procedure is discussed in (Foster 1982). In a patent by Gestermann *et al.* (1995) a subsequent distillation step is mentioned to separate Cl_2 from remaining amounts of HCl . When employing a gas-phase electrolyzer however, the anode outlet stream does not only contain traces but significant amounts of HCl , contrary to (Freire 1993, Gestermann 1995, Foster 1982), posing a new separation problem. Also, a simple condensation of Cl_2 like in (Freire 1993, Foster 1982) is not sufficient to separate it from HCl with the desired purity of 99.5%, since the fugacity differences between HCl and Cl_2 are significantly smaller than between Cl_2 and O_2 . Therefore, a low-temperature distillation column is used for the separation of both gases in the ELECTRA-DIST process.

In addition to the simulation at atmospheric pressure, four simulations in which the column feed was compressed to 2, 5, 8 and 10 bar were carried out, since higher column pressures, and hence increased temperatures in the condenser, facilitate cooling by allowing for the use of ammonia, propane or mixtures of propane and ethane as cooling agents (Chakravarthy 2011).

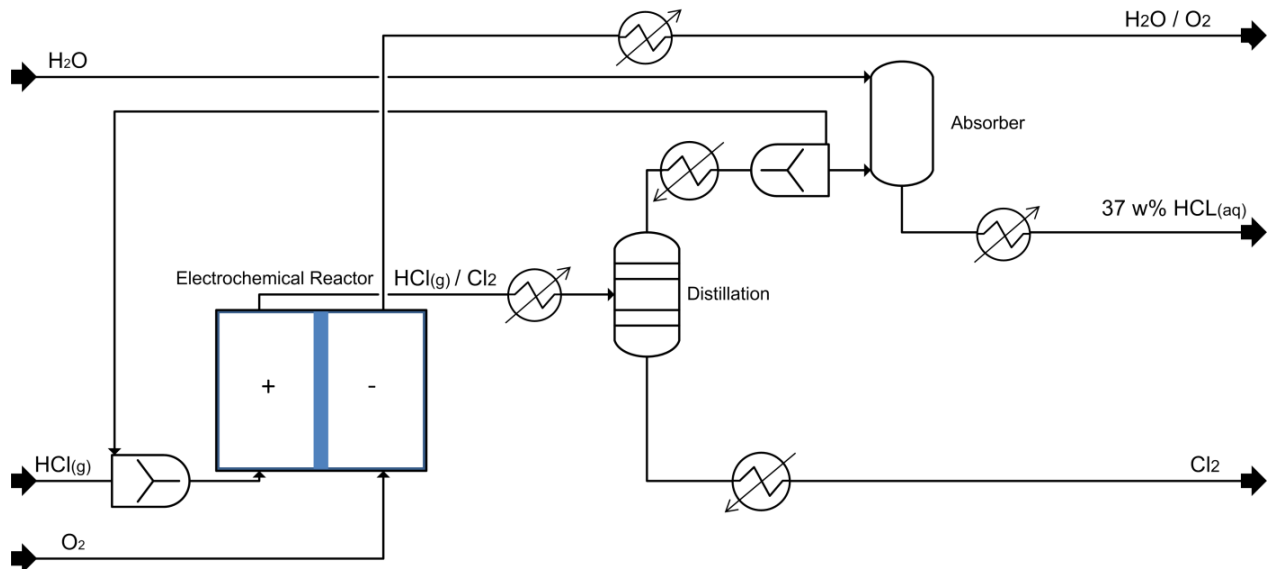


Fig. 2.2, Process flow scheme of the ELECTRA-DIST process. Since the distillation step takes place at atmospheric pressure in the standard simulation, no compressor is displayed in the flow scheme prior to the column, where it would be added, if distillation at elevated pressures was desired. This process variant was simulated with a single pass conversion of 60% and 80%. Adopted from (Bechtel 2018a) with permission from John Wiley and Sons.

Model settings

For this process, the predictive SRK method (PSRK) was chosen. It is based on the Soave-Redlich-Kwong equation of state and a mixing rule in which the excess Gibbs free energy estimated with the UNIFAC method is incorporated. One of the advantages is a better accuracy compared to the SRK method, if polar components like HCl are present in the gas mixture. Furthermore, this method is also more precise than the UNIFAC model at higher pressures (Edwards 2008). To assess the applicability of the PSRK method in this specific process, the column was also simulated with the NRTL-RK method and deviations of only 1% in the heat duty and 2 K in the reboiler and condenser temperatures between both variants were observed. Therefore, the PSRK method can be considered suitable for simulating this process. The absorption of HCl in water forming hydrochloric acid however, must still be modeled with the ENRTL-RK method due to the presence of ionic species. To allow for comparability with the Bayer UHDENORA process, the temperature in the absorber was set to 308 K. The compression of the HCl/Cl₂ mixture prior to the distillation

column in the simulations with a column pressure of 2, 5, 8 and 10 bar was simulated isentropically using the ASME method.

2.4. ELECTRA-ABS process

As an alternative to the previously described ELECTRA-DIST process, the following variant utilizes differences in the solubilities of Cl_2 and HCl in an organic solvent. Dissolving hydrogen chloride in water and thereby separating both gases, as it is common procedure in the heterogeneously catalyzed high temperature processes, is not considered for two reasons. Firstly, this would leave the remaining Cl_2 gas stream to be too humid so that an additional drying step is inevitable. Secondly, a part of the HCl , which in that case would be dissolved in water in the form of hydrochloric acid, has to be separated and fed back to the reactor, if the single pass conversion is lower than the desired overall conversion. Due to the significant enthalpy of solution of HCl in water, this would be a highly energy intensive and very inefficient proposition.

In Deacon-like processes, tetrachloromethane was proposed for the absorption of organic solvent impurities and parts of the Cl_2 with the purpose to separate it from unreacted oxygen (Foster 1982). However, in the here discussed gas-phase electrolysis processes, it is not possible to separate Cl_2 from the remaining HCl by absorption alone while still satisfying the purity constraints discussed in chapter 2.1. Nonetheless, the concept of physical absorption of either Cl_2 or HCl can also be applied here, as long as it is followed by an additional separation step, as discussed in more detail below.

Absorbing HCl in polar organic solvents like acetic acid or acetone has the major disadvantages of a low selectivity, meaning that the solubility of Cl_2 is not significantly lower than the one of HCl . Furthermore, many of these solvents (e.g. acetone, DMSO) exhibit an insufficient stability in the presence of HCl and Cl_2 . However, there is a range of common organic solvents in which the solubility of Cl_2 is distinctly higher than the one of HCl , for example chloroform, benzene and alkanes (Young 1983). Especially the alkanes (C_6 - C_{12}) are inexpensive, readily available and significantly less hazardous and damaging to the environment than halogenated solvents as well as more stable than unsaturated hydrocarbons and were hence chosen as solvent class in the present

work. While higher homologues display slightly lower Henry constants for Cl₂, their boiling point is also significantly higher, leading to an increased heat duty in the subsequent desorption step. As further discussed in chapter 2.5.3 octane was therefore chosen as a compromise. Values for the Henry constants of HCl and Cl₂ in H₂O and octane were obtained from the Aspen Plus database and, in the case of Cl₂, the IUPAC solubility data series (Young 1983).

As mentioned above, despite of a distinct difference in the Henry constants of Cl₂ and HCl, the selectivity of the absorption step is not sufficient, so that either significant amounts of HCl are also absorbed in the solvent, or a considerable proportion of Cl₂ remains in the gas stream leaving the top stage of the absorber. The following calculation illustrates this problem. As specified earlier, the purity of the Cl₂ product should be at least 99.5 wt% which is equivalent to a mole fraction of 99%.

$$x_{Cl_2} \geq \frac{0.99}{0.01} x_{HCL} \quad (2.8)$$

With the equilibrium constant $K_i = \frac{y_i}{x_i} = \frac{H_i}{p}$ and under the assumption that the gas phase only contains negligible amounts of octane follows

$$\frac{y_{Cl_2}}{K_{Cl_2}} \geq 99 \frac{1 - y_{Cl_2}}{K_{HCL}} \quad (2.9)$$

$$y_{Cl_2} \geq 99 \frac{K_{Cl_2}}{K_{HCL} \left(1 + 99 \frac{K_{Cl_2}}{K_{HCL}}\right)} = 99 \frac{H_{Cl_2}}{H_{HCL} \left(1 + 99 \frac{H_{Cl_2}}{H_{HCL}}\right)} \geq 95.2\% \quad (2.10)$$

With H_{Cl_2} and H_{HCL} being the Henry constants of Cl₂ and HCl in octane respectively. This means that the gas phase has to consist of at least 95.2% Cl₂ during the absorption process, not even taking into account that the solvent becomes more and more saturated with Cl₂ in the course of the absorption. If there is less than 95.2% Cl₂ in the gas phase, the amount of HCl absorbed in the octane stream is too high, so that a subsequent desorption step would leave the Cl₂ product stream with more than 0.5 wt% HCl.

Such high Cl₂ concentrations in the gas stream are not realistic and would also mean that nearly all Cl₂ is leaving the column on the top stage together with the not absorbed HCl, which again would have to be separated. Therefore, physical absorption alone is not sufficient to separate both

gases. The key is to employ the exact amount of octane necessary to absorb practically all Cl_2 . In this case, the gas stream leaving at the top of the absorber consists of almost pure HCl with only traces of octane and Cl_2 . If the conversion in the reactor already is at 80%, this HCl stream can be absorbed in water forming concentrated hydrochloric acid which leaves the process as a by-product. However, if the single pass conversion in the reactor is lower, for example 60%, a part of the gas leaving the column has to be recycled back to the reactor so that the overall conversion remains at 80%.

For a single pass conversion of 80%, 0.27 kmol/s octane are required to absorb essentially all Cl_2 . However, underlining the above discussed selectivity problem, the solvent stream leaving the absorber then contains 8% HCl as well, which is approximately 50% of the HCl entering the column. For that reason, a subsequent extraction of the absorbed HCl using pure water as a solvent is proposed. In this unit, all of the HCl absorbed in octane dissolves in the aqueous phase due to its highly exergonic dissociation reaction. By subsequently absorbing the pure HCl from the top of the absorption column in this diluted hydrochloric acid solution, a 20% fraction of the overall HCl feed leaves the process in the form of concentrated hydrochloric acid, as desired. If the single pass conversion of the reactor is below 80%, then only parts of the HCl stream obtained from the column top are absorbed in the diluted hydrochloric acid and the rest is recycled to the reactor.

The remaining octane phase now only contains Cl_2 and traces of diluted hydrochloric acid. The equilibrium mole fraction of water in octane at room temperature is $5 \cdot 10^{-4}$ and the corresponding fraction of octane in water is $9.96 \cdot 10^{-8}$ according to experimental data by Maaczynski *et al.* (2003). The low miscibility of water and octane leads to only small impurities of dilute hydrochloric acid in the octane stream and vice versa. Hence, essentially pure Cl_2 can be desorbed from the solvent stream by means of distillation, while the octane stream leaving at the bottom of the distillation column, still containing traces of diluted hydrochloric acid, is recycled. Since in every cycle an equilibrium between the octane and the aqueous phase is achieved in the extraction unit, no accumulation of hydrochloric acid in the octane stream over time can occur. Fig. 2.3 displays the flowsheet of this process variant.

The extraction unit could not be simulated in a physically and chemically consistent way with the predesigned device available in Aspen Plus, due to the complex nature of the mixture. Therefore, the extraction step was approximated analytically, assuming chemical and physical equilibrium in both phases, and then implemented into a separator block in Aspen Plus with the help of design specifications. The main focus in this calculation is on the distribution of H₂O and Cl₂ in both phases to estimate the loss of Cl₂ into the aqueous phase, which would also contaminate the hydrochloric acid byproduct, and to determine the amount of diluted hydrochloric acid transitioning into the organic phase, since this significantly influences the subsequent desorption step in which the Cl₂ with a maximum water content of 100 ppm (mg/kg) is obtained. The liquid-liquid equilibrium was approximated using the above mentioned solubility data from (Alkan 2005) and (Mańczyński 2003). The detailed procedure is described in the appendix A1. Although the assumptions made in these calculations are physically reasonable, small deviations of the results from the real liquid-liquid equilibrium (LLE) are to be expected. Therefore, an additional simulation was carried out where the amount of all substances changing the phase in the extraction unit was increased by 50%. This is supposed to represent a worst-case scenario in which more Cl₂ is lost via the aqueous phase and more octane and water impurities will be found in each phase.

The exergy analysis is also performed for this worst-case scenario in order to determine the sensitivity of the exergy efficiency of the process with respect to the uncertainties in the calculated equilibrium concentrations of the extraction step.

Model settings

As before, the absorption of HCl in the diluted acid stream producing concentrated hydrochloric acid was simulated with the ENRTL-RK method. The absorption in octane can be best described with the NRTL-RK method, since no ionic species are present. The distillation unit has been modelled with the PSRK method introduced above and is to be preferred over the SRK method due to the presence of small amounts of diluted hydrochloric acid. The compression of the gas mixture prior to the absorption column was again simulated isentropically using the ASME method.

2.4.3 ELECTRA-IL process

As discussed in the previous chapter, the selectivity of classical organic solvents for either HCl or Cl₂ is not high enough to separate both gases in a single absorption step. However, a different class of solvents, ionic liquids (IL), can be designed to display a high selectivity for polar molecules like HCl. They are therefore investigated in the following as a possible solvent in a separation sequence based on a single absorption and desorption step, bearing the potential of significant reductions in material costs and environmental impact.

ILs are molten salts with a melting point below 373 K (Lei 2017, Ventura 2017) and are often described as designer solvents due to their versatile properties that can be adjusted by choosing from a vast amount of possible anion and cation combinations. In addition to that, their good thermal stability and low volatility led to the application of ILs as solvents for the absorption of various gas species like CO₂ or O₂, but also as a reaction medium (Mallakpour 2012). Due to the variety of possible anion and cation combinations, the first step in developing an IL-based separation strategy is to screen for the most suitable candidate. In previous literature (Song 2017, Farahipour 2016, Yongsheng Zhao 2017), the screening of ILs is based on the thermodynamic and/or physical properties of ILs. However, as mentioned before, the system considered in this work is highly reactive. Therefore, a modified screening procedure is proposed and depicted in Figure 2.4. Step two and three including the COSMO-RS simulations were mainly carried out by Dr. Song and Dr. Zhou (Bechtel 2018b), so that the focus in this work lies on step one and four of the screening process.

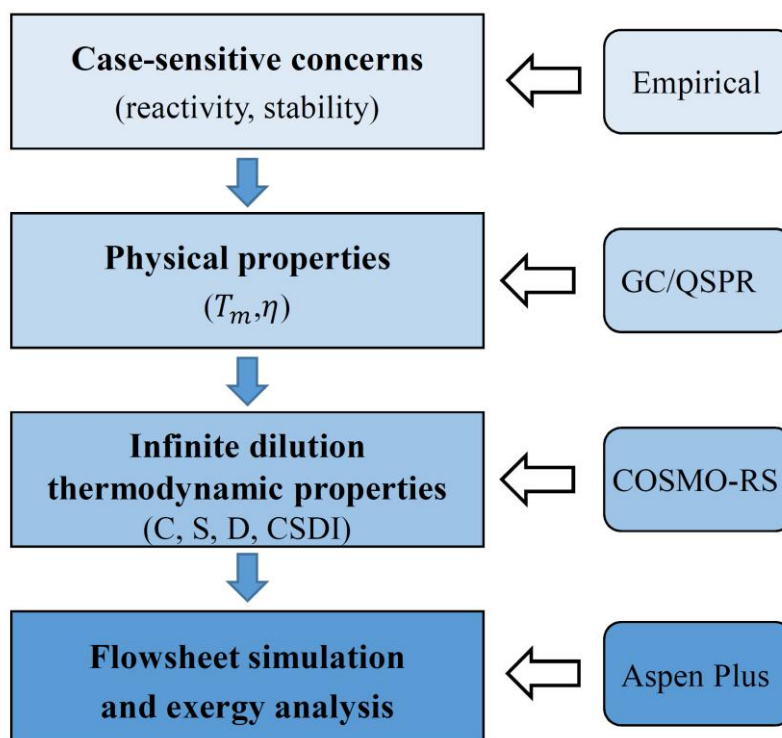


Fig. 2.4, Process design methodology consisting of a three step IL screening procedure and the flowsheet simulation. Adopted from (Bechtel 2018b) with permission from Elsevier.

At the start of the screening procedure, all ILs listed in the COSMOtherm IL database, a comprehensive database consisting of 372 cations and 98 anions, are treated as possible candidates. In the first step, ILs with functional groups that are prone to react with either Cl_2 , HCl or traces of water, which can be present in the gas stream due to crossover in the electrochemical reactor, were excluded. For this reason, amines, ammonium cations and related functional groups were not considered in order to avoid the formation of chloramines (Yee 2008). Furthermore, no aromatic systems, alkynes or alkenes were allowed, since they are prone to electrophilic substitution, halogenation and hydrohalogenation (Morrison 1983). This is especially critical, if they are substituted with functional groups that increase the electron density in the π -bond. Additionally, no carbonyl, carboxyl, imine or amide group should be present since they can be halogenated in alpha position (Clayden 2012). Moreover, metal salts that are prone to hydrolysis in the presence of water, like tetrachloroaluminate, or salts that are in general easily oxidized, were discarded in this first screening step (Huheey 2006). In addition, cyanides or related groups are also prone to react with halogens (Müller 2014). Due to increased temperatures in the desorption step of the

process, the IL furthermore has to be thermally stable, which excludes nitrates, chlorates and other candidates prone to thermal decomposition (Villada 2018). For the same reason, anions that can be protonated in the presence of HCl and do not have a significantly lower fugacity than HCl are to be avoided, since this would lead to the evaporation of the corresponding acid of the anion rather than of HCl in the subsequent desorption step. To give but one example, this excludes fluoride as an anion due to the higher fugacity of HF compared to HCl but allows for sulfonates due to the low fugacity of sulfonic acid derivatives. Finally, highly fluorinated molecules were disregarded for environmental and economic reasons. This first screening step reduced the eligible candidates to 37 cations and 47 anions.

In the second step, the melting temperatures T_m of the remaining ILs were estimated using the group contribution method developed by Lazzús *et al.* (2012) while the viscosities η were calculated with the group contribution feed-forward artificial neural network (FFANN) method developed by Padaszyń and Domańska (2014), by group contribution or quantitative structure-property relationship methods. Only ILs with a melting temperature below 298 K and a viscosity smaller than 150 mPa·s were considered for the last screening step, leaving 39 candidates for which the infinite dilution thermodynamic properties were calculated. These are the absorption capacity C , the absorption selectivity towards hydrogen chloride S , the ability for desorption D and the overall $CSDI$ value, all determined using COSMO-RS (Farahipour 2016, Yongsheng Zhao 2017):

$$C = \frac{1}{H_{HCl}^{25}} \frac{M_{HCl}}{M_{IL}} \quad (2.11)$$

$$S = \frac{H_{Cl_2}^{25}}{H_{HCl}^{25}} \frac{M_{HCl}}{M_{Cl_2}} \quad (2.12)$$

$$D = H_{HCl}^{55} / H_{HCl}^{25} \quad (2.13)$$

$$CSDI = C \cdot S \cdot D = \frac{H_{HCl}^{25} \cdot H_{HCl}^{55}}{(H_{HCl}^{25})^3} \frac{(M_{HCl})^2}{M_{Cl_2} \cdot M_{IL}} \quad (2.14)$$

where H_i stands for the Henry constant of the substance i in the IL and M_i for the molar mass of the according substance. The results of this last screening step are displayed in Figure 2.5.

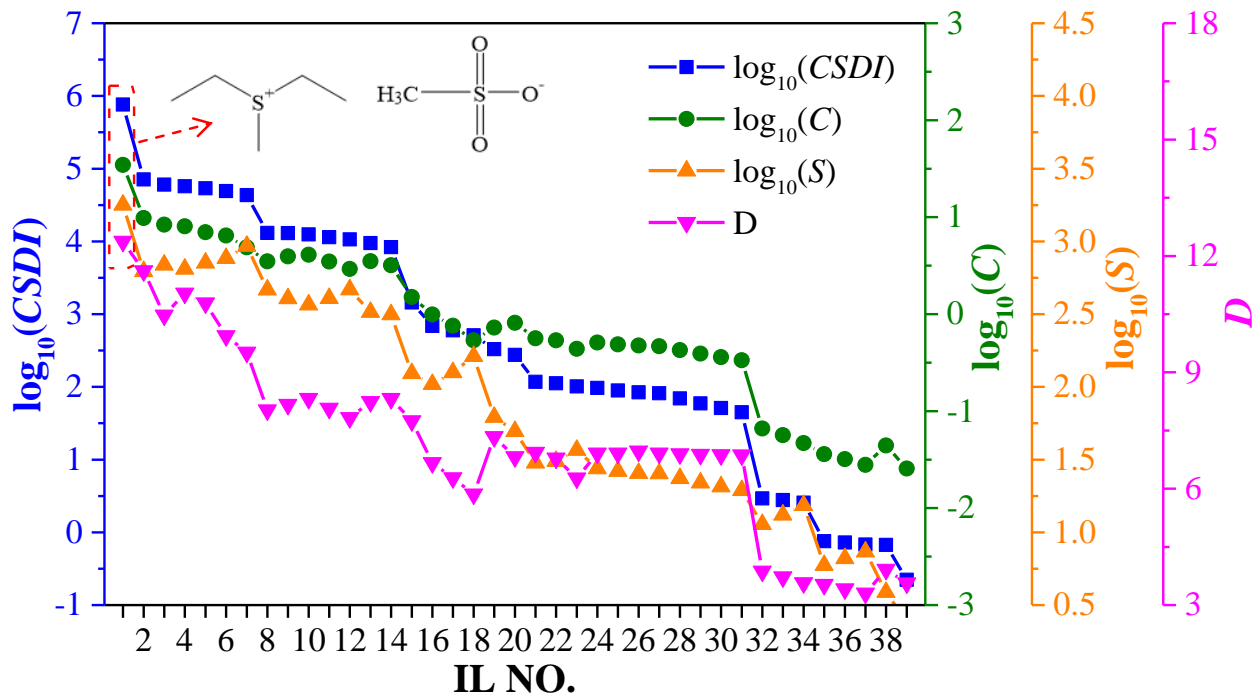


Fig. 2.5, Infinite dilution thermodynamic properties calculated according to equation 2.11-2.14 for the remaining 39 ILs. Adopted from (Bechtel 2018 b) with permission from Elsevier and Dr. Song.

The IL with the highest values in all four categories is diethyl-methylsulfonium methanesulfonate ([S221][MeSO₃]). The chemical structure is included in Figure 2.5. Since it furthermore has a comparably low heat capacity of only 310 J/mol/K at room temperature, which reduces the heat duty in the desorption step, it is chosen for the fourth step, the process simulation in Aspen Plus. The process flowsheet is displayed in Figure 2.6.

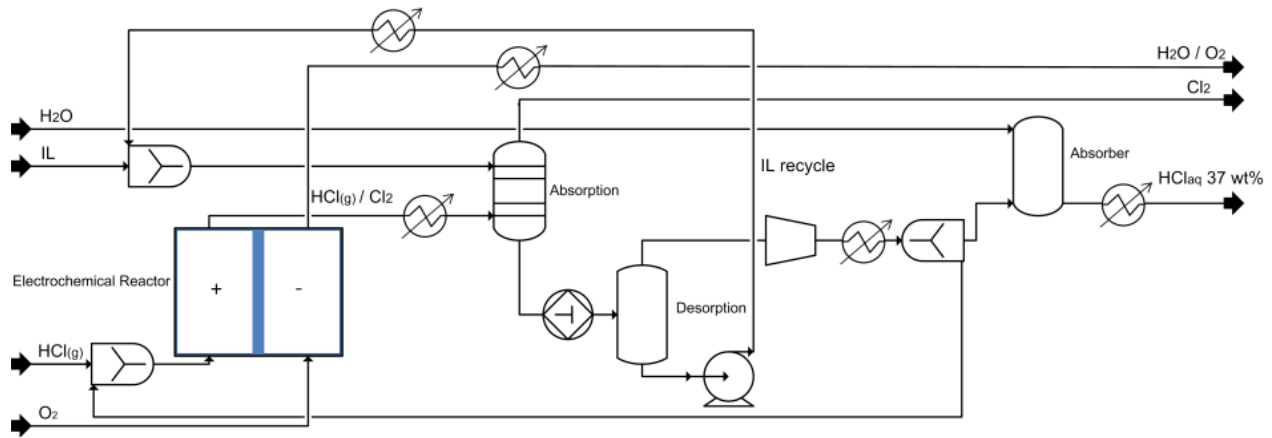


Fig. 2.6, Process flow scheme of the IL process. This process was only simulated at a single pass conversion of 80%. In the case of lower single pass conversions, parts of the HCl emerging from the desorption unit are recycled back to the reactor, as shown in the flow chart. Adopted from (Bechtel 2018b) with permission from Elsevier.

The HCl in the anode outlet stream of the reactor is absorbed in the IL, leaving essentially pure Cl₂ in the gas phase. The absorption step takes place at atmospheric pressure and 298.15 K. As mentioned in chapter 2.4, these process conditions can certainly be further optimized, which however is out of the scope of this work. In order to motivate the choice of parameters and to set a frame for future optimizations, the relevant physical trends are discussed in the following.

A reduction of the temperature below 298 K would increase the selectivity of the IL for HCl following the van't Hoff equation, since the enthalpy of solution of HCl in the IL is significantly higher than the corresponding one of Cl₂. However, providing cooling to the absorber at temperatures below 298 K would contribute negatively to the overall exergy demand of the process.

An increase in the pressure above 1.013 bar would reduce the amount of necessary solvent and hence the heat duty in the desorption step. It has to be considered however, that the IL has a high capacity (see Figure 3) so that its flowrate is already low enough for interactions between the absorbed gas species to become relevant. As a consequence, further reducing the IL flowrate decreases the selectivity, since HCl-Cl₂ interactions are less selective for HCl than the IL-HCl and IL-Cl₂ interactions. On the other side, decreasing the pressure too much, requires increased IL flowrates to ensure the absorption of essentially all HCl and hence the desired purity of the Cl₂ product stream. Hence, while from a selectivity point of view pressures below 1.013 bar would be feasible, this requires additional energy to reduce the pressure within the absorption column and would also negatively impact the exergy demand of the subsequent desorption step, due to the increased IL flow rate.

Following the absorption step, HCl is desorbed at a pressure of 50 mbar and a temperature of 483.15 K. These values were chosen as a compromise between too high temperatures at which the IL might decompose with time and too low pressures that are coupled to increased safety risks, material costs due to thicker columns and more sophisticated vacuum pumps as well as an increased energy demand of these pumps. Subsequently, the IL is compressed to atmospheric pressure and recycled into the process again.

The HCl leaving the desorption unit is compressed towards atmospheric pressure in 4 steps with intermediate cooling, approximately doubling the pressure in each step. Following that, the HCl can be recycled back to the electrochemical reactor or absorbed in water forming concentrated hydrochloric acid. Since the single pass conversion in the ELECTRA-IL simulation is set to 80% and no simulation at 60% is carried out for this process variant, the unreacted HCl is not recycled in this specific scenario.

Model settings

In the Aspen Plus simulation, the IL was treated as a user-defined component for which the molecular structure, the boiling point, the density, the critical properties and the acentric factor were manually entered. These properties were determined using the fragment contribution-corresponding states method proposed by Huang *et al.* (2013). The temperature dependence of the

Henry constants of Cl_2 and HCl in the IL was fitted with the method of least squares based on values determined with COSMO-RS in a temperature range from 298 – 483 K in steps of 20 K. COSMO-SAC was chosen as a property method, requiring the screening charge density profile as well as the molecular volume, which were calculated with COSMO-RS and implemented into the flowsheet simulation. The corresponding values for Cl_2 and HCl are already part of the Aspen Plus databases.

2.5 Results of the exergy analysis

In this chapter, the results of the exergy analysis of the three novel process variants in comparison to the state-of-the-art Bayer UHDENORA process are discussed. The overall exergy demand of all processes are summarized in Table 2.3.

Table 2.3, Total exergy consumption of the analyzed five process configurations.

Process variant	Exergy consumption / MW
State-of-the-art	42.3
ELECTRA-DIST at 80% single pass conversion	26.26
ELECTRA-DIST at 60% single pass conversion	26.45
ELECTRA-ABS at 80% single pass conversion	27.04
ELECTRA-ABS at 60% single pass conversion	28.39
ELECTRA-IL at 80% single pass conversion	27.0

Before interpreting the data, a brief context is given in the following. The aggregate state of the water leaving the gas-phase reactor has an influence of only 1.2% on the exergy demand of the reactor. Since furthermore all streams leaving the process in the present analysis are cooled/heated to 298 K (please see chapter 2.1) most of the water, if it was to leave the reactor in its gaseous state, e.g. due to a polytropic reactor operation in a real industrial plant, would condensate before leaving the process. Hence, the data given in Table 2.3 is with good accuracy valid for both

aggregate states. Please note that the exergy demand of the ELECTRA-ABS process given in Table 2.3 corresponds to the simulations at an elevated pressure of 8.104 bar in the absorption column, which display a reduced exergy demand compared to the simulations at 2.026 and 1.013 bar. In the case of the ELECTRA-DIST process, the exergy demand of the simulation at atmospheric pressure within the distillation unit is the lowest one, as discussed in more detail in chapter 2.5.3, and is also the one listed in Table 2.3.

The exergy consumption of the state-of-the-art process is 42.3 MW while the most efficient variant, the ELECTRA-DIST process, displays a significantly lower demand of 26.26 MW at a single pass conversion of 80%, which is equivalent to overall exergy savings of 38%. The remaining two novel processes EXCTRA-ABS and ELECTRA-IL display a slightly higher exergy demand than the ELECTRA-DIST variant, but are still 36% more efficient than the Bayer UHDENORA process.

Hence, it can be concluded that the exergetic advantage of the gas-phase reactor compared to the liquid-phase reactor can not only be maintained, but even increased on the overall process level. The extent of these exergy savings furthermore confirms that the gas-phase electrolysis of HCl indeed has the potential to contribute significantly to the goal of the European Union to reduce energy consumption and GHG emissions in the chemical industry. To be more specific, based on the data given in chapter 1.1, 4.9 million metric tons of HCl are emerging every year from the production of polyurethanes alone, not taking into account other products like chlorinated alkanes. If all of this byproduct was fed into the ELECTRA-DIST process instead of the Bayer UHDENORA process, savings of 208 MW in pure exergy could be achieved. In comparison, the production of all Cl₂, including the brine electrolysis, consumes 4375 MW assuming an uptime of 8000 hours per year and a 35 TWh yearly electricity consumption (Boulamanti 2017). Please note that the above estimation of exergy savings does not consider that a significant amount of HCl is converted to Cl₂ by Deacon-like processes or not converted at all and that a one-to-one comparison of the electricity consumption and the exergy demand of a process is not feasible. Hence, the above given numbers are not to be put into direct relation. Nonetheless, the estimated savings measured against the overall electricity consumption of the chlorine sector underline the significance of the gas-phase electrolyzer technology in making an impact on the energy consumption of the overall chemical industry. This holds true especially, when considering that the production of chlorine is,

together with steam cracking, the number one energy consumer in the chemical industry (Bazzanella 2017, Boulamanti 2017).

Before investigating the contribution of different process units to the exergy demand in the next chapter, further insights from the data displayed in table 2.3 are discussed briefly in the following. Comparing the two investigated single pass conversions, it becomes obvious that a single pass conversion of 80% is slightly more efficient in both the ELECTRA-DIST and ELECTRA-ABS process. Changing the single pass conversion to 60% results in a 0.7% and 5% higher exergy demand respectively. The higher impact of the single pass conversion on the exergy demand in the ELECTRA-ABS process is due to the fact that firstly, at lower conversions more octane is needed for the absorption of Cl_2 , since more of the competing component HCl is present in the gas mixture leaving the electrochemical reactor. The more octane is employed, the higher is the heat duty in the distillation column used for Cl_2 desorption. Secondly, also the electricity demand in the compression unit is significantly increased at reduced single pass conversions due to the higher gas flow rates.

Therefore, the ELECTRA-ABS process variant appears to be less attractive compared to the ELECTRA-DIST variant, if for some reasons only a low single pass conversion can be achieved in an industrial production plant. It has to be emphasized however, that even at a single pass conversion of 60%, the ELECTRA-ABS variant is still 33% more exergy efficient than the state-of-the-art process. It can hence be concluded that also intermediate single pass conversions in the gas-phase reactor are feasible and do not significantly affect the exergetic advantage of the gas-phase processes over the Bayer UHDENORA variant significantly. This discussion is extended to the dependence of the exergy demand on the overall conversion in chapter 2.5.5.

Similarly, the simulation of the worst-case scenario of the ELECTRA-ABS process, as explained in chapter 2.4.2, in which the flux of all species transferred between the aqueous and the organic phase within the extraction unit was increased by 50%, showed a deviation in the overall exergy demand of only 0.1% while the product specifications could be still achieved. This demonstrates that the process is not sensitive even to severe changes or uncertainties in the liquid-liquid-equilibrium composition of the extraction unit.

2.5.1 Contribution of different process units to the overall exergy demand

In the following, the presented exergy assessment is broken down into contributions from the reactor, pressure changers, heat exchangers and the distillation columns. This serves the purpose of understanding where the significant differences between the Bayer UHDENORA process and the three novel gas-phase processes originate from. Furthermore, by investigating which units display the highest exergy demand and by analyzing the underlying reasons, the most relevant targets for future process optimization can be identified.

These contributions are displayed in Fig. 2.7 for the state-of-the-art process as well as the ELECTRA-IL process at a single pass conversion of 80%. The graphs for the remaining process variants are displayed in the appendix (A2). Please note that the configurations with a single pass conversion of 60% show a similar composition and are therefore not shown.

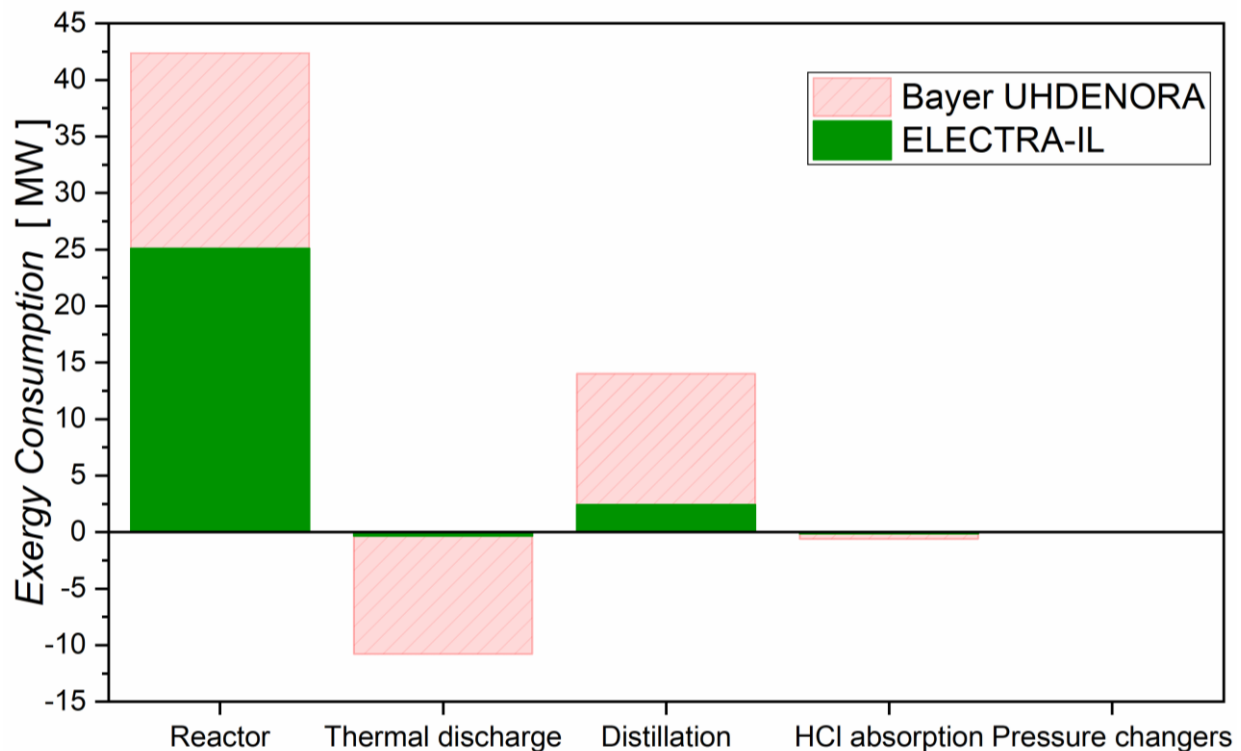


Fig. 2.7, Exergy demand of different unit operations of the ELECTRA-IL and Bayer UHDENORA process. Bars with a negative sign indicate that the specific operation leads to an exergy gain. Adopted from (Bechtel 2018b) with permission from Elsevier.

In all processes, the electrochemical reactor contributes most to the overall exergy demand. This is especially striking in the three gas-phase process variants. In the state-of-the-art technology, the distillation unit has an exergy demand of 14.3 MW. In the three novel gas-phase processes, the separation units display an exergy demand of 2.1 to 2.4 MW depending on the separation strategy. Based on this, three major conclusions can be drawn at this point.

Firstly, this shows quantitatively that not only the novel gas-phase reactor itself is notably more efficient than the state-of-the-art liquid-phase reactor, but also the three proposed separation sequences. Secondly, since the exergy demands of all three processes are comparable, the choice of the best separation strategy is mainly dictated by practical, site specific decision factors. Thirdly, one can conclude that the investigation and simulation of different separation methods is important in order to evaluate the feasibility of the overall process, which depends on a viable separation of reactants and products. However, optimization attempts aiming at further increasing the efficiency of the gas-phase processes should focus on the reactor rather than the separation strategies due to its dominant impact on the overall exergy demand. These three insights are reviewed in more detail in the following subchapters.

2.5.2 Efficiency of the investigated separation strategies

In the following, the first conclusion concerning the efficiencies of the separation steps is discussed for all process variants. As a consequence of the low single pass conversion of 22.9% in the state-of-the-art process, the mass flow of the diluted hydrochloric acid recycle stream is 25 times higher than the mass flow of gaseous HCl entering the process. This, in addition to the high heat capacity of hydrochloric acid, results in the significant energy demand of the distillation unit in the state-of-the-art process compared to the novel gas-phase processes. Again, please note that the exergy demand might be reduced if the separation strategy based on drying the chlorine product stream with sulfuric acid, as discussed in chapter 2.3, is chosen, which should be investigated in future research.

Interestingly, Figure 2.7 and Figure A.3 – A.5 in the appendix show that a significant portion of the exergy demand of the distillation column in the state-of-the-art process can be regained through

subsequent heat exchangers compared to for example the distillation column in the ELECTRA-DIST process. This is due to the column's molar reflux ratio, which is an order of magnitude smaller in the Bayer UHDENORA process due to the larger differences in fugacities between $\text{Cl}_2/\text{HCl}_{(\text{aq})}$ versus $\text{HCl}_{(\text{g})}/\text{Cl}_2$. A lower reflux ratio leads to a reduction in the heat duty of the column, so that more of the supplied heat can be regained after cooling the streams leaving the column in the Bayer UHDENORA process compared to the ELECTRA-DIST process. For the same reason, the separation of Cl_2 from octane in the ELECTRA-ABS process allows for regaining 59% of the exergy demand of the distillation column by subsequent heat exchangers as a consequence of the significant difference in the fugacities of octane and Cl_2 , compared to only 39% in the case of the ELECTRA-DIST process. Also, the compression and subsequent cooling of the absorption column feed provide additional heat to be regained in the ELECTRA-ABS variant, explaining the significant amount of exergy recovered from thermal discharge in Figure A.5 in the appendix. Nonetheless, a significant amount of electric energy, 8% of the overall exergy demand, have to be invested into the above-mentioned compression step in the ELECTRA-ABS variant, so that in the overall balance, the ELECTRA-DIST process remains to be the most efficient variant.

On the other side of the spectrum is the ELECTRA-IL process, in which the exergy recovered through thermal discharge in the heat exchangers is less than 14% of the exergy required to desorb HCl . This is due to the fact that the absorber operates at room temperature so that the exergetic portion of the 5 MW heat, which is dissipated in this unit, is zero, while in the desorption step the enthalpy of absorption has to be supplied to the process at a temperature level of 483.15 K, explaining the significant energy demand of the desorption step and why only a small fraction of it can be recovered. As mentioned in chapter 2.4, a rigorous global optimization of the process parameters is out of scope, but the above discussed insights confirm that this would certainly be a worthwhile effort for future investigations from a scientific point of view, although major increases in the exergetic efficiency of the processes are not to be expected due to the dominance of the electrochemical reactor in the composition of the overall exergy demand.

2.5.3 Further characteristics of the three proposed separation strategies

In this chapter, the second major conclusion about the decision criteria for choosing either one of the three gas-phase processes being of practical nature rather than being influenced by the overall efficiency, is further elaborated. To that end major advantages and disadvantages of the three process variants are discussed to aid in the decision process for an industrial application of the gas-phase electrolysis.

One major advantage of the ELECTRA-DIST and ELECTRA-IL process is the low number of apparatuses, compared to the ELECTRA-ABS and the Bayer UHDENORA process. Since there is no auxiliary substance introduced in the ELECTRA-DIST variant and only small volumetric flowrates of the IL in the ELECTRA-IL process, the recycle streams and hence also the apparatus sizes are markedly smaller than in the ELECTRA-ABS and especially the Bayer UHDENORA process as well.

A distinct benefit of the ELECTRA-IL process is that, contrary to both other process variants as well as the state-of-the-art process, no cooling streams at temperature levels significantly below room temperature are required. Since the efficiencies of the cooling systems for the distillation columns are not considered in the exergy analysis of this work, this could mean an additional exergetic advantage of the ELECTRA-IL process on top of lower investment and operating costs for the cooling systems. The ELECTRA-DIST process on the other side would require compression of the column feed gas if classical cooling agents like ammonia or propane/ethane are to be used (Chakravarthy 2011), since the condenser temperature at atmospheric pressure is only 187 K. Fig. 2.8 displays the additional overall exergy demand of the ELECTRA-DIST process as well as the condenser temperature as function of the column feed pressure for the simulation with a single pass conversion of 80%, assuming constant pressure on all stages equivalent to the feed pressure. At a pressure of 10 bar, the condenser temperature of the ELECTRA-DIST variant is at 240 K, which is comparable to the 244 - 248 K in the column of the ELECTRA-ABS process. The increased pressure leads to a lower exergy consumption of the distillation column. However, taking into consideration the power input of the compressor as well as the thermal discharge in the heat exchangers implemented in the process, the overall exergy demand rises with increasing pressure. Therefore, taking into consideration the positive effect on

the cooling effort, a moderate pressure between 2 and 5 bar is likely the most feasible choice in an industrial application, leading to an additional exergy demand of ca 0.15 MW. While the ELECTRA-DIST variant would still be the most exergy efficient of the three processes, the more complex cooling system compared to the ELECTRA-ABS and especially the ELECTRA-IL should be considered in choosing one of the process variants in an industrial application.

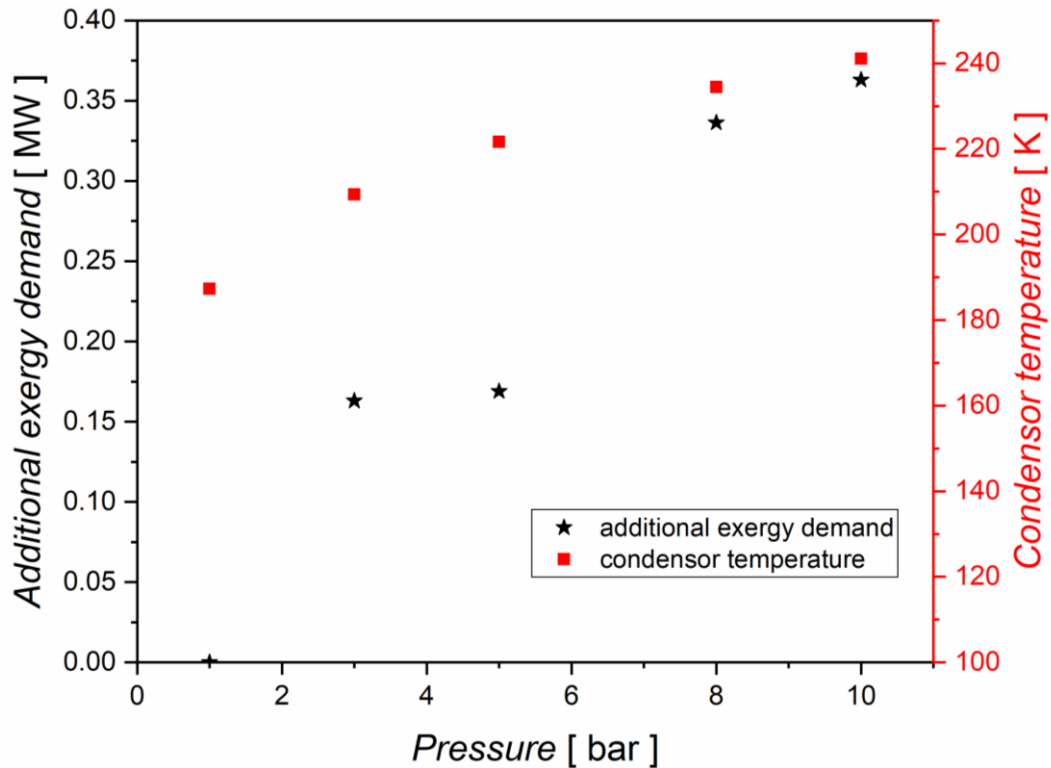


Fig. 2.8, Additional exergy demand and condenser temperature in dependence of the operating pressure of the distillation column in the ELECTRA-DIST process. The reflux ratio in the column was slightly adjusted with varying pressure in order to meet the specified purity of HCl (99.9 wt%) and Cl₂ (99.5 wt%). Since the variation in the reflux ratio was lower than 5%, the number of stages was kept constant at 16 for all pressure levels investigated. Adopted from (Bechtel 2018a) with permission from John Wiley and Sons.

The ELECTRA-IL process shows distinct advantages not only in regards to the cooling system but also concerning the utilization of heat dissipated within the heat exchanger of the process. Subsequent to the desorption step, the IL is cooled down from 483 K and the temperature level of the heat exchangers in-between the compression steps of HCl is even higher. Hence, it is practically more feasible to utilize these heat streams for generating steam or for heat integration

in general compared to the lower temperature heat streams in the other two process variants and the state-of-the-art process. In the Bayer UHDENORA process for example, most of the regained heat stems from the dilute hydrochloric acid stream at a temperature of ca. 380 K. As highlighted in chapter 2.3, such heat streams could be regarded as waste heat in a real industrial setting, due to their low temperature level. This would pose a significant advantage of the ELECTRA-IL process above the other variants and especially the Bayer UHDENORA process, which would exhibit a markedly higher exergy demand without considering the exergy gained from thermal discharge in these heat exchangers (please see Figure 2.7).

Lastly, the ELECTRA-ABS variant features a major advantage, too. It is not prone to potential water traces in the anode gas stream of the electrochemical reactor as a consequence of water-crossover from the cathode compartment through the membrane to the anode side. This is due to the fact that in the extraction step, where HCl is separated from the organic phase containing octane and Cl₂, water is used as a solvent. Water traces in the anode outlet stream can therefore not accumulate within the process, since they are transferred into the aqueous phase during the extraction step. In the ELECTRA-DIST and ELECTRA-IL process however, the anode stream would have to be dried before entering the distillation column, since water would contaminate the chlorine product leaving the subsequent distillation column in the ELECTRA-DIST process and in the case of the ELECTRA-IL variant, would negatively impact the efficiency of the desorption step. This due to fact that in the ELECTRA-IL process, water would either contaminate the HCl obtained from the head of the desorption unit, limiting the maximum possible recycle ratio towards the reactor, or would have to be separated from the IL in an additional desorption step. So far, the extent of water crossover in the gas-phase reactor at industrially relevant conditions has not been experimentally investigated. However, if these water amounts prove to be significant, the anode outlet stream of the ELECTRA-DIST and ELECTRA-IL process can be dried by cooling it in order to condense the potentially present water, so that both process variants will still be feasible for an industrial application.

Also, while octane was chosen as a solvent in the current design, other alkanes – particularly heptane or hexane - could be suitable alternatives. The Henry constants of Cl₂ in these solvents are higher, leading to a lower selectivity and a higher necessary flow rate of organic solvent. However, the atmospheric boiling point of hexane is 341 K compared to 399 K for octane, which would lead

to a significant reduction in the heat duty of the distillation column, and hence the overall exergy demand. Designing the process based on decane instead of octane leads to an increase in the exergy demand of ca 0.8 MW. Hence, while lower homologues have not been investigated yet, it can be expected that according exergy savings are possible when further reducing the chain length of the alkane from octane to e.g. heptane or hexane. Therefore, systematic investigations using different solvents may reveal that the ELECTRA-ABS variant is even more exergy efficient than so far assumed.

2.5.4 Impact of the gas-phase reactor on the overall exergy demand of the process

The third major conclusion, that the main optimization potential lies within the electrochemical gas-phase reactor making up for 88 - 95% of the overall exergy demand of the gas-phase processes, is visualized by an exemplary Sankey diagram of the ELECTRA-DIST process in Figure 2.9, assuming a single pass conversion of 80%. The diagram underlines the high relevance of the electrical energy input of the reactor unit in comparison to the relatively small heat duty of the distillation column.

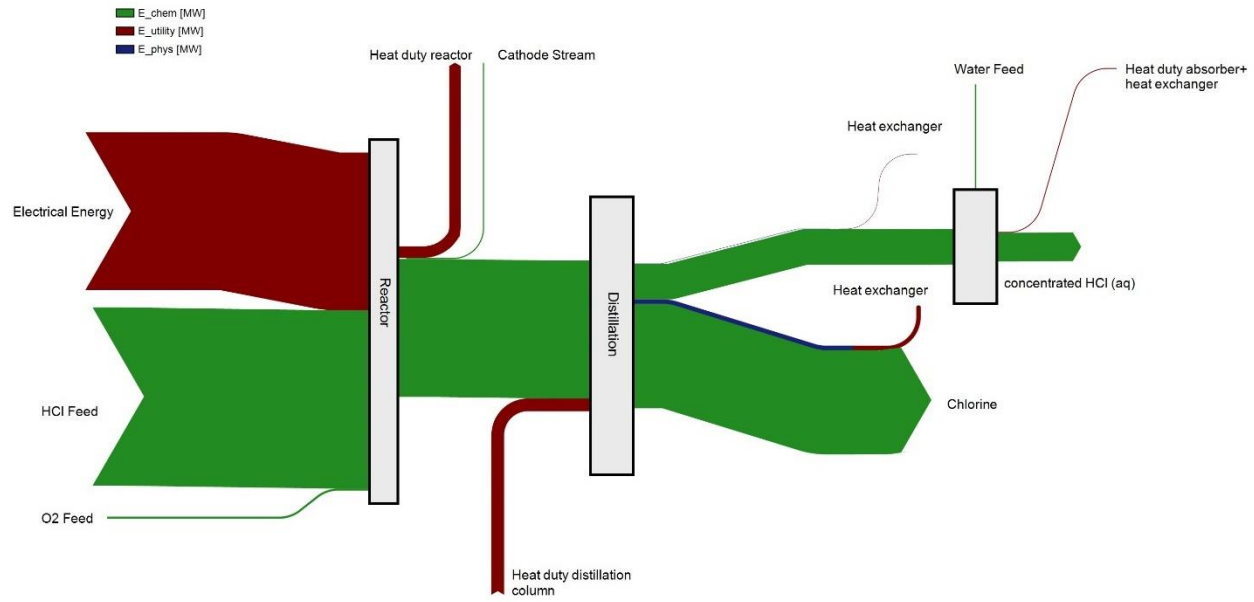


Fig. 2.9, Sankey diagram for the ELECTRA-DIST process with a single pass conversion of 80%. The chemical and physical exergy flow of each stream is depicted in green and blue respectively, while the exergy flow of the incoming and outgoing heat and work streams is shown in red. The physical exergy is negligible in all streams except for the liquid Cl_2 leaving at the bottom of the distillation column (blue line leaving the Distillation unit). Since the temperature of this stream is far below room temperature its vaporization leads to a noticeable exergy recovery. Adopted from (Bechtel 2018a) with permission from John Wiley and Sons.

Due to the significant heat dissipated in the electrochemical reactor as a consequence of the high overpotential, the negative reaction entropy and the exothermic dissociation of HCl forming hydrochloric acid within the ionomer of the anode catalyst layer, the temperature level of the reactor has a significant impact on its exergetic efficiency. A possible optimization strategy would hence be to operate the reactor at a higher temperature. A reactor temperature of 353 K instead of 313 K for example, would lead to a 18% lower exergy demand of this unit, since the exergetic proportion of the discharged heat increases with rising temperature. This is however only relevant, if the heat is utilized in a real application of the process and not discharged as waste heat. An operating temperature of 410 - 420 K, similar to high temperature PEM fuel cells, would already allow for the generation of medium pressure steam (≥ 3.5 bar) that could be integrated within the overall production site.

2.5.5 Influence of the conversion on the specific exergy demand

In chapter 2.5, the influence of the single pass conversion on the overall exergy demand was investigated for the ELECTRA-DIST and ELECTRA-ABS process, while the overall conversion was set to 80%, showing that both processes are still significantly more efficient than the state-of-the-art process even at intermediate single pass conversions of 60%. In the following, different overall conversions and their impact on the specific exergy demand per kilogram of produced Cl_2 are investigated for the same two process variants, since the overall conversion has a significant impact on designing not only the separation steps but also the electrochemical reactor.

Fig. 2.10 displays the specific exergy demand b_{spec} of the ELECTRA-DIST and ELECTRA-ABS process, which is calculated as follows

$$b_{spec} = \frac{\sum B_{chem,out} - \sum B_{chem,in} + \sum B_{heat} + \sum B_{electrical}}{\dot{m}_{Cl_2}} \quad (2.16)$$

In these equations \dot{m}_{Cl_2} stands for the mass flow of produced Cl_2 , and $\sum B_{heat} + \sum B_{electrical}$ summarizes the exergy of all heat and work streams entering the system. Please note that also the chemical exergy of input and output streams $\sum B_{chem,in}$ and $\sum B_{chem,out}$ are incorporated into the calculation, while in the determination of the total exergy demands of the different processes, which are listed in table 2.3, only the exergy of the incoming and outgoing work and heat streams was considered. This is due to the fact the chemical exergy of the in- and output streams was so far constant in all process variants due to the fixed overall conversion of 80%. With a changing conversion however, the chemical exergy has to be considered as well, making the specific total exergy demand b_{spec} a more suitable indicator for evaluating the impact of the overall conversion on the efficiency of the process. All non-converted HCl is assumed to be utilized for the generation of concentrated hydrochloric acid, as before. Furthermore, the single pass conversion is set identical to the overall conversion in all cases, so that no HCl recycle streams are required, since the effect of an HCl recycle on the exergy efficiency was already discussed in chapter 2.5 and would interfere with the investigations on the overall conversion.

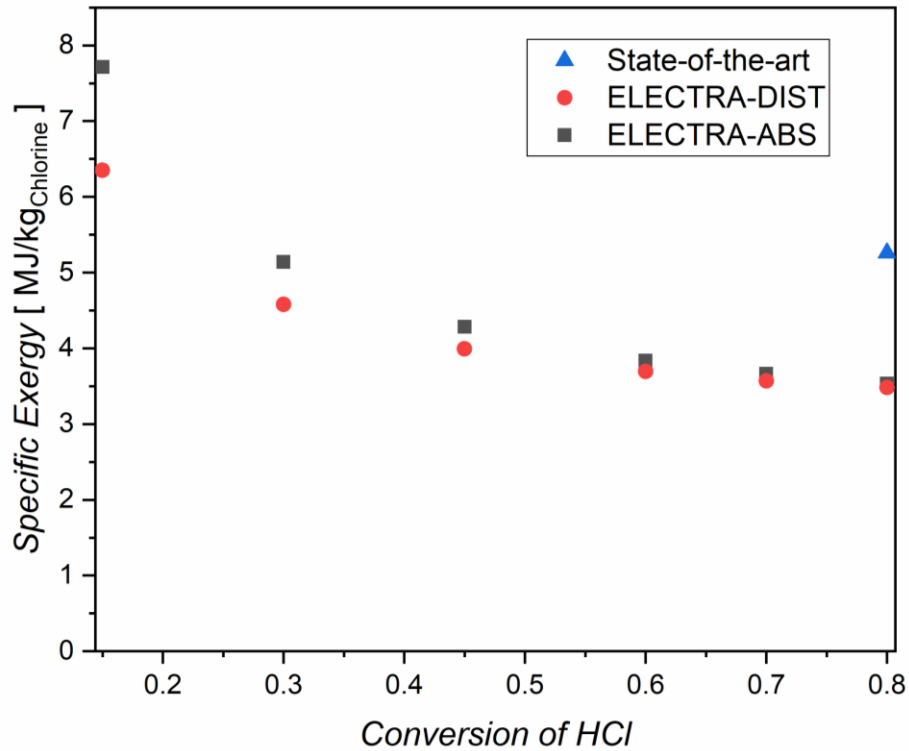


Fig. 2.10, Specific total exergy demand of the ELECTRA-DIST process (red) and the ELECTRA-ABS process (black) as well as for the state-of-the-art liquid-phase variant (green) in dependence of the HCl conversion. Please note that the single pass conversion in these specific cases is equivalent to the overall conversion, except for the single data point of the state-of-the-art process (blue), which was simulated with a single pass conversion of 22.9% and an overall conversion of 80%, since a higher single pass conversion is physically impossible in the Bayer UHDENORA process. Adopted from (Bechtel 2018a) with permission from John Wiley and Sons.

Fig. 2.10 shows that the specific exergy demand b_{spec} plateaus at conversions of 60% or more. Of course, other criteria like the site-specific chlorine and hydrochloric acid demand as well as market prices of the products play a significant role in determining the most feasible total conversion. However, when considering only the specific exergy demand, an overall conversion of 60% is already sufficient. Furthermore, as already observed for the single pass conversion in chapter 2.5, the ELECTRA-ABS variant is more sensitive to changes in the overall conversion than the ELECTRA-DIST process. However, the difference in the specific exergy demand between both processes does not exceed 10% at conversions greater than 40%. Fig. 10 also contains the specific exergy demand of the state-of-the-art process, illustrating the already discussed remarkable energetic advantage of the novel gas-phase processes.

2.6 Summary of the investigations on novel processes for the HCl gas-phase electrolysis

Three novel processes based on the gas phase and reactor different strategies for the separation of unreacted HCl from the desired product Cl_2 were proposed and compared to the Bayer UHDENORA process by means of an exergy analysis supplied with data from detailed flowsheet simulations of all four processes. In the case of the ELECTRA-IL process, utilizing an ionic liquid as an absorbent for separating HCl and Cl_2 , the process design included a four-step screening procedure for determining the optimal IL from the vast number of possible candidates taking into account its chemical stability as well as selected physical and thermodynamic properties.

Three major findings were discussed within this chapter. Firstly, the exergetic advantage of the gas-phase electrolyzer over the state-of-the-art liquid-phase reactor can be maintained and even extended on the overall process level, demonstrating that the gas-phase electrolysis of HCl is indeed an energy efficient alternative to the Bayer UHDENORA process. A further important insight in this context is that already intermediate single pass and overall conversions are exergetically feasible, which allows for more flexibility in designing and operating the electrochemical reactor.

Secondly, all three novel process variants exhibit a comparable exergy demand, with the ELECTRA-DIST process displaying only a slight exergetic advantage. Due to this, other site-specific selection criteria determine which of the three processes is most suitable in a real industrial application. To aid this decision procedure, the main advantages and disadvantages of all three variants were discussed in detail. The four most important decision criteria turned out to be the humidity of the anode outlet stream of the reactor, the feasibility of intermediate single pass as well as overall conversions, the practical integration of discharged heat within the overall production or Verbund site and the availability and practicability of low temperature cooling systems.

Thirdly, it is certainly important to develop feasible separation strategies for the gas-phase electrolysis of HCl, since only then the industrial applicability of the overall process is warranted. However, 88 - 95% of the overall exergy demands of the three novel processes originates in the electrochemical reactor. For this reason, a detailed understanding of the physicochemical processes

occurring within the reactor and using this knowledge to optimize the reactor has a significantly higher potential for further increasing the efficiency of the overall process than the optimization of existing, or the development of new, separation strategies. Nonetheless, the detailed discussion of process parameters and their influence on the overall exergy demand in this chapter can also serve as a basis for a future rigorous optimization of the three proposed separation strategies.

Due to the significant impact of the gas-phase reactor on the overall efficiency of the process, the second major part of the present work is dedicated to a more detailed understanding of the HCl gas-phase electrolyzer itself.

3 Development of a numerical reactor model of the HCl gas-phase electrolyzer

After investigating the feasibility of the gas-phase electrolysis on the overall process level in the previous chapter, this chapter focuses on the gas-phase reactor itself. For this purpose, a numerical reactor model based on the experimental setups of Kuwertz *et al.* (2013) and Martínez (2015) is developed and the insights thereof serve as a basis for the design of own experiments in chapter 4 of this work as well as first systematic reactor optimization strategies. Since the accurate description of the interplay between reaction kinetics and mass transfer was defined as one major focus of this model, a new method for a more accurate determination of transport properties is proposed in the end of this chapter and implemented into the numerical reactor model.

In the following, a brief literature review concerning the relevant mathematical and physicochemical aspects is given, in order to put the here developed reactor model into a broader perspective.

3.1 Review of the relevant history of PEM fuel cell modeling

The HCl gas-phase electrolyzer is structurally similar to hydrogen PEM fuel cells, as can be derived from its working principle explained in chapter 1.3, allowing for decades of experimental and theoretical research in this field to be used as a guideline for developing a numerical model of the gas-phase reactor. For this reason, relevant aspects in the history of hydrogen PEM fuel cell modeling are briefly delineated in the following in an attempt to embed the here developed model into a historical and methodological context and to allow for a better understanding of the made assumptions. For a more comprehensive overview on PEM fuel cell modeling the reader may refer to (A. Z. Weber 2004a, C. Y. Wang 2004, A. Z. Weber 2014a).

The first commercial fuel cell developed by General electrics in the 1950s, which was used for the Gemini space mission, delivered 1 kW at a platinum loading of 35 mg Pt/cm² (Y. Wang 2011). In comparison, a 2 MW fuel cell power plant was implemented within a Chinese chlor-alkali plant in recent years, using hydrogen emerging from the chlorine production to generate electricity for

onsite use (Barret 2016). Also, platinum loadings have been greatly reduced throughout the years to 0.3 mg/cm^2 or lower in various demonstration units (Y. Wang 2011). Besides continuous experimental investigations of improved fuel cell materials and operating conditions, a lot of the insights leading to these significant performance improvements by several orders of magnitude stem from modeling of PEM fuel cells, offering a time- and cost-effective way to investigate phenomena that cannot be resolved or uncoupled by means of pure experimental research (A. Z. Weber 2014a, Wu 2016).

Taking aside first 0-dimensional models based on a single equation fitted to experimental data, the first major models treating the entire fuel cell sandwich including gas diffusion media, membrane and catalyst layers in a 1D model were developed by Bernardi and Verbrugge (1992) as well as Springer *et al.* (1991) in the 1990s (A. Z. Weber 2004a). These models gave important insights on the transport phenomena in direction of the sandwich coordinate, however, come short to accurately model the behavior of a fuel cell in scenarios where reactant and water concentrations along the channel become more relevant, e.g. in the case of high fuel utilization or lower feed humidification (C. Y. Wang 2004).

Following these 1D models, in the next generation of models, so called pseudo 2D models, mainly developed by Fuller and Newman (1993), Nguyen and White (1993), and Yi and Nguyen (1999, 1998), the gas channels were discretized into a series of nodes and the sandwich model was then solved for each of these nodes sequentially (C. Y. Wang 2004, A. Z. Weber 2004a). Later on, full 2D (Um 2000) and 3D models (Dutta 2000) of the complete PEM fuel cell were developed and partly complemented by the use of the CFD framework, enabling the investigation of structural anisotropies in gas diffusion media (Promislow 2001, Stockie 2003), the effect of rib spacing in gas channels (West 1996) or the reactant and water distribution within the cell (Berning 2003, Wu 2010) amongst others.

In the early 2000s, models became more and more complex due to the multiphase treatment of water (Baschuk 2000) as well as the consideration of microscopic effects like the detailed modeling of agglomerates, the microscopic building blocks of the catalyst layer, or the membrane becoming a major concern (A. Z. Weber 2004a). In regards to the two-phase flow of water, Wang

and coworkers (C. Y. Wang 1996, C. Y. Wang 1997, Z. H. Wang 2001) showed that the consideration of liquid water is crucial for the transport of reactants and water within the fuel cell (A. Z. Weber 2004a). Besides the inclusion of liquid water, the consideration of non-isothermal behavior proved to be important for the water household as well as the overall performance of the cell (Nguyen 1993). Concerning the microstructure of the catalyst layer, Harvey *et al.* (2008) emphasized that of the three modeling approaches describing the catalyst layer; the thin film model, the discrete catalyst volume model or the agglomerate model; the latter one predicts additional non-negligible mass transfer resistances and is more accurate in modeling the current density of the cell at a given potential.

While intensive research was done and is still being carried out in the field of hydrogen PEM fuel cells, there has been very little effort in modeling the electrochemical oxidation of HCl so far. Besides the obvious difference in reaction kinetics, the utilization of HCl instead of H₂ as a reactant poses several other challenges that make modeling the HCl gas-phase reactor a scientifically worthwhile endeavor. Amongst these challenges are the highly non-ideal vapor-liquid equilibrium of HCl and water relevant for the reaction kinetics and mass transport within the agglomerates and the significantly higher overpotentials compared to classical hydrogen PEM fuel cells that, together with the strongly exothermic dissociation reaction of HCl in water, make the thermal and water management of the reactor more complex. While these effects justify focusing efforts on the development of a model specifically for the HCl electrolysis, not all of them can be comprehensively considered in such a model yet due to the lack of experimental data. Hence, this chapter also serves as a guideline for future complementary experimental studies to be carried out, ultimately allowing for a more precise and comprehensive modeling of the HCl gas-phase oxidation.

Before going into more detail about the numerical model developed in the present work, a brief summary of the existing models for the gas-phase electrolysis of HCl is presented. The first simplified model was developed by Eames and Newman (1995) for a cell comparable to the Dupont reactor introduced in chapter 1.2. They predicted the experimentally observed limiting behavior to be caused by dehydration of the membrane adjacent to the anode catalyst layer (aCL) and the corresponding strong increase in the ohmic resistance. However, they did not consider the crossover of water from the cathode chamber, which is filled with liquid water, through the

membrane to the anode chamber of the reactor. Since no water crossover is included in their model, the best performance, meaning a higher limiting current before membrane dehydration starts to manifest, is obtained in simulations at the highest reactor temperature. This is due to the slight increase in the diffusion coefficient of water in the membrane with temperature leading to a faster diffusional transport of water to the anode side, delaying membrane dehydration. However, as is well known from PEM fuel cell studies (Hogarth 2006), higher temperatures actually facilitate the dehydration of the membrane due to an increasing flux of water leaving the membrane towards the anode chamber. If the limiting behavior was indeed a consequence of membrane dehydration, one would therefore expect lower limiting current densities when increasing the temperature, which contradicts the experimental results of (Trainham 1993, Eames 1995 and Martínez 2015) introduced in chapter 1 of the present work. Hence, while the model of Eames and Newman (1995) is, after some adjustments to the diffusion coefficient of water in Nafion, able to reproduce the experimentally observed limiting behavior, a consideration of the underlying physics indicate that the model is incomplete and that the limiting behavior is not necessarily a consequence of membrane dehydration.

Seven years later, Motupally *et al.* (2002) developed a model for determining the water flux across the membrane in the presence of gaseous hydrogen chloride, again for a setup similar to the one reported in (Eames 1995) and the Dupont reactor. While they present important insights on the influence of HCl on membrane transport properties like the osmotic drag coefficient, their model does not investigate the performance of the overall cell. More recently, Martínez (2015) proposed a basis for an isothermal single-phase model of the HClOR as well as of the full cell employing an ODC, which is discussed in his dissertation but was not published in a scientific journal. As discussed in the course of this chapter, there are various assumptions regarding the reaction kinetics, the mathematical treatment of the mass balance within the agglomerates, the vapor-liquid equilibrium of HCl and H₂O in the aCL and the mass transfer within the GDL in this model that have to be viewed with caution. Moreover, the simulation results of Martínez do not exhibit a limiting behavior as it is seen in the experimental full-cell investigations by Kuwertz *et al.* (2013).

Based on insights from the brief historical review of PEM fuel cell models above and motivated by the lack of a sufficiently comprehensive model of the gas-phase electrolysis of HCl, the numerical model presented in this work was chosen to be a 1D non-isothermal two-phase

agglomerate model. The choice of this modeling framework takes into account the original objectives of modeling the gas-phase reactor discussed in chapter 1.5 as well as the following implications of the experimental conditions in the setup of (Martínez 2015 and Kuwertz 2013).

In the experiments of Martínez. (2015), the conversion never exceeded 5% and their experimental cyclone cell setup allows for mostly uniform concentration profiles in the boundary layer above the GDL, as further explained in chapter 4.1. In the experiments of (Kuwertz 2013), the HCl and O₂ conversion also did not exceed 33% and 8% respectively and in chapter 2 of the present work, intermediate conversions were identified to be sufficient for a high efficiency of the HCl gas-phase electrolysis on the overall process level. Since furthermore the purpose of the here developed model is a qualitative understanding of the physicochemical phenomena within the reactor rather than an exact quantitative prediction of the cell performance at high conversions, a 1D model is sufficient, allowing for a more detailed description of the physics within the cell sandwich while keeping the overall simulation costs at a reasonable level.

Since furthermore the phenomena of flooding in the cathode compartment as well as dehydration of the membrane were identified to be crucial in the understanding of the HCl electrolyzer performance in chapter 1.5, the here presented model additionally considers non-isothermal behavior of the cell as well as rigorously describes the flow of liquid and gaseous water.

Another open question discussed in chapter 1.4 is the impact of mass transfer on the reaction kinetics, especially in regards to the experimentally observed limiting behavior of the HClOR. For this reason, the model includes not only a rigorous treatment of the mass transfer of all substances within the diffusion media but also considers the catalyst agglomerates as well as the strongly non-ideal vapor-liquid equilibrium of HCl and water impacting the transport and reaction kinetics within these agglomerates.

The 1D non-isothermal two-phase agglomerate model presented in the following chapter is hence the first comprehensive and published model of the HCl gas-phase electrolyzer (Bechtel 2019b, Bechtel 2020a).

3.2 1D nonisothermal two-phase agglomerate model

The presented model resembles the full-cell experiments by Kuwertz *et al.* (2013) employing an ODC as well as the half-cell setup by Martínez (2015) as visualized in Figure 3.1. Please note that major parts of this chapter are extracted from Bechtel *et al.* (2019b, 2020a).

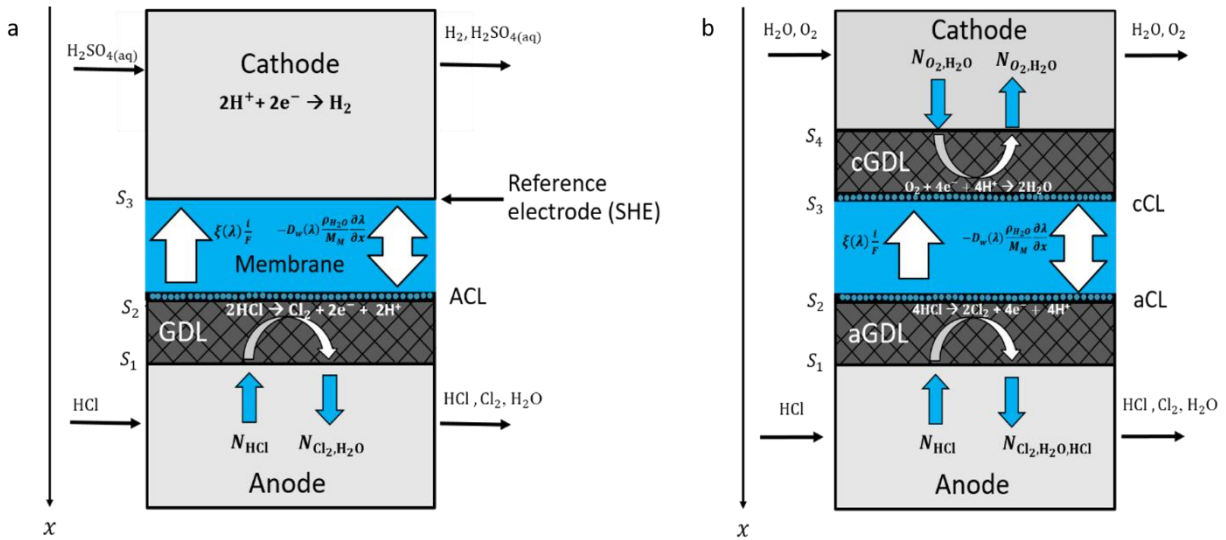


Fig. 3.1, Depiction of the modeling domains aligned with the half-cell experiments of Martínez (2015) a) and the full-cell experiments of Kuwertz *et al.* (2013) b). The following domains are included in the both models: anode gas channel (aGC), anode gas-diffusion layer (aGDL), anode catalyst layer (aCL), Nafion membrane (M). In the full-cell model, the cathode catalyst layer (cCL), cathode gas-diffusion layer (cGDL) and the cathode gas channel (cGC) are included on top of that. The hydrodynamic diffusion layer (HDL) at the interface between the GDL and the bulk gas is neglected, since Martínez (2015) showed that the mass transfer resistance in the GDL is 16 times greater than in the HDL. Adopted from (Bechtel 2019b) a) and from (Bechtel 2020a) b).

From mathematical point of view, the half-cell setup of Martínez (2015) is treated as a special case of the full-cell setup. Hence, the numerical model resembling the full-cell is discussed in the following, and the adjustments made for simulating the half-cell setup are explained in chapter 3.2.6.

The model is based on the following general assumptions which are discussed in more detail in the according subchapters 3.2.1 to 3.2.5.

- All gases are treated as ideal gases and the reactor temperature is assumed to be uniform throughout the reactor, meaning a lumped energy balance that is not a function of the spatial coordinate is implemented.
- Water in the anode compartment of the cell is assumed to be in its gaseous state only, while in the cathode compartment a two-phase model is employed.
- Condensation and evaporation of water is assumed to be fast due to a large enough interfacial area so that a local equilibrium can be assumed at all times.
- The membrane is modeled as impermeable for all species besides water and protons.
- The gaseous HCl is absorbed and dissociates within the water containing agglomerates of the catalyst layer. Hence, the expressions for the reaction kinetics are based on the activity of the aqueous Cl^- species and not the vapor pressure of $\text{HCl}_{(g)}$.

Species considered in the anode compartment of the cell are HCl, Cl_2 and gaseous H_2O , while in the cathode compartment O_2 and H_2O are allowed. H_2O is restricted to its gaseous state in the cGC, whereas both liquid and gaseous states are accounted for in the cGDL and cCL. Like in the experiments of Kuwertz *et al.* (2013), the cathode feed humidity is essentially at 100% RH, small reductions being made in order to facilitate convergence, while the anode feed consists of pure HCl. The governing equations, boundary conditions and the values of all parameters employed in the model are summarized in tables 3.1, 3.2 and 3.3, respectively, and further explained in the following subchapters.

Table 3.1, Governing equations in the gas channel, GDL and membrane.

Variable	Governing equation	Eq.	Domain
Partial pressure	$V \frac{dP_i^{GC}}{dt} = (\dot{V}_{in} P_{i,in}^{GC} - \dot{V}_{out} P_i^{GC}) + RTN_i _{s1,t}$	3.1	GC
Partial pressure of gaseous species in Anode compartment	$\frac{\partial P_i^{aGDL}}{\partial t} = -\nabla \left[p_{tot,A} \sum_{j \neq i} \bar{D}_{ij}^{-eff} \nabla \frac{P_j^{aGDL}}{p_{tot,A}} \right] + \frac{k_G^{eff}}{\eta_{G,A}} \nabla (P_i^{aGDL} \nabla p_{tot,A})$	3.2	aGDL
Partial pressure of H ₂ O in Cathode compartment	$\frac{\partial P_{G,H_2O}^{cGDL}}{\partial t} = \nabla \left[p_{tot,c} D_{H_2O-O_2}^{eff} \nabla \frac{P_{G,H_2O}^{cGDL}}{p_{tot,c}} + \frac{D_{H_2O-O_2}^{eff}}{RT} \left(\frac{P_{G,H_2O}^{cGDL}}{p_{tot,c}} - \frac{P_{G,H_2O}^{cGDL} M_{H_2O}}{P_{G,H_2O}^{cGDL} M_{H_2O} + P_{O_2}^{cGDL} M_{O_2}} \right) \nabla p_{tot,c} \right] + \frac{k_G^{eff}}{\eta_{G,c}} \nabla (P_{G,H_2O}^{cGDL} \nabla p_{tot}) + \nabla \left(\frac{RT c_{H_2O,L}}{\eta_{L,H_2O}} k_L^{eff} \nabla p_{L,H_2O} \right)$	3.3	cGDL
Partial pressure of n-th species in anode and cathode compartment	$p_n = p_{tot} - \sum_{i=1}^{n-1} p_i$	3.4	aGDL and cGDL
Total gas pressure in anode and cathode compartment	$\frac{\partial p_{tot}}{\partial t} = \frac{k_G^{eff}}{\eta_g} \nabla (p_{tot} \nabla p_{tot})$	3.5	aGDL and cGDL
Water content in membrane	$\frac{\partial \lambda_M}{\partial t} = -\frac{\partial N_W}{\partial x} \frac{M_W}{\rho_W} = +\nabla (D_W(\lambda_M) \nabla \lambda_M) + \frac{M_W}{\rho_W} \nabla \xi(\lambda_M) \frac{j}{F}$	3.6	Membrane
Chloride ion concentration within agglomerate	$\frac{\partial c_{Cl^-}}{\partial t} = -\frac{1}{r^2} \frac{\partial}{\partial r} \left(r^2 D_{HCl(aq)}^{\mu,eff} \frac{\partial c_{Cl^-}}{\partial r} \right) + a^\mu \nu_{Cl^-} r_i^\mu (a_{Cl^-}^\mu, \eta,)$	3.7	Agglomerates in aCL

Anode and cathode overpotential	$\frac{d\eta}{dt} = \frac{j + d_{CL} N_i^\mu F}{C_{DL}}$	3.8	aCL and cCL
Temperature	$T_r = \frac{1}{\frac{1}{R} + (G_{in}^A C_{p,in}^A + G_{in}^C C_{p,in}^C) \cdot \left[-\Delta_R H (G_{in}^A x_{HCl,in}^A - G_{out}^A x_{HCl,out}^A) - P_{el} + \frac{T_{wall}}{R} + T_{in} (G_{in}^A C_{p,in}^A + G_{in}^C C_{p,in}^C) \right]}$	3.9	Whole cell

Table 3.2, Boundary conditions.

Variable	Boundary condition	Boundary
Partial pressure gas phase	$p_i^{GDL} _{x=S1,S3,t} = p_i^{GC}$	aGC aGDL and cGC cGDL
Partial pressure gas phase	$N_i _{x=S2,t} = d_{ACL} N_{i,A}^\mu$ $N_i _{x=S3,t} = d_{CCL} N_{i,C}^\mu$	aGDL aCL and cGDL cCL
Total pressure gas phase	$p_{tot}^{GDL} _{x=S1,S4,t} = p_{tot}^{GC} = 1 \text{ bar}$	aGC aGDL and cGC cGDL
Total pressure gas phase	$\left(\frac{p_{tot} k_{eff,g}}{\eta_g} \nabla p_{tot} \right) \Big _{x=S2,S3,t} = S_{tot}$	aGDL aCL and cGDL cCL
Water content membrane	$\lambda_M _{x=S3,t} = \lambda_{CCL}$ $= (1 - S) \left[0.043 + 17.81 \frac{P_{H_2O}^{CCL}}{P_{sat}} - 39.85 \left(\frac{P_{H_2O}^{CCL}}{P_{sat}} \right)^2 + 36 \left(\frac{P_{H_2O}^{CCL}}{P_{sat}} \right)^3 \right] + 17S$	cCL M

Water content membrane	$\lambda_M _{x=s_2,t} = \lambda_{ACL}$ $= 0.043 + 17.81 \frac{P_{H_2O}^{ACL}}{P_{sat}} - 39.85 \left(\frac{P_{H_2O}^{ACL}}{P_{sat}} \right)^2$ $+ 36 \left(\frac{P_{H_2O}^{ACL}}{P_{sat}} \right)^3$	M aCL
Chloride ion activity at the surface of anode agglomerates	$a_{Cl^-}^\mu(r = R) = f(T, P_{HCl}^{ACL})$	aCL Agglomerate
Chloride ion flux in the center of anode agglomerates	$J_{Cl^-}^\mu(r = 0) = 0$	Agglomerate center

3.2.1 Energy balance

Contrary to the mass balances of the reactants and products, the energy balance (eq. 3.9) is not discretized in the direction of the x-coordinate (please see Figure 3.1). Furthermore, local thermal equilibrium (LTE) between all phases is assumed. The LTE approach is widely used for modeling PEM fuel cells in the scientific literature (A. Z. Weber 2014a, Hwang 2006). According to Hwang and Cheng (2016) it is justified, if the temperature difference ΔT_{loc} between the solid phase and the fluid phase in a volume element is significantly smaller than the temperature difference ΔT_{sys} across the whole system.

$$\frac{\Delta T_{loc}}{\Delta T_{sys}} = \frac{|T_{solid} - T_{fluid}|}{|T_{fluid,in} - T_{fluid,out}|} \ll 1 \quad (3.10)$$

With

$$O \left[\frac{\Delta T_{loc}}{\Delta T_{sys}} \right] \sim \frac{(\rho c_p)_{fluid} \varepsilon v_d}{h_v \delta} \quad (3.11)$$

Where v_d is the pore velocity, h_v the interstitial heat transfer coefficient and δ a characteristic length defined as the electrode thickness of the carbon fiber based porous electrode that Hwang and Cheng (2016) investigated in their work. In the experiments of Kuwertz *et al.* (2013), Martínez (2015) and the ones in the present work, a Nafion based catalyst ink is sprayed on the membrane, which is afterwards thermally bonded with a GDL. Hence, to estimate a value for the ratio given in equation 11, the characteristic length δ is defined as the combined thickness of the GDL and CL and the porosity is set to 0.7, which lies in-between the GDL and CL porosity employed in the numerical model (please see table 3.3 in chapter 3.2.7). For this porosity, Hwang and Cheng (2016) proposed a value of $1.5 \cdot 10^5$ W/m³/K for h_v based on measurements of aluminum foam with a supposedly similar structure; a value that is also used in the present work. The pore velocity is calculated with Darcy's law under consideration of the porosity ε . The according pressure gradients were taken from the simulation results introduced in chapter 5.3 for a reactor feed and coolant temperature of 333 K at a current density of 4000 A/m². As a result, values of $\left[\frac{\Delta T_{loc}}{\Delta T_{sys}} \right] = 1.1 \cdot 10^{-3}$ and $4.9 \cdot 10^{-3}$ were determined for the anode and cathode respectively according to equation 3.11. This ratio is clearly higher for the cathode side due to the increased pressure gradient between the cGC and cCL and hence higher pore velocity. Nonetheless, both values are significantly smaller than 1, justifying the LTE treatment.

The second approximation, neglecting the temperature gradient in x-direction, is based on various experimental studies of H₂ PEM fuel cells exhibiting only small reactor-internal temperature differences of ca 2 K at current densities relevant for the gas-phase electrolysis of HCl. To name a few exemplary studies, G. Zhang *et al.* (2010) found temperature variations between the flow plate and cCL to be between 1.5 - 3 K at up to 5000 A/m² for various reactant flow rates. Similarly, Vie and Kjelstrup (2004) determined temperature changes in-between the anode and cathode GDL to not exceed 2 K at current densities up to ca 5000 A/m². M. Wang *et al.* (2006) measured temperature variations of up to 2 K across the membrane surface with infrared imaging technology. Lastly, Wilkinson *et al.* (2006) measured the temperature differences between thermocouples located in the anode and cathode to be less than 1 K in a current-density interval of 1000-10000 A/m². While even such small temperature changes might impact the water household of the cell, especially at high operating temperatures due to the exponential increase of the water vapor

pressure with temperature, values for ΔT_{sys} are markedly higher at these current densities as shown in the discussion of the simulation results in chapter 5.3.

Based on these insights, the lumped treatment of the energy balance appears to be a valid approximation. If, however in future work, a precise quantitative analysis of the water household of the cell was desired, a spatial discretization of the energy balance within the LTE framework (single equation) would be recommendable.

The values for all parameters of equation 3.9 are given in table 3.3 in chapter 3.2.7 and are based on the properties of the reactor employed in the experimental work of Kuwertz *et al.* (2013, 2016a,bc), where also a scheme of all their reactor components and its layer structure can be found. The thermal resistance R of the reactor, considering the heat transfer through the plate, the PTFE gasket the FKM gasket and the titanium endplate, is calculated as

$$R = 0.5 \left(\frac{d_{plate}}{A\lambda_{plate}} + \frac{d_{PTFE}}{A\lambda_{PTFE}} + \frac{d_{FKM}}{A\lambda_{FKM}} + \frac{d_{endplate}}{A\lambda_{endplate}} \right) \quad (3.12)$$

where the surface of the plate facing the GDL is assumed to be at thermal equilibrium with the inside of the reactor having a temperature of $T = T_R$. The factor of 0.5 is a consequence of the simultaneous heat transfer through both the anode and cathode side. Contact resistances between the above-mentioned layers are neglected in the model. All values for the according conductivities and layer thicknesses are listed in table 3.3. Please note that the thickness of the titanium endplate is not given in the publications of Kuwertz *et al.* (2013, 2016a,b,c), but is estimated to be 0.5 cm from pictures of their reactor setup (Kuwertz 2016c). Furthermore, it is important to note that the thermal resistance R in equation 3.12 does not include heat transfer from the titanium endplate into the cooling medium, which is flowing through that plate and has the same temperature as the reactor feed gases in the setup of Kuwertz *et al.* (2013, 2016a,b,c). This is based on the fact that the area in contact with the cooling media and the coolant flowrate in their experiments are unknown. Hence, the coolant is assumed to be in thermal equilibrium with the outer surface of the titanium end plate T_W . Also, the possibility of heat transfer to the ambient air surrounding the reactor via the surface area not in contact with the cooling medium is not included in the model for the same reasons.

3.2.2 Gas-phase mass transport

The anode and cathode gas channels are treated as perfectly mixed compartments (eq. 3.1). In addition to the convective flux through the gas channels, a source or sink term $J_i|_{S1,t}$, considering the anode and cathode reactions as well as the crossover of water through the membrane into the anode chamber, is included. Here, \dot{V}_{in} and \dot{V}_{out} describe the volumetric flow rate entering and leaving the reactor respectively. Based on the experimental setup of Kuwertz *et al.* (2013) and Martínez (2015), the outlet pressure of the reactor, and hence the pressure in the gas channels P_{tot}^{GC} , can be assumed to be approximately 1 bar, neglecting pressure gradients. Hence, the reactor outlet flow rate can be calculated as follows:

$$\dot{V}_{out} = \dot{V}_{in} + \frac{RT}{P_{tot}^{GC}} A_{surf} (J_{HCl}|_{S1,t} + J_{Cl_2}|_{S1,t} + J_{H_2O}|_{S1,t}) \quad (3.13)$$

The diffusive mass transfer of all gaseous species within the GDL is described by the multicomponent Stefan-Maxwell equations (Krishna 1997), while the convective mass transfer in equation 3.2 and 3.3 is modeled based on Darcy's law (Zenyuk 2016). Similarly, the total pressure is determined based on mass conservation employing the continuity equation in combination with Darcy's law (eq. 3.5). In the cGDL, the effect of pressure-diffusion is considered additionally, since water condensation can lead to higher pressure losses compared to the anode side, which might be a considerable driving force for mass transfer under certain conditions (eq. 3.3) (Zenyuk 2016).

Due to the large pores in the diffusion media employed in the experiments of Martínez (2015), Knudson diffusion has a negligible impact on the diffusive mass transfer. As determined by Kuwertz *et al.* (2016a), 19.2% of the pores had a radius of approximately 100 μm , 49% a pore radius of 10 μm and 31.8% a pore radius of 25 nm. Simulating the diffusive mass transport based on the dusty gas model (Krishna 1997)

$$\nabla x_i = \sum_{j=1}^3 \frac{N_i x_j - N_j x_i}{D_{ij}^{eff}} + \frac{N_i}{D_{iM}^{eff}} \quad (3.14)$$

showed deviations of less than 0.1% compared to the assumption of pure molecular diffusion. Here, the effective Knudsen diffusion coefficient is denoted as D_{iM}^{eff} and calculated as follows, employing the Bruggeman correlation

$$D_{iM}^{eff} = \varepsilon_{GDL}^{1.5} \frac{\int rV(r)dr}{3} \sqrt{\frac{8RT}{\pi M_i}} \quad (3.15)$$

This is in agreement with experimental investigations of mass transfer in porous diffusion media by Spingler *et al.* (2017) and justifies the use of the Maxwell-Stefan equations (eq. 3.2 and 3.3). Please note that the microporous layer (MPL) and the GDL are treated as a homogenous structure employing an average porosity value measured by Kuwertz *et al.* (2016a). Since the permeability of the GDL and MPL are known to differ significantly (Mukherjee 2020), this approximation surely leads to an uncertainty in the model. However, as Kuwertz *et al.* (2016a) showed by means of digital microscopy, their microporous coating permeated into the GDL so that most of the MPL is located in-between the fibers of the GDL, with only a thin layer on top, justifying the above mention homogenous treatment.

The viscosity of the overall mixture μ_g was assumed to be identical to the viscosity of pure gaseous HCl in the anode and pure O₂ in the cathode compartment, since these are the main components in the gas mixture on each side. The effective diffusion coefficients in equations 3.2-3.4 can be modeled according to the Bruggeman correlation:

$$\overline{D_{ij}}_{eff} = \overline{D_{ij}} \varepsilon^{1.5} \quad (3.16)$$

Where $\overline{D_{ij}}$ in a three component mixture is a function of the Stefan-Maxwell diffusion coefficients D_{ij} (Balliet 2011, Zenyuk 2016)

$$\overline{D_{12}} = \frac{\frac{\omega_3(\omega_2 + \omega_3)}{y_1 D_{23}} + \frac{\omega_2(\omega_1 + \omega_3)}{y_2 D_{13}} - \frac{\omega_3^2}{y_3 D_{13}}}{\frac{y_1}{D_{12} D_{13}} + \frac{y_2}{D_{12} D_{23}} + \frac{y_3}{D_{13} D_{23}}} \quad (3.17)$$

In the first approximation of the Chapman and Enskog approach to the kinetic theory of gases, the Stefan-Maxwell diffusion coefficients are identical to the binary Fickian diffusion coefficients (Marrero 1972, Hirschfelder 1954). These Fickian diffusion coefficients were calculated based on

the Chapman and Enskog approach. As discussed in chapter 1.4 and 1.5, mass transfer is a critical aspect in the investigation of the experimentally observed limiting behavior so that not only a rigorous modeling of gas-phase diffusion by means of the above introduced governing equations, but also a precise determination the diffusion coefficients themselves is of importance in the here presented model. For this reason, a novel method for determining the Lennard-Jones (LJ) parameters employed in the calculation of transport coefficients according to the Chapman Enskog approach is proposed and presented in more detail in chapter 3.4.

The effective gas-phase permeability k_G^{eff} in equations 3.2, 3.3 and 3.5 is calculated as a product of the relative gas-phase permeability $k_{r,G}$ and saturated permeability k_{sat} .

$$k_G^{eff} = k_{sat}k_{r,G} = k_{sat}(1 - S_{L,GDL})^{\beta_G} \quad (3.18)$$

where S_L is the liquid-phase saturation. Since all water in the anode compartment is assumed to be in its gaseous state, the relative gas-phase permeability is fixed to be one in the aGDL. The values for the exponent β_G and the saturated permeability k_{sat} were extracted from (Zenyuk 2016) and are given in table 3.3.

As listed in table 3.2, the continuity of partial pressures at the GC|GDL interface and the GDL|CL interface is chosen as boundary conditions.

3.2.3 Two-phase modeling of water

Due to the assumption of local equilibrium between gaseous and liquid water, the mass transfer of H₂O in both phases (eq. 3.4) can be described with a single equation so that rate terms describing evaporation and condensation can be omitted. Compared to the rate-based approach used in the PEM fuel cell literature (A. Z. Weber 2004a), this novel method leads to better convergence and lower simulation costs, since n ODEs, with n being the number of discretization cells in the cGDL, can be omitted. The equilibrium assumption is justified by studies showing that water in both the gas and liquid phase is essentially in equilibrium due to the extended vapor/liquid interfacial areas

and rapid phase-change kinetics in the CL and GDL leading to a fast evaporation and condensation rate (Pant 2019, Siegel 2004, A. Z. Weber 2004b).

In this case, the liquid-water pressure can be calculated from the partial pressure of water by setting the chemical potentials in both phases equal, leading to

$$p_L - p_G = p_c = \frac{RT \ln \left(\frac{p_{H_2O}}{p_{sat}} \right)}{V_0 + \frac{M_{H_2O}}{RT \rho_{H_2O}}} \quad (3.19)$$

where the curvature of water droplets is considered by means of the Kelvin equation (A. Z. Weber 2004b). However, since $V_0 = \frac{M_{H_2O}}{\rho_{H_2O}}$ and $1 \gg \frac{1}{RT}$ equation 3.19 can be simplified to

$$p_L = p_G + \frac{RT \rho_{H_2O} \log \left(\frac{p_{H_2O}}{p_{sat}} \right)}{M_{H_2O}} \quad (3.20)$$

The transport of both liquid and gaseous water is then combined in equation 3.3, with the transport of gaseous water being modeled as discussed above for all other gas species, and the convective transport in the liquid phase being described by Darcy's law. Similar to the gas-phase permeability, the liquid-phase permeability is calculated as

$$k_L^{eff} = k_{sat} k_{r,L} = k_{sat} (S_{L,GDL} - S_{L,GDL,irr})^{\beta_L} \quad (3.21)$$

with $S_{L,GDL,irr}$ being the irreversible liquid-phase saturation, which takes isolated domains filled with water into account that do not participate in the convective mass transport (Zenyuk 2016).

The liquid-phase saturation is calculated based on experimental data from Gostick *et al.* (Gostick 2009) relating $S_{L,GDL}$ to the capillary pressure for a GDL consisting of Toray 090 Paper. The following fit-function was developed to obtain an equation for the saturation as a function of the capillary pressure

$$S_{L,GDL} = 0.48 \tanh \left(\frac{p_C - 2500}{8000} + 1 \right) + 0.0358 \quad (3.22)$$

Both the fit-function as well as the corresponding experimental data are displayed in Figure 3.2.

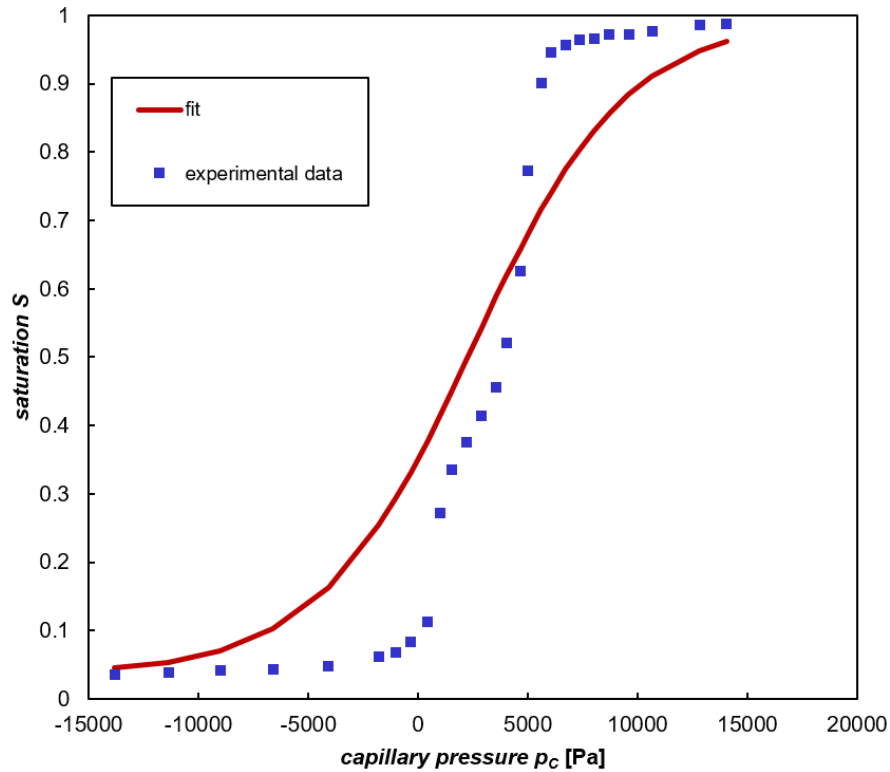


Fig. 3.2, Experimentally determined (Gostick 2009) and fitted saturation within the GDL as a function of the capillary pressure. Adopted from (Bechtel 2019b).

Please note that Kuwertz *et al.* (2013,2016a,b) used a different GDL material so that slight deviations between the actual and simulated properties cannot be avoided. However, since the goal of the present work is a qualitative evaluation of phenomena causing the observed limiting behavior this uncertainty is acceptable, especially since carbon-based GDL properties are not expected to vary significantly. The same procedure was repeated for obtaining a fit for the saturation $S_{L,CL}$ in the cCL employing experimental data from Kusoglu *et al.* (2012) leading to

$$S_{L,CL} = 0.405 \tanh\left(\frac{p_c - 3000}{8000} + 1\right) + 0.18 \quad (3.23)$$

Both the data and the fit-function are displayed in Figure 3.3.

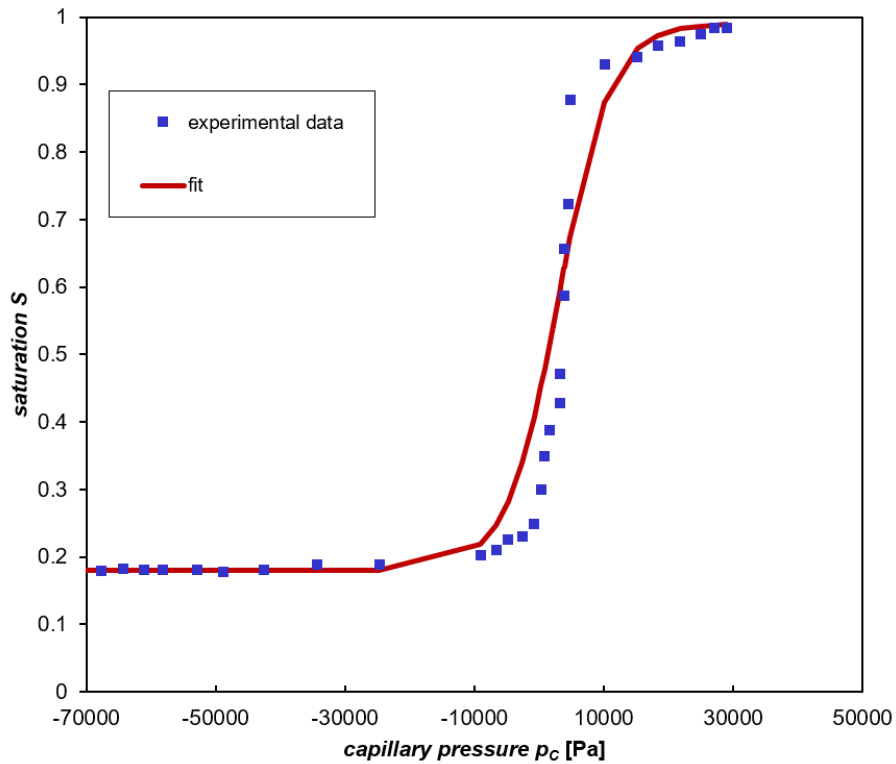


Fig. 3.3, Experimentally determined (Kusoglu 2012) and fitted saturation curves within the CL as a function of the capillary pressure. Adopted from (Bechtel 2019b).

As a boundary condition, the partial pressure of water at the $cGC|cGDL$ interface is set equal to its value in the cathode gas channel, identical to the treatment of other gas species. For the liquid-phase transport, a no-flux condition is enforced as long as the liquid pressure at the boundary between $cGDL$ and cGC does not exceed the total gas pressure in the cGC . This is based on the assumption that there are no liquid-water reservoirs in the cGC , so that no liquid flux from the cGC into the $cGDL$ is allowed (Zenyuk 2016). At liquid pressures greater than the total gas pressure, they are set equal to the total gas pressure. Please note that this is not a classical boundary condition, since the equilibrium assumption entails the need of only one boundary condition due to the equilibrium expression in equation 3.19 replacing the other one. However, since both the partial pressure of water and the liquid pressure are directly coupled, solving for the partial pressure by the above described scheme leads to identical results compared to solving for the liquid pressure with the no-flux condition enforced as a classical boundary condition and a simple continuity assumption for the partial pressure at the $cGC|cGDL$ interface.

3.2.4 Membrane

The water flux through the membrane along the sandwich coordinate consists of three components: A diffusive flux due to the activity gradient of water, an electroosmotic flux due to the protons migrating from anode to cathode dragging water molecules with them and, lastly, a convective flux which originates in a capillary pressure gradient along the sandwich coordinate (Xing 2014). In the absence of a gradient in the total gas pressure, the gradient in the liquid pressure p_L can be used as a driving force for both the diffusive flux and the convective flux, since the gradient of the chemical potential is proportional to the gradient in p_L at phase equilibrium (Eikerling 1998, A. Z. Weber 2004b,c). Hence, a simplified approach by Sorrentino *et al.* (2017), based on the work of Eikerling *et al.* (1998), is employed in the present work, in which the diffusive and convective flux are described together by defining an effective diffusion coefficient D_W (eq. 3.6). Furthermore, the gradient in the membrane water content λ_W is used as driving force (Sorrentino 2017), where λ_W is defined as the number of water molecules per sulfonic acid group (Kusoglu 2017). Certainly, employing the gradient in the water content instead of the chemical potential as a driving force is less accurate from a physical point of view. Also, more sophisticated membrane models for example distinguish between convective and diffusive flux depending on whether the membrane is in contact with vapor or liquid water (A. Z. Weber 2004b,c). However, as the purpose of the model is not to obtain a quantitative fit of experimental data and since furthermore the presented approach proved to be reasonably reliable in the work of Sorrentino *et al.* (2017), this approximation appears to be reasonable. Based on this, the dynamic balance of the water content can be formulated according to equation 3.6, where $\xi(\lambda_M)$ is the osmotic drag coefficient, which is a function of the water content and is calculated based on equation 3.24.

The presence of HCl has a significant impact on the transport properties of the Nafion membrane (Vidaković-Koch 2012, Motupally 2002), which is discussed in more detail in the following. While Zawodzinski *et al.* (1993a) proposed a value of 2.5 for the osmotic drag coefficient in a fully hydrated Nafion membrane in contact with water, Motupally *et al.* (2002) experimentally determined a value of 3.5 at a temperature of 333 K in their HCl gas-phase electrolyzer, which is similar to the Dupont reactor introduced in chapter 1. They assumed that a thin liquid forms on the aCL due to the exergonic reaction of water and HCl leading to the condensation of parts of the

water crossing over through the membrane from the cathode side. Hence, their osmotic drag coefficient was determined in a setup where the membrane supposedly is in equilibrium with water on the cathode side and hydrochloric acid on the anode side. While in the present work, all water in the anode chamber of the reactor is presupposed to be in its gaseous state, HCl is considered to absorb in the agglomerates of the catalyst layer, as mentioned in the model assumptions. Hence, also in the present work, the membrane can to a certain extent be expected to be in contact with aqueous hydrochloric acid in the aCL. Due to the lack of other experimental data determined under more fitting conditions, the value for the drag coefficient determined by Motupally *et al.* (2002) seems to be a reasonable choice for the here presented model. It has to be considered, that these authors assumed a maximum membrane water content of 22, due to the membrane being in contact with water on the cathode side of their reactor. This value is however based on experimental findings of for example Zawodzinski *et al.* (1993a), who measured the equilibrium water content of Nafion membranes in contact with pure water. To account for the presence of hydrochloric acid on the anode side of the membrane, the equilibrium water content is hence defined to be 17 in the present work. This is based on the work of Balko *et al.* (1981), who showed that a membrane in contact with hydrochloric acid exhibits equilibrium water contents that strongly decrease with higher acid concentrations and that can go down to a value of 5, as the water activity is suppressed in $\text{HCl}_{(\text{aq})}$ solutions (Kusoglu 2017). In the experiments of Kuwertz *et al.* (2013) HCl is only present on one side of the membrane. The maximum value of 17 for the water content is hence an average between the water content determined by Balko *et al.* (1981) at typical acid concentrations present in the HCl gas-phase electrolyzer and the value of 22 for membranes in contact with pure water. More details for the half-cell scenario resembling the experiments of Martínez (2015) are discussed in chapter 3.2.6.

Hence, the maximum osmotic drag coefficient of the fully hydrated membrane in the setup of Kuwertz *et al.* (2013) is calculated to be $17/22 \cdot 3.5 = 2.7$. Assuming a linear relationship between drag coefficient and water content following experimental evidence from Luo *et al.* (2009), for any other given water content λ_M below the equilibrium value of 17, the drag coefficient is calculated accordingly:

$$\xi(\lambda_M) = 2.7 \frac{\lambda_M}{17} \quad (3.24)$$

The diffusion coefficient of water in Nafion in equation 3.6 can be described according to the following empirical equation by Fuller (1992), as already employed in (Sorrentino 2017).

$$D_W(\lambda_M) = \lambda_M D_W^0 e^{-\frac{2436}{T}} \quad (3.25)$$

To account for the presence of HCl, Motupally *et al.* (2002) proposed an expression, which additionally considers the influence of hydrochloric acid on the dependence between water activity and water content within the membrane, as displayed in equation 3.26

$$\begin{aligned} D_W(\lambda_M)_{HCl} &= D_{W,I}(\lambda_M)_{HCl} \frac{\partial \ln(a_W)}{\partial \ln(\lambda_M)} \\ &= \frac{2.5 \cdot 10^{-7} \lambda_M (\lambda_M - 0.0209 \lambda_M^2 - 0.501)}{\lambda_M - 2} e^{-\frac{2436}{T}} \end{aligned} \quad (3.26)$$

For reasons discussed in detail in the appendix (A3), the expression by Motupally *et al.* (2002) is to be viewed with caution, so that in the here presented reactor model, equation 3.25, proposed by Fuller (1992), is employed. In future investigations, however, the effect of gaseous HCl on the diffusion coefficient of H₂O in Nafion as well as on the overall water content should be investigated experimentally in a consistent and rigorous way to reduce the uncertainties in describing the water transport through the membrane within a hydrogen chloride gas-phase electrolyzer. Lastly, the potential loss within the ionomer can then be calculated as

$$\Delta\Phi_M = i \left(\int_0^{d_M} \frac{dx}{\kappa_M(\lambda_M)} \right) \quad (3.27)$$

Equation 3.27 (Sorrentino 2017) slightly underestimates the potential loss, since the contribution of the osmotic drag of water molecules through the membrane is not accounted for as for example done in (A. Z. Weber 2004b). Furthermore, the contribution of the aCL and cCL to the proton conduction is neglected. Since the membrane employed in the experiments of Kuwertz *et al.* (2003) is 18 times thicker than the catalyst layers, this is a good approximation under most conditions. However, if the aCL and adjacent membrane is dehydrated, it is possible that neglecting the aCl contribution to the proton conduction leads to inaccuracies. In order to consider this contribution, the catalyst layer would have to be discretized. Then the electrical and ionic resistance in the CL could both be accounted for, weighted by an average reaction location within

the CL that can be derived from a transmission line approach as discussed for example in (Makharia 2005, Eikerling 1999). Since the CL is treated as a thin film with a spatially constant overpotential in the present model, this approach is not feasible at the current state for numerical reasons but should be considered in future investigations.

The ionic conductivity κ_M in equation 3.27 is calculated as follows

$$\kappa_M = \kappa_{M,0}(f - 0.042)^{0.88} = 50e^{\frac{15000}{R}\left(\frac{1}{303.15} - \frac{1}{T}\right)}(f - 0.042)^{0.88} \quad (3.28)$$

With f being the volume fraction of water in the membrane

$$f = \frac{V_0\lambda_M}{V_0\lambda_M + V_M} \quad (3.29)$$

assuming additive molar volumes, where V_0 is the molar volume of water and $V_M = \frac{EW}{\rho_M}$ is the molar volume of the polymer. The experimentally determined percolation threshold of 0.042 and exponent of 0.88 for a Nafion 117 membrane were extracted from the work of Ochi *et al.* (2009). The temperature dependence of the ionic conductivity is included in $\kappa_{M,0}$ for which the expression on the right-hand side of equation 3.28, proposed by A. Z. Weber and Newman (2004c), is used. Again, it has to be considered that just as the above-mentioned transport coefficients, also the ionic conductivity of the membrane is influenced by the presence of HCl (Vidaković-Koch 2012). However, in order to include this effect, measurements of the ionic conductivity at different water contents in the membrane in presence of gaseous hydrogen chloride are needed. The interval of measured water contents should also include the equilibrium values for a membrane in contact with water vapor and not only liquid water or acid, since the water vapor pressure in the anode compartment is below its saturation pressure. This data however is not available in the scientific literature. Therefore, it is assumed that the ionic conductivity of Nafion membranes will not be significantly influenced by the presence of gaseous HCl and can be described by equation 3.28.

Overall, the presence of gaseous HCl introduces various uncertainties due to its influence on the transport properties within the membrane, which only to a certain extent can be accounted for by utilizing the experimental data of Motupally *et al.* (2002) and Balko *et al.* (1981). Since the purpose of this work is to explain the experimentally observed limiting behavior instead of a quantitative

fit, this uncertainty is acceptable. However, the discussed effects can serve as an inspiration for further experimental work on the influence of gaseous HCl on the properties of Nafion membranes.

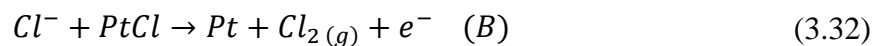
As boundary conditions, continuity of the water content in direction of the both the aCL and cCL is assumed (please see table 3.2).

3.2.5 Catalyst layer and reaction kinetics

3.2.5.1 Kinetics of the HClOR and ORR

It should be noted beforehand that all investigations of the HClOR and ORR kinetics are carried out for a Pt/C based anode and cathode catalyst as used in the experiments of Kuwertz *et al.* (2013) and Martínez (2015) and that the reaction pathways and/or rate constants likely differ for alternative catalyst materials.

Due to the highly exergonic dissociation reaction of HCl in water and the ubiquity of water in the Nafion-based agglomerates of the aCL, dissolved chloride anions instead of gaseous HCl are assumed to be the reacting species. Consequently, the following reaction network is employed to derive an expression for the overall reaction rate:



This mechanism is identical to the one proposed for the electrolysis of brine (Tilak 1979). Even though the chemical nature of the system, pH and reactant concentration differ clearly, the presence of chloride anions in both systems is a common foundation, and hence, selected developments in regards to the reaction kinetics of the brine electrolysis shall be mentioned shortly: Depending on the catalyst system and the experimental conditions, there are various works that assumed the Tafel step (A) to be predominant over the electrochemical Volmer step (B) and to limit the overall reaction rate (Conway 1979, Faita 1970) while other investigations showed the step (B) to be predominant and rate limiting (Tilak 1979). For the sake of completeness, it should be mentioned

that for the brine electrolysis a third possible mechanism, the chloronium ion pathway, was suggested (Tilak 1979, Krishtalik 1981, Guerrini 2005).

In the present work considering the gas-phase oxidation of HCl, step (A) is assumed to be predominant and rate limiting based on simulation with the here presented model as well as a reevaluation of the experimental data from Martínez *et al.* (2014, 2015). This leads to the following expression for the current density on the microscale j^μ , which is derived and discussed in detail in chapter 5.1.

$$\begin{aligned} j^\mu &= 2Fk_A \left(\frac{K_0 a_{Cl^-}^\mu}{1 + K_0 a_{Cl^-}^\mu e^{\frac{F\eta_A}{RT}}} \right)^2 e^{\frac{2F\eta_A}{RT}} - 2Fk_{-A} p_{Cl_2} \\ &= 2Fk_A \left(\frac{K_0 a_{Cl^-}^\mu}{1 + K_0 a_{Cl^-}^\mu e^{\frac{F\eta_A}{RT}}} \right)^2 e^{\frac{2F\eta}{RT}} \left(1 - e^{\frac{-2F\eta_A}{RT}} \right) \end{aligned} \quad (3.33)$$

Here, k_A is the rate constant of the Tafel step, $a_{Cl^-}^\mu$ stands for the activity of chloride anions within the agglomerates and K_0 represents the equilibrium constant for the adsorption and desorption of chloride anions on the platinum surface according to equation 3.30.

For the ORR, which has been extensively investigated in the scientific literature, a first order reaction is assumed, employing the following expression by Neyerlin *et al.* (2006) for the rate constant k_{ORR}^μ

$$k_{ORR}^\mu = (1 - S_{L,CCL}) a^\mu \frac{j_{o,s}}{4F c_{O_2,ref}} \exp\left(\frac{-\alpha_c F}{RT} \eta_c\right) \quad (3.34)$$

and

$$j_{o,s} = j_{o,s}^* \exp\left(-\frac{E_c^{rev}}{RT} \left(1 - \frac{T}{T^*}\right)\right) \quad (3.35)$$

with E_c^{rev} being the activation energy of the ORR at the reversible cell potential and a^μ the specific internal area of the agglomerates in $\frac{m_{act}^2}{m_{agg}^3}$. Inserting equation 3.35 into equation 3.34 yields

$$\begin{aligned}
k_{ORR}^{\mu} &= (1 - S_{L,CCL}) \frac{a^{\mu} j_{o,s}^*}{4F c_{O_2,ref}} \exp\left(\frac{-\alpha_c F}{RT} \eta_c - \frac{E_c^{rev}}{RT} \left(1 - \frac{T}{T^*}\right)\right) \\
&= (1 - S_{L,CCL}) \frac{k_{ORR}^{\mu,0}}{4F} \exp\left(\frac{-\alpha_c F}{RT} \eta_c - \frac{E_c^{rev}}{RT} \left(1 - \frac{T}{T^*}\right)\right) \quad (3.36)
\end{aligned}$$

where the term $\frac{a^{\mu} j_{o,s}^*}{c_{O_2,ref}}$, with $c_{O_2,ref}$ being the reference concentration of O₂ in the agglomerate, is summarized in the catalyst specific standard rate constant $k_{ORR}^{\mu,0}$ in units of $\frac{1}{s}$, whose value is given in table 3.3. The factor $(1 - S_{L,CCL})$ accounts for the fact that flooding due to water condensation in the cCL renders affected catalyst sites inactive.

3.2.5.2 Modeling of the catalyst layer

On the macroscale, the anode and cathode catalyst layer are modeled stationary as a thin film, while on the microscale, an agglomerate model is employed. Hence, the catalyst layer is described by the balances of fluxes entering and leaving from both sides as listed in table 3.2. For more information on the concept of the agglomerate model, the reader may refer to (Vidaković-Koch 2017).

From these algebraic equations, the partial pressure of all gaseous species, the total pressure and the water content in the aCL and cCL can be calculated. The source term s_{tot} in the boundary condition for the total pressure (table 3.2) includes the fluxes N_i^{μ} into and out of the agglomerates, the water flux at the CL|M interface, as well as the diffusive and convective flux of all gaseous species and, on the cathode side, the liquid water flux at the cGDL|cCL interface. Due to the presence of liquid water, the algebraic equation for the total gas pressure in the cCL has to be adjusted so that it only accounts for the portion of water that is in its gaseous state, since the liquid portion does not contribute to the gas-phase pressure. Hence, this liquid portion is discriminated by multiplying the water flux at the cGDL|cCL and the cCL|M interface with a factor of $(1 - S_{L,CCL})$. The underlying assumption is that at full saturation, all water will be in the liquid phase, at zero saturation, all water will be in the gas-phase, and at saturations in-between these two limits,

the portion of water in both phases is approximated by employing the above-mentioned factor. The necessity of such an approach arises from the use of only one equation for describing the water flux due to the assumed phase equilibrium.

The fluxes N_i^μ into and out of the agglomerates can be calculated based on the reaction rate averaged over the whole agglomerate

$$N_i^\mu = -\frac{1}{R_{agg}^2} a \int_{r=0}^{r=R_{agg}} r^2 a^\mu r^\mu(a_i^\mu, \eta) dr \quad (3.37)$$

where R_{agg} is defined as the radius of the agglomerates, $a = \frac{3}{R_{agg}}(1 - \varepsilon_{CL})$, r^μ is the reaction rate on the microscale and a_i^μ the activity of species i within the agglomerate (Vidaković-Koch 2017). The radius of the agglomerates in the experiments of Kuwertz *et al.* (2013) and Martínez (2015) is not precisely known. Hence, a literature value of 200 nm proposed by Xing *et al.* (2013) is chosen, instead of treating the agglomerate size as a fit parameter, in order to obtain physically feasible and realistic results and not simply enhance the accuracy of the model with an increased amount of fitting parameters. It should be noted that there are also various literature sources assuming greater radii (Barton 2005, Krewer 2011) as well as smaller radii (Secanell 2008), hence in chapter 5.1.3 the influence of the agglomerate size on the presented results is investigated and discussed in more detail.

To solve equation 3.37, the activity a_i^μ of species i within the agglomerate as a function of the spatial coordinate r must be determined by solving the mass balance on the microscale (eq. 3.7). Please note that diffusion within the agglomerates is described by Fick's law, assuming a two-component system of H_2O and $HCl_{(aq)}$. Since the equilibrium mole fraction of Cl_2 in water at 333 K is only 0.00094 at a vapor pressure of 1.013 bar, the influence of dissolved chlorine on the diffusion of $HCl_{(aq)}$ in water can be neglected. The composition dependence of the diffusion coefficient $D_{HCl_{(aq)}-H_2O}^{\mu,eff}$ in Nafion is not known. Hence, a constant value obtained from the work of Vidaković-Koch *et al.* (2012) is employed.

Employing the kinetic expression in equation 3.33, equations 3.7 and 3.37 are solved numerically for the HClOR, since an analytical solution is untenable due to the non-ideality of the HCl/H_2O system. As the first boundary condition, vapor-liquid equilibrium between HCl in the gas-phase

and in the water containing agglomerates is assumed at the surface ($r = R$). Due to the strongly non-ideal nature of the system, it is not possible to employ Henry's law as oftentimes done for the ORR (Xing 2013, Sun 2005). Hence, fit functions were generated to correlate the equilibrium mole fraction of chloride anions to the HCl partial pressure based on experimental data (Green 2018) for temperatures between 298 and 363 K. Similarly, the activity coefficients of the chloride anions as a function of their mole fraction in the aqueous solution were fitted to experimental data by Cerquettie *et al.* (1968). The fit functions as well as more details on the underlying assumptions are given in the appendix (A4). The second boundary condition consists of a no-flux criterion in the center of the spherical agglomerate ($r = 0$) for reasons of symmetry.

For the ORR however, the following analytical solution for a first order reaction can be employed, as described in more detail in (Vidaković-Koch 2017, Neyerlin 2006)

$$N_{O_2}^{\mu} = \frac{p_{O_2,CCL}}{H_{O_2}} \left(\frac{1}{k_{ORR}^{\mu} E_{ORR} (1 - \varepsilon_{CCL})} + \frac{\delta}{D_{O_2}^{\mu,eff}} \frac{R}{3(1 - \varepsilon_{CCL})} \right)^{-1} \quad (3.38)$$

$$E_{ORR} = \frac{1}{\phi_{ORR}} \left(\frac{1}{\tanh(3\phi_{ORR})} - \frac{\phi_{ORR}}{3} \right) \quad (3.39)$$

$$\phi_{ORR} = \frac{3}{R_{agg}} \sqrt{\frac{k_{ORR}^{\mu}}{D_{O_2-H_2O}^{\mu,eff}}} \quad (3.40)$$

where E_{ORR} is the effectiveness factor and ϕ_{ORR} the Thiele modulus.

Finally, the charge balance for the aCL and cCL is formulated with the electrode double layer acting as a capacitor and the charge transfer acting as an ohmic resistance in parallel according to equation 3.8 (Sorrentino 2017). Here, C_{DL} is the capacity of the double layer and d_{CL} the catalyst layer thickness. The overall cell potential is calculated as

$$E_{cell} = -(E_{OC} + \eta_A - \eta_C + \phi_M + \phi_{RI}) \quad (3.41)$$

where ϕ_{RI} is the potential loss due to ohmic resistances within the CL, GDL and plate on both the anode and cathode sides

$$\phi_{RI} = 2i \left(\frac{d_{CL}}{\sigma_{CL}} + \frac{d_{GDL}}{\sigma_{GDL}} + \frac{d_{plate}}{\sigma_{plate}} \right) \quad (3.42)$$

The electronic conductivities σ_i and thicknesses of all layers d_i are given in table 3.3. The contact resistance between the different layers is neglected in a first approximation, since it depends on factors like the assembly pressure (Atyabi 2019) and structural details of the reactor employed by Kuwertz *et al.* (2013, 2016a,b,c) that are not known. The temperature-dependent values for the open-circuit potential E_{OC} are adopted from the experimental work of Kuwertz *et al.* (2013). This indirectly accounts for effects like the poisoning of the cathode catalyst as a consequence of potential HCl/Cl₂ crossover, as investigated in more detail in chapter 3.3.

3.2.6 Half-cell model

In the experiments of Martínez (2015), the cathode chamber is filled with dilute sulfuric acid. According to Tang *et al.* (Tang 2013), the approximate water content of a Nafion 117 membrane equilibrated with 1 M H₂SO₄ is 17. Hence, the water content at the boundary between the membrane and the cathode chamber (S_3 in Figure 3.1 a) is set to 17, like in the full-cell scenario. Since the polarization curves of Martínez (2015) were measured against a reversible hydrogen electrode adjacent to the membrane in the cathode compartment, the CE, and hence the whole cathode compartment, is not considered in the model. Furthermore, since their experiments were carried out at low conversions of ca. 5% and since the sulfuric acid circulating through the CE chamber removes significant parts of the reaction heat through convection, the reactor temperature is not expected to increase significantly during operation so that the temperature in the half-cell simulations is set to be constant. Lastly, since the measurements of Martínez (2015) were corrected for ohmic drop online, the half-cell model does not consider ohmic losses as well.

3.2.7 Numerical methods and parameters

The differential equations discussed in the previous chapters are discretized based on the finite volume method. In the full-cell setup, 40 discretization cells are employed for each layer in simulations where membrane dehydration can occur and 20 cells in simulations with well hydrated

membranes, except for the agglomerates which always contain 10 discretization cells only. In the second scenario, the half-cell setup of Martínez (2015), the lower concentration gradients due to the sufficient membrane hydration and the low conversions allow for the use of only 10 discretization cells everywhere.

The obtained ODE system together with the algebraic equations listed in tables 3.1 and 3.2 were solved in MATLAB R2015b using the ode15s solver. With the exception of the standard rate constant $k_{ORR}^{\mu,0}$ of the ORR (on the right side of eq. 3.36), the rate constant k_A of the HClOR and the equilibrium constant K_0 describing the adsorption and desorption of chloride anions on the platinum catalyst surface (eq. 3.33), all model parameters were obtained from literature (please see table 3.3). The rate constant for the HClOR can be directly calculated from the limiting current densities j_{limit} determined experimentally by Martínez (2015) (please see Figure 5.9 in (Martínez 2015)).

$$k_A = \frac{j_{limit}}{2F(1 - \varepsilon_{CL})L_{ACL}} \quad (3.43)$$

This relation is based on the assumption that the experimentally observed limiting behavior is caused by a reaction limitation in the rate determining Tafel step (eq 3.31) and that the surface coverage is approximating values of one throughout the whole agglomerate at the supposedly reaction limited current density. The validity of both assumptions is discussed in detail in chapter 5.1.1 and 5.1.3.

Since the highest current densities investigated in the experiments of Martínez *et al.* (2015) are still slightly below the reaction limited current, they have to be approximated by an extrapolation of their polarization data. Certainly, a better fit could be obtained by fitting the simulated polarization curve to the entire experimental data set over the whole current density range with the rate constant as a fit parameter. However, approximating the rate constant from the experimentally determined reaction limited current density according to equation 3.43 while still being able to reproduce the experimental polarization curve over the whole current density range would further validate the assumption of a reaction limitation and make the model more reliable than introducing an additional fit parameter. Hence, the reaction rate constant is not systematically treated as a fitting parameter.

The anode catalyst loading in experiments of Kuwertz *et al.* (2013) differs from the one used by Martínez (2015). According to half-cell measurements of the HClOR by Martínez (2015), this difference in the catalyst loading leads to a reduction in the reaction limited current of ca. 11%. Hence, in the full-cell simulations the rate constant k_A was corrected with a factor of 0.89 compared to the value employed in the half-cell simulations (eq. 3.43), in order reproduce the conditions of the experiments of Kuwertz *et al.* (2013).

Lastly, Zhu *et al.* (2019) showed that the electrochemically available surface area (ECSA) in PEM fuel cells is heavily dependent on the water content at low humidity ($\lambda < 3$). To not introduce more parameters than necessary, this effect is neglected in the half-cell model due to sufficient hydration under the conditions investigated in the present work ($\lambda \geq 4$). In the anode of the full-cell model, the change of ECSA with water content must however be considered due to possible dehydration (the cathode is sufficiently hydrated even when parts of the membrane adjacent to the anode start to dehydrate, as shown in chapter 5.3.2). This is done by creating a fit for the ECSA as a function of the water content based on the experimental data by Zhu *et al.* (2019) and using the water content at the limiting current density in the half-cell simulations as a reference to then determine the rate constant k_A , which is proportional to the ECSA, at any given water content. More details about the procedure are given in the appendix (A5).

In conclusion, the only two independent fitting parameters of the model are the standard rate constant $k_{ORR}^{\mu,0}$, or to be more precise, the active catalyst area per cubic meter of agglomerate a^μ , which is contained in the standard rate constant, since the active area of the catalyst employed by Kuwertz *et al.* (2013) is unknown, and, secondly, the equilibrium constant K_0 . The equilibrium constant predominantly shifts the polarization curve of the HClOR towards lower or higher potentials. Hence, it was obtained directly by comparing the experimental U-I curve (Martínez 2015) with the half-cell simulation of the present work and adjusting the value of K_0 so that both curves are not parallel to each other, but align.

Employing only two fit parameters in the overall model serves to ensure that the model is physically realistic and predictive and that agreement with experimental results from the half-cell as well as the full-cell measurements of and Martínez (2015) and Kuwertz *et al.* (2013) is not just a consequence of various fit parameters.

Please note that both, K_0 and k_A , are functions of the temperature. Hence, in the full-cell simulations where the reactor temperature is not constant, their temperature dependence is fitted to the experimental data of Martínez (2015), as described in more detail in the appendix (A5). In non-isothermal scenarios, this hence lead to the necessity of two additional fit parameters.

Table 3.3, Model parameters used in the reactor simulation.

Parameter	Symbol	Value	Unit
Wall and feed temperature	T_{in}, T_{wall}	313, 323, 333	K
Rate constant of Tafel step (HClOR)	$k_A(T)$	$0.89 \frac{ECSA_{rel}(\lambda)}{ECSA_{rel}(\lambda = 4)} 32.188e^{0.01788T}$	$\frac{\text{mol}}{\text{m}^3 \text{ s}}$
standard reaction rate (ORR)	$k_{ORR}^{\mu,0}$	22.227	$\frac{1}{\text{s}}$
Reference temperature ORR (Neyerlin 2006)	T^*	353	K
Oxygen reference concentration at 1 bar partial pressure and 60 K	$c_{O_2,ref}$	5.5545	$\frac{\text{mol}}{\text{m}^3}$
Activation energy ORR at reversible cell potential (Neyerlin 2006)	E_c^{rev}	67000	$\frac{\text{J}}{\text{mol}}$
Charge transfer coefficient cathode	α_c	1	-
Cathode catalyst (Pt) loading	L	5	$\frac{\text{g}}{\text{m}^2}$
Henry constant O ₂ (Xing 2013)	H_{O_2}	$0.1e^{(14.1 - \frac{666}{T})}$	$\frac{\text{Pa m}^3}{\text{mol}}$
Ionomer volume fraction in CL	ϕ_{Nafion}	0.374	-
Effective diffusion coefficient of oxygen in agglomerates (Sethuraman 2009)	$D_{O_2}^{\mu,eff}$	$\phi_{Nafion}^{1.5} 24.82e^{\frac{-1949}{T}}$	$\frac{\text{m}^2}{\text{s}}$
Effective Diffusion coefficient of hydrochloric acid in agglomerates (Vidaković-Koch 2012)	$D_{HCl(aq)}^{\mu,eff}$	$\phi_{Nafion}^{1.5} 1.2 \cdot 10^{-11}$	$\frac{\text{m}^2}{\text{s}}$
Porosity CL	ε_{CL}	0.6	-
Porosity GDL (Kuwertz 2016a)	ε_{GDL}	0.75	-

Anode and cathode gas channel pressure	p_{tot}^{GC}	100000	Pa
saturated permeability (Zenyuk 2016)	k_{sat}	$1.54 \cdot 10^{-15}$	m^2
Exponents for the liquid and gas-phase permeability (Zenyuk 2016)	β_L, β_G	3.5	-
Anode gas viscosity (Coker 2007)	$\eta_{G,A} \approx \eta_{HCl}$	$(-9.188 + 0.555T - 0.000113T^2)10^{-7}$	Pa s
Cathode gas viscosity (Coker 2007)	$\eta_{G,C} \approx \eta_{O_2}$	$(44.224 + 0.562T - 0.00011T^2)10^{-7}$	Pa s
Potential independent part of the equilibrium constant for chloride adsorption/desorption	$K_0(T)$	$584684.86e^{-\frac{75497.5}{RT}}$	$\frac{m^3}{mol}$
prefactor of the equilibrium constant for chloride adsorption/desorption	K_0^*	584684.86	-
Agglomerate radius (Xing 2013)	R_{agg}	200	Nm
GDL thickness (Kuwertz 2016c)	d_{GDL}	400	μm
Thickness CL (Kuwertz 2016c)	d_{CL}	10	μm
Thickness Membrane (Kuwertz 2016c Martínez (2015))	d_M	178 (if not otherwise specified)	μm
Electrode area (Kuwertz 2016c Martínez (2015))	A	$3 \cdot 10^{-3}$ full-cell $2.3 \cdot 10^{-4}$ half-cell	m^2
Volumetric flow rate of HCl at standard temperature and pressure (STP) (Kuwertz 2016c, Martínez (2015))	\dot{V}_{HCl}	$10 \cdot 10^{-6}$ full-cell $8.3 \cdot 10^{-6}$ half-cell	$\frac{m^3}{s}$
Volumetric flow rate of O ₂ at standard temperature and pressure (STP) (Kuwertz 2016c)	\dot{V}_{O_2}	$10 \cdot 10^{-6}$	$\frac{m^3}{s}$
Pre-factor, Diffusion coefficient of water in Nafion (Fuller 1992)	D_W^0	$2.1 \cdot 10^{-7}$	$\frac{m^2}{s}$

Density of dry membrane (Kusoglu 2017)	ρ_M	2000	$\frac{\text{kg}}{\text{m}^3}$
Equivalent weight of membrane (Kusoglu 2017)	EW	1.1	$\frac{\text{kg}}{\text{mol}}$
Drag coefficient membrane (Motupally 2002)	ξ	2.7 at full membrane hydration	-
Flow plate thickness (Kuwertz 2016c)	d_{plate}	0.0057	m
PTFE gasket thickness (Kuwertz 2016c)	d_{PTFE}	0.00012	m
FKM gasket thickness (Kuwertz 2016c)	d_{FKM}	0.0005	m
Titan endplate thickness (Kuwertz 2016c)	$d_{endplate}$	0.005	m
Thermal conductivity endplate (Powell 1961)	$\lambda_{endplate}$	15.6	$\frac{\text{W}}{\text{m K}}$
Thermal conductivity flow plate (Stübler 2012)	λ_{plate}	20	$\frac{\text{W}}{\text{m K}}$
Thermal conductivity PTFE gasket (Price 2002)	λ_{PTFE}	0.245	$\frac{\text{W}}{\text{m K}}$
Thermal conductivity FKM gasket (KB Roller Tech 2020)	λ_{FKM}	0.75	$\frac{\text{W}}{\text{m K}}$
Total thermal resistance	R	0.294	$\frac{\text{K}}{\text{W}}$
Interstitial heat transfer coefficient	h_v	1.5·105	$\frac{\text{W}}{\text{m}^3\text{K}}$

3.2.8 Reactor model summary

In conclusion, a 1D non-isothermal two-phase agglomerate model was developed for the purpose of gaining an in-depth understanding of the physicochemical phenomena that lead to the limiting behavior observable in the half-cell experiments of Martínez (2015) as well as the full-cell investigations of Kuwertz *et al.* (2013). Based on the discussion of possible limiting mechanisms earlier in this work, a special focus was put on the rigorous modeling of mass transfer within the GDL, as well as the interplay between the HClOR reaction kinetics and mass transfer within the agglomerates of the aCL. This includes the consideration of two-phase flow and nonisothermality due to the significant impact of the water household and thermal management of the reactor on both the reaction rate and mass transfer. Lastly, various opportunities for future experimental research serving the purpose of reducing the uncertainty in modeling the gas-phase electrolysis of HCl were identified, like investigating the influence of $\text{HCl}_{(g)}$ on the transport properties of the membrane.

3.3 Numerical model for investigating the crossover of HCl and chlorine

While the evaluation of Cl_2 and HCl crossover and its impact on the reactor performance under realistic operating conditions was defined as an important part of present work, the Nafion membrane of the reactor model presented in the previous chapter, is treated as impermeable for all species but water and protons. Potential crossover of HCl and Cl_2 as well as its effect on the reactor performance was only indirectly considered by employing the experimentally determined OCV from Kuwertz *et al.* (2013) instead of the thermodynamic value and by fitting the rate constant of the ORR to their experimental polarization data (please see chapter 3.2.7). Since the focus of the numerical reactor model is the investigation of the limiting behavior, this approximation is justified and, due to the lack of quantitative data on the crossover of HCl and Cl_2 as well as its exact effect on the reactor performance, the only feasible option at the current state.

To shed more light on this topic, a numerical steady state model for simulating HCl and Cl_2 crossover through the membrane is introduced in this chapter and serves as one pillar of a

combined theoretical and experimental approach (please see chapter 4.1). The crossover model can be easily integrated into the reactor model introduced in chapter 3.2, if this becomes of interest in future investigations. This is however only purposeful, if not only the crossover but also its impact on the ORR kinetics can be modeled quantitatively, which would certainly be an interesting subject for future research but is out of the scope of the present work. Therefore, and because the variety of implemented physical phenomena makes the reactor model computationally very costly already at the current state, the crossover equations have not yet been integrated into the overall reactor model. Please note that major parts of this chapter are in the process of being published (Bechtel 2020c) and that the following equations were mainly formulated and solved by the second author A. Crothers.

Both HCl and Cl₂ are assumed to absorb in the water constituting the hydrophilic domains of the Nafion membrane. Hence, only the crossover of the aqueous form of HCl_(aq) is considered, which, due to the highly exergonic dissociation reaction of HCl in water, appears to be a valid approximation. Similarly, in the case of Cl₂, only the transport of dissolved chlorine through the hydrophilic domains of the membrane is considered, while diffusion through the hydrophobic Nafion domain is neglected due to significantly lower diffusion coefficients.

At steady state, the divergence of the flux N_i across the membrane (1D, x-direction) is zero for all species i (Bird 2006).

$$-\frac{\partial N_i}{\partial x} = 0 \quad (3.44)$$

For H₂O, this flux N_w was introduced in the form of equation 3.6 (table 3.1) and for HCl_(aq) and Cl₂ it consists of three terms; convection of the aqueous solution through the membrane, diffusion through the hydrophilic domains, and, for charged Cl⁻ species, migration (Newman 2004, Darling 2016, Kodým 2016).

$$N_i = c_i v - D_i^w \frac{\partial c_i}{\partial x} + \left(\frac{t_i^w}{z_i F} \right) i \quad (3.45)$$

Here, c_i is the concentration of i , v is the velocity of the aqueous solution relative to the membrane, D_i^w and t_i^w are the diffusion coefficient and transference number, respectively, of i in the aqueous solution-filled pores and z_i is the charge number of the ionic species (Darling 2016).

The two last terms on the right hand side of equation 3.45 account for diffusion and migration of species relative to the movement of the aqueous solution in the membrane pores, meaning that the aqueous solution is the reference velocity for these terms, denoted by the superscripts w on the diffusion coefficient and transference number. The first term accounts for the movement of the aqueous solution relative to the membrane. Assuming a small concentration of ions compared to the concentration of water in the membrane, the velocity of the aqueous solution through the membrane equals to the velocity of water, v_w (Bird 2006).

$$v \approx v_w = \frac{N_w}{c_w} \quad (3.46)$$

Please note that equation 3.45 neglects frictional interactions between the membrane, Cl^- , and Cl_2 and that the concentrations, velocities, and fluxes have a superficial basis, meaning that quantities are averaged over both the aqueous solution and the Nafion phases of the wet membrane. The diffusion coefficients D_i^m are challenging to measure and reported values vary by orders of magnitude (Vidaković-Koch 2012). In the crossover model, they are hence calculated by correcting the diffusion coefficient of species i in bulk water $D_i^{w,\infty}$, with $D_{\text{Cl}^-}^{w,\infty} = 1.89 \cdot 10^{-9} \text{ m}^2/\text{s}$ and $D_{\text{Cl}_2}^{w,\infty} = 2.03 \cdot 10^{-9} \text{ m}^2/\text{s}$ (Weast 1978), by the tortuosity of the hydrophilic domains of the membrane τ , where the tortuosity is specified by Archi's law (Dullien 1979).

$$D_i^w = \frac{D_i^{w,\infty}}{\tau} = \frac{D_i^{w,\infty}}{f^{-\chi}} \quad (1.47)$$

Here, f is the water volume fraction (eq. 3.29) and χ is a scaling coefficient set to 1.33 according to Crothers *et al.* (Crothers 2020). The transference number t_i^m in equation 3.45 is defined according to the dilute-solution theory (Newman 2004)

$$t_i^w = \left(\frac{F^2}{RT} \right) \frac{z_i^2 D_i^w c_i}{\kappa} \quad (3.48)$$

where κ is the membrane conductivity (eq. 3.28). Solving conservation equation 3.44 with the constitutive equations 3.45 and the formulation of the water flux according to equation 3.6 requires two boundary conditions for each species, adding up to a total of six boundary conditions. Specifying the concentration of species in the membrane at the anode/membrane and cathode/membrane interfaces ($x = 0$ and $x = d_M$ respectively) provides these boundary conditions. In the present work, the crossover of HCl and Cl₂ is investigated for the full-cell setup and, in a second scenario, also for a liquid-phase reactor resembling the one employed in the Bayer UHDENORA process, where hydrochloric acid is fed into the anode chamber instead of gaseous HCl. The concentrations of Cl⁻ and Cl₂ at the cathode/membrane surface is set to zero in all simulations, while their concentrations on the anode/membrane interface vary in both scenarios and are obtained in three steps.

For the full-cell setup, the water content and the partial pressures of Cl₂ and HCl in the aCL are extracted from a simulation of the full-cell setup based on the reactor model introduced in chapter 3.2 as a function of the current density in a first step. In the second step, the partial pressures as a function of the current density obtained from the numerical reactor model are converted into aqueous interface-concentrations by employing the same vapor-liquid equilibrium (VLE) relation for HCl-H₂O already used in the full-cell model (please see appendix A4) and Henry's law for Cl₂ (Young 1983).

$$c_{\text{Cl}_2}^{\infty} = x_{\text{Cl}_2}^{\infty} c_{\text{T}}^{\infty} = (9.397 \cdot 10^{-4} [\text{atm}^{-1}]) p_{\text{Cl}_2}^{\text{aCL}} c_{\text{T}}^{\infty} \quad (3.49)$$

Here, $p_{\text{Cl}_2}^{\text{aCL}}$ is extracted from the full-cell model as a function of the current density and given in units of atmospheres and c_{T}^{∞} is the total molar concentration of the aqueous solution which is assumed to be the reciprocal of the molar volume of water (55.6 mol/l). This assumption is valid since the total concentration of the aqueous solution does not change strongly with the concentration of HCl_(aq) under the investigated conditions (Clegg 2011) and because the concentration of dissolved Cl₂ is negligibly small. Since the full-cell model described in chapter 3.2 is validated by experimental data of Kuwertz *et al.* (2013), this procedure ensures realistic conditions for modeling the HCl and Cl₂ crossover. All crossover simulations for the full-cell setup are carried out at 333.15 K.

In the third step, a partition coefficient, $K_{M,i}$, relates the above introduced concentrations $c_i^\infty(p_i)$ to an actual concentration within the membrane c_i , considering that the presence of the polymer and possible species-membrane interactions lead to a different concentration of the species in Nafion compared to pure water.

$$c_i = c_i^\infty(p_i)K_{M,i} \quad (3.50)$$

For Cl_2 , $K_{M,\text{Cl}_2} = f$ with f being the volume fraction of water in the membrane (eq. 3.29), because this species is not expected to have significant electrostatic or other specific interactions with the membrane and, therefore, it partitions uniformly into the hydrophilic phase of the membrane but not into the hydrophobic polymer regions. Fitting a sorption isotherm from literature for chloride ions in Nafion (Beers 2011) gives $K_{M,\text{Cl}^-} = 0.6363f$. At chloride concentrations relevant for this study ($> 0.1 \text{ M}$), the HCl isotherm displays negligible Donnan exclusion, so that this effect is not expected to impede the crossover of Cl^- (Beers 2011). These so obtained concentrations can then be employed as boundary conditions.

For the second scenario of a liquid-phase reactor, the anode chamber is filled with an aqueous 2 M solution of hydrochloric acid ($c_{\text{Cl}^-}^\infty$), which partitions into the membrane according to K_{Cl^-} . To allow for comparability with the experimental investigations discussed in chapter 4.2 and 5.2, the temperature in the simulation was set to 293.15 K. Due to the lack of precise data for Cl_2 partial pressures, a value of 1.013 bar is assumed leading to $c_{\text{Cl}_2}^\infty = 1.88 \cdot 10^{-3} c_{\text{T}}^\infty$ (Young 1983). The water content of the membrane at the anode is set to 17, as done for the cathode in the numerical model for the half-cell setup in chapter 3.2.6, which, due to the slight differences in the acid concentration, is an approximation. The cathode is assumed to be at 90% RH at which the membrane has a water content of 10 (Kusoglu 2017).

Equations 3.44, 3.55, and the expression for the water flux in equation 3.6 were solved simultaneously using the finite element software COMSOL 5.4 with the MUMPS numerical solver. The relative tolerance was set to $1 \cdot 10^{-10}$ and 100 mesh elements were employed. A summary of the relevant model parameters is listed in table 3.4.

Table 3.4. Parameters for the simulation of HCl and Cl₂ crossover.

Parameter	Full-cell setup	Liquid-phase reactor
$c_{\text{Cl}^-}^{\infty}$	current density dependent	2 mol/l
$c_{\text{Cl}_2}^{\infty}$	Current density dependent	$1.88 \cdot 10^{-3} c_{\text{T}}^{\infty}$
c_{T}^{∞}	55.6 mol/l	55.6 mol/l
K_{M,Cl_2}	f	f
K_{M,Cl^-}	0.6363 f	0.6363 f
$D_{\text{Cl}^-}^{w,\infty}$	$2.03 \cdot 10^{-9} \text{ m}^2/\text{s}$	$2.03 \cdot 10^{-9} \text{ m}^2/\text{s}$
$D_{\text{Cl}_2}^{w,\infty}$	$1.89 \cdot 10^{-9} \text{ m}^2/\text{s}$	$1.89 \cdot 10^{-9} \text{ m}^2/\text{s}$
χ	1.33	1.33
T	333.15	293.15
d_M	178 μm	178 μm

3.4 Novel method for the precise determination of transport coefficients

As discussed in chapter 3.3.2, the accurate modeling of mass transfer plays an important role in the analysis of the experimentally observed limiting behavior in the gas-phase electrolysis of HCl. Hence, in the following, a novel approach for determining binary diffusion coefficients, viscosities and thermal conductivities is proposed. Please note that major parts of this chapter are extracted from Bechtel *et al.* (2020b) and that first (very basic) investigations in that field were already discussed in (Bechtel 2014).

3.4.1 Modeling of transport coefficients based on the kinetic gas theory

For modeling these transport coefficients, the kinetic gas theory, in particular the equations of Chapman and Enskog (CE), proved to be good approximations that have been widely used in the field of chemical engineering over the past decades (McGee 1991). In recent years, there has been

significant further development, for example in the investigation of potential energy surfaces (PES) for interactions between two gas molecules using quantum mechanical ab initio calculations. This enabled the calculation of properties like the second virial coefficient, diffusion coefficients, thermal conductivities and viscosities of gases based on the kinetic theory for polyatomic gases (Hellmann 2018, Crusius 2018). While this approach is fully predictive and showed good accuracy for a variety of gases (Crusius 2015, Hellmann 2014), it is computationally very expensive and requires expert knowledge to be carried out. Hence, the classical CE equations (Chapman 1970, Hirschfelder 1954) for calculating the binary diffusion coefficients D_{ij} , viscosities η and thermal conductivities λ remain to be the more practical and easily applicable approach for most chemical engineering applications. Before discussing the method proposed in this work, a brief introduction into the calculation of these transport coefficients based on the CE theory is given in the following. For more detailed information, the reader may refer to (Chapman 1970, Hirschfelder 1954)

$$D_{ij} = \frac{3}{16\pi M \sigma^2 \Omega_{ij}^{(1,1)*}} \sqrt{\frac{2\pi k_B^3 T^3}{\mu_{ij}}} \quad (3.51)$$

$$\lambda = \frac{25}{32\pi M \sigma^2 \Omega^{(2,2)*}} \sqrt{m\pi k_B T} \quad (3.52)$$

$$\eta = \frac{5 \cdot \sqrt{m \cdot \pi \cdot k_B \cdot T}}{16 \cdot \pi \cdot \sigma^2 \cdot \Omega^{(2,2)*}} \quad (3.53)$$

In these equations, M is the molar mass, m the mass of one molecule, μ the reduced mass of two gas molecules, k_b the Boltzmann constant, σ , the collision diameter and $\Omega_{12}^{(l,s)*}$ the collision integral reduced by the potential depth ε . The collision integral of the order l, s can be described with the following equation (Hirschfelder 1954).

$$\Omega^{(l,s)} = \frac{1}{2\sqrt{\pi}} \int_0^\infty e^{\frac{-\mu \cdot v'^2}{2k_B \cdot T}} \cdot \left(\frac{-\mu \cdot v'^2}{2 \cdot k_B \cdot T} \right)^{s+1.5} \cdot Q^l_{(g)} \cdot dg \quad (3.54)$$

where v' is the relative velocity of two colliding molecules towards each other and $Q^l_{(g)}$ contains information about the intermolecular potentials. More information on the collision integral can be found in (McGee 1991, Chapman 1970).

3.4.2 Shortcomings in the classical approach of determining LJ parameters and motivation of a new methodology

Equation 3.51 to 3.53 rely on at least the (LJ) parameters and, for polar gases, also the dipole moment of a gas species due to its influence on the collision integral. In the scientific literature, the LJ parameters are fitted to experimental data of only one transport coefficient, mostly the viscosity due to the comparably high precision of experimental methods for its determination (Kee 2003). The so obtained LJ parameters lead to a good agreement between the CE equations and the experimental data for this specific transport property. However, utilizing the same parameters for modeling different transport properties oftentimes leads to distinct deviations. Mason and Monchick (1962a) for example calculated binary diffusion coefficients for a variety of gases with a given set of LJ parameters from literature. The binary diffusion coefficient for a water-oxygen mixture showed a mean relative deviation from experimental data of 9.5%, for water-methane mixtures it was even 15.5%. Hanley and Klein (Hanley 1970) determined LJ parameters for hydrogen from viscosity data and were able to reproduce the experimental data with a maximum deviation of less than 3% in a temperature range from 200 to 2000 K. However, when using the same LJ parameters to calculate the thermal conductivity, the maximum deviation ranged from +8% to -6%. In chapter 3.4.4, the viscosity of nitrous oxide as well as its binary diffusion coefficient with nitrogen calculated based on LJ parameters from Hirschfelder *et al.* (1954) are compared to experimental data from Kestin and Wakeham (1979), Johnston and McCloskey (1940), and Matsunaga *et al.* (1994) and the same underlying problem can be observed.

In some cases, as for example in the work of Hanley and Klein (1970) it is argued that the uncertainty of the experimental data is too high in order to obtain precise parameters from a fit. This is true for some gases and transport properties. Also, it has to be stated that for certain gases, the agreement between calculated and experimentally measured transport properties indeed lies within the experimental uncertainty when using LJ parameters from fitting to a different transport property. Still there are numerous examples, like the ones mentioned above, where this is not the case despite low uncertainties in the experimental data employed for the fit, showing that there is significant room for an improved accuracy in determining the LJ parameters. Hence, the question arises where this disagreement is originating from.

The hypothesis of this chapter is that the subsets of LJ parameters $M \subseteq \mathbb{R}_{>0}^2$, with which the Chapman Enskog equations can predict transport coefficients with an accuracy that is within the experimental uncertainty $\xi > 0$, are not identical for each transport property. This is due to the fact that the binary diffusion coefficient is based on a collision integral with a different order than the thermal conductivity and the viscosity (eq. 3.51 to 3.53). Hence, fitting towards one transport coefficient only, does not necessarily yield parameters that are suited to describe the other transport properties as well.

$$\begin{aligned}
M_{\mu} &= \left\{ (\varepsilon, \sigma) \in \mathbb{R}_{>0}^2 : \left\| \frac{\eta_{CE}(\varepsilon, \sigma) - \eta_{experiment}}{\eta_{experiment}} \right\|_2 \leq \xi_{exp,\eta} \right\} \\
&\neq \left\{ (\varepsilon, \sigma) \in \mathbb{R}_{>0}^2 : \left\| \frac{D_{ij\ CE}(\varepsilon, \sigma) - D_{ij\ experiment}}{D_{1,2\ experiment}} \right\|_2 \leq \xi_{exp,D_{1,2}} \right\} \\
&\neq \left\{ (\varepsilon, \sigma) \in \mathbb{R}_{>0}^2 : \left\| \frac{\lambda_{CE}(\varepsilon, \sigma) - \lambda_{experiment}}{\lambda_{experiment}} \right\|_2 \leq \xi_{exp,\lambda} \right\} \quad (3.55)
\end{aligned}$$

If there however is an overlap between these subsets, fitting towards all three transport properties simultaneously, will likely result in LJ parameters that allow for an accurate modeling of all three transport properties based on the CE equations.

$$\begin{aligned}
M' &= M_{\eta} \cap M_{D_{1,2}} \cap M_{\lambda} \\
&= \left\{ (\varepsilon, \sigma) \in \mathbb{R}_{>0}^2 : \left\| \frac{\eta_{CE}(\varepsilon, \sigma) - \eta_{experiment}}{\eta_{experiment}} \right\|_2 \leq \xi_{exp,\eta}, \right. \\
&\quad \left. \left\| \frac{D_{ij\ CE}(\varepsilon, \sigma) - D_{ij\ experiment}}{D_{1,2\ experiment}} \right\|_2 \leq \xi_{exp,D_{1,2}}, \right. \\
&\quad \left. \left\| \frac{\lambda_{CE}(\varepsilon, \sigma) - \lambda_{experiment}}{\lambda_{experiment}} \right\|_2 \leq \xi_{exp,\lambda} \right\} \quad (3.56)
\end{aligned}$$

To visualize this, Fig. 3.4 depicts the relative deviation

$$\frac{|D_{NH_3-N_2,exp} - D_{NH_3-N_2,calc}|}{D_{NH_3-N_2,exp}} \quad (3.57)$$

between the calculated binary diffusion coefficient of ammonia in nitrogen based on the CE theory and the experimentally determined values from Zhavrin *et al.* (Zhavrin 2013) as an average over

the three temperatures 400, 500 and 600 K in dependence of the two LJ parameters. Only values of up to 3% relative deviation, calculated with equation 3.57, are included in Figure 3.4, representing a typical experimental uncertainty in the determination of binary diffusion coefficients. As anticipated, Figure 3.2 shows that there is a wide range of LJ parameters that lead to good agreement, meaning deviations of 3% or less, between CE theory and experiments.

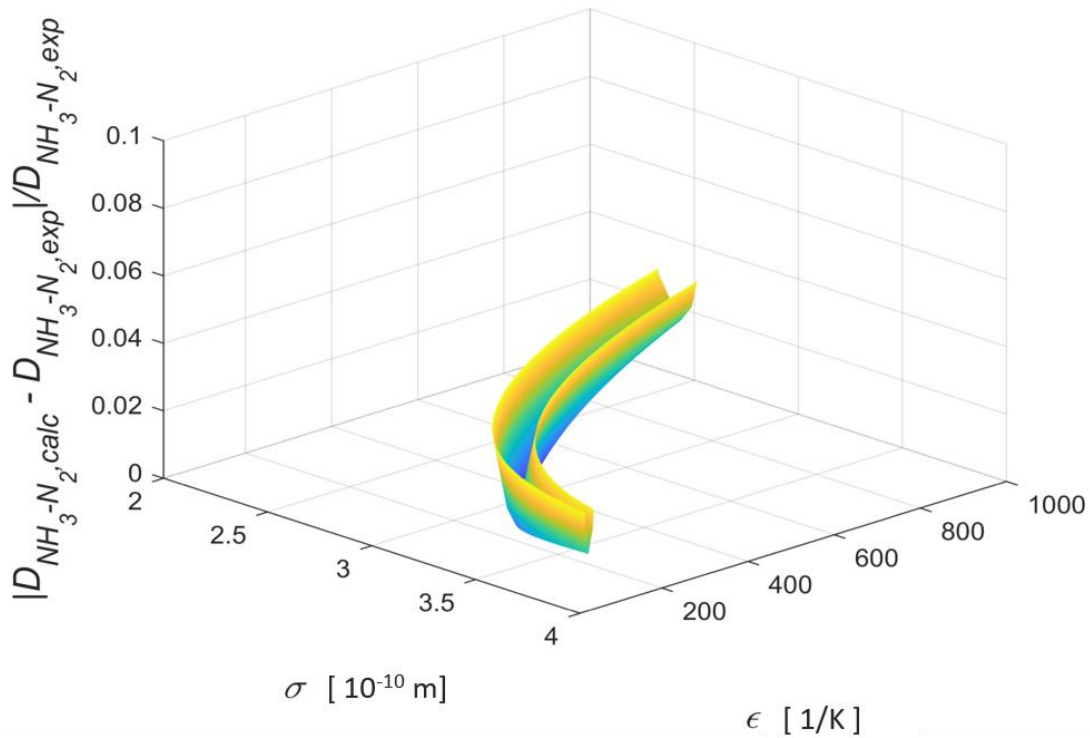


Fig. 3.4, Absolute values of the relative difference between experimental and calculated binary diffusion coefficients of NH_3 in N_2 in dependence of the two LJ parameters, only showing the subset of LJ parameters that lead to the deviation being less or equal to the assumed experimental uncertainty of 3%. Since the binary diffusion coefficient depends on the LJ parameters of both substances in the gas mixture, the parameters for nitrogen were fixed to the values obtained from the fitting procedure of this work. Adopted from (Bechtel 2020b).

Figure 3.5 shows these subsets $M_{D_{1,2}}$ combined with the subsets for the thermal conductivity of ammonia M_λ with a cutoff at 3% relative deviation and for the viscosity of ammonia M_μ with a cutoff at 2% relative deviation. The uncertainties of 2 and 3% are an exemplary representation of experimental uncertainties given in the scientific literature for the thermal conductivity and viscosity, which vary strongly between literature sources, experimental methods and the

temperature (Mian 1969, Zhavrin 2013, Nelson 1956, Afshar 1981). In earlier works the binary diffusion coefficients of gases were usually only accurate up to 5% for temperatures of up to 1000 K even in the most reliable studies, as Marrero and Mason (1972) showed in their comparison of different literature sources. Also, the thermal conductivities exhibit experimental uncertainties of up to 4.5% depending on the temperature and source (Afshar 1981). On the other hand, especially since the late 20th century, there are various scientific contributions that claim a significantly higher accuracy. Gotoh *et al.* (1974) for example state that their measurements of binary diffusion coefficients for various gas mixtures are accurate within 1%. Schley *et al.* (2004) estimate the experimental uncertainty for their viscosity measurements of methane and natural gas to be between 0.3 - 0.5%. Lastly, De Groot *et al.* (1974) believe that their measurements of thermal conductivities of gases have an accuracy of 0.2%. Besides these given examples there are many more with a comparably low experimental uncertainty. It should be noted that on top of the experimental uncertainty, the CE theory itself comes with uncertainties, too due to various approximations in its derivation, of which some are discussed in the course of this chapter, which would have to be considered as well in this discussion. However, for most of the experimental data, especially concerning many industrially relevant gases that have not been as extensively investigated as the noble gases or air components, the uncertainties of the CE theory are comparably small.

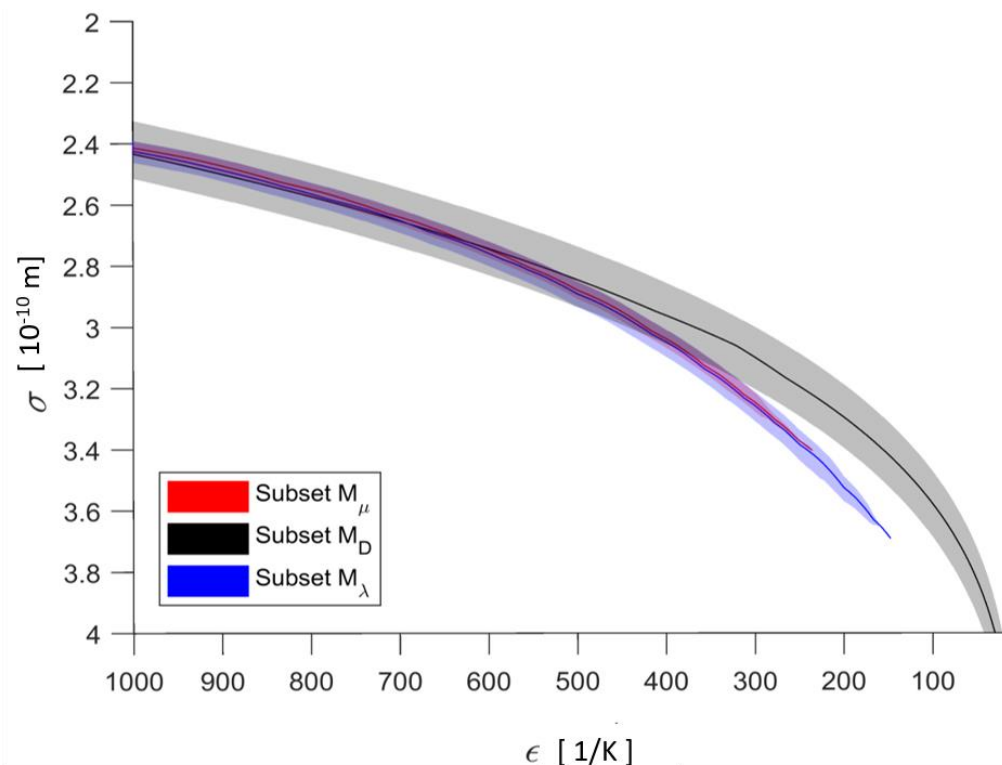


Fig. 3.5, Subsets that lead to a deviation between experimental and calculated transport properties of NH_3 below the experimental uncertainty. Here, the experimental uncertainty was set to 3% for the binary diffusion coefficient of $\text{NH}_3\text{-N}_2$ as well as the thermal conductivity, and 2% for the viscosity. The subset for the diffusion coefficient is shown in grey, the one for the thermal conductivity in blue and the subset for the viscosity is displayed in red. The corresponding solid lines assign a value of σ to every value of ϵ for which the deviation between the experimental and the calculated transport property is lowest. Hence, the optimal parameter set for a certain transport property is found on the respective solid line. Adopted from (Bechtel 2020b).

Figure 3.5 can hence be seen as a projection of Figure 3.4 combined with corresponding graphs for the thermal conductivity and viscosity. It becomes clear that there is a significant overlap between the subsets. However, if the LJ parameters were fitted to viscosity data alone, as it is oftentimes done in the literature, there is a considerable chance that the obtained parameters are not suited for describing the thermal conductivity or the binary diffusion coefficient. This is the case, if they are outside of the overlapping areas and hence only element of M_η , but not of M' (eq. 3.56). The chance of not obtaining suitable parameters for all transport properties increases, if the parameters are fitted to experimental thermal conductivity data, as it is sometimes done when no accurate viscosity data is available for a gas species (Kee 2003), due to the higher experimental uncertainty. This proves the hypothesis that the standard procedure in the scientific literature of fitting towards only one transport property can lead to deviations between experiments and CE

theory that exceed the experimental uncertainties, as already discussed above for some exemplary literature cases.

Furthermore, Fig. 3.5 shows that there is indeed a subset of parameters M' which predicts all three transport properties with an accuracy well within the experimental uncertainty. For this reason, a new procedure for determining LJ parameters by simultaneously fitting towards all three transport properties, instead of just one as done in the scientific literature, is proposed in the present work. This leads to LJ parameters that are an element the subset M' and therefore fulfill the criteria of being able to describe all three transport properties accurately.

3.4.3 Framework of the proposed methodology

In the following, the three main theoretical concepts necessary for carrying out such a fitting procedure are briefly explained. Subsequently, the three transport properties are calculated and compared to experimental literature data over a wide range of temperatures for seven exemplary gases that are of high industrial relevance, including the species involved in the HCl gas-phase oxidation, and the oxidation of NH_3 in the frame of the Ostwald process, as a proof of concept. This sample of gases intentionally contains polyatomic and non-polar as well as polar species to test the accuracy of the novel approach with a wide range of substances.

As equations 3.51 to 3.53 show, all three transport coefficients are a function of the collision integral, which itself strongly depends on the interatomic or intermolecular potential. Hence, a suitable potential has to be identified in a first step. For non-polar gases, the LJ potential is employed and for polar gases, the Stockmayer potential. In principal any other potential can be used as well, as long as it is spherically symmetric. These simple potentials have the advantage of reducing the complexity of the approach and making it easy to apply by scientists from different fields.

For the reduced collision integral based on the LJ potential, numerous approximate solutions exist in the scientific literature. Kim and Monroe (2014) proposed the following equation, which is stated to be accurate to the seventh decimal place and is also used in the present work.

$$\Omega^{(l,s)*} = A^{(l,s)} + \sum_{k=1}^6 \frac{B_k^{(l,s)}}{(T^*)^k} + C_k^{(l,s)} \cdot \ln(T^*)^k \quad (3.58)$$

The values for the parameters in Eq. (3.58) can be found in (Kim 2014). For polar molecules, here described with the Stockmayer potential, the collision integral becomes more complicated (McGee 1991, Itean 1961).

$$V_{(r,\theta_1,\theta_2,\varphi)} = 4 \cdot \varepsilon \left[\left(\frac{\sigma}{r} \right)^{12} - \left(\frac{\sigma}{r} \right)^6 - \delta \left(\frac{\sigma}{r} \right)^3 \right] \quad (3.59)$$

$$\delta = \frac{\mu^2}{4 \cdot \varepsilon \cdot \sigma^3} g_{(\theta_1,\theta_2,\varphi)} \quad (3.60)$$

As can be extracted from equation 3.59 and 3.60, the Stockmayer potential is a function of a third parameter δ , in addition to the two LJ parameters, which depends on the dipole moment μ of the molecule and the angular dependent parameter $g_{(\theta_1,\theta_2,\varphi)}$. More detailed information can be found in (McGee 1991, Itean 1961). For head to tail collisions, in which the partially positively charged part of one molecule is colliding with the partially negative part of the second molecule, $g_{(\theta_1,\theta_2,\varphi)} = 2$. This corresponds to a maximum value for δ , denoted as δ_{max} . Monchick and Mason (1961) tabulated approximate solutions for the collision integral as a function of the reduced temperature and δ_{max} , which are used in the present work. The dependence of the collision integral on δ_{max} and again the dependence of δ_{max} on the LJ parameters, makes the fitting process of the two LJ parameters towards experimentally measured transport properties more complex. This is due to the fact that δ_{max} is changing in every iteration step. Hence, the collision integral as a function of the reduced temperature and δ_{max} has to be interpolated from the tabulated values and implemented into the fitting procedure for the LJ parameters. Many publications dealing with polar gases in the scientific literature either neglect the influence of the polarity for this reason and employ a potential for nonpolar gases, like the LJ potential (Kestin 1979), or they fix δ_{max} , so that the collision integral is only a function of the reduced temperature and hence constant in each iteration of the fitting procedure for a given temperature (Brokaw 1969). In the latter case, one of the LJ parameters is then directly dependent on the other one, according to equation 3.60, and cannot be fitted in order to maintain physical coherence. Both approaches introduce errors into the fitting process that become more severe with an increasing

polarity of the investigated gases. For highly polar molecules like hydrogen chloride, ammonia and water, the dependence of the collision integral on both, the reduced temperature and δ_{max} is therefore taken into account in the present work by means of a linear spline interpolation of the tabulated data by Monchick and Mason (1961).

Secondly, while the viscosity and the thermal conductivity of pure gases can be directly calculated based on the LJ parameters and the collision integral, the binary diffusion coefficient involves parameters from two species i and j so that mixing rules have to be defined. In the present work, the following mixing rules are employed (Hirschfelder 1954):

$$\sigma_{ij} = \frac{\sigma_i + \sigma_j}{2} \quad (3.61)$$

$$\varepsilon_{ij} = \sqrt{\varepsilon_i \cdot \varepsilon_j} \quad (3.62)$$

For the interaction of two polar gases, $\delta_{ij,max}$ can be calculated according to equation 3.63.

$$\delta_{ij,max} = \frac{\mu_i \mu_j}{2 \varepsilon_{ij} \sigma_{ij}^3} = \frac{1}{2} \mu_{red,ij}^2 \quad (3.63)$$

For a mixture of a nonpolar with a polar gas, $\delta_{ij,max}$ is zero and the Stockmayer potential transitions into the LJ potential. To account for the polarity of one of the gas species, a correction factor ζ is introduced according to Hirschfelder *et al.* (1954) and Fan (2002):

$$\sigma_{ij} = \frac{\sigma_i + \sigma_j}{2} \zeta^{-\frac{1}{6}} \quad (3.64)$$

$$\varepsilon_{ij} = \sqrt{\varepsilon_i \cdot \varepsilon_j} \cdot \zeta^2 \quad (3.65)$$

$$\zeta = 1 + 0.25 \cdot \alpha_{red} \cdot \mu_{red,ij}^2 \cdot \sqrt{\frac{\varepsilon_{polar}}{\varepsilon_{non-polar}}} \quad (3.66)$$

where α_{red} is the reduced polarizability of the nonpolar species.

$$\alpha_{red} = \frac{\alpha}{\sigma_{non-polar}^3} \quad (3.67)$$

In the third step, it must be considered that the above introduced equations 3.51 to 3.53 for modeling the three transport coefficients are only valid for monoatomic and spherical species and

that all intermolecular collisions are assumed to be purely elastic so that no internal degrees of freedom are taken into account. The effect of this approximation on the diffusion coefficients and viscosities of polyatomic gases can be neglected in most cases (McGee 1991). Since in addition to the energy transport in the form of kinetic energy, also vibrational and rotational degrees of freedom can be excited in polyatomic species, it is however necessary, to consider these internal degrees of freedom when describing the heat conductivity of such gases. Hence, Eucken (1913) proposed a correction factor, weighing the translational degrees of freedom with the factor $f_{trans} = 2.5$, which follows directly from the relation between viscosity and thermal conductivity in the Chapman-Enskog theory (McGee 1991), known historically as the Eucken correction. The underlying assumption is that the transport of kinetic energy is unaffected by internal degrees of freedom, meaning that an exchange between internal and translational energy only occurs rarely. This assumption was supported by experimental investigations (Srivastava 1959). Eucken (1913) weighted the internal degrees of freedom with a factor $f_{int} = 1$ (Srivastava 1959, Barua 1959), leading to the following equation for the thermal conductivity of polyatomic gases

$$\lambda = \frac{\eta}{M} (f_{trans} c_{v,trans} + f_{int} c_{v,int}) \quad (3.68)$$

For a monoatomic gas, having no internal degrees of freedom, this is equivalent to the expression that can be obtained by dividing equation 3.52 and 3.53. Based on equation 3.68, the thermal conductivity of a polyatomic gas can then be calculated by multiplying the Chapman Enskog expression for monoatomic gases with the classical Eucken correction:

$$\lambda = \lambda_{monoatomic} \left(\frac{4}{15} \frac{c_v}{R} + \frac{3}{5} \right) \quad (3.69)$$

Hereby, c_v is the molar heat capacity of a gas at constant volume. However, according to (Chapman 1970, Schäfer 1943), the transfer of internal energy is based on a diffusion mechanism (Srivastava 1959). Hence, $f_{int} = \frac{\rho D}{\eta}$ should be employed in the Eucken correction instead of $f_{int} = 1$ (Srivastava 1959, Hirschfelder 1957). In this case f_{int} assumes values of about 1.3 for most force laws and shows only a slight temperature dependence (Hirschfelder 1957). However, Istomin *et al.* (2014) visualized graphically that f_{int} exhibits an almost linear temperature dependence at industrially relevant temperatures of up to 1500 K. More details can be found in

Srivastava and Srivastava (1959) and Hirschfelder (1957). Also, (Barua 1959, Srivastava 1959) showed that the experimentally determined values for f_{int} are clearly dependent on the species and the temperature, contrary to the value in Hirschfelder's (1957) approach. Mason and Monchick (1962b) state that only at high temperatures the theoretical value of 1.3 is approached and proposed a more complex approach in which both f_{int} and f_{trans} are variable.

In the present work, a linear, species specific temperature dependence of f_{int} is assumed as supported by the data of from Istomin *et al.* (2014) and the work of Srivastava and Srivastava (1959) and Barua (1959), while f_{trans} is set to a value of 2.5 as in the classical Eucken correction.

$$f_{int} = aT + b \quad (3.70)$$

Here, a and b are species specific parameters. Hence,

$$\lambda = \frac{\eta}{M} (2.5c_{v,trans} + (aT + b)c_{v,int}) \quad (3.71)$$

The new modified Eucken correction factor can then be formulated as

$$\frac{\lambda}{\lambda_{monoatomic}} = \left(\frac{4}{15} \frac{c_v}{R} (aT + b) + \frac{\frac{5}{2} - (aT + b)}{\frac{5}{2}} \right) \quad (3.72)$$

where $\lambda_{monoatomic}$ is calculated according to the CE theory (eq. 3.52). This simplified, semi-empirical approach serves the purpose of being able to accurately calculate all three transport coefficients while keeping the complexity of the approach low so that it is computationally inexpensive and easily applicable. Based on these theoretical concepts, the fitting procedure can be carried out with the LJ parameters and the two parameters a and b (eq. 3.70) as variables.

$$\begin{aligned}
& \min_{\varepsilon, \sigma, a, b} \left\{ \begin{aligned} f(\varepsilon, \sigma, a, b) = & \left\| \frac{\eta_{CE}(\varepsilon, \sigma, T) - \eta_{experiment}(T)}{\eta_{experiment}(T)} \right\|^2 \\ & + \left\| \frac{D_{ij CE}(\varepsilon, \sigma, T) - D_{ij experiment}(T)}{D_{1,2 experiment}(T)} \right\|^2 \\ & + \left\| \frac{\lambda_{CE}(\varepsilon, \sigma, a, b, T) - \lambda_{experiment}(T)}{\lambda_{experiment}(T)} \right\|^2 \end{aligned} \right\} \\
& s. t. \quad aT + b \geq 0 \\
& \quad a \geq 0
\end{aligned} \tag{3.73}$$

The two constraints in equation 3.73 are based on the fact, that the internal degrees of freedom cannot be weighted negatively in the Eucken correction to ensure physical consistency. Furthermore, Istomin *et al.* (2014) showed that f_{int} increases with temperature in the here investigated interval, which is why a is enforced to be positive. If the amount of experimental data points employed in the fitting process differ for each transport property, the respective relative differences are weighted in a way that all three transport properties are considered equally in the fitting process.

The optimization problem was solved in MATLAB for every gas species by using the least square method. In order to reduce the probability of finding local minima instead of the global minimum, the fitting process for each gas was carried out 200 times with different starting points. The obtained parameters indeed changed slightly for the first 20 starting points but then remained constant, indicating that using 200 starting points is sufficient.

The accuracy of the fitting process strongly depends on the quality and availability of experimental data on transport coefficients. For this reason, the experimental data available in the scientific literature was critically reviewed and the employed sources are listed in Table 3.6 for each of the investigated gases, namely oxygen, nitrogen, chlorine, nitrous oxide, ammonia, hydrogen chloride and water vapor. For fitting the thermal conductivity, polynomials from Yaws (2009) based on experimental data were employed for all gases except for ammonia for which the fit from Afshar *et al.* (1981), also based on experimental data, was used, since it is based on data in a wide temperature interval from 358 to 925 K. For some species, additional experimental data is available in the scientific literature, e.g. for nitrogen from Le Neindre (1972), for oxygen from Hirschfelder *et al.* (1954) and for water from Brain (1967) which all showed good agreement with the

polynomials from Yaws (2009). Binary diffusion coefficients for the investigated gases in the scientific literature are mostly available in combination with nitrogen. For this reason, the fitting procedure was initiated with nitrogen and with the so generated LJ parameters and the two parameters a and b from the modified Eucken correction, the equivalent parameters for the remaining gases were determined. The parameters for nitrogen in turn were determined using helium as a partner species to fit the theoretical binary diffusion coefficients of a He-N₂ mixture together with the thermal conductivity and viscosity of nitrogen towards according experimental data. The LJ parameters for Helium required for modeling the binary diffusion coefficient of the He-N₂ mixture were taken from Hirschfelder *et al.* (1954) and it was ascertained that these values from the literature are also in good agreement with experimental data for the viscosity and thermal conductivity of Helium as well. Helium is one of the few species for which LJ parameters from the scientific literature are well able to describe all three transport properties within the experimental uncertainty. Since helium is a monoatomic gas, no Eucken correction is needed according to the CE theory. Please note that De Groot *et al.* (1974) experimentally investigated the thermal conductivity of noble gases and came to the conclusion that a minor Eucken correction of 1.5% would be needed even for these monatomic species. However, the experimental uncertainty in determining the transport coefficients of most gas species, especially in the early literature, exceeds the extent of this correction markedly and hence it can be neglected.

The advantage of this approach is that the utilization of a very well investigated simple gas like helium as a starting point for the fitting procedure leads to physically meaningful and not only mathematically optimal values for the parameters of nitrogen and from there on all other investigated gases.

3.4.4 Evaluation of the accuracy of the novel parameter set

This chapter serves to evaluate whether the proposed fitting procedure indeed leads to a better agreement between the CE equations employing the so obtained parameters (please see table 3.5) and experimental data compared to the classical approach of fitting towards only one transport property.

Table 3.5, Values for the LJ parameters σ and ϵ^* , as well as for a and b and, in the case of polar molecules, for the parameter δ , obtained from the here proposed fitting procedure.

species	$\sigma / \text{\AA}$	ϵ^* / K	$a / 1/\text{K}$	b	δ
N ₂	3.5961	104.35	$2.22 \cdot 10^{-14}$	1.1200	0
N ₂ O	3.2396	444.81	$2.22 \cdot 10^{-14}$	1.1040	0
O ₂	3.4770	96.92	0.000178	1.0473	0
Cl ₂	3.2919	829.51	$7.14 \cdot 10^{-8}$	1.3136	0
H ₂ O	3.2842	152.21	0.00103	$8.12 \cdot 10^{-5}$	2.299
NH ₃	2.9356	467.18	0.000969	0.3219	0.6622
HCl	3.0501	480.08	0.000102	0.7949	0.3101

To evaluate the quality of these parameters, nitrous oxide is investigated as an example species in a first step. LJ parameters from Hirschfelder *et al.* (1954) as well as the parameters presented in table 3.5 are used to calculate the three transport properties based on the CE theory. The deviations between the so calculated transport properties and experimental data are depicted in Figure 3.6 to 3.8.

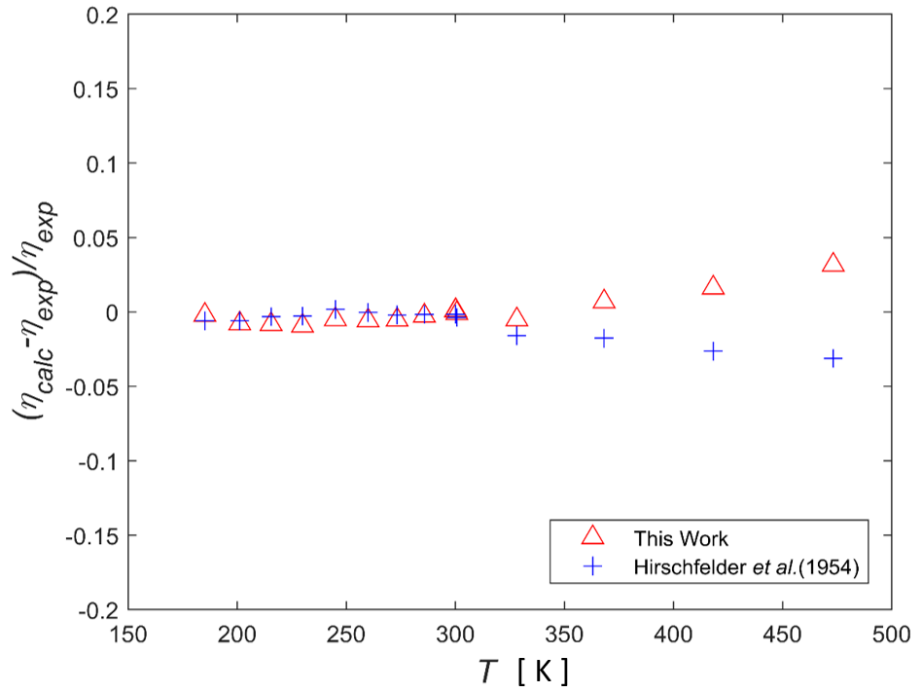


Fig. 3.6, Comparison of the experimentally determined viscosity of nitrous oxide (Kestin 1979, Johnston 1940) with calculated values using the CE equations based on LJ parameters from Hirschfelder *et al.* (1954) (blue) and the present work (red). Adopted from (Bechtel 2020b).

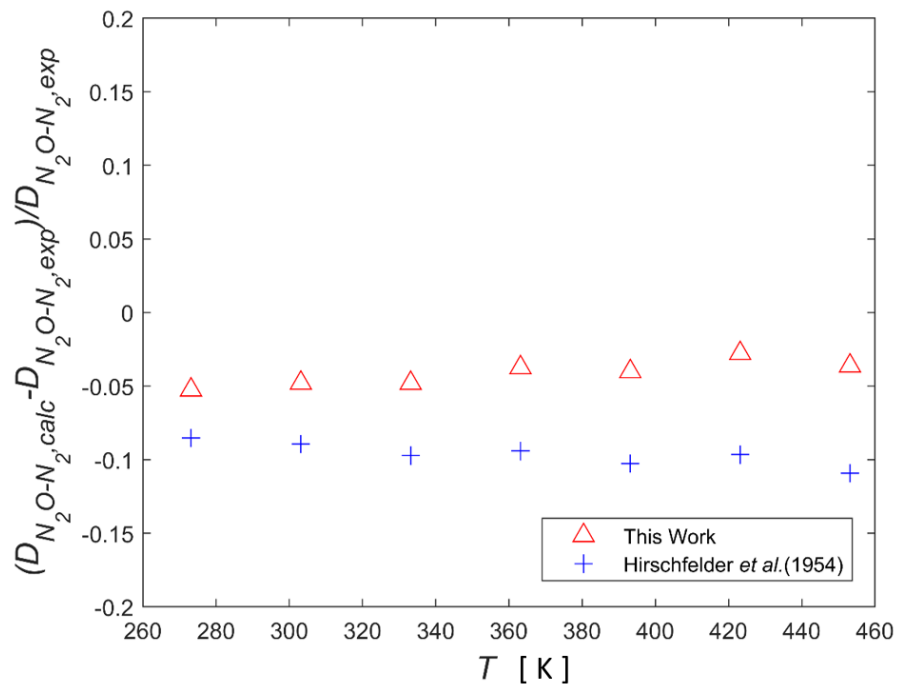


Fig. 3.7, Comparison of the experimentally determined binary diffusion coefficient of nitrous oxide in nitrogen (Matsunaga 2002) with calculated values using the CE equations based on LJ parameters from Hirschfelder *et al.* (1954) (blue) and the present work (red). Adopted from (Bechtel 2020b).

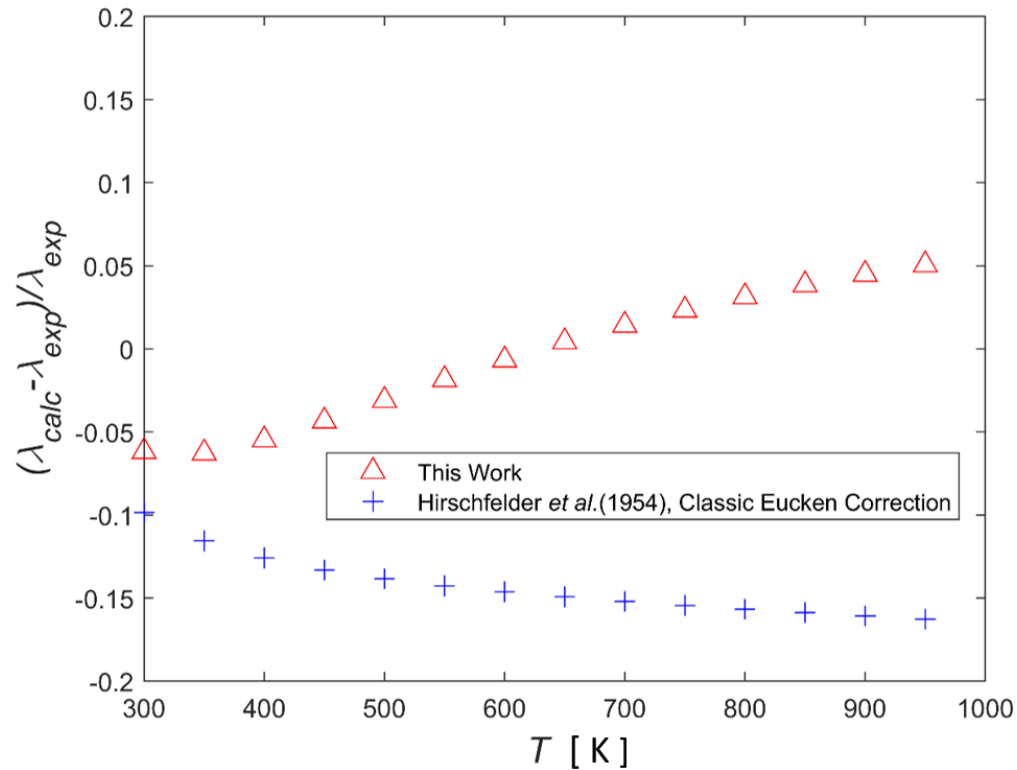


Fig. 3.8, Comparison of the experimentally determined thermal conductivity of nitrous oxide (Yaws 2009) with the calculated values based on the CE equations employing LJ parameters from Hirschfelder *et al.* (1954) in combination with the classical Eucken correction (blue), as well as the parameters obtained in the present work and the modified Eucken correction (red). Adopted from (Bechtel 2020b).

For the parameters from Hirschfelder *et al.* (1954), good agreement between the calculated and experimental values was obtained only in the case of the viscosity, towards which these LJ parameters were originally fitted. However, for the binary diffusion coefficient and the thermal conductivity, the deviation between calculated and experimental values is markedly greater than the experimental uncertainty. Furthermore, the CE equations employing the parameters of Hirschfelder *et al.* (1954) seem to systematically underestimate the experimental data by ca. 10% in the case of the binary diffusion coefficients and by 10 - 16% in the case of the thermal conductivities. The proposed fitting procedure however leads to significantly better agreement with experimental data for the thermal conductivity and diffusion coefficient while showing comparably good results for the viscosity, even though the parameters were not fitted solely to this transport coefficient.

Please note that the classical Eucken correction was employed for the calculation of the thermal conductivity based on the parameters of Hirschfelder *et al.* (1954), while the temperature dependent modification of the Eucken correction proposed in this work was employed in the calculation based on the parameters obtained from the novel fitting procedure. Hence, the significant deviation between the calculated data based on the parameters from Hirschfelder *et al.* (1954) and the experimental thermal conductivity data is to a certain extent also due to the insufficiency of the classical Eucken correction for predicting the thermal conductivity of polyatomic gases, as discussed in more detail in the course of this chapter. This shows that the here proposed temperature dependent modification indeed appears to be a more precise alternative.

Employing the CE equations and the fitting parameters of the present work, the mean and maximum deviation between calculated and experimentally determined viscosities, thermal conductivities and binary diffusion coefficients for nitrous oxide and all other gas species are listed in Table 3.6.

Table 3.6, Values for the mean and maximum relative deviation between the calculated and experimentally determined transport properties for all seven investigated species. The table additionally includes the temperature of the data point which showed the highest deviation between theoretical and experimental values as well as the literature sources used for the fitting procedure.

Species	Mean relative deviation, thermal conductivity / %	Maximum relative deviation, thermal conductivity / % and corresponding temperature / K
N ₂	1.05 (Yaws 2009)	2.01 (950 K)
N ₂ O	3.47 (Yaws 2009)	6.27 (350 K)
O ₂	0.71 (Yaws 2009)	2.31 (300 K)
Cl ₂	1.24 (Yaws 2009)	2.47 (300 K)
H ₂ O	1.38 (Yaws 2009)	4.01 (400 K)
NH ₃	0.131 (Afshar 1981)	0.35 (400 K)
HCl	0.84 (Yaws 2009)	2.04 (300 K)

Species	Mean relative deviation, viscosity / %	Maximum relative deviation, viscosity / % at and corresponding temperature / K
N ₂	0.15 (Perry 1997)	0.44 (500 K)
N ₂ O	1.22 (Kestin 1979)	3.16 (473.15 K)
O ₂	1.21 (Perry 1997)	1.83 (250 K)
Cl ₂	1.15 (Perry 1997, Reid 1987)	3.81 (600 K)
H ₂ O	3.14 (Kestin 1960)	5.35 (411.15 K)
NH ₃	1.07 (Perry 1997)	1.66 (300 K)
HCl	0.51 (Brokaw 1969)	0.97 (523 K)

Species	Mean relative deviation, diffusion coefficient / %	Maximum relative deviation, diffusion coefficient / % and corresponding temperature / K
N ₂	In He: 1.44 (Ellis 1969)	2.95 (415 K)
N ₂ O	In N ₂ : 5.46 (Matsunaga 1994)	6.56 (273.15 K)
O ₂	In N ₂ O: 4.49 (Matsunaga 1994)	6.42 (273.15 K)
Cl ₂	In Air: 2.02 (Andrew 1955)	2.02 (293 K)
H ₂ O	In N ₂ : 2.99 (Nelson 1956)	3.90 (312.94 K)
NH ₃	In N ₂ : 2.35 (Zhavrin 2013)	5.64(298 K)
HCl	In N ₂ : 1.50 (Mian 1969)	2.26 (423.1 K)

The mean deviation for all gases and all of the three transport properties is never greater than 5.5% and if N₂O is disregarded, the mean deviation is even below 3.1%. Finally, the maximum deviations for all gases and all transport properties is always below 6.6%, the highest value again being the deviation in the binary diffusion coefficient of N₂O in N₂. It seems that the reduced accuracy of the fit in the case of N₂O is most likely due to an increased uncertainty in the employed experimental data by Matsunaga *et al.* (1994) and not the fitting procedure itself. Since industrially relevant gases were purposefully chosen in the present work, a higher experimental uncertainty compared to simpler species, like the noble gases, must hence be accepted.

It can be concluded that the presented fitting procedure indeed leads to highly accurate LJ parameters and a significantly better agreement between the CE theory and experimental results than the fitting procedure of the previous scientific literature not only for the N₂O example elaborated in the discussion of Figure 3.6 to 3.8, but also for all other investigated gases. This is visualized in Figure 3.9 to 3.11 displaying the deviations between calculated and experimental data for HCl, N₂ and O₂.

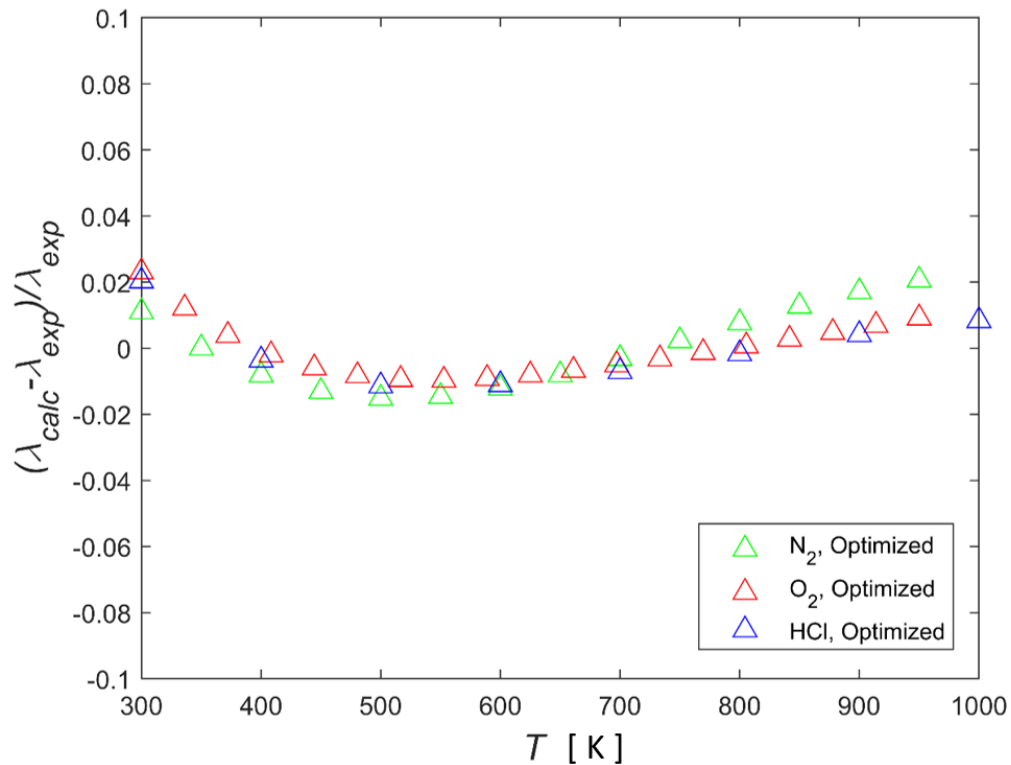


Fig. 3.9, Comparison of experimentally determined thermal conductivities of HCl, N₂ and O₂ to values calculated based on the parameter set listed in Table 3.5. Adopted from (Bechtel 2020b).

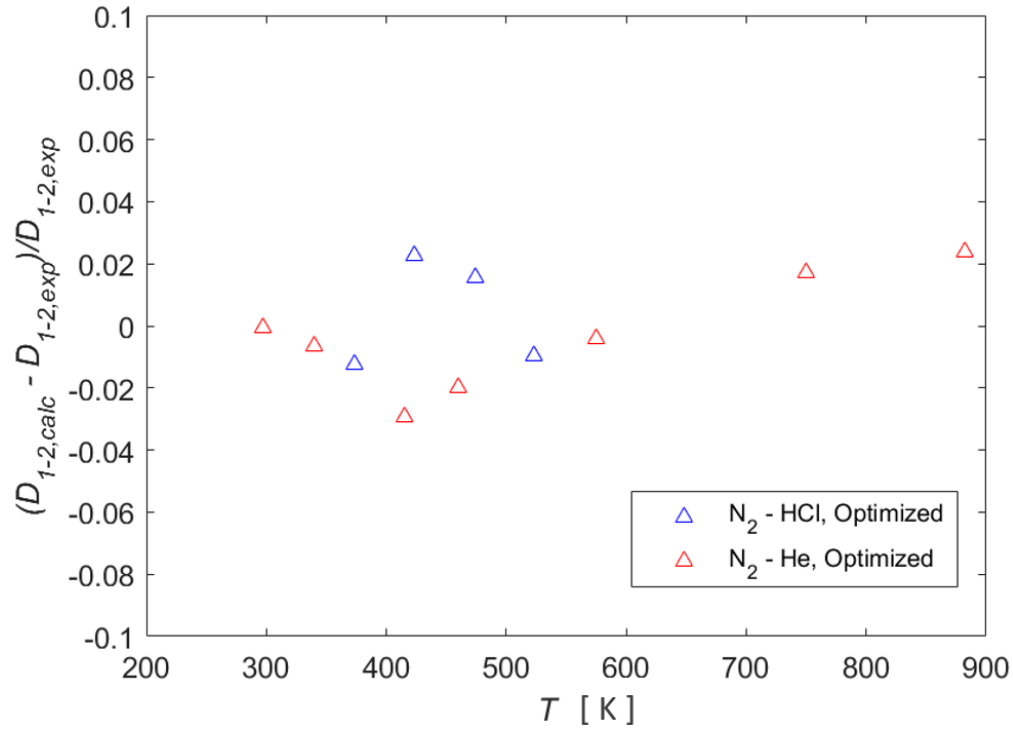


Fig. 3.10, Comparison of experimentally determined binary diffusion coefficients of N_2 -HCl and N_2 -He to values calculated based on the parameter set listed in Table 3.5. Adopted from (Bechtel 2020b).

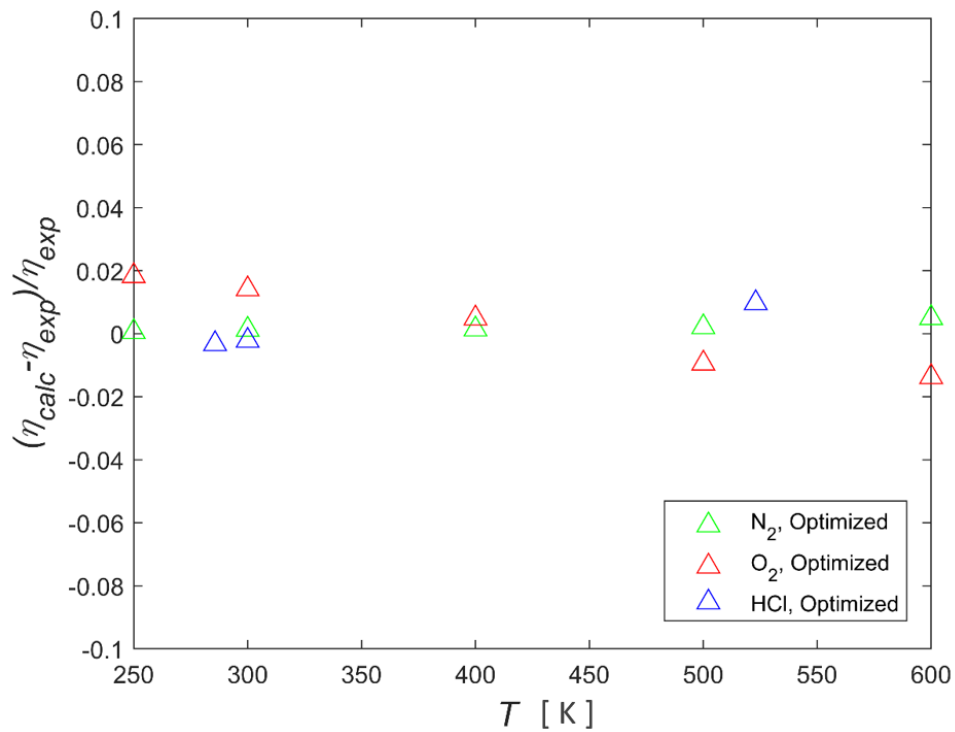


Fig. 3.11, Comparison of experimentally determined viscosities of HCl, N_2 and O_2 to values calculated based on the parameter set listed in Table 3.5. Adopted from (Bechtel 2020b).

Lastly, a more detailed focus is put on the modification of the Eucken correction proposed in the present work. Figure 3.12 displays the deviation between experimentally determined thermal conductivities of ammonia and values calculated based on the fitting procedure presented in this work using the classical Eucken correction, the correction proposed by Hirschfelder (1957) and lastly the new modification introduced above. Figure 3.12 clearly shows that the classical Eucken correction and the modification from Hirschfelder (1957), even though the LJ parameters were fitted towards experimental values for all three transport properties simultaneously, are not able to reproduce the experimental data well. As explained in chapter 3.4.3, Hirschfelder (1957) proposed a weighting of the internal degrees of freedom with the factor $f_{int} = \frac{\rho D}{\eta}$, which assumes a value of ca. 1.3 for most species and force laws and displays only a negligible temperature dependence (Istomin 2014). Hence, it was assumed to be constant in the small temperature range considered here. The fact that the temperature dependence of the experimentally determined data is not well described neither by the classical Eucken correction nor by Hirschfelder's variant, indicates that the temperature independent treatment of f_{int} is not justified. On the other hand, the modified Eucken correction presented in this work, leads to an excellent agreement between experimental and calculated results in the whole temperature range. As can be extracted from Table 3.6, this holds true for all other investigated gas species as well.

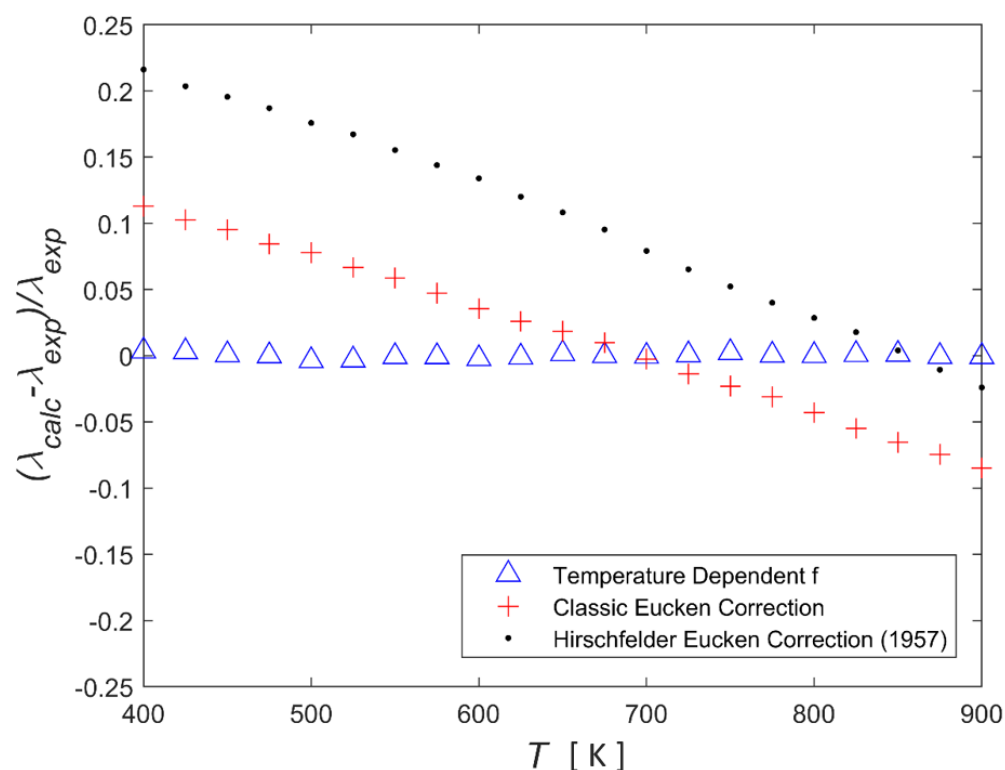


Fig. 3.12, Comparison of the experimentally determined thermal conductivity of ammonia to values obtained by employing the novel fitting procedure in combination with the classical Eucken correction (red), the modified version of Hirschfelder (1957) (black) and the modified temperature dependent Eucken correction presented in this work (blue). Adopted from (Bechtel 2020b).

Lastly, the insights on the here proposed fitting procedure are related to the method of developing a potential energy surface, as briefly introduced in chapter 3.4.1. There are various examples where the agreement between the theoretically predicted transport properties employing this method and experimental data is good (Crusius 2015, Hellman 2014). However, there are also numerous publications that show significant deviations. Hellman (2018) for example determined the thermal conductivity and viscosity of ethane. When comparing the results of his theoretical approach with experimental data of the thermal conductivity, deviations of up to 6% can be observed. In a similar article, Crusius *et al.* (2018) determined the transport properties for a CO₂-N₂ mixture and showed maximum deviations of up to 8% from experimental data for the binary diffusion coefficient and also the thermal conductivity. For nitrous oxide, the authors were able to predict the viscosity within the experimental uncertainty, the second virial coefficient however, was predicted poorly (Crusius 2015). It has to be mentioned however that the experimental data scattered markedly, just as it is the case for some of the data of the gas species investigated in the present work. It can hence

be concluded that the agreement between experimental data and both theoretical approaches, the here presented one and the method of developing a potential energy surface, is comparably good, except in a few cases where the experimental uncertainty is very high. As mentioned before, the approach presented in this work has a natural limit in its accuracy inherent to the CE model. However, as the low mean deviations listed in Table 3.6 show, the precision of this approach is not only significantly higher compared to the classical fitting approaches in the literature but is at the current state also mostly limited by the experimental uncertainty in measuring these transport properties and not the CE equations itself. For most engineering applications, the presented approach therefore offers an accurate while still simple and computationally inexpensive way of calculating the transport properties over a wide range of temperatures.

3.4.5 Summary of the investigations on the modeling of transport coefficients

The investigations of this chapter proved that the traditional approach of fitting LJ parameters to experimental data of only one transport property does not necessarily lead to a parameter set that is able to describe all three transport properties within the experimental uncertainty.

This is due to the fact that the subsets of LJ parameters, with which the Chapman Enskog equations can predict transport coefficients with sufficient accuracy, are not identical for each transport property. However, it was demonstrated that a subset of parameters M' exists which predicts all three transport properties with an accuracy well within the uncertainty of the underlying experimental data and which can be found by the fitting towards all three transport properties simultaneously. The fitting procedure furthermore accounts for the dependence of the collision integral on the parameter δ_{max} in the case of polar species as well as for a modified temperature dependent Eucken correction for determining thermal conductivities.

The so obtained Lennard-Jones parameters and modified Eucken correction factors lead to an excellent agreement between calculated and experimental values for the three transport coefficients of the 7 exemplary gas species investigated in this chapter, clearly outperforming the classical fitting approach employed in the previous scientific literature. More specifically, the

temperature dependent treatment of the Eucken correction exhibits significant advantages over the classical Eucken correction as well as the more recent approach by Hirschfelder *et al.* (1957).

The presented method can be extended to any gas for which experimental data are available. In future investigations the quality of these parameters could be even further refined by employing more precise experimental data and more sophisticated potential functions. Furthermore, it has the advantage of being computationally very inexpensive and easily applicable. It is therefore not to be seen as a substitution of the more complex approach of developing a potential energy surface, but as a simple and yet still precise alternative that can be easily employed in various engineering problems like modeling the gas-phase electrolysis of HCl.

4 Experimental setup for investigating the gas-phase electrolysis of HCl

In the following, the setup for the experimental investigation of the HCl gas-phase electrolysis, which was designed and built in the frame of this thesis, is explained. The experiments consist of half-cell investigations of the HClOR, ORR and the crossover of HCl/Cl₂ as well as full-cell investigations of the HCl gas phase oxidation employing an ODC in two different setups.

4.1 Half-cell setup

All half-cell measurements were carried out with the experimental setup depicted in Figure 4.1. Additionally, photographs of the setup are shown in the appendix (A6).

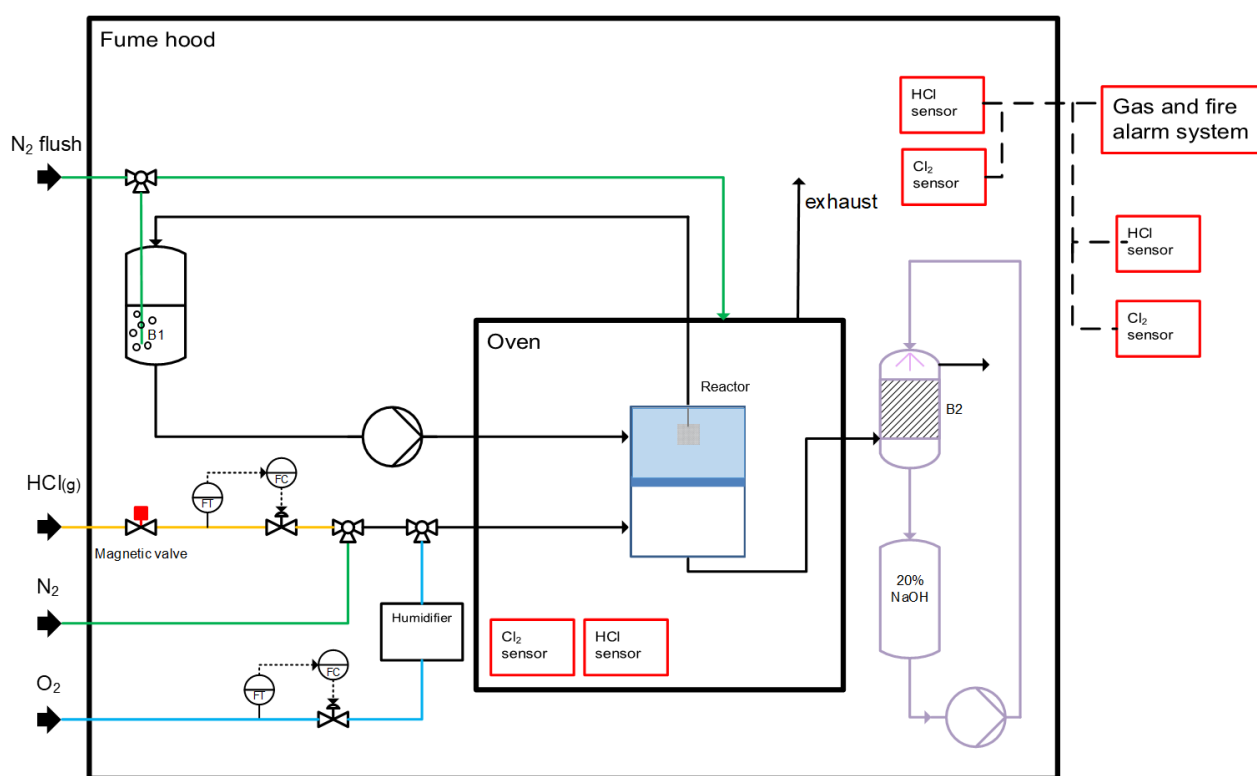


Fig. 4.1, Experimental setup for the half-cell investigations of the HClOR and ORR and the crossover of HCl and Cl₂. The working electrode compartment of the reactor is depicted in white and the counter electrode compartment, through which the electrolyte is cycled, in blue.

The center of the experimental setup is the electrochemical reactor. Its working electrode (WE) compartment can be supplied with either HCl, O₂ or N₂, depending on the nature of the experiment, and its CE compartment with a liquid electrolyte, either hydrochloric or sulfuric acid (both Rotipuran® supra quality by Roth), being stored in the vessel B1. The gases are supplied via pressurized gas bottles from Linde and are of grade 5 (99.999% purity) in the case of O₂ and N₂ and grade 4.5 (99.995% purity) in the case of HCl. The flow of HCl and O₂ is controlled via EL-FLOW (Bronkhorst) mass flow controllers (MFC). The oxygen stream can be humidified in the range of 0 - 100% relative humidity (RH) by means of a gas bubbler coupled with a thermostat. While the availability of an additional thermostat and the oven surrounding the reactor theoretically allow for measurements at up to 353 K if desired, all experiments were carried out at room temperature (RT) in the present work. This is due to the fact that gas leakages in the reactor were observed during operation at elevated temperatures, to which the employed cyclone flow-cell is more prone to compared to classical cells employing a flow-field.

Due to the high toxicity of HCl and Cl₂, the following safety measures were undertaken. In experiments where HCl or Cl₂ is present, the gaseous reactor outlet stream is fed into a packed column, which serves the purpose of absorbing and neutralizing the acidic gas species in counterflow with a 20 wt% NaOH solution (99% purity by Roth). Moreover, if Cl₂ concentrations of more than 0.5 ppm and HCl concentrations of more than 2 ppm are measured by gas sensors in and in front of the fume hood, a local alarm is triggered, which is extended to a building wide alarm if concentrations reach 1 ppm and 4 ppm respectively. On top of these permanently installed alarm systems, two hand sensors, which are not coupled to the central alarm system but serve for an early detection and localization of gas leaks, are placed in the oven in direct proximity to the reactor.

The electrochemical reactor employed in these experiments is a cyclone flow cell, as depicted in Figure 4.2. The working principle and distinct features of this reactor are described in detail in (Sundmacher 1999, Kubanek 2016, Martínez 2015) and are hence only briefly summarized here. A main feature is a homogenous concentration boundary layer over wide areas of the membrane electrode assembly (MEA) (Kubanek 2016). This allows for a more direct evaluation of mass transfer and kinetic effects, since, in comparison to classical flow-field based cells, 2D and 3D effects are minimized. Due to the fact that the numerical reactor model developed in the present

work is a 1D model, this homogeneity also enhances the comparability of simulation and experimental results.

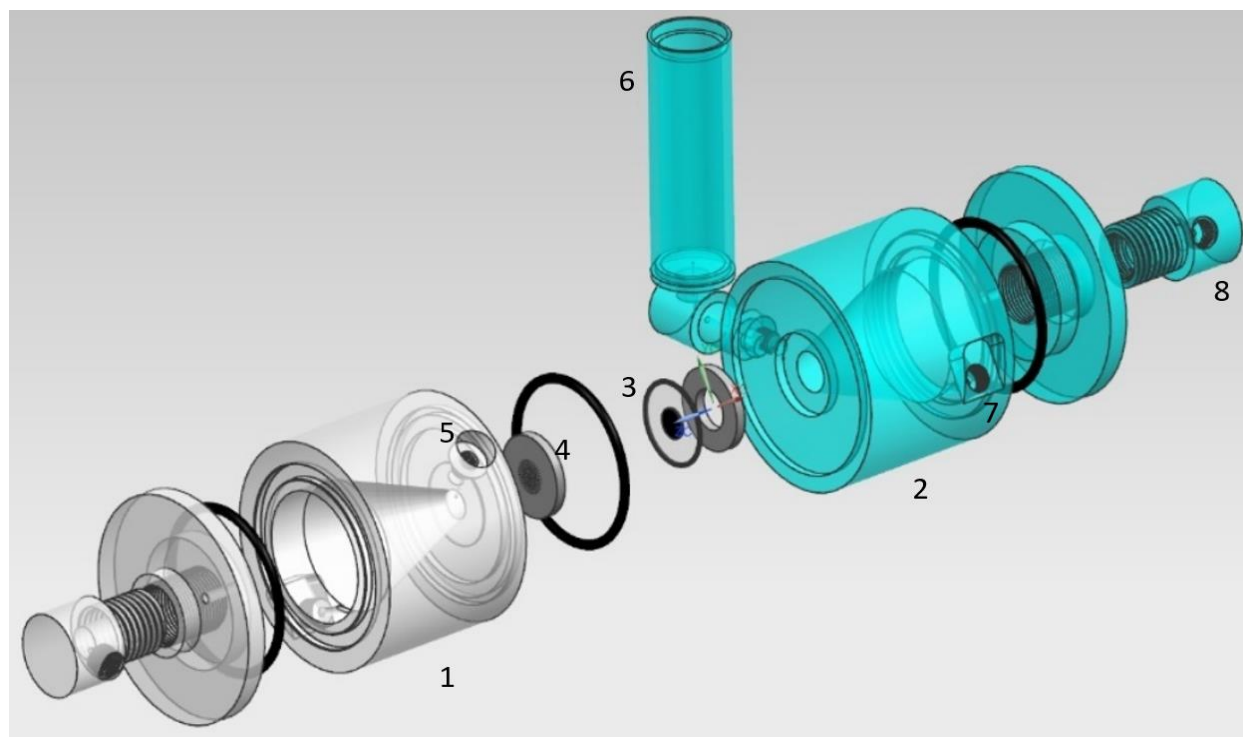


Fig. 4.2, Exploded view of the cyclone flow half-cell consisting of the working electrode compartment (1), the counter electrode compartment (2), the membrane electrode assembly (3), a titanium plate (4) connected to a titanium pin screwed into the orifice (5), which both together work as the current collector, and the reference electrode compartment (6). The reactants and the electrolyte enter the reactor at the inlets (7) and leave through the outlets (8) that are identical on both sides.

The reactor is similar to the cyclone cell employed by Martínez, however the working electrode compartment was made of glass fiber reinforced PTFE (20% glass fiber, PTFE Nüchteritz GmbH), due to its chemical resistance against HCl and Cl₂, while polycarbonate (Makrolon®, Bayer), which was used by Martínez (2015) for the whole cell, was only chosen for the counter electrode compartment due to its transparency and impact resistance. Both compartments are held together by a titanium frame and six titanium screws fixed with a torque of 17 Nm. Photographs of the reactor are shown in Figure A.11 in the appendix. The CE is a platinum net immersed into the electrolyte flowing through the CE compartment, since the MEA employed in all half-cell measurements disposes of a catalyst layer on only one side of the membrane. More details on the different MEAs employed in all experiments are given in chapter 4.3. Lastly, the reference

electrode compartment shown in Figure 4.2 contains a HydroFlex H₂-Reference Electrode by Gaskatel.

4.2 Full-cell setup

In the full-cell setup displayed in Figure 4.3, the gas-phase electrolysis employing an ODC is investigated.

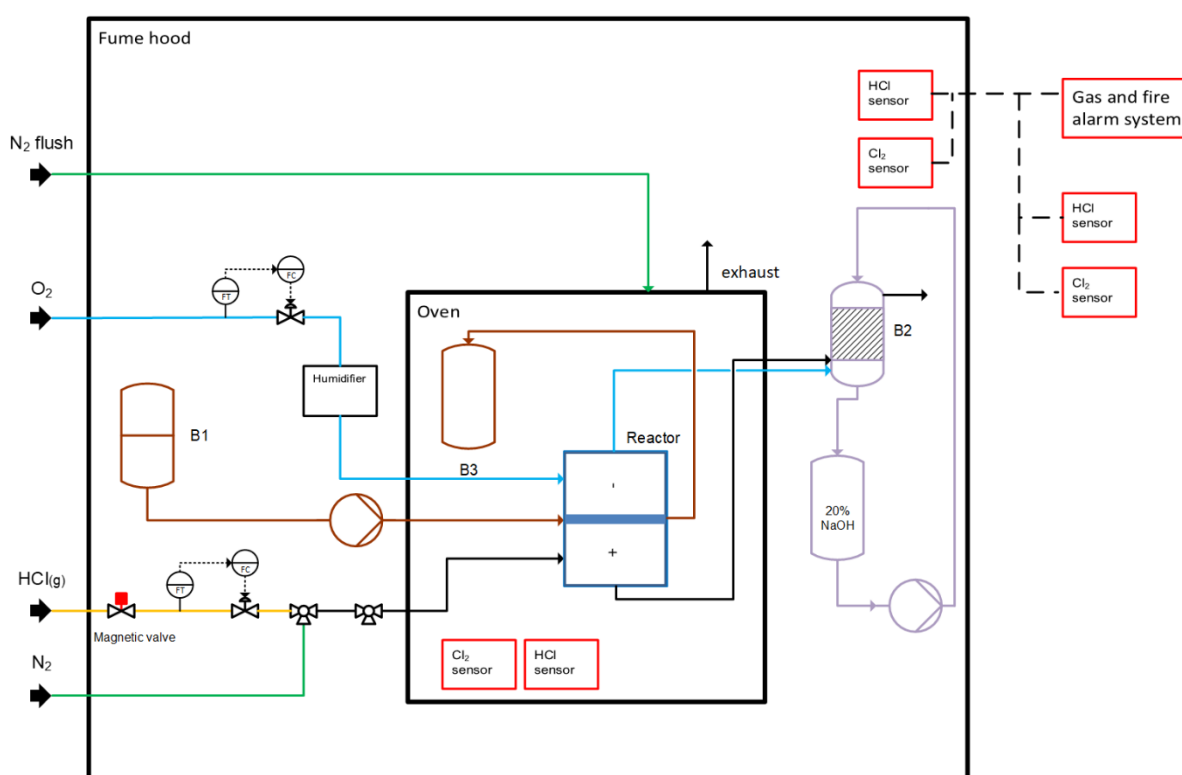


Fig. 4.3, Experimental setup for the full-cell investigations.

The setup is similar to the above discussed half-cell setup, with the main difference that now gaseous HCl is fed into the anode compartment and O₂ into the cathode compartment in all experiments. Furthermore, the temperature in the oven as well as in the oxygen outlet stream is now measured with Pt 100 thermal sensors and a PCE-T390 thermometer, since, contrary to the half-cell setup, there is no electrolyte flowing through the CE chamber, so that the convective heat transfer is reduced, leading to a possible increase in the reactor temperature during operation.

Lastly, the full-cell setup allows for a solution of 20 wt% NaOH (Rotipuran® by Roth) to be directed into the electrochemical cell (please see brown colored parts in Figure 4.3). This however is only needed for one of two investigated gas-phase reactors, as explained in more detailed in the following.

The first reactor, depicted in Figure 4.4, is a cyclone cell similar to the one shown in Figure 4.2. The major differences are that the full-cell disposes of two titanium supports serving as current collectors and does neither comprise a reference electrode nor a platinum net as CE, since now the MEA consists of a catalyst layer on each side of the membrane. Photographs of the reactor are shown in Figure A.12 in the appendix.

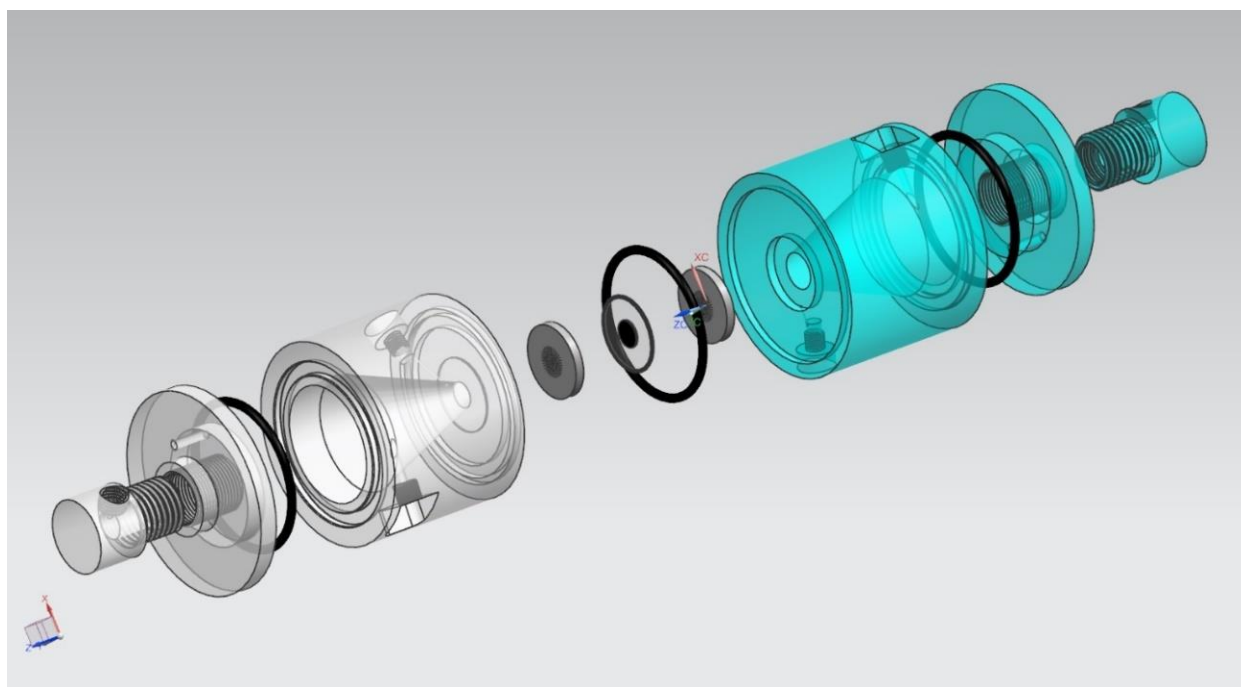


Figure 4.4, Exploded view of the cyclone flow full-cell. Please see Figure 4.2 for the labeling of the parts.

The second reactor, from now on referred to as the alkaline electrolyzer, is a novel concept inspired by an alkaline fuel cell and is depicted in Figure 4.5. A 20 wt% NaOH solution is directed through the middle section of the reactor between the anode and cathode gas diffusion electrodes at a flowrate of 2.5 ml/min with the help of a Microlab 500 syringe pump by Hamilton. Photographs of the reactor are displayed in Figure A.13 in the appendix.

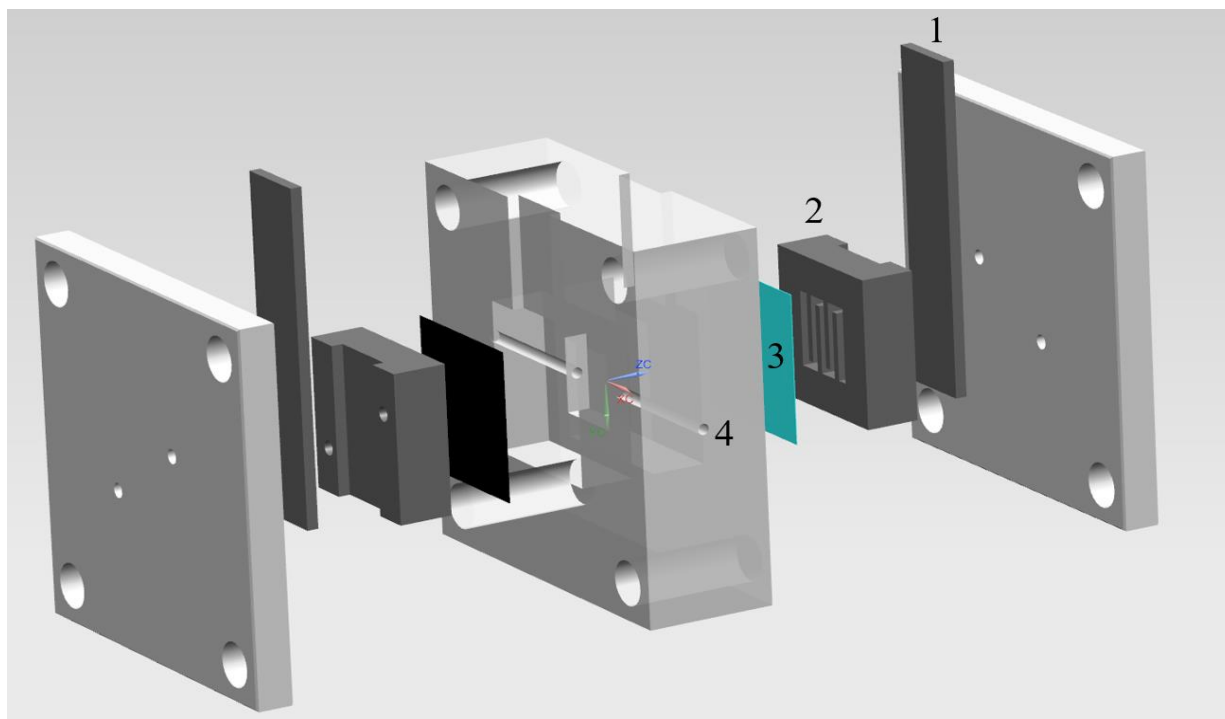


Figure 4.5, Exploded view of the alkaline electrolyzer including the current collector (1) and the flow field plate (2) both made of titanium as well as the GDE (3). The NaOH solution is entering/leaving the reactor through channels on both sides of the middle piece (4).

4.3 Catalyst, membrane and gas diffusion media

In experiments with the alkaline electrolyzer, a gas diffusion electrode (Oxag by Gaskatel) containing 80 mg/cm^2 silver and 4.8 mg/cm^2 PTFE was employed on the cathode side and a Pt/Ru based gas diffusion electrode (Quintech) with a catalyst loading of 1.5 mg/cm^2 with 20 wt% Pt/Vulkan XC-72 and 10 wt% Ru/Vulkan XC-72 on graphite paper on the anode side.

In all experiments concerning the cyclone full- and half-cell reactor, a membrane electrode assembly was used. The MEAs employed in all half-cell measurements were supplied by HIAT and are based on Nafion 115 membranes (Dupont) with a catalyst suspension of Pt/C (60 wt% Pt, by Alfa Aesar) in Nafion sprayed on one side of the membrane. The final platinum loading was 1 mg/cm^2 and the Nafion loading 0.5 mg/cm^2 . To facilitate reactant distribution and product removal from the WE, a GDL (by Quintech) with a thickness of $400 \mu\text{m}$ was employed.

The GDL consisted of carbon cloth coated first with a 20 wt% PTFE suspension and subsequently with a mixture of Ketjenblack (Akzo Nobel) and PTFE, generating a microporous layer (MPL), resulting in a total loading of 4.5 mg/cm^2 with 20 wt% PTFE. To ensure electrical contact, the MEA by HIAT and the GDL were thermally bonded together at a pressure of 50 bar and 398 K for 150 s employing a laboratory press (Polystat 200 T by Servitec) as visualized in Figure 4.6.

In the full-cell measurements employing a cyclone flow cell (please see Figure 4.4), two different catalysts were investigated. The first one consisted of the same MEAs as used in the half-cell experiment but additionally, a gas diffusion electrode (GDE) based on rhodiumsulfide (Rh_xS_y) serving as the cathode catalyst, is bonded together with the above described MEA (including the aGDL) for 4 minutes at a temperature of 398 K and a pressure of 50 bar. To ensure better contact, the GDE is wetted with a few drops of 5% Nafion in isopropanol (by Quintech) before the bonding step. The Rh_xS_y GDE was kindly supplied by De Nora and details on its composition are not known.

The second investigated MEA was kindly provided by the research group of Prof. Turek at the Technical University of Clausthal and consists of a Pt/C catalyst (BASF SE) sprayed on a Nafion 117 membrane (Dupont) and two GDLs, all bonded together by the same method as for the rhodiumsulfide based MEA. The Nafion 117 membrane was pretreated according to methods adopted in modified form from Ticianelli *et al.* (1988) and Zawodzinski *et al.* (1993b). The platinum loading was 1 mg/cm^2 on both the anode and cathode side and the Nafion loading was 2 mg/cm^2 on the anode and 0.5 mg/cm^2 on the cathode side. The application of the catalyst was done by a wet-spraying process, which is described in detail in (Kuwertz 2016b). The bonding procedure is visualized in Figure 4.6 and the active area is 2.27 cm^2 in all cases.

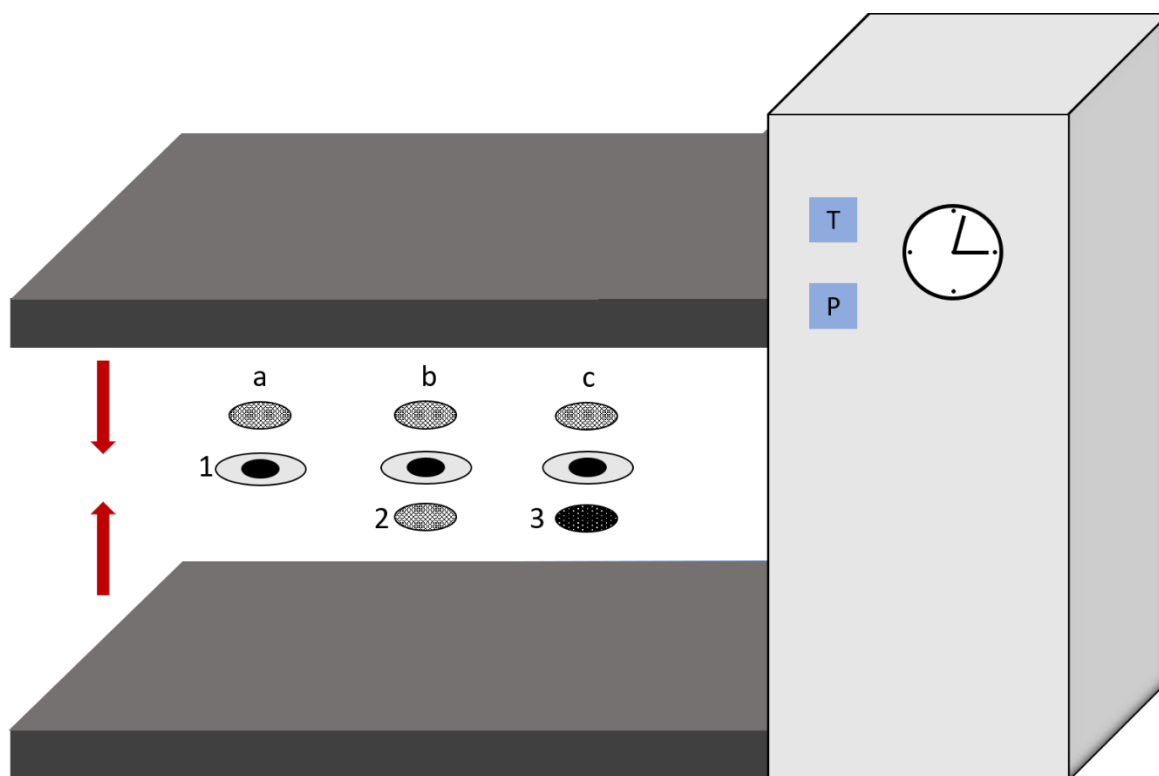


Figure 4.6, Scheme of the thermal bonding procedure for the three different MEAs: half-cell experiments (a), full-cell experiments based on the MEA from TU Clausthal (b) and full-cell experiments employing the Rh_xS_y catalyst (c). The three main components are the Nafion membrane sprayed with catalyst (1), the GDL (2) and the Rh_xS_y based GDE.

4.4 Operation and electrochemical measurements

The feed gas flow rate of HCl, O_2 and N_2 was set to 500 ml/min in all half- and full-cell experiments with the exception of the experiments concerning the alkaline reactor, where a flow rate of 140 ml/min was chosen, since gas bubbles were forming in the NaOH solution cycled through the reactor at higher flow rates. The oxygen feed in the half- and full-cell experiments employing a cyclone flow cell was humidified at 100% relative humidity (RH). All measurements were carried out at atmospheric pressure and neither the feed gases nor the reactor were cooled or heated.

Three different methods; cyclic voltammetry, linear sweep voltammetry and chronoamperometry were employed in the investigations involving the half-cell reactor while both full-cell reactor types were investigated by means of linear sweep amperometry. Martínez (2015) showed that linear sweep voltammetry with a scan rate of 1 mV/s leads to essentially identical polarization

curves as steady state measurements. Due to the strong similarity between the reactor of the present work and the one used by Martínez (2015), linear sweep voltammetry measurements were recorded with a scan rate of 1 mV/s and linear sweep amperometry measurements with a scan rate of 0.5 mA/s in order to converge towards steady-state behavior. The cyclic voltammograms were performed with a scan rate of 20 mV/s. All experiments were carried out with a ModuLab XM ECS potentiostat (Solartron Analytics) with internal booster allowing for currents of up to 2 A.

5 Results of the theoretical and experimental investigations of the HCl gas-phase electrolysis

5.1 Investigations of the HClOR

5.1.1 Role of reaction kinetics in the limiting current behavior of the HClOR

In this chapter the insights gained from the combined theoretical and experimental investigations of the HClOR are discussed. Please note that major parts of this chapter are extracted from Bechtel *et al.* (2019b). The guiding hypothesis is that the limiting current observed in the experiments of Martínez (2015) is neither caused by mass transfer limitations nor by membrane dehydration but is actually a reaction limited current.

In order to motivate this hypothesis, the Tafel plots from the work of Martínez *et al.* (2014, 2015) are briefly discussed. Martínez *et al.* corrected all but one of their Tafel plots for what the authors believed to be mass transfer resistance. The one Tafel plot that was not corrected (please see Figure A15b in the appendix), shows the Tafel slope approaching infinity at high current densities in comparison to the 60 mV dec^{-1} in the corrected Tafel plots. Furthermore, the limiting current density varies strongly for the different investigated catalyst systems and loadings, which is not typical for a mass transfer limitation.

Excluding mass transfer resistances as a cause for the limiting current behavior, a clear discrimination of mechanism B (eq. 3.30 and 3.32) is now possible as this reaction pathway would lead to Tafel slopes of $39\text{-}131 \text{ mV dec}^{-1}$ depending on the overpotential (Martinez 2015, Gileadi 1993). Also, the previously mentioned chloronium pathway is not able to explain the observed infinite Tafel slope, since the rate determining step is electrochemical, as discussed in (Krishtalik 1981). However, if the purely chemical step in mechanism A (eq 3.31), the Heyrovsky-Tafel mechanism, is rate determining, a further increase in the overpotential does not accelerate the reaction as soon as the catalyst surface is fully saturated with chloride species. This would explain the infinite Tafel slope at higher overpotentials (please see Figure A.14b in the Appendix). Hence, for the present system and catalyst, the Heyrovsky-Tafel mechanism appears to be the logical

reaction sequence. Based on these microkinetic considerations, the rate expression given in equation 3.33 can be derived as follows:

Assuming a pre-equilibrium of the adsorption and desorption of chloride anions on the catalyst surface (eq. 3.30) followed by the rate determining recombination step forming Cl_2 (eq. 3.31) leads to the following expression for the current density j^μ

$$j^\mu = 2Fr_A = 2k_A\theta^2 e^{\frac{2\alpha g\theta}{RT}} \quad (5.1)$$

With θ being the surface coverage of Pt-Cl species and g the rate of change of the free energy of adsorption with the surface coverage. If the reverse reaction is considered as well, equation 5.1 changes to:

$$j^\mu = 2k_A\theta^2 e^{\frac{2\beta g\theta}{RT}} - 2k_{-A}(1-\theta)^2 e^{\frac{-(1-\beta)g\theta}{RT}} p_{\text{Cl}_2} \quad (5.2)$$

Based on the assumption of a pre-equilibrium in equation 3.30, the surface coverage can be calculated utilizing the following expression for the Frumkin isotherm:

$$\frac{\theta}{1-\theta} e^{\frac{g\theta}{RT}} = K_0 a_{\text{Cl}^-} e^{\frac{\eta_{AF}}{RT}} \quad (5.3)$$

While the Frumkin isotherm is simplified in many publications by assuming certain intervals for θ in order to obtain an analytical solution (Conway 1979, Gileadi 1993), the complete equation is solved numerically in the present work during every iteration of the simulation, and the so obtained surface coverage is employed in the expression for the current density (eq. 5.2). This ensures validity of the obtained solution for all possible values of the surface coverage. However, simulations with $g = 0$ in equation 5.2 and 5.3, which is equivalent to the Langmuir isotherm, showed comparable or even better agreement with the experimental data of Martínez (2015) compared to the ones employing the full Frumkin isotherm with values of $g \neq 0$. Hence, while the model is able to employ the Frumkin isotherm, all further simulations are based on the Langmuir isotherm. Furthermore, assuming that the back reaction is only relevant at low overpotentials and hence low surface coverages so that $1 - \theta \approx 1$, the current density can be expressed as follows by combining equation 5.2 and 5.3 and by further presuming the current density to be zero at the equilibrium potential

$$\begin{aligned}
 j^{\mu} &= 2Fk_A \left(\frac{K_0 a_{Cl^-}}{1 + K_0 a_{Cl^-} e^{\frac{F\eta_A}{RT}}} \right)^2 e^{\frac{2F\eta_A}{RT}} - 2Fk_{-A} p_{Cl_2} \\
 &= 2Fk_A \left(\frac{K_0 a_{Cl^-}}{1 + K_0 a_{Cl^-} e^{\frac{F\eta_A}{RT}}} \right)^2 e^{\frac{2F\eta_A}{RT}} \left(1 - e^{\frac{-2F\eta_A}{RT}} \right) \quad (5.4)
 \end{aligned}$$

This equation is identical to the one given in chapter 3.2.5.1. So far, it is the only published rate expression for the electrochemical gas phase oxidation of HCl that yields infinite Tafel slopes in the high overpotential regime, contrary to the Tafel equation proposed by Eames and Newman (1995) and the expression in the work of Martínez (2015), which was adopted from Gileadi's (1995) kinetic expression for the brine electrolysis and is only valid for intermediate surface coverages and hence does not result in a kinetic limitation at high overpotentials.

Regarding the nature of active sites, it should be noted that under the experimental conditions of Martínez (2015), the formation of platinum oxide species, competing with the chloride ion adsorption, is to be expected, as further discussed in chapter 5.1.6 and 5.2. Conway and Novak (1979) even suggest that in the brine electrolysis, which exhibits a similar reaction mechanism as the HClOR, the reaction largely takes place via $Cl \cdot$ species that are adsorbed on the platinum oxide surface. Due to the lack of data on the nature distribution of active sites available for the adsorption of chloride species as a function of the potential under the conditions of the gas-phase oxidation of HCl, the numerical model is based on the assumption that all active sites are identical and that there is only one form of adsorbed chloride species. A kinetic limitation hence occurs, when these active sites are fully saturated with chloride species. The validity of this assumption and the implications of two or more surface species are further investigated in chapter 5.1.6.

In the following, the experimental polarization data of Martínez (2015) is compared to the polarization curve obtained from simulations with the half-cell model introduced in chapter 3.2.6, including the above discussed rate expression, for temperatures of 313 and 333 K.

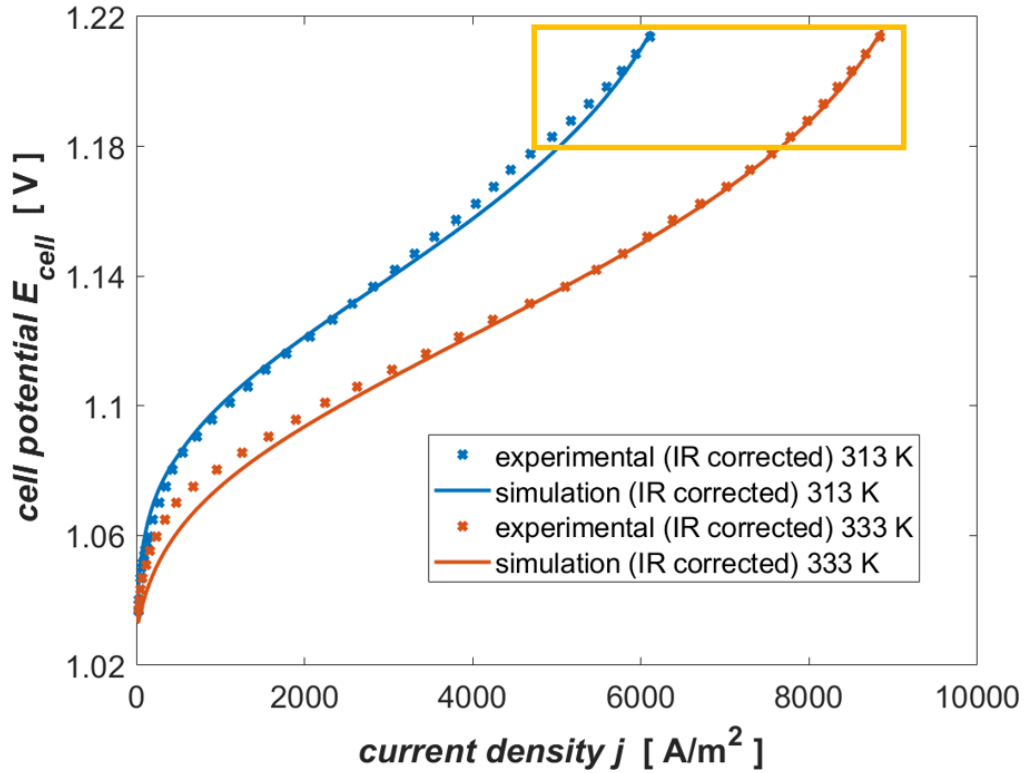


Fig. 5.1, Simulation results obtained with the presented model compared to experimental polarization data from Martínez (2015) at 313 K and 333 K. All depicted data is expressed on the scale of a reversible hydrogen electrode and the orange box visualizes the onset of the limiting behavior. Please note that the experimental data was corrected for ohmic resistance by Martínez (2015) and that consequently also the half-cell simulations do not consider ohmic resistances for reasons of comparability. Adopted from (Bechtel 2019b) with permission from Elsevier.

A comparison of experimental and simulation results in Figure 5.1 shows good agreement over the whole interval of current densities with only the equilibrium constant of the chloride adsorption/desorption step treated as a fitting parameter. The slight disagreement that is observable at higher current densities in the 313 K case and at lower current densities in the 333 K case could be due to various reasons. Firstly, in the half-cell model, the ECSA is assumed to be independent of the water content in the aCL, since the water content is greater than 4 under all investigated conditions. Nonetheless, even if the ECSA does not change as drastically as in the full-cell setup, a better fit would certainly be achieved if the ECSA was treated as a function of the water content as done in (Zhu 2019) and for the cathode side of the here presented full-cell model. Secondly, further uncertainties lie in the water transport through the membrane being influenced by the presence of HCl, which, due to the lack of consistent data as discussed in detail in chapter 3.2.4, can currently only be partly taken into account. Thirdly, the agglomerate size, which was extracted

from the previous literature (Xing 2013), poses an additional uncertainty, even if of relatively minor influence as shown in chapter 5.1.3. Lastly, the nature and amount of the available active sites and hence also the relative surface coverage might be a function of the potential and even the potential history, as further discussed in chapter 5.1.6. Considering the above-mentioned uncertainties, the nevertheless good agreement between the experimental and simulated polarization curves strongly supports the major hypothesis of a reaction limited instead of a mass transfer limited current. This is visualized in Figure 5.2 showing that the surface coverage in the 333 K simulation indeed approaches values of 1 at the current densities where the onset of the limiting behavior was observed in the measurements of Martínez (2015).

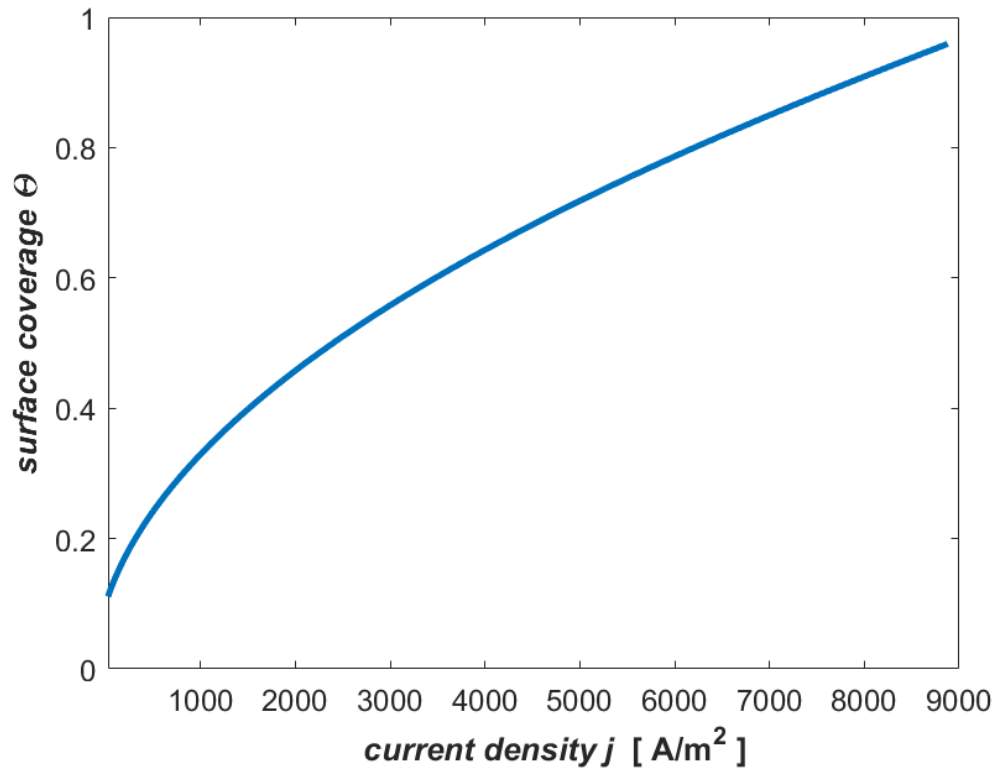


Fig. 5.2, Catalyst surface coverage under the conditions present at the agglomerate surface as a function of the current density at 333 K. Adopted from (Bechtel 2019b) with permission from Elsevier.

5.1.2 Role of mass transfer in the GDL

In the following, the mass transfer resistance is analyzed in detail to ensure that the observed limiting behavior is indeed a kinetic and not a mass transfer limitation. As discussed earlier, the major contributions to the overall mass transfer resistance are expected to come from within the GDL and the agglomerates. The concentration gradient within the porous catalyst layer can be assumed to be markedly smaller according to Gasteiger *et al.* (2004), especially since the CL in the experiments of Kuwertz *et al.* (2013, 2016a,b,c) and Martínez (2015) is about 40 times thinner than their GDL. The experimentally observed limiting behavior at a temperature of 333 K is starting at current densities between 7500-8000 A/cm². Figure 5.3 depicts the mole fraction of HCl, water and chlorine throughout the whole thickness of the aGDL at a current density of 8000 A/m², where severe mass transfer limitations should be visible, if the limiting behavior was a consequence of slow mass transfer, as assumed by Martínez (2015).

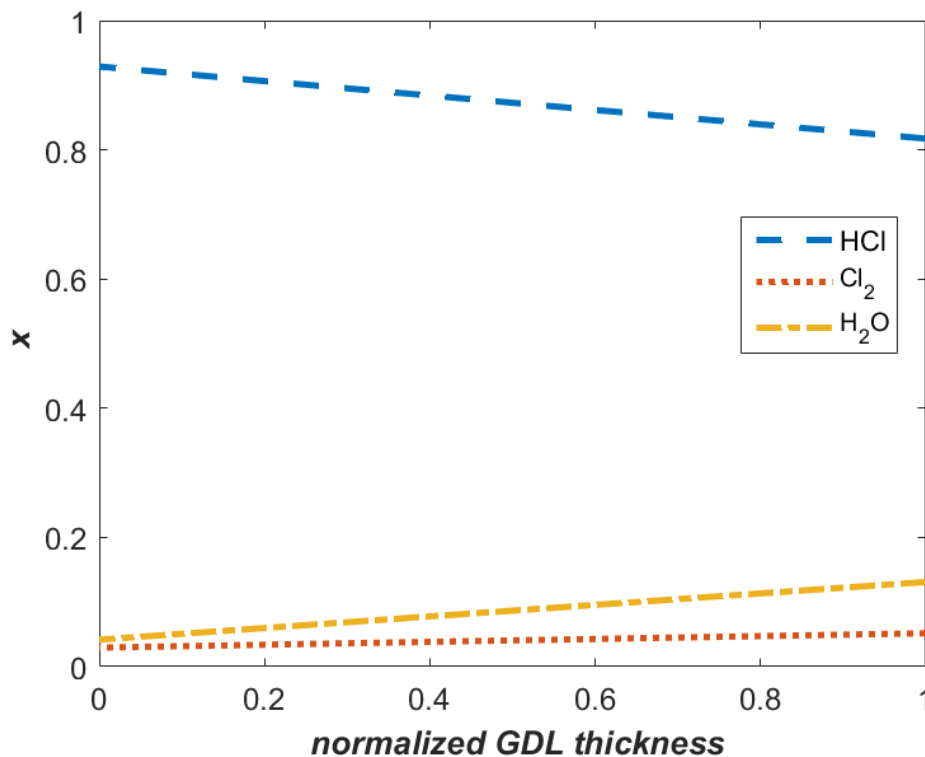


Fig. 5.3, Mole fractions of HCl, Cl₂ and H₂O over the normalized thickness of the aGDL at a current density of 8000 A/m². The anode gas channel is located at a normalized thickness of 0. Adopted from (Bechtel 2019b) with permission from Elsevier.

While there certainly is a non-negligible concentration gradient of HCl in the aGDL, it cannot explain the observed limiting behavior. Furthermore, as explained in chapter 3.2, the reaction kinetics are based on the activity of chloride ions absorbed in the agglomerates of the catalyst layer and not on the gas-phase pressure of HCl. This further reduces the influence of mass transport resistances in the GDL, since the slight gradient observed in Figure 5.3 is mitigated by the steepness of the VLE of HCl and H₂O. This becomes obvious when looking at the VLE data displayed in Figure A.6 in the appendix.

5.1.3 Mass transfer and catalyst utilization within the agglomerates

After proving that the mass transfer resistance of the aGDL is not responsible for the observed limiting behavior, the mass transfer within the agglomerates of the aCL is investigated. A well-known coefficient for relating reaction kinetics to mass transfer within a porous particle is the effectiveness factor E , which can be calculated according to equation 5.5 (Wijngaarden 2008). The effectiveness factor is defined as the ratio of the amount of reactant converted within the agglomerate to the amount that would have been converted if the same conditions that are present on the agglomerate surface prevailed throughout the whole agglomerate (Wijngaarden 2008).

$$E_{HClOR} = \frac{\iiint_{V_{agg}} r^{\mu} dV}{V_{agg} r^{\mu}|_{surf}} = \frac{N_{HCl}^{\mu}}{N_{HCl}^{\mu}(a_{HCl}^{\mu} = a_{HCl,surface}^{\mu})} \quad (5.5)$$

The effectiveness factor as a function of the current density at a temperature of 333 K is depicted in Figure 5.4 for two different agglomerate radii.

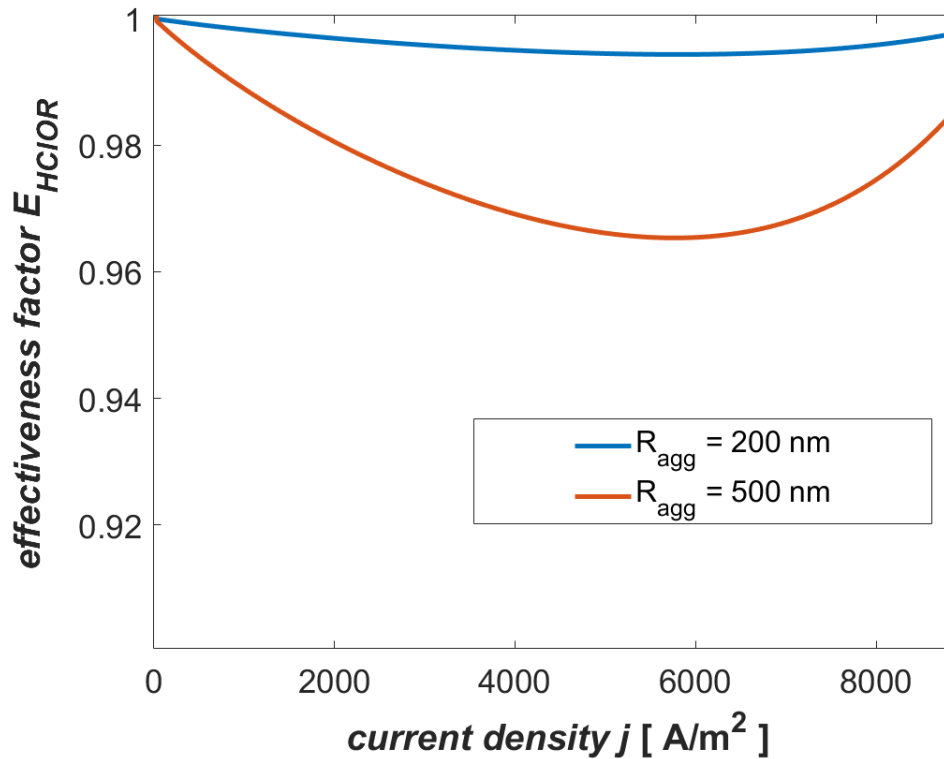


Fig. 5.4, Effectiveness factor for agglomerates with two different radii of 200 nm (blue) and 500 nm (red) in dependence of the current density of the reactor. Adopted from (Bechtel 2019b) with permission from Elsevier.

The graph clearly underlines that the mass transfer resistance within the catalyst layer is significantly smaller than the kinetic resistance over the whole investigated interval of current densities. The initial decrease in the effectiveness factor with increasing current density is due to the acceleration of the reaction rate that comes with higher current densities. The reason for the increase in the effectiveness factor after reaching a minimum at 4000 - 5000 A/m^2 , is that the overpotential rises strongly as the reaction limited current is reached. When looking at equation 5.3, it becomes obvious that at high potentials, the surface coverage approaches one. Hence, even though the activity of chloride anions within the agglomerate is declining with an increasing current density, the high overpotential increases the surface coverage more strongly so that it approaches values of one throughout the whole agglomerate, leading to the observed increase in the effectiveness factor. At significantly higher current densities, when mass transfer resistances in the agglomerate are becoming significant, the effectiveness factor decreases again. However, these mass transfer limitations only become relevant at current densities far beyond the reaction limited current densities for the catalyst loading investigated by Martínez (2015).

Since the size of the agglomerates in the MEA employed by Martínez (2015) is not known and was hence adopted from (Xing 2013), the effectiveness factor for a 2.5 times larger agglomerate, $R = 500 \text{ nm}$, is also included in Figure 5.4 to investigate the sensitivity of these results on uncertainties in the agglomerate size. Even for this increased agglomerate sizes, the mass transfer resistance is clearly smaller than kinetic resistance, with the effectiveness factor being greater than 96% ($E_{HClOR} > 96\%$) in the whole range of investigated current densities. This stands in an interesting contrast to studies of the ORR in PEMFCs (Epting 2012) and can be explained with the high concentration of $HCl_{(aq)}$ at the agglomerate surface which is 3 orders of magnitudes higher than the one of O_2 (Martínez 2015).

The mass transfer resistances discussed above certainly reduce the chloride ion activity in the agglomerates. As equation 5.3 shows, this leads to a slight increase in the overpotential in order to maintain the according surface coverage at any given current density. The reaction limited current however is not influenced by this and only depends on the ECSA and the potential independent rate constant, summarized in k_A .

5.1.4 Role of membrane hydration

Lastly, also membrane dehydration and the associated increase in the ohmic resistance of the membrane, as assumed by Eames and Newman (1995), can be excluded as the cause for the observed limiting behavior for various reasons. Firstly, the temperature dependence of the limiting current density in the experiments of Eames and Newman (1995) and Martínez (2015) is very atypical for membrane dehydration, in which case the limiting current density would be expected to decrease with temperature. Secondly, Martínez (2015) corrected their measurements for ohmic resistances but still, their data exhibits a limiting behavior. Lastly, the water content in the aCL is always ≥ 4 at both investigated temperatures in the here presented half-cell simulations. Hence, the aCL and adjacent membrane is sufficiently hydrated. Based on these insights it can be concluded that the observed limiting behavior is purely kinetic, conforming the hypothesis formulated in the beginning of this chapter. This also means that the Tafel plots in Martínez (2015) should not be corrected for what the author believed to be mass transfer resistances, as the

increasing Tafel slope at high overpotentials is now proven to be a consequence of the above discussed reaction limitation.

5.1.5 Deriving reactor optimization strategies

In this chapter, reactor optimization strategies based on the above discussed insights are proposed. In their experiments, Kuwertz (2013) employed a so called “standard loading” of 1 mg/cm² Pt and 0.5 mg/cm² Nafion. Martínez (2015) however, employed an “optimized loading” for the anode of 0.5 mg/cm² Pt and 1 mg/cm² Nafion. The approach of Martínez (2015) to raise the Nafion content is justified by their experiments showing that increasing the Nafion content at constant platinum loading lead to a significantly higher reaction limited current density and a lower overpotential compared to the standard loading. This can be attributed to the fact that the higher Nafion loading increases the amount of platinum particles in contact with the electrolyte and hence also the amount of active sites, which, based on the new insights discussed in the previous chapter, turns out to be critical for the performance of the half-cell reactor.

However, in light of the above discussed findings, it is not recommended to reduce the platinum loading, especially if operation at high current densities is desired. Experiments of Martínez (2015) showed that the reaction limited current could be increased from ca 6000 A/m² at 0.5 mg Pt/cm² to 8000 A/m² at 1 mg Pt/cm² while keeping the Nafion loading constant at 0.5 mg/cm². This is again in good agreement with the insights of the previous chapters, since a reaction limited current is expected to increase proportionally with the amount of active sites. The most feasible strategy is hence to raise both the Nafion and platinum loading in the catalyst layer in order to further increase the ECSA. While this would also build up the thickness of the catalyst layer, the modeling results indicate that mass transfer resistances are not significantly impeding the reactor performance. To visualize this, the simulation was repeated with a two times higher amount of active sites, as it can be achieved with an increased Nafion and platinum loading, and the results are graphically depicted in Figure 5.5.

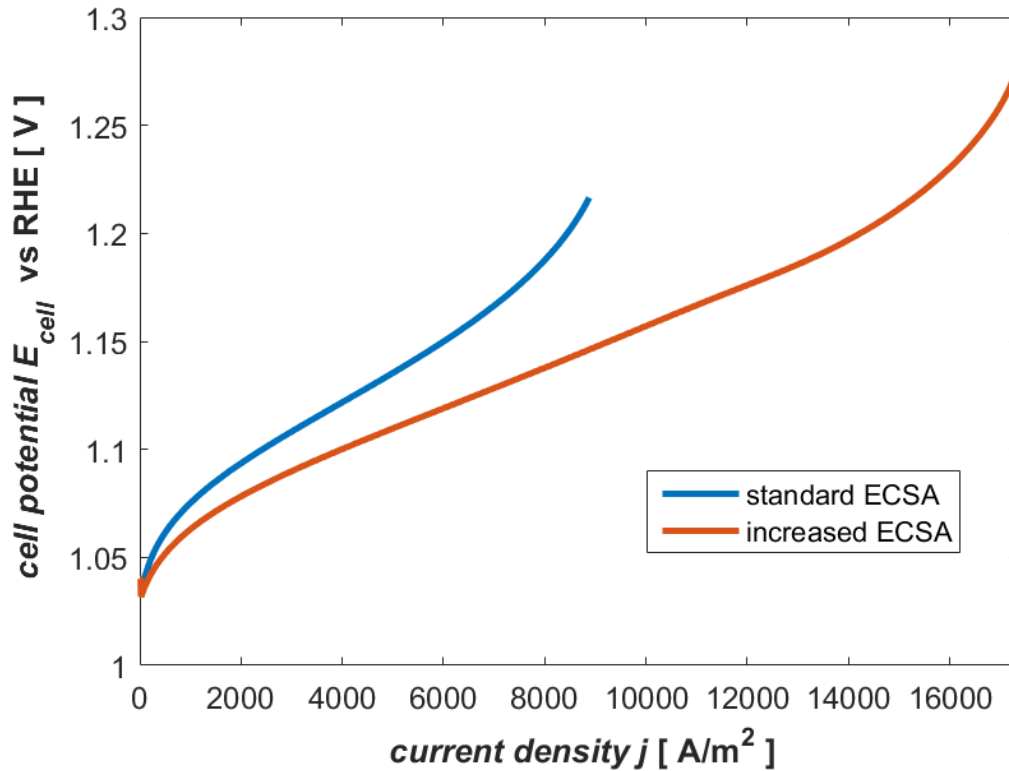


Fig. 5.5, Simulated polarization curves for the standard loading of 0.5 mg/cm^2 Pt and 1 mg/cm^2 Nafion (red) and for an increased loading corresponding to a 100% increase in the ECSA (blue). Adopted from (Bechtel 2019b) with permission from Elsevier.

As expected, the overpotential is clearly reduced over the whole current density regime and the reaction limited current increases by a factor of ca. 2. Please note that the macroscopic mass transfer resistance of the catalyst layer is still not considered, so that Figure 5.5 strictly speaking only proves that the kinetic resistance continues to dominate over the mass transfer resistances in the GDL and the agglomerates even at current densities beyond 16000 A/m^2 . However, even when doubling the thickness of the CL, the GDL would still be 20 times thicker, so that the previous assumption of a negligible mass transfer resistance on the macroscopic level of the CL is still justified. While an increased Pt loading comes with higher investment costs for an industrial reactor, it has to be considered that the impact on the energy consumption of the reactor is enormous. At a current density of 4000 A/m^2 , the anode potential is reduced by 22 mV as a consequence of doubling the amount of active sites. In chapter 2, the exergy demand for the electrochemical gas-phase oxidation of HCl emerging from an MDI production site of BASF SE in Antwerp was investigated assuming an operating current density of 4000 A/m^2 . The above predicted savings of 22 mV on the anode side are equivalent to electrical energy savings of

$5 \cdot 10^6$ kWh per year for this industrial example plant. This translates to an annual cost reduction of 500.000 € assuming a typical electricity price in Germany of 10 ct/kWh (Sönnichsen 2020). Furthermore, if the reactor can be operated at higher current densities, the size of the reactor, and therefore also the amount of catalyst, can be proportionally decreased, which dampens the effect of a higher catalyst loading on the investment costs.

5.1.6 Experimental validation

In addition to the model based analysis, this chapter focuses on experimental studies further investigating the limiting behavior in the electrochemical gas-phase oxidation of HCl building on insights of the previous literature, which are briefly discussed in the following.

Gilman (1964) showed that the adsorption of chloride anions on a Pt electrode immersed in HClO_4 containing hydrochloric acid in low concentrations of 10^{-4} mol/l is reversible up to a potential of 0.8 V and strongly potential dependent. Above 0.8 V, irreversible formation of PtOH takes place, which competes with the adsorption of chloride anions and vice versa. The author concluded that the surface coverage of chloride species on the catalyst in the potential range of 0.8 - 1.6V hence greatly depends on the path taken to reach this potential. Raising the potential from a starting value smaller than 0.8 V, increases the surface coverage of chloride species also at potentials beyond 0.8 V. Similarly, Arruda *et al.* (2008) showed that already small concentrations of 10^{-3} mol/l HCl severely impaired the formation of Pt-OH at potentials lower than 0.8 V and that upon subsequently increasing the potential to 1.4 V, chloride species remained adsorbed on the catalyst surface to some extent.

In the HCl gas-phase electrolysis, chlorine evolution starts at potentials of ca. 1 V according to the experimental data of Martínez (2015). Hence, contrary to the conditions in the work of Arruda *et al.* (2008) and Gilman (1964), adsorbed chloride species now recombine at potentials greater than 1 V, forming chlorine and leaving free adsorption sites on which again PtCl or PtOH species can be formed. Hence, it is questionable, whether the surface coverage still remains a function of potential history under conditions where chlorine evolution takes place. Interestingly, Conway and Novak (1979) demonstrated that during the oxidation of chloride anions in solution, the formation

of platinum surface oxide could be observed upon halting the potential. Furthermore, the surface oxide charge increased continuously with halting time, even beyond 20 minutes. If this phenomenon is occurring in the HCl gas-phase oxidation as well, it can be expected that the potential history would impact the coverage of chloride anions on the platinum catalyst, even under conditions where chlorine evolution occurs.

In that case, if the limiting behavior observed in the experiments of Martínez (2015) is indeed a consequence of a reaction limitation in the Tafel step due to the saturation of the catalyst surface with chloride species, the potential history would not only impact the surface coverage but also the reaction limited current. If, however, other reasons like mass transfer or membrane dehydration are at cause for the limiting behavior, the potential history should not significantly impact the reactor performance at steady state.

Hence, to validate the hypothesis of a reaction limitation, two linear sweep voltammetry measurements with a starting potential of 0.4 V and two additional ones with a starting value of 0.8 V were performed with the half-cell setup introduced in chapter 4.1. Besides the differences in the starting potential, conditions are identical in both measurements and the resulting polarization curves are depicted in Figure 5.6. Please note that the observed scattering is likely due to the pulsations of the peristaltic pumps used for the circulation of the electrolyte through the CE compartment of the cell.

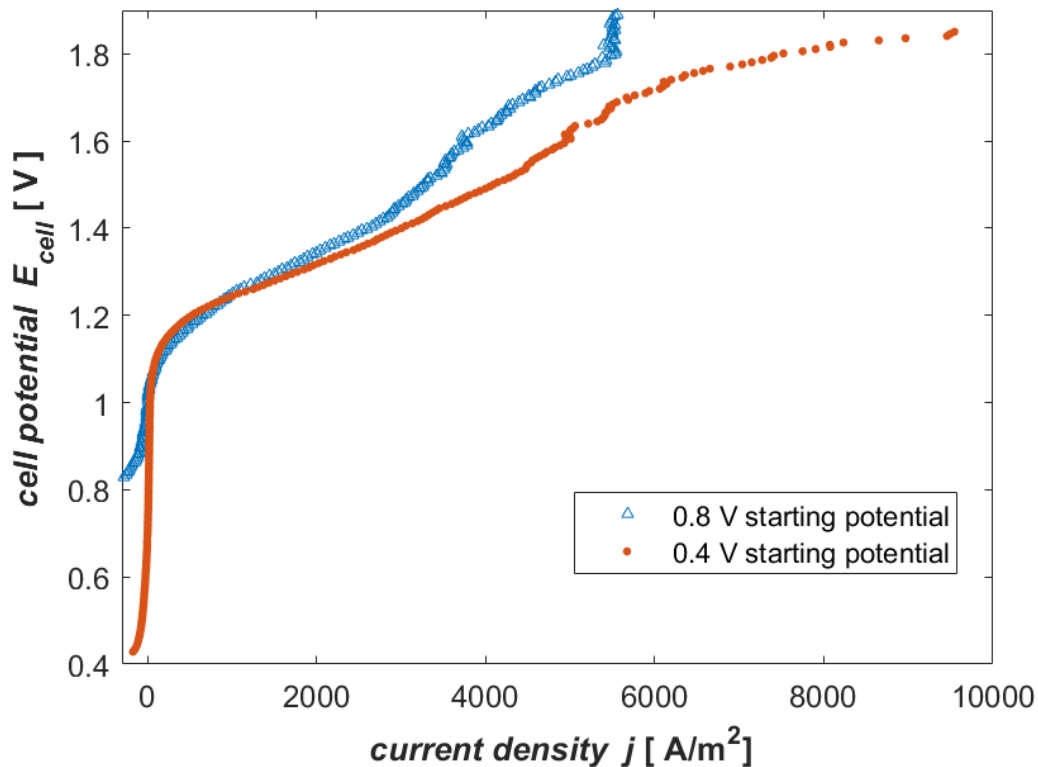


Figure 5.6, Experimental polarization data for a starting potential of 0.8 V (blue) and 0.4 V (red) measured at RT. The electrolyte circulated through the CE chamber of the half-cell setup is 1 M sulfuric acid. The measurements are partly corrected for ohmic resistance online, a full correction was however generally not possible due to technical reasons. For this reasons, the cell potentials are significantly higher than in the work of Martínez (2015), who online corrected their polarization data for ohmic drop.

The reaction limited current is ca. $5500 \text{ A}/\text{m}^2$ in the 0.8 V case, while no limiting behavior can be observed in the 0.4 V case up to a total current of 2 A, which is the natural limit of the employed potentiostat. There is no difference in the steady state mass transfer resistances in-between the measurements. Also, from a dynamic point of view, due to the low scan rate of 1 mV/s in all experiments as well as the essentially isothermal conditions in the half-cell experiments, it is highly unlikely that transient mass transfer or temperature effects play a significant role either. Hence, the fact that the limiting current density is strongly potential-history dependent supports the claim of a reaction limitation instead of a mass-transfer limitation. The increase in the limiting current density in the 0.4 V case beyond 2 A can hence be explained by a higher catalyst surface saturation with chloride species compared to the 0.8 V experiment.

Furthermore, a shoulder is visible in both polarization curves, indicating a first limitation, which, in the 0.4 V case, is followed by a second final limitation. Interestingly, Chen and Kucernak (2004) observed a similar shoulder and second limitation in their investigations of the hydrogen oxidation reaction (HER) on submicron platinum particles where mass transfer is sufficiently fast to observe kinetic limitations. The authors attribute the shoulder in their polarization data to a kinetic limitation in the Tafel step and the final limiting current density to mass transfer resistances.

As discussed above, for the data presented in Figure 5.6, a diffusion limitation can be ruled out. Hence, other possible reasons for the shoulder observed in the polarization data of the HClOR are discussed in the following. One explanation could be the onset of the oxygen evolution reaction (OER) at ca 1.6 – 1.8 V facilitated by water present in the aCL. For this reason, the HCl feed was subsequently replaced with N₂ at the same flow rate and a linear sweep with a scan rate of 5 mV/s was performed. The obtained polarization curve is depicted in Figure A.15 in the appendix and indicates that the OER currents is negligibly small even at potentials of up to 2 V compared to the HClOR currents in the measurements depicted in Figure 5.6.

Another effect possibly playing a role in the occurrence of the above discussed shoulder could be the HClOR activity of the carbon support, which Martínez (2015) showed to be significantly smaller than that of platinum, yet still noticeable at kinetic overpotentials of more than 15 mV. Hence, the acceleration of the HClOR observable in Figure 5.6 subsequent to the shoulder could be correlated to the onset of the HCl oxidation on the carbon support.

A cause that can be ruled out, is the possible involvement of the Heyrovsky step in the reaction kinetics of the HClOR. This reaction cannot exhibit a kinetic limitation, as discussed in chapter 5.1.1 and by Chen and Kucernak (2004), but only a mass transport limitation in the diffusion of Cl_(aq) to the catalyst surface, which was already refuted above.

Another explanation could be the onset of the direct electrochemical formation of hypochlorous acid with the standard potential $E^0 = (1.482 + 0.03pH)$ vs RHE. According to Vos and Koper (2018) this reaction is however only competing with chlorine evolution at pH > 4 and is hence not likely to play a significant role in the here investigated HClOR due to the highly acidic environment in the aCL.

The most plausible explanation for both the shoulder and the second limitation in the here presented data, seems to be the presence of at least two $\text{Cl} \cdot$ surface species and a reaction limitation in the recombination step of both species (Tafel step), leading to two different limiting current densities.

Chen and Kucernak (2004) suggested that there are two different hydrogen species on the catalyst surface, a strongly and a weakly adsorbed one, whose surface coverage exhibit a different potential dependence. Moreover, Conway and Novak (1979) proposed that the brine electrolysis might proceed to a significant extent via $\text{Cl} \cdot$ species adsorbed on platinum oxide, presenting a second surface species in addition to PtCl . According to Sabatier's principle, the recombination of $\text{Cl} \cdot$ adsorbed on platinum oxide would exhibit a fast rate constant than the recombination of the more strongly adsorbed PtCl . Hence, the presence of two surface species would result in two limiting current densities manifesting itself in a shoulder and a subsequent final limiting current density as observed in the experimental data depicted in Figure 5.6.

Which of the two species is responsible for the first and which for the second limiting current density, depends not only on the rate constant of the recombination step but also the fraction of active sites that are covered with the respective surface species, both considered in the apparent rate constant k_A employed in the numerical model. This hypothesis is supported by another measurement started at a potential of 1.05 V depicted in Figure A.16 in the appendix. For this starting potential, only a minor shoulder is visible in the polarization curve. This might be explained by the fact that, as discussed above, PtCl formation is suppressed by the formation of platinum oxide at potentials higher than 0.8 V. Hence, the catalyst surface in this experiment can be expected to be predominantly covered with oxide species and far less PtCl species compared to the measurements with a lower starting potential. If the chloride oxidation also proceeds via $\text{Cl} \cdot$ adsorbed on platinum oxide, as suggested by Conway and Novak (1979), the lack of significant amounts of a second adsorbed species (PtCl) would explain the less pronounced shoulder. Similarly, the 0.4 V case exhibits a smaller shoulder than the 0.8 V case, too, which could be again explained by the predominance of one surface species, in this case PtCl .

To validate this hypothesis, the reactor simulation at 333 K was repeated, but this time with two separate surface species. One species was given a high rate constant k_A but low equilibrium constant K of the adsorption/desorption step of chloride species on the catalyst surface, emulating

a weakly adsorbed surface species. A second species was given a lower rate constant but increased equilibrium constant, emulating a strongly adsorbed species.

The equilibrium constant K is a function of the the potential and due to the difference in the Gibbs free energy of the adsorption/desorption step, the equilibrium potential for both species should be different. However, this difference can be shifted into the prefactor K_0 so that the same (over)potential can be employed in the rate expressions for both surface species, by accordingly adjusting K_0 , since

$$K = K_0 e^{\frac{\eta_{AF}}{RT}} = K_0^* e^{-\frac{75497.5}{RT}} e^{\frac{\eta_{AF}}{RT}} \quad (5.6)$$

This simulation only serves to show the effect of two surface species rather than focusing on their exact adsorption/desorption equilibrium constants. For simplicity, both reactions were modeled in parallel without influencing each other. The simulated polarization curve displayed in Figure 5.7 indeed exhibits a shoulder similar to the one observed in the above discussed experimental investigations and as such provides qualitative justification of the experimental data and the physicochemical origin of the shoulder. Hence, the simulation and experimental results are both consistent with the hypothesis of a reaction limitation of the HClOR on platinum and indicate the presence of at least two different surface species.

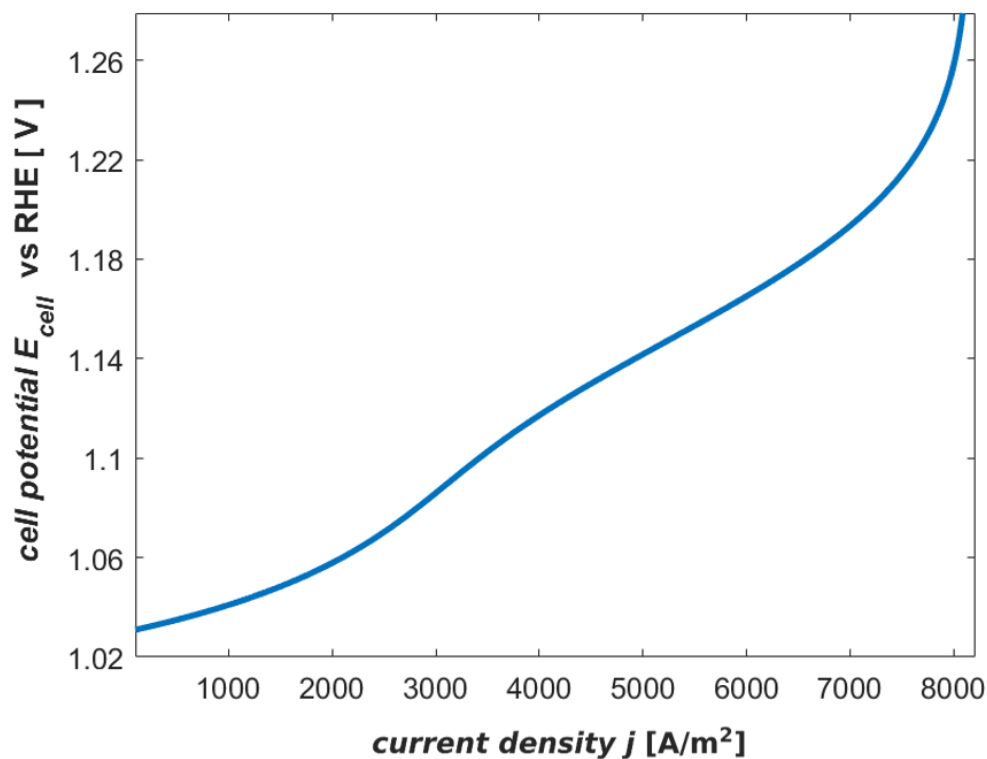


Fig. 5.7, Simulated polarization curve at a temperature of 333 K assuming the presence of two different Cl⁻ surface species.

The fact that the measurements of Martínez *et al.* (2013, 2014, 2015) do not show such a shoulder could be an indication that they stopped their experiments at the first limitation. The shoulder and the final limitation should appear if measurements were continued to higher potentials. In fact, their experimental data depicted in Figure 5.1 shows that the limiting current density is not fully reached but that the measurements are stopped at the onset of the limiting behavior, which was the reason why the limiting current density had to be extrapolated from their data for calculating k_A , as described in chapter 3.2.7. Alternatively, their high starting potential close to the OCV could be the reason why the catalyst surface is mostly oxidized and hence only small amounts of PtCl were present. This scenario is similar to the measurement at a starting potential of 1.05 V of this thesis, which also barely exhibits a shoulder.

Based on these findings as well the insights of the previous chapter, the limiting behavior observed in the experiments of the present work and the one of Martínez (2015), can with great certainty be attributed to a reaction limitation in the Tafel step of the HClOR. The presence of two or more surface species can lead to two or more different limiting current densities and hence the formation

of a shoulder in the polarization curve. In future investigations the same methodology should be applied to other catalyst systems, e.g. ruthenium oxide, that are more resistant to corrosion and dissolution in the aggressive environment characteristic for the HClOR. As such, these systems are more suited for an industrial application of the process. Furthermore, as Figure 5.6 shows, reducing the starting potential of the measurement to 0.4 V allowing for increased platinum chloride formation allows for reaching current densities of 10000 A/m^2 with no signs of a limiting current at a temperature of only 298 K. Future investigations should hence also focus on the stability of this potential history effect over a prolonged course of time. If it is long lasting, it could enable the operation at significantly higher current densities by simply preparing or reforming the catalyst surface with an according potential sweep beforehand or periodically.

5.1.7 Summary of the new insights on the HClOR

In this chapter, the HClOR was investigated by means of a numerical reactor model combined with experimental half-cell studies. The model exhibited excellent agreement with experimental literature data, demonstrating that the experimentally observed limiting currents are due to the rate-determining Tafel step in the microkinetic mechanism and that neither mass-transfer resistances nor membrane dehydration are the cause for the limiting behavior. Based on this, a reactor optimization strategy aiming at an increased Nafion and catalyst loading in the aCL was proposed, which was shown to harbor significant potential for energetic and financial savings in an industrial application of the process.

These insights were validated experimentally by utilizing the dependence of the catalyst-surface coverage with oxide and chloride species on the potential history of the cell. The significant impact of the potential history on the limiting behavior in these experiments further supports the hypothesis of a reaction limitation. Starting the linear sweep voltammetry measurements at a lower potential of 0.4 V led to current densities that surpass all previously measured ones in the work of Martínez (2015), including those recorded at elevated temperatures. . If this potential history effect proves to last over an extended period of time, it would be an effective and simple method to significantly increase the limiting current density. This is not only relevant for the HCl oxidation

in a half-cell but also the operation of the full-cell employing an ODC, where current densities of at least 5000 A/m^2 must be reached to make the process industrially feasible.

Lastly, a shoulder was observed in these experimental polarization curves that indicates the presence of at least two $\text{Cl} \cdot$ surface species differing in their adsorption strength and rate constant for the subsequent recombination step forming chlorine. This hypothesis was supported by simulations with the numerical model introduced in chapter 3.2.6, which also showed a comparable shoulder upon adding a second surface species. In future investigations, the surface chemistry of the HClOR on platinum and other catalysts should hence be investigated in more detail.

5.2 Crossover of HCl and chlorine and its influence on the ORR

In chapters 1.4 and 1.5, the low OCV of the ORR and the increased kinetic overpotential compared to classical hydrogen PEM fuel cells was presented as another distinct feature in the experimental data of Kuwertz *et al.* (2013) having a significant impact on the energy demand of the reactor. After investigating the anode half-cell reaction in detail within the last chapter, the present chapter hence focuses on an understanding of these performance losses in the cathode half-cell reaction, the ORR. The main hypothesis investigated in this chapter, is that the performance losses are caused by the crossover of HCl and Cl_2 and subsequent poisoning the platinum cathode catalyst.

In addition to the literature reviewed in chapter 5.1 focusing on the effect of chloride anions on the formation of platinum oxides, there are various studies directly investigating the impact of the presence of chloride anions on the ORR activity of platinum based catalysts as well. Schmidt *et al.* (2001) for example showed that the ORR activity of their carbon supported platinum catalyst immersed in an electrolyte decreased by an order of magnitude upon adding chloride anions at a concentration of 10^{-4} mol/l into the solution. Moreover, the authors also observed increased H_2O_2 production. Baturina *et al.* (2011) investigated the impact of 4 ppm gaseous HCl in the cathode reactor feed of a PEM fuel cell and suggested that not only the ORR activity but also the wetting properties of the cCL and cGDL are affected and that platinum corrosion can become problematic even at such low HCl concentrations.

While there is no doubt that the presence of HCl or dissolved chloride species has detrimental effect on the ORR on platinum catalysts, it has not yet been investigated whether and to what extent HCl and Cl₂ crossover occurs in the operation of the HCl gas-phase oxidation employing an ODC. While Motupaly *et al.* (2002) observed pH changes in the anode chamber for a Dupont-like reactor with hydrogen evolution as the anode reaction, from which the authors estimated the HCl crossover, their investigation does not allow for a differentiating between the crossover of HCl and Cl₂. This is due to the fact that the dissociation of Cl₂ in the aqueous solution fed into the cathode chamber (please see Fig. 1.2) or its oxidation in the cCL would also lead to a pH reduction, similar to the crossover of HCl.

In the absence of a liquid electrolyte in the cathode chamber of the gas phase reactor employing an ODC, crossed over Cl₂ would be reduced to chloride anions, which would accumulate in the aCL and poison the platinum catalyst in a similar manner as HCl. Since furthermore the flux of both species is influenced differently by operating conditions like the current density or cathode feed humidification, as shown in the course of this chapter, determining which of the two species is mainly responsible for the observed cathode catalyst poisoning, might allow for the development of tailored counter measurements aiming at mitigating this crossover. Furthermore, the presence of liquid water in the cathode chamber of the reactor employed by Motupally *et al.* (2002), drastically affects the transport of H₂O, HCl and Cl₂ through the membrane so that their results cannot be directly applied to the gas-phase electrolyzer employing an ODC investigated in the present work.

Hence, in the following, the crossover of HCl and Cl₂ and its impact on the ORR in the gas-phase reactor as well as a liquid-phase reactor similar to the one employed in the Bayer UHDENORA process is further investigated by means of a combined theoretical and experimental approach employing the numerical crossover model introduced in chapter 3.3 and the experimental setup explained in chapter 4.1.

5.2.1 HCl and chlorine crossover in a liquid-phase reactor employing an ODC

In a first step, a half-cell setup, which closely resembles the Bayer UDENORA liquid-phase reactor, is employed to determine to which extent the presence of aqueous hydrochloric acid in the anode chamber of the reactor influences the surface properties and the ORR activity of the platinum catalyst in the cathode department as a consequence of crossover. Various literature studies showed that cyclic voltammograms of a platinum electrode immersed in an electrolyte (e.g. sulfuric acid) changes in the presence of chloride anions in three distinct ways. Firstly, the platinum oxide formation is delayed to higher potentials as a consequence of surface passivation with chloride anions (Pavlišič 2014, Hudak 2017, Novak 1981), as already discussed in chapter 5.1.6, while the oxide formation at higher potentials of more than 1.1 V vs RHE remains mostly unaffected (Hudak 2017). Secondly, the corresponding reduction peak declines with increasing chloride concentration (Pavlišič 2014, Hudak 2017, Novak 1981). Lastly, at ca 0.7 V, an additional peak is observable in the presence of chloride anions that (Hudak 2017) and (Priyantha 1996) attribute to the reduction of a platinum chloride complex, which might be formed during the oxidative scan.

While feeding gaseous N₂ into the WE chamber of the above mentioned the half-cell setup (please see chapter 4.1 for more details), the two cyclic voltammograms depicted in Figure 5.8 were recorded. In the first cyclic voltammogram, 1 M H₂SO₄ was fed into the CE chamber and in the second one 0.9 M hydrochloric acid. If crossover of chloride ions from the CE chamber filled with hydrochloric acid to the WE does occur, then the two cyclic voltammograms depicted in Figure 5.8 should exhibit the above mentioned differences caused by the presence of chloride species. Please note that due to technical reasons correction of the ohmic resistance was not possible. Hence, the obtained cyclic voltammograms cannot be quantitatively compared to other studies in the scientific literature, but since all here depicted data was obtained under these circumstances, trends resulting from the substitution of sulfuric acid with hydrochloric acid can nonetheless be analyzed.

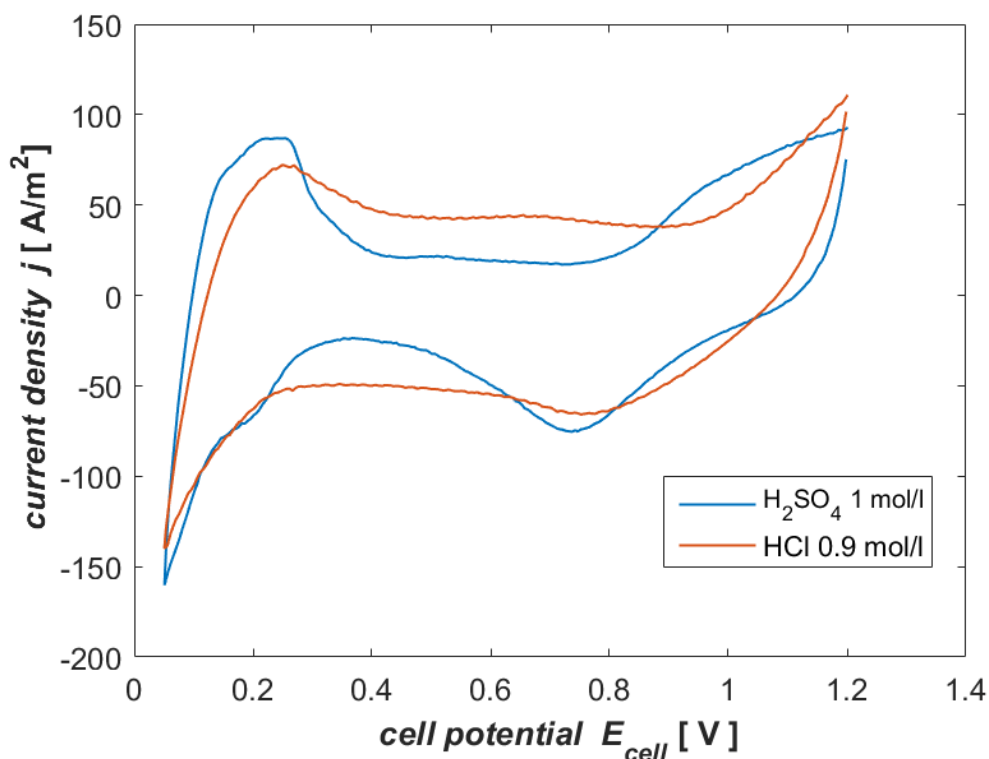


Fig. 5.8, Cyclic voltammograms of the Pt/C WE with sulfuric (blue) and hydrochloric acid (red) circulating through the CE chamber referenced versus RHE. Each time, 10 cycles were recorded until essentially no changes in the cyclic voltammograms with increasing number of cycles was observed.

As expected, the platinum-oxide formation is delayed upon switching from sulfuric to hydrochloric acid, however remains mostly uninfluenced at potentials greater than 1.1 V as in the work of Hudak *et al.* (2017). Consequently, also the reduction peak is diminished. Whether there is an additional peak caused by the reduction of a platinum chloride complex can however not be determined due to the dominant platinum oxide reduction peak in the same potential range. While a detailed discussion of these cyclic voltammograms and their implications on the state of the platinum catalyst surface is out of the scope of the present work, the occurrence of the expected phenomena upon changing the electrolyte in the CE chamber to hydrochloric acid implies that indeed HCl or Cl_2 are crossing over to an extent that markedly impacts the surface properties of the WE. Please note that this measurement does not allow for a clear differentiation between $\text{HCl}_{(\text{aq})}$ and Cl_2 crossover, since Cl_2 emerges at the CE upon switching from sulfuric to hydrochloric acid and is hence present in the electrolyte.

In an attempt to further understand the influence of this crossover on the ORR, O_2 is fed into the WE chamber instead of N_2 in a second experiment and a chronoamperometry measurement is carried out starting with 1M sulfuric acid in the anode chamber at a potential of 0.6 V vs RHE. After 600 s, the sulfuric acid is substituted with 7 M hydrochloric acid without stopping the measurement. The experimental data is depicted in Figure 5.9.

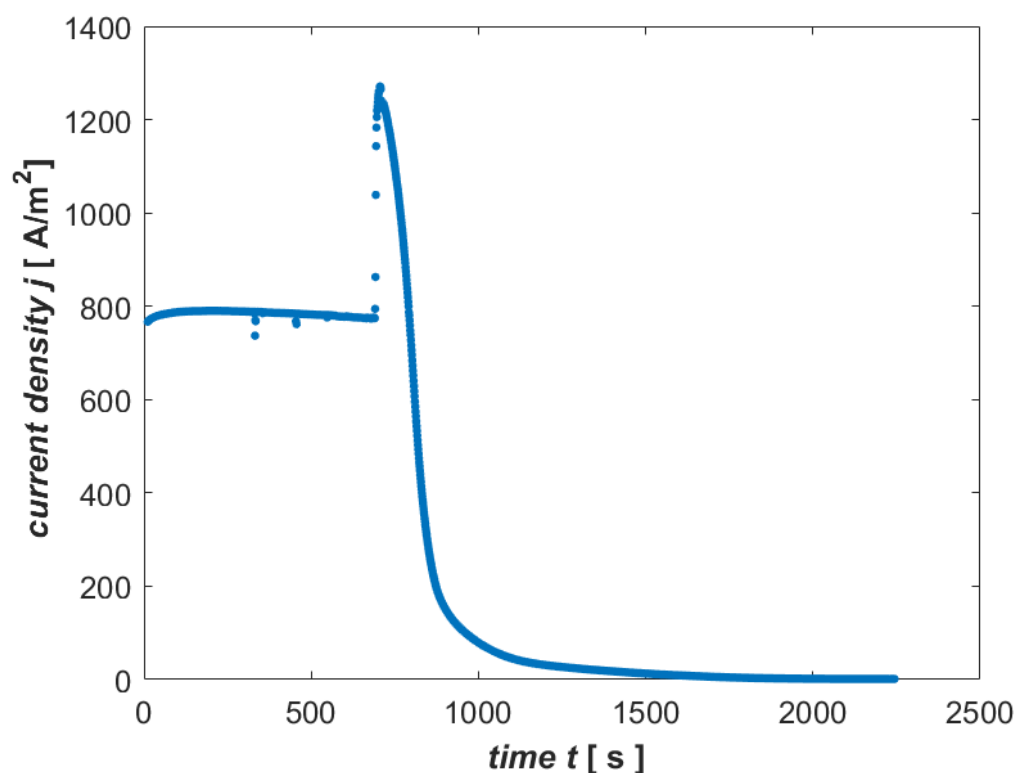


Fig. 5.9, Chronoamperometry at 0.6 V vs RHE with the sulfuric acid stream flowing through the CE chamber being exchanged with hydrochloric acid after 600 s. No ohmic correction was performed.

In the first 600 s, the current density is mostly constant at ca 800 A/m^2 . The low current density is a consequence of the significant ohmic resistance of the electrolyte and membrane in-between the WE and RE. Upon switching the 1 M sulfuric acid with the more concentrated hydrochloric acid, the current density sharply increases due to the reduced ohmic resistance of the electrolyte. However, shortly after this spike, the current density continuously declines until it reaches a value of essentially 0 A/m^2 after 1500 s. As explained in the following, this decay is at least partly caused by chloride ion poisoning.

One contribution to this decay is certainly the negative impact of the 7 M hydrochloric acid on the proton conductivity of the membrane compared to the less concentrated sulfuric acid. The ionic conductivity of a Nafion 117 membrane in contact with 1 M H₂SO₄ is 0.088 S/cm (Slade 2002), compared to 0.018 S/cm in the case of 7 M HCl (Vidaković-Koch 2012), so that switching to a 7 M HCl solution results in a ca. 5 times lower ionic conductivity of the membrane. On the other side, the ionic conductivity of the electrolyte in-between the membrane and the reference electrode is increasing. Nonetheless, changes in the ohmic resistance do not account for the full extent of the current-density decay since the ohmic contribution to the overpotential diminishes with lower current densities and hence does not explain the drop to essentially zero current.

Secondly, the significant difference in the proton activity between the WE and reference electrode reduces the ORR overpotential and hence the current density. However, the decrease in the ORR-overpotential due to switching from 1 M sulfuric acid to 7 M HCl, approximately $\frac{RT}{F} \ln \left(\frac{a_{HCl}}{a_{H_2SO_4}} \right)$, does not exceed 0.1 V. Since the OCV of the ORR on Pt/C is known to be at least 0.9 V in the absence of catalyst poisoning species (J. Zhang 2006), this Nernstian correction hence does not explain the drop to essentially zero current either. Therefore, the significant current density decay must partly be caused by chloride ion poisoning of the platinum based WE. The time scale of the above experiment also shows that the crossover and subsequent catalyst poisoning occurs within a few minutes of operation. Interestingly, Kuwertz *et al.* (2016a) measured an OCV of the ORR half-cell reaction of 0.6 to 0.7 V vs RHE in the presence of gaseous HCl in the anode chamber. This is in good agreement with the observed decay of the current density to 0 A/m² at a potential of 0.6 V.

These experiments prove the significant impact of chloride-ion poisoning on the platinum cathode catalyst as a consequence of crossover in the above discussed half-cell experiments. Since furthermore platinum exhibits a lack of stability in the chemically aggressive environment of the HCl electrolysis, especially under open-circuit conditions (Kuwertz 2016c), investigating alternative catalyst materials that are stable and less prone to chloride ion poisoning is of great importance for the industrial applicability of the process.

To allow for a more quantitative evaluation and a differentiation between the fluxes of HCl and Cl₂ through the membrane in the liquid-phase reactor, both fluxes were estimated using the numerical crossover model presented in chapter 3.3 and are depicted in Figure 5.10 as a function of the current density.

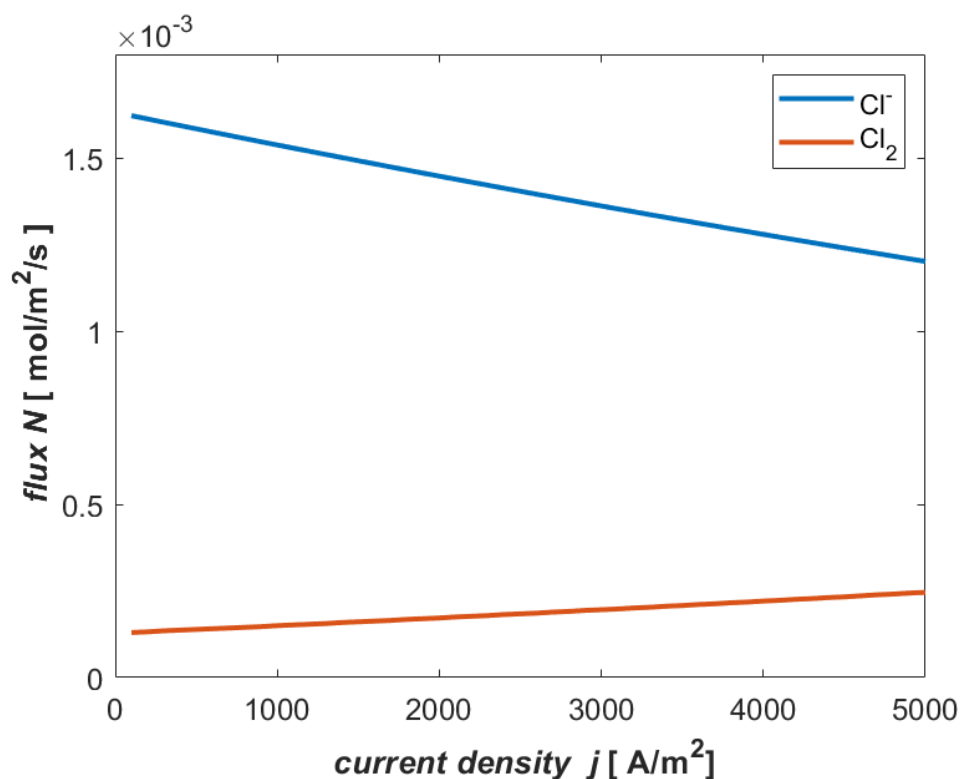


Fig. 5.10, Fluxes of Cl⁻ (blue) and Cl₂ (orange) through the membrane in the liquid-phase reactor as a function of the current density.

The simulations show that approximately 10⁻³ mol/m²/s of Cl₂ and HCl cross over from the CE compartment to the WE. It should be considered that Cl₂ would be reduced at the WE and that most of crossed over species would hence accumulate in the catalyst layer due to the absence of an electrolyte in the WE chamber. Since furthermore Schmidt *et al.* (2001) showed that already chloride ion concentrations of 10⁻⁴ mol/l reduce the ORR activity of a carbon supported platinum catalyst by an order of magnitude, a flux of 10⁻³ mol/m²/s of Cl₂ and HCl would lead to significant poisoning effects within seconds (at steady state). This once more supports the hypothesis of a crossover related performance decay, at least in the liquid-phase reactor setup.

As Figure 5.10 shows, the flux of chloride ions clearly dominates over the flux of Cl_2 through the membrane over the whole current density range. This is mostly due to the fact that while the diffusion coefficient of Cl_2 in Nafion is slightly higher than the one of HCl (please see chapter 3.3), the concentration of chloride anions in the CE chamber significantly exceeds the one of Cl_2 , leading to an overall increased diffusive and convective flux. Please note that the concentration of Cl_2 in the CE chamber is already overestimated in the simulation, since full saturation of the liquid phase, corresponding to a chlorine partial pressure of 1 bar, was assumed due to a lack of according experimental data and in order to show that nonetheless the crossover of chloride anions dominates over the one of Cl_2 . Hence, the Cl_2 flux through the membrane is even smaller than here depicted and can be neglected in the investigated current-density interval.

Another interesting insight is that the flux of chloride species decreases with higher current densities while the Cl_2 flux increases. The reason for this becomes clear when looking at the contribution of diffusion, convection and migration to the overall flux as depicted in Figure 5.11a for HCl and Figure 5.11b for Cl_2 .

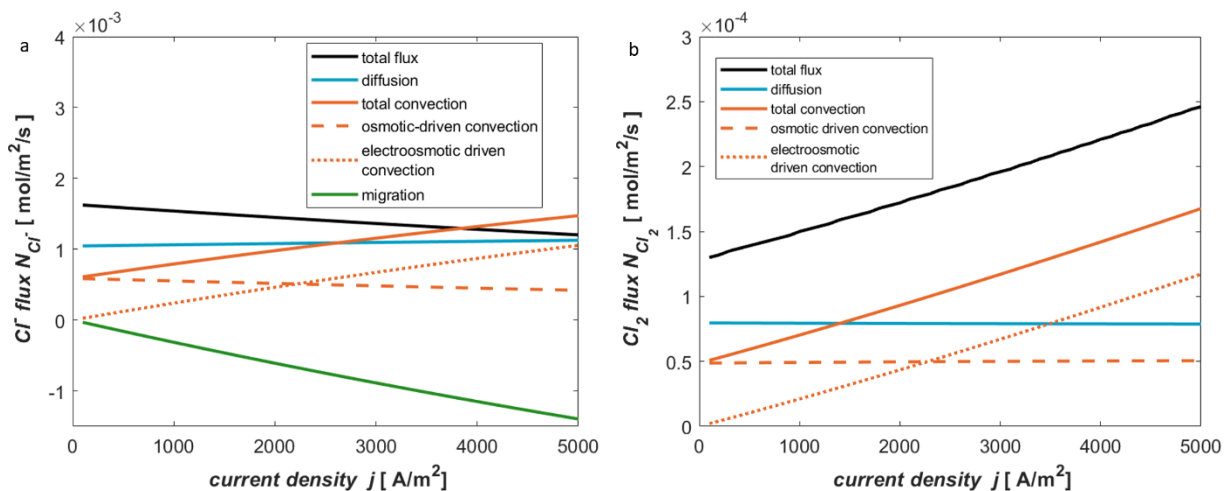


Fig. 5.11, Contributions of diffusion, osmotic-driven convection, electroosmotic-driven convection and migration to the overall flux of a) Cl^- and b) Cl_2 through the membrane in the liquid-phase reactor as a function of the current density.

As a consequence of the potential gradient in the solution between both electrodes, chloride ions, due to their negative charge, migrate to the anode. According to Ohm's law, this potential gradient is proportional to the current density. For this reason, the migration flux of chloride species depicted in Figure 5.11a becomes increasingly negative with higher current densities, leading to

the decline in the overall flux observed in Figure 5.10. Contrary to that, Cl_2 is not affected by the electric field, as it is not charged.

The second component of the overall flux, convection, increases with the current density and becomes the most dominant of all three flux components for both species at intermediate to high current densities ($>1000 - 3000 \text{ A/m}^2$). It consists of an osmotic component, caused by a water activity gradient across the membrane due to the presence of the aqueous solution in the CE compartment, as well as an electroosmotic part due to the electroosmotic drag of protons. Consequently, the electroosmotic flux increases linearly with current density, while the osmotic flux remains fairly constant over the whole current-density interval, since the water content of the membrane is set as a current-density-independent boundary condition on both sides (please see chapter 3.3). The slight decrease in the osmotic flux with current density that is still observable, originates in the electroosmotic drag flattening the water concentration gradient in parts of the membrane close to the CE side. Similarly, the boundary conditions for chloride anions and Cl_2 also lead to an almost constant diffusive flux across the membrane.

These fixed boundary conditions are an approximation made in the liquid-phase reactor scenario due to a lack of experimental data on the concentration changes as a function of the current density. One could either experimentally or through a numerical model of the overall liquid-phase reactor determine the boundary conditions as a function of the current density, as done for the gas-phase reactor. However, such studies exceed the scope of the present work focusing on the gas-phase electrolysis. Furthermore, due to the presence of an aqueous solution on the anode side and the low single pass conversion in the Bayer UHDENORA process, the current density dependency of the activity gradients of all species can be expected to be significantly smaller than in the full-cell setup, so that this approximation seems reasonable.

It can be concluded at this point that the crossover of Cl^- and Cl_2 as well as its effect on the ORR was experimentally and theoretically confirmed for the investigated half-cell resembling the Bayer UHDENORA liquid-phase reactor. Since the concentration of hydrochloric acid in the anode chamber was set to 2 M in the simulation, the crossover of Cl^- anions can be expected to be even higher in the real liquid-phase reactor of the Bayer UHDENORA process where hydrochloric acid at a concentration of ca. 4 M is employed. Furthermore, the numerical model indicates that the crossover of chloride ions dominates over the flux of Cl_2 over the whole current density range.

Lastly, due to the significant effect of migration at increased potential gradients, operation at higher current densities is not only beneficial in an industrial application due to the decreased cell and stack size but also impedes the crossover of chloride anions significantly.

5.2.2 HCl and chlorine crossover in the gas-phase reactor employing an ODC

After investigating the Cl^- and Cl_2 crossover in the liquid-phase reactor, the following chapter serves to investigate to which extent these insights can be applied to the gas-phase reactor as well. Since the crossover in the full-cell setup is difficult to (quantitatively) investigate experimentally, amongst other reasons due to the lack of a liquid electrolyte in the anode and cathode chamber, the numerical crossover model is used again for an estimation of the fluxes under full-cell conditions. To ensure realistic conditions, the concentrations of all species at both membrane boundaries are taken from the simulation results of the numerical full-cell model presented in chapter 3.2 as a function of the current density for a temperature of 333 K and 100% cathode humidification.

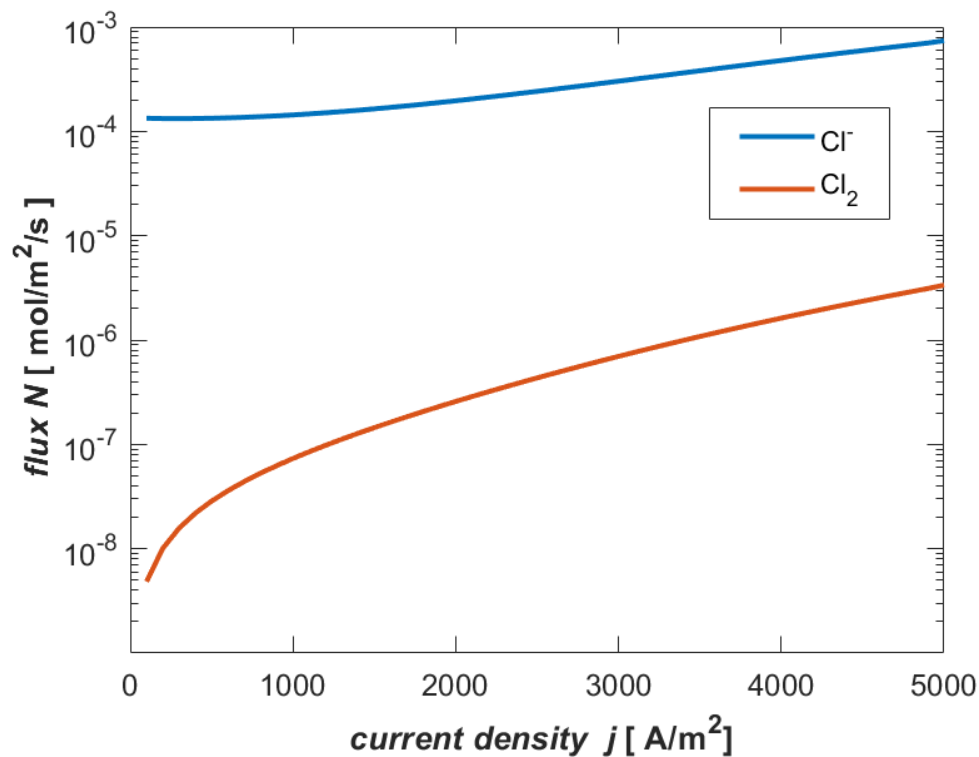


Fig. 5.12, Fluxes of Cl^- and Cl_2 through the membrane in the gas-phase reactor as a function of the current density.

As Figure 5.12 shows, the flux of chloride ions and especially Cl_2 through the membrane is clearly lower than in the liquid-phase reactor. The significant reduction in the Cl_2 crossover is mainly a result of the lower Cl_2 concentration. Moreover, since no liquid water is present in the gas-phase reactor under the here investigated conditions, the water content within the membrane is lower compared to the liquid-phase reactor, leading to reduced partitioning coefficients for Cl_2 and Cl^- as a consequence of the smaller water volume fraction f . Furthermore, the direction of the convective flux changes, now impeding the transport of both species through the membrane.

On the other side there is a significantly higher concentration of HCl in the anode of the gas-phase reactor compared to the 2 M solution in the liquid-phase reactor, leading to an increased number of chloride ions in the membrane. Furthermore, migration is suppressed in this cell compared to the liquid-phase reactor as a consequence of a lower water content. These effects somewhat offset the reduced crossover resulting from the direction of convection and the lower partitioning coefficient in the gas-phase cell compared to the liquid-phase cell. As a result, the chloride-ion flux of $1 \cdot 10^{-4}$ to $8 \cdot 10^{-4}$ mol/m²/s in the gas-phase reactor is only slightly lower than the flux of 10^{-3} mol/m²/s in the liquid-phase reactor. The surge in the Cl_2 crossover in the gas-phase reactor at higher current densities observable in Figure 5.12 is a consequence of the Cl_2 production rate in the aCL increasing with the current density (please see Figure A.17 in the appendix). These trends are visualized in Figure 5.13a and 5.13b.

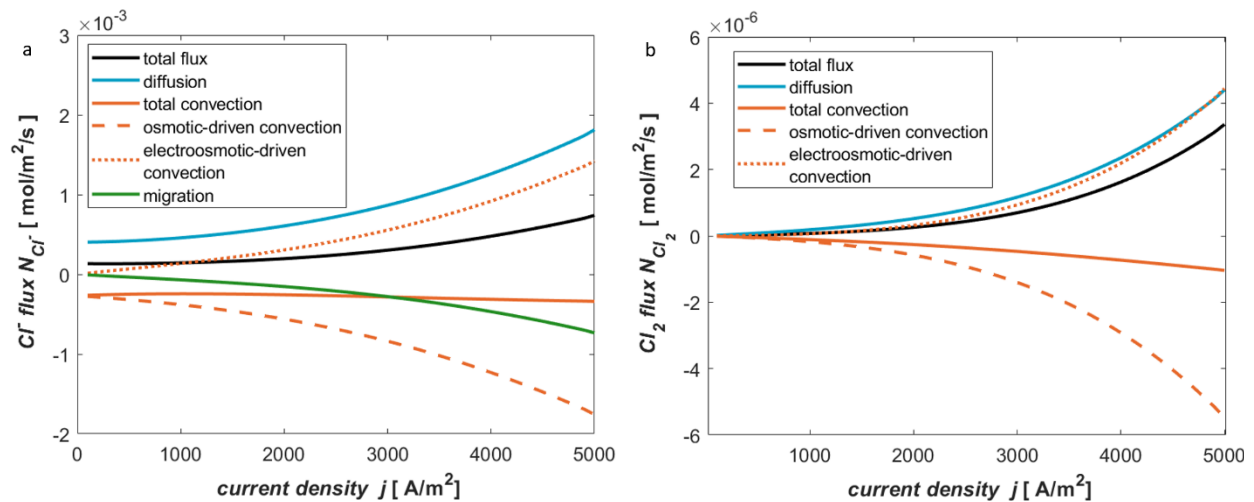


Fig. 5.13, Contributions of diffusion, osmotic-driven convection, electroosmotic-driven convection and migration to the overall flux of a) Cl^- and b) Cl_2 through the membrane in the gas-phase reactor as a function of the current density.

Figure 5.13 shows significant changes of all three flux components with current density. One reason for this is certainly the above mentioned strong current density dependence of the membrane water content. Hence, in Figure 5.14, the crossover of Cl^- and Cl_2 is visualized for three scenarios differing in the RH of the cathode chamber. The reference case is the original simulation depicted in Figure 5.12 and in both other cases, the water content on the membrane/cathode (M|cCL) interface was increased or decreased by a value of 2 respectively.

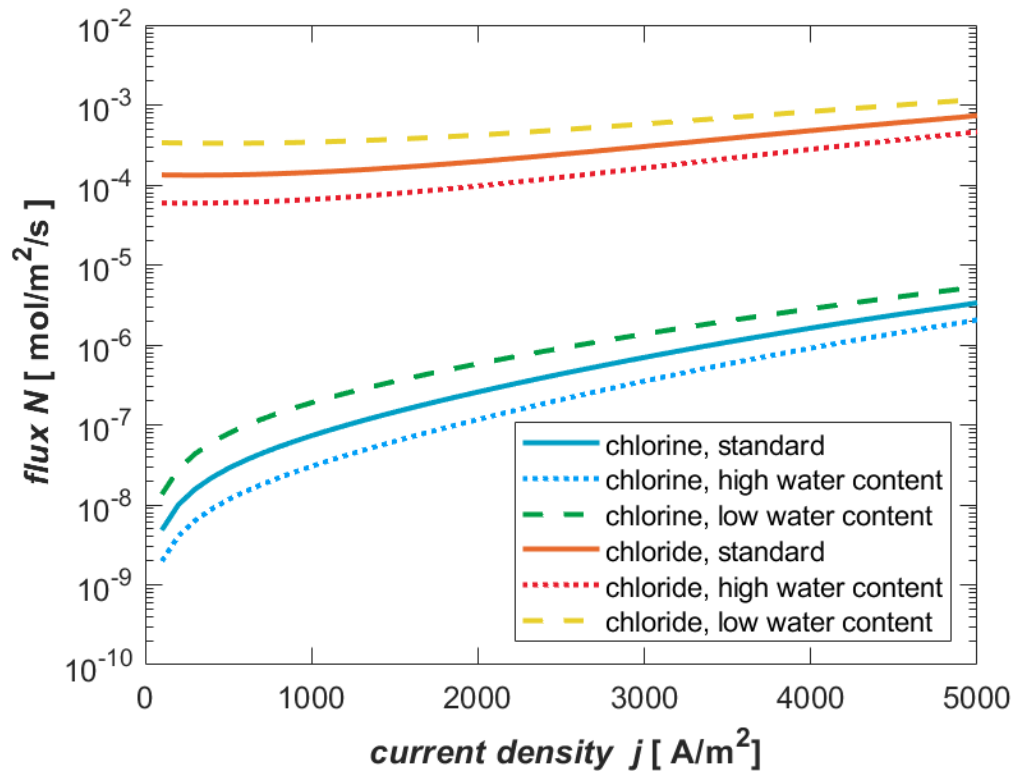


Fig. 5.14, Fluxes of Cl^- and Cl_2 through the membrane in the gas-phase reactor as a function of the current density for three different water contents at the M|cCL interface.

Increasing the M|cCL water content leads to a decrease in the Cl^- and Cl_2 flux over the entire current-density interval. The reason for this effect is the increase in the osmotic driven convection with rising water activity in the cathode department, resulting in higher water activity gradients across the membrane. Also, the migration component grows with increasing humidity. These effects dominate over the increased diffusive flux of both species that comes hand in hand with a higher water content leading to the observed reduction in the overall Cl^- and Cl_2 flux with higher RH. Hence, to minimize crossover in an industrial application of the gas-phase electrolysis, it

would be beneficial to operate at high cathode RHs, e.g. by sufficiently humidifying the oxygen feed and controlling the reactor temperature.

Lastly, since there is significant uncertainty in the diffusion coefficients of HCl and Cl₂ in Nafion, Figure 5.15 displays the crossover flux of both species as a function of their effective diffusion coefficients at a fixed current density of 1000 A/m² to evaluate the sensitivity of the above discussed insights on the accuracy of the diffusion coefficients. It is clear that even if the diffusion coefficient of HCl_(aq) was by an order of magnitude smaller, there would still be significant chloride ion crossover of 10⁻⁴ - 10⁻⁵ mol/m²/s, again enough to impede the ORR activity of platinum, considering the small volume of the cCL and the accumulation of chloride species therein. Secondly, even in this scenario the chloride ion flux would still dominate over the Cl₂ flux, so that the main conclusion of a significant and dominant HCl_(aq) crossover very likely remains valid, despite the uncertainties in the diffusion coefficients.

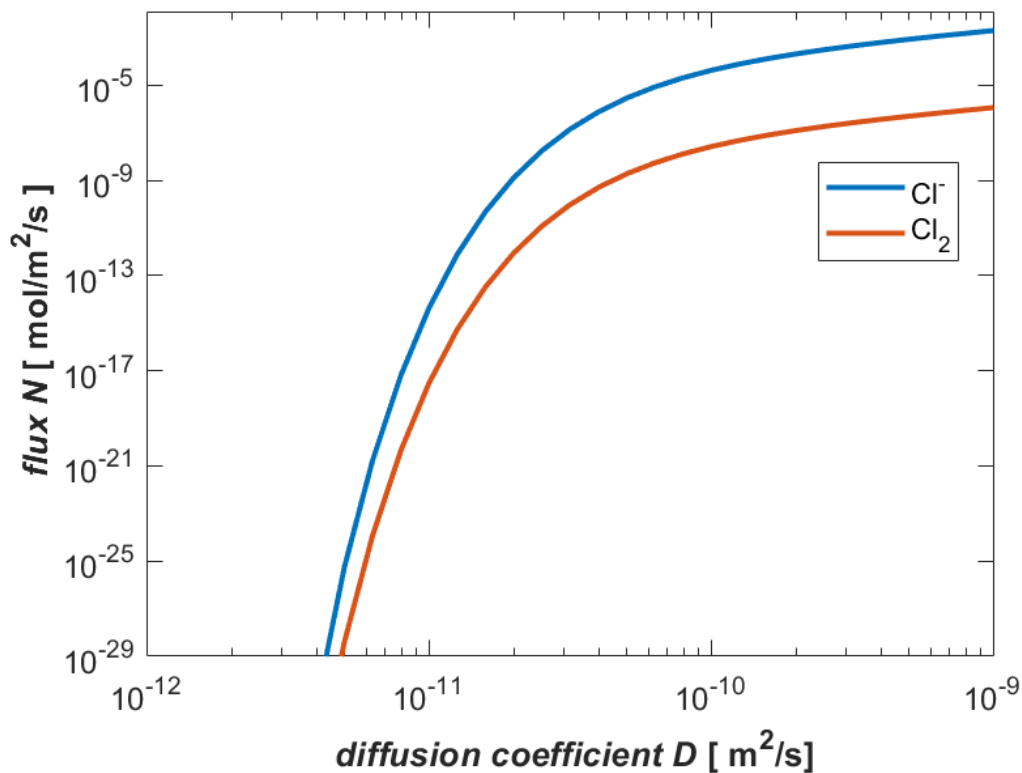


Fig. 5.15, Fluxes of Cl⁻ and Cl₂ through the membrane in the gas-phase reactor as a function of the effective diffusion coefficients of both species in the Nafion membrane.

5.2.3 Summary of the crossover investigations

The hypothesis that HCl and Cl₂ crossover is causing the reduced ORR performance in the experiments of Kuwertz *et al.* (2013) is now proven with sufficient certainty by means of experimental investigations and a numerical crossover model. It was furthermore shown that crossover occurs to an even larger extent in the half-cell setup closely resembling the Bayer UHDENORA liquid-phase reactor and that catalyst poisoning manifests within minutes of operation. In both reactor types, the simulations suggest that the flux of HCl_(aq) through the membrane dominates over the one of Cl₂ under all investigated operating conditions, mostly due to the significant differences in the concentration of both species in the anode chamber. Moreover, the simulations show that crossover in the full-cell setup can be reduced by operation at lower current densities and increased cathode humidification, while in the liquid-phase reactor, operation at higher current densities proved to be beneficial. Alternative methods to reduce crossover would be the use of thicker membranes or different ionomers, which would however affect the ohmic resistance of the membrane and hence the performance of the electrolyzer.

These investigations underline that the use of a different cathode catalyst resistant to chloride ion poisoning is of significant importance for the industrial applicability of the gas-phase electrolysis. Similarly, future investigations should also focus on investigating different anode catalysts, e.g. ruthenium oxide, since not only catalyst poisoning, but also the reduced stability of platinum-based catalysts in the chemically aggressive environment limit the use of platinum in an industrial reactor.

5.3 Investigations of the full-cell setup employing an ODC

After investigating both the HClOR and the ORR separately in the course of chapter 5.1 and 5.2, this chapter discusses additional insights on the full-cell level with a major focus on the limiting behavior observed in the experiments of Kuwertz *et al.* (2013). The main hypothesis is that the water household and the thermal management of the reactor are the major drivers behind the limiting behavior and are hence investigated in depth, discussing theoretical results from the

reactor model introduced in chapter 3.2 validated by own experiments employing the setup explained in chapter 4.2. Please note that major parts of this chapter are extracted from Bechtel *et al.* (2020a).

5.3.1 Simulated polarization data and model-based investigation of the limiting behavior

In the following, simulated polarization curves for temperatures of 313, 323 and 333 K are discussed. As in the experiments of Kuwertz *et al.* (2013), the temperatures refer to the temperature of the reactor feed gas and the reactor coolant. The simulation at 333 K is the one employed in the crossover investigations in chapter 5.2.1.

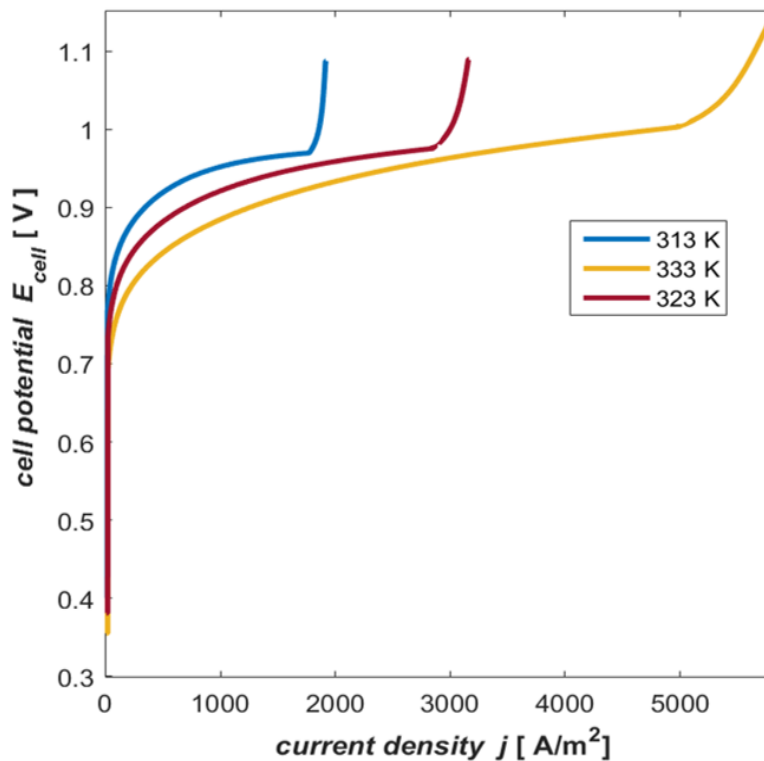


Fig. 5.16, Simulated polarization curves at 313, 323 and 333 K. The slight discontinuities at the onset of the limiting currents are due to the solution switching between a partially saturated and non-saturated state as a consequence of the flooding process, leading to numerical artefacts. Adopted from (Bechtel 2020a).

A qualitative comparison of the simulated polarization curves in Figure 5.16 with the experimental data of Kuwertz *et al.* (2013) shows that their limiting current densities between 4000-5000 A/m² are reproduced by the model, even though the range of 2000-5700 A/m² is wider in the simulations. Furthermore, the sequence in the values of the limiting current densities for the three investigated temperatures is different in the experiments of Kuwertz *et al.* (2013), with the 333 K experiment displaying the lowest and the 313 K case displaying the highest limiting current density. There are two explanations for this, both being discussed at the end of chapter 5.3.2 after gaining a better understanding about the water and thermal management of the cell in the following. Other, more general factors contributing to such quantitative differences certainly are the use of literature values for most model parameters, the assumption of a one-dimensional reactor, which neglects reactant depletion and water accumulation along the channel, and the use of a lumped energy balance, as explained in more detail in chapter 5.3.3.

Another common phenomena in both the simulated and experimental polarization curves is the reduced slope in the ohmic regime at 313 and 323 K compared to a markedly steeper slope at 333 K. The limiting current onset however, is less abrupt and steep in the 333 K simulation. The origin of these phenomena becomes clear when looking at the water content in the aCL and cCL as a function of the current density for the lowest and highest investigated temperature as depicted in Figure 5.17.

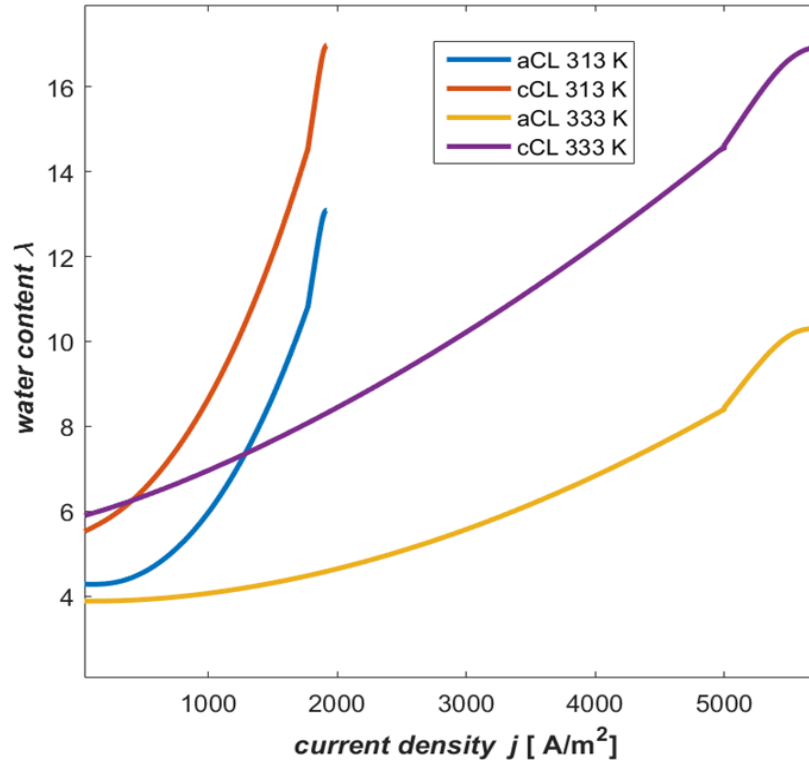


Fig. 5.17, Water content in the aCL and cCL at 313 K and 333 K as function of the current density. Adopted from (Bechtel 2020a).

The water content in the aCL and cCL at both temperatures is increasing with current density, reaching a value of 14 on the cathode side, at which water condensation is initiated, and then going up to a value of 17 corresponding to full saturation and flooding of the cCL. Hence, the first major conclusion to be drawn is that the limiting current densities at all simulated temperatures are caused by flooding and hence blocking of the reaction sites in the cCL. The differences between the water contents in the aCL and cCL, and hence the gradient within the membrane in between both catalyst layers, is more strongly pronounced in the 333 K case compared to the 313 K case, while the cCL is well humidified in both cases. The reason for the lower aCL water content in the 333 K case is the higher saturation pressure of water, which leads to a larger driving force for the evaporation of water out of the membrane and aCL into the aGDL. Due to this driving force, more water is being transported into the anode compartment leading to a higher concentration gradient within the membrane. As soon as water starts to condensate in the cCL, λ_{cCL} surpasses the gas-phase equilibrium value of 14, and the water crossover increases further. This becomes obvious when looking at the molar flow rate v_{H_2O} of water crossing over from the cathode to the anode considering the diffusive flux as well as the osmotic drag depicted in Figure 5.18 as a function of

the current density for the 313 and 333 K simulation. The crossover at the onset of the limiting behavior is almost 3 times higher in the 333 K simulation than in 313 K simulation for the above discussed reasons.

As a consequence, more water emerging from the electrochemical reaction, and hence a higher current density, is necessary to compensate for the crossed over fraction, so that the flooding process is stretched over a wider current-density interval at higher reactor temperatures, explaining the above discussed phenomena of a slower onset in the limiting behavior at 333 K in comparison to the 313 K case in Figure 5.16.

The markedly higher membrane humidification levels and lower gradients in the water content in the 313 K simulation also lead to a decrease in the ohmic resistance of the membrane according to equation 3.28, explaining why the potential remains almost constant despite increasing current densities within the ohmic regime of both the simulation results and the experimental data of Kuwertz *et al.* (2013) at a temperature of 313 K.

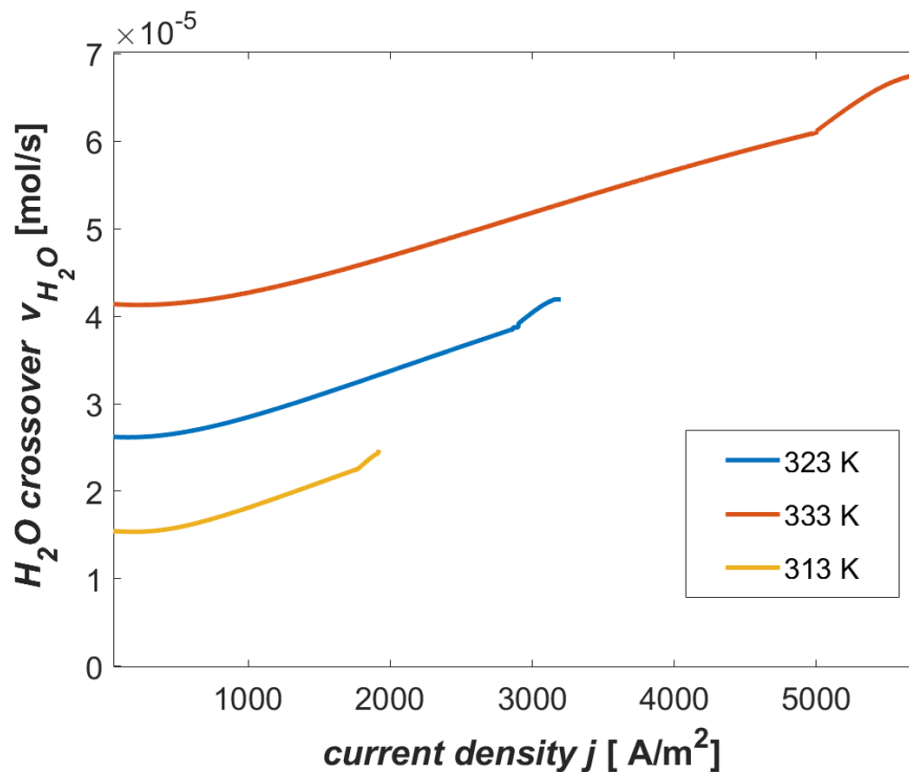


Fig. 5.18, Molar flowrate of water through the membrane as a function of the current density for the 313, 323 and 333 K simulation. Adopted from (Bechtel 2020a).

These results illustrate that even when flooding is causing the observed limiting behavior, the membrane humidification, being strongly influenced by the thermal management of the cell, still has a significant impact on the reactor performance. The significant impact of this insight on the feasibility of a technical application becomes clear, when comparing the cell potentials in the experiments of Kuwertz *et al.* (2013) in the ohmic regime at a current density of 3000 A/m^2 for 313 K and 333 K. Following a similar calculation as carried out in chapter 2.3 and 5.1.5, the difference of about 300 mV in the cell potential at these two temperatures would correspond to annual savings of more than 6 million Euro in an industrial application of the HCl gas-phase electrolysis within the MDI production site in Antwerp. At higher current densities than 3000 A/m^2 , the potential differences and hence the impact on the operating costs increase even further. This underlines the importance of understanding the physical mechanisms involved in the above discussed phenomena.

5.3.2 The role of thermal management

As discussed above, the thermal management plays a significant role in the performance of the gas-phase reactor. For this reason, and to assess the sensitivity of the reactor performance on its temperature in general, Figure 5.19 displays the same polarization curves as Figure 5.16, but now with an increased thermal resistance of $R = 0.8 \text{ K/W}$ compared to the standard resistance of 0.294 K/W given in table 3.3. At this value, the cause of the limiting behavior in the 313 K simulation remains flooding of the cCL, although, as the slower onset in the limiting current indicates, it is on the verge to switch towards membrane dehydration. Furthermore, the limiting current density of 4000 A/m^2 is now almost identical to the experimentally determined one from the work of Kuwertz *et al.* (2013). At temperatures of 333 K and beyond, already a 30% increase in the thermal resistance compared to the standard value given in table 3.3 leads to dehydration of the membrane, which is even stronger pronounced at the here investigated thermal resistance of 0.8 K/W , as can be seen in the polarization curve by the steeper slope in the ohmic regime and the sharp onset of the limiting current as a consequence of the water content in the membrane falling below the percolation threshold.

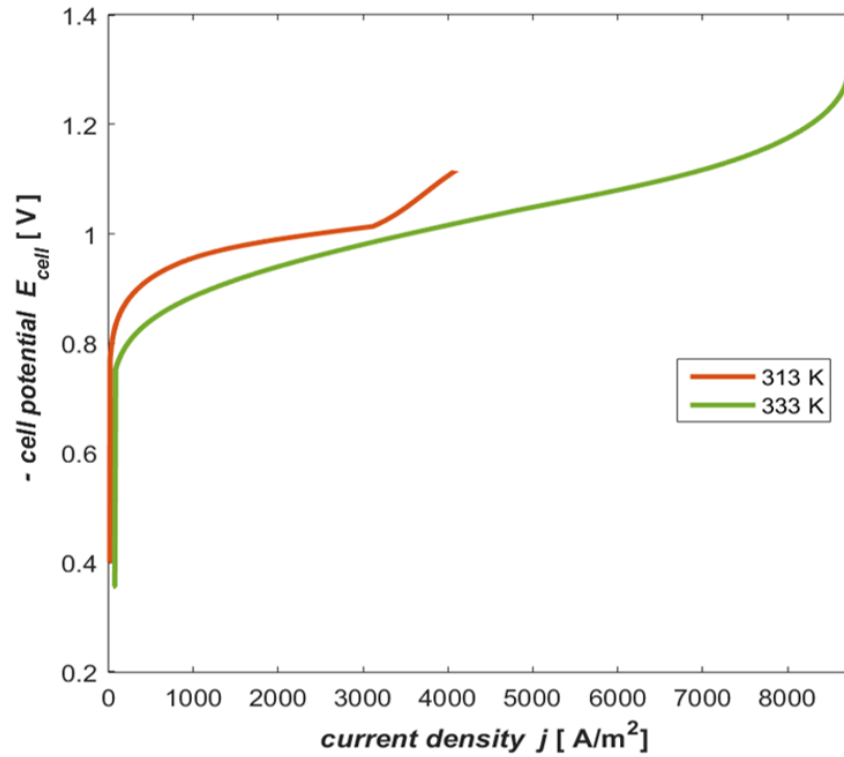


Fig. 5.19, Polarization curves employing a thermal resistance of 0.8 K/W and temperatures of 313 and 333 K. Adopted from (Bechtel 2020a).

The membrane dehydration in the 333 K simulation is confirmed in Figure 5.20, where the anode and cathode overpotential as well as the potential loss in the membrane are depicted as a function of the current density. While the cathode potential remains almost constant, η_A and ϕ_M are increasing sharply at the limiting current density, since the low water content reduces the ECSA and $HCl_{(aq)}$ concentration in the aCL as well as the proton conductivity in the membrane drastically.

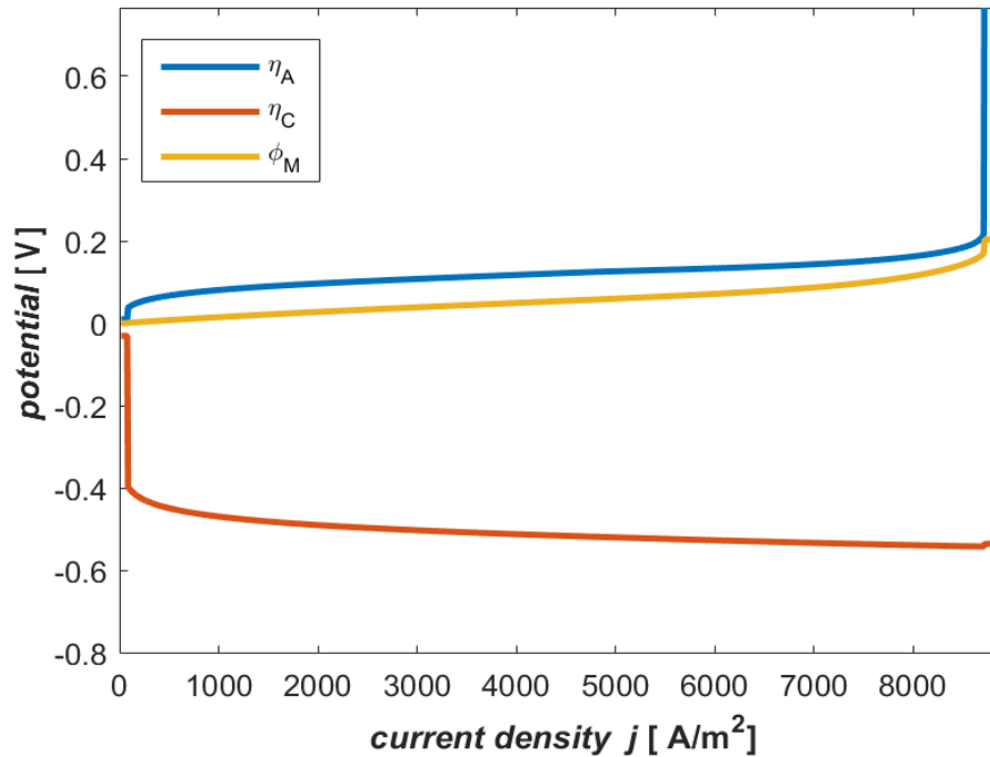


Fig. 5.20, Anode and cathode overpotential as well as the potential loss in the membrane as a function of the current density for the 313 and 333 K simulation employing a thermal resistance of 0.8 K/W. Adopted from (Bechtel 2020a).

Similar conclusions can be drawn from Figure 5.21a where again the water contents in the aCL and cCL are depicted as a function of current density, and from Figure 5.21b, displaying the reactor temperature over the investigated current-density interval. After an initial increase in the water content due to the electrochemical production rate of water increasing with the current density, the above-mentioned effect of a higher crossover due to the saturation pressure rising with temperature overcomes the hydrating effect of the ORR and eventually dehydrates the membrane. Moreover, the so caused increase in the membrane potential losses and the anode overpotential due to the reduced ECSA and hydrochloric acid concentration in the aCL in turn raises the reactor temperature, further accelerating the dehydration in an autocatalytic fashion. This explains the significant temperature increase in the 333 K simulation in Figure 5.21b. In contrast, at a lower temperature of 313 K, where flooding remains the cause for the limiting behavior at an increased thermal resistance of 0.8 K/W and only intermediate current densities of ca. 4000 A/m² are reached, the difference between the feed temperature and the reactor temperature is significantly smaller, not exceeding 17 K. More so, for the standard thermal resistance the reactor temperature

changes only by a 2 K in the 313 K simulation and by 7 K in the 333 K simulation over the whole current-density interval.

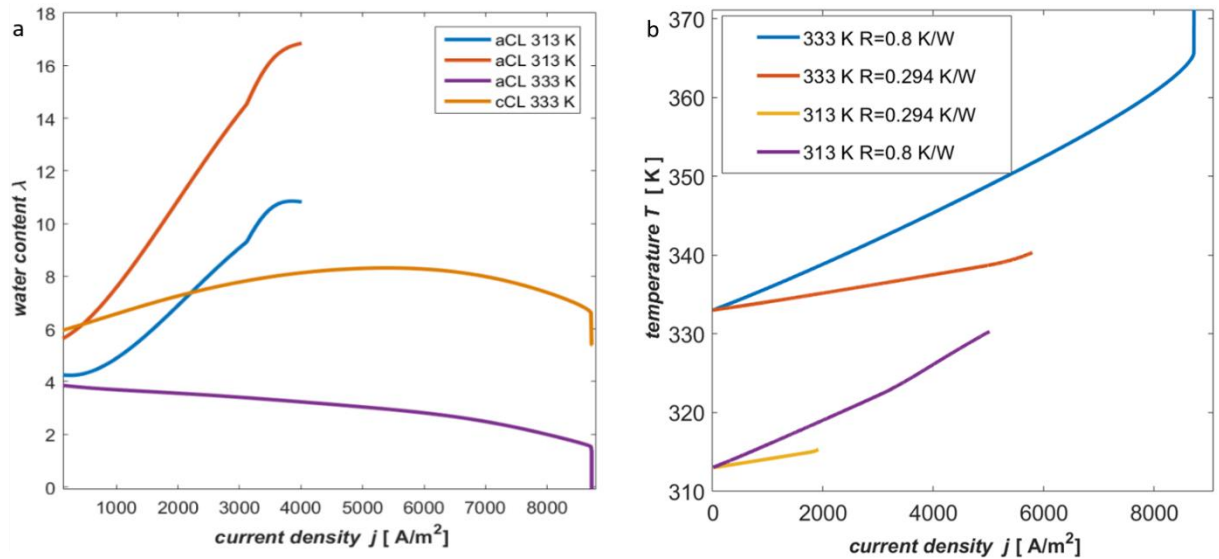


Fig. 5.21, aCL and cCL water content employing an increased thermal resistance of 0.8 K/W a), and reactor temperature for the standard and the increased thermal resistance b), both for the 313 and 333 K simulation as a function of the current density. Adopted from (Bechtel 2020a).

Hence, already slight changes in the structural parameters or operating conditions of the cell can lead to a different physical mechanism causing the observed limiting behavior, especially at operating temperatures of 333 K and beyond. Therefore, while the model reveals that flooding is the cause at all three investigated temperatures when employing the standard thermal resistance, already an underestimation of the real thermal conductivity of 30% could mean that in the experiments of Kuwertz *et al.* (2013), the limiting cause at a reactor temperature of 333 K is not flooding but membrane dehydration. Such an underestimation of the thermal resistance in the numerical model would explain the shift of the limiting current density to lower values in the 313 and 323 K simulation compared to the measurements of Kuwertz *et al.* (2013), since the increased heat accumulation in the experiments would postpone flooding to higher current densities. In the 333 K case, an increased thermal resistance would quickly lead to membrane dehydration, and if the temperature increase is high enough, this could occur already at intermediate current densities. Furthermore, this would explain the significantly increased slope in the ohmic regime in the measurements of Kuwertz *et al.* (2013) at 333 K. The real thermal resistance being significantly

greater than 0.8 K/W, is hence a possible explanation for why the sequence in the limiting current densities in the experiment is different than the one in the here presented simulations.

The second possible explanation is based on the fact that the presented model only considers heat transfer to the coolant but not the environment. Especially for the simulations at higher feed and reactor temperatures, this component of the heat transfer becomes more important as the temperature gradient between the reactor and the environment increases. Hence, neglecting the heat transfer towards the surrounding air could result in an underestimation of the heat transfer in the 333 K simulation, especially at higher current densities and hence reactor temperatures.

Since the cathode feed has a RH of essentially 100% in the simulation and the experiments of Kuwertz *et al.* (2013), the faster than expected heat removal in the could lead to flooding already at lower current densities in the 333 K experiment, where the heat transfer to the surrounding air would be particularly dominant. This is another possible explanation for the limiting current densities being lower in the experiment compared to the simulation in the 333 K case, while they are higher for the 313 and 323 K case, where heat transfer to the environment is less dominant. As underlined in Figure 5.17, the increased saturation pressure of water at a temperature of 333 K leads to a steeper slope in the ohmic regime even when the membrane is sufficiently hydrated. Hence, also in the case of an overestimated heat dissipation in the 333 K case, one would expect an increased slope in the ohmic regime compared to simulations at 313 and 323 K. Hence, also the observed slopes in the ohmic regime can be explained based on this second hypothesis.

This underscores the importance of not only the thermal management of the cell but also the availability of accurate geometrical data on the experimental reactor, since only then a clear discrimination of the physicochemical phenomena is possible. Hence, in future investigations, these simulations should be repeated for a completely characterized setup like the one introduced in chapter 4.2, which would however require experiments at several reactor temperatures. For now it can be summarized that at low reactor temperatures of up to 313 K, flooding is certain to be at cause for the limiting behavior observed in the experiments of Kuwertz *et al.* (2013) while at higher temperatures already small changes in the thermal resistance of the reactor lead to a transition from flooding to membrane dehydration, making an exact prediction of the cause of the limiting behavior difficult due to the lack of precise values for certain geometrical parameters of the reactor.

5.3.3 Outlook on reactor optimization strategies

In an industrial application of the gas-phase electrolysis of HCl, operation at higher current densities than the so far experimentally achieved ones is essential and would translate into significant material and hence financial savings as well as a reduction of the environmental impact of such a process. For this reason, the insights on the physical mechanisms discussed in the previous chapters are utilized in the following to derive various strategies on how to control the reactor humidification and temperature in a way that both flooding and membrane dehydration are postponed and the limiting behavior is shifted to significantly higher current densities.

As shown before, especially at higher temperatures, the significant water concentration gradients in the membrane can impede the overall reactor performance up to the point where the water content in the membrane falls below the percolation threshold, leading to a limiting current. Hence, it seems to be promising to employ thinner membranes that allow for more water crossover into the anode compartment. Moreover, this also mitigates flooding of the cCL due to a more effective water removal and is expected to reduce the overall cell potential due to a lower ohmic drop in the membrane as well as an increased ECSA and chloride ion concentration in the aCL. These considerations are confirmed by simulation results displayed in Figure 5.22, where the polarization curve for a standard Nafion 117 membrane, as already depicted in Figure 5.16, is compared to two further polarization curves employing membranes with a thickness of 80 and 100 μm , all at a temperature of 333 K.

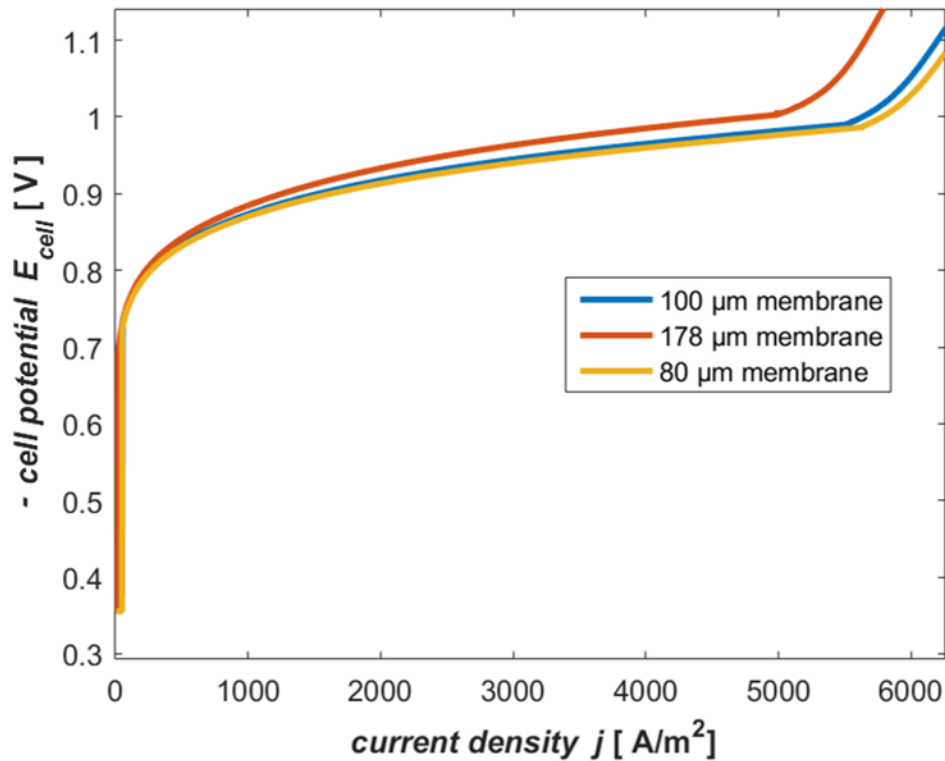


Fig. 5.22, Polarization curves for three different membrane thicknesses at 333 K, employing the standard thermal resistance. Adopted from (Bechtel 2020a).

The thinnest membrane leads to a shift in the onset of the limiting current by ca. 700 A/m^2 and to slightly lower cell potentials over the whole current-density interval compared to the standard Nafion 117 membrane. These findings are in good agreement with theoretical and experimental insights in the field of classical PEM fuel cells stating that thinner membranes lead to a better water management (Stanic 2003, Springer 1992). As both Stanic *et al.* (2003) as well as Springer *et al.* (1991) showed, a thinner membrane can indeed significantly increase the limiting current density by avoiding flooding of the cCL as well as dehydration of the membrane.

As can be extracted from Figure 5.21, both simulations with $100 \mu\text{m}$ and $80 \mu\text{m}$ membranes exhibit very similar limiting currents. The effect of the membrane thickness seems to become less and less relevant below $100 \mu\text{m}$, since the water saturation level on the anode and cathode side of the membrane become very similar, so that a further reduction only slightly shifts the flooding of the cCL towards higher current densities. It should be noted however, that in scenarios where membrane dehydration becomes the limiting cause, a further reduction in the membrane thickness below $80 \mu\text{m}$ is expected to lead to more substantial increases in the limiting current densities, in

agreement with the above cited literature on classical hydrogen PEM fuel cells. However, as explained below, reducing the membrane thickness beyond a certain degree is not recommended in the specific case of the HCl electrolysis, especially with the catalyst system employed by Kuwertz *et al.* (2013) and Martínez (2015).

Besides the risk of a reduced durability (Ji 2009), thinner membranes facilitate water crossover, which is undesired in the sense that the anode outlet stream should be as dry as possible to allow for a more efficient product purification and HCl recycling (please see chapter 2). The aspect of the mechanical stability of the membrane becomes especially critical when considering that the active area per cell is 2.5 m² in the Bayer UHDENORA process (Thyssenkrupp 2012), which is significantly larger than in classical hydrogen PEM fuel cell applications due to the enormous amounts of HCl being recycled within industrial processes like the polyurethane production. Due to the presence of liquid hydrochloric acid in the anode chamber of the Bayer UHDENORA process, uniform hydration of the membrane is easier to facilitate than in the here proposed gas-phase variant, so that additional mechanical stress on the membrane is to be expected in the gas-phase electrolyzer, likely rendering very thin membranes technically unfeasible. Lastly, thinner membranes facilitate the crossover of HCl and Cl₂, poisoning the platinum catalyst employed by Kuwertz *et al.* (2013) and Martínez (2015) as shown in chapter 5.2.

Taking all these aspects into consideration, the exploration of additional, alternative methods to increase the limiting current density, while keeping the crossover of HCl, H₂O and Cl₂ to a minimum, appears to be sensible. This becomes especially clear when considering that in most hydrogen PEM fuel cell studies current densities of more than 10000 A/m² can easily be reached even with classical Nafion 117 membranes, which stands in strong contrast to the experimentally observed maximum values of ca. 4000 - 5000 A/m² in the work of Kuwertz *et al.* (2013) and even the slightly higher limiting current densities in the here presented simulations. Reasons for this are the ability to humidify the anode in H₂ PEM fuel cells, which is not feasible in the case of the HCl electrolysis due to the imminent formation of aqueous hydrochloric acid, the strongly exothermic dissociation of HCl in the aCL of the electrolyzer, as well as the overpotential, which is almost two times higher than in classical H₂ PEM fuel cells. All in all, this leads to a significantly more sensitive and complex heat management problem in the HCl gas-phase reactor. For these reasons,

alternative methods for increasing the limiting current density based on an efficient water and thermal management are discussed in the following.

As can be extracted from a comparison of Figure 5.19 and Figure 5.16, the increase in the thermal resistance to a value of 0.8 K/W led to a markedly higher limiting current density in the 333 K simulation, which was then caused by membrane dehydration instead of flooding. If one imposes a current density dependent thermal resistance, flooding can be avoided at low current densities by means of a higher thermal resistance and dehydration of the membrane can be postponed by subsequently decreasing the resistance at higher current densities. Figure 5.23 shows the polarization curve simulated at a temperature of 333 K with a thermal resistance of 0.8 K/W, which is already depicted in Figure 5.19, in comparison to a polarization curve obtained under the exact same conditions with the exception of a modified thermal resistance R_{mod} , now being a function of the current density.

$$R_{mod} = 0.8 \frac{\text{K}}{\text{W}} \text{ for } j \leq 7500 \frac{\text{A}}{\text{m}^2} \quad (5.7)$$

$$R_{mod} = 0.8 - \frac{\left(j - 7500 \frac{\text{A}}{\text{m}^2}\right)}{10300 \frac{\text{AW}}{\text{Km}^2}} \text{ for } j > 7500 \frac{\text{A}}{\text{m}^2} \quad (5.8)$$

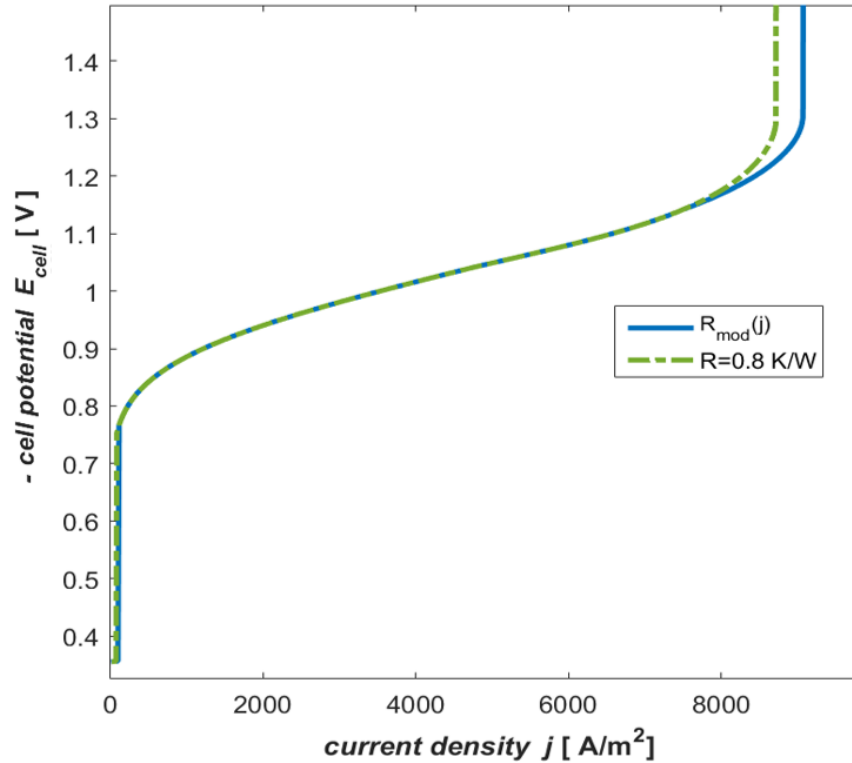


Fig. 5.23, Polarization curves simulated at 333 K with a constant thermal resistance of 0.8 K/W (green dots) and a current density dependent thermal resistance according to equation 5.8 and 5.7 (blue). Adopted from (Bechtel 2020a).

Up to a current density of 7500 A/m^2 , the thermal resistance and hence the polarization curves in both scenarios are identical and flooding, as it occurs at the standard thermal resistance as displayed in Figure 5.16, is again successfully avoided. At higher current densities, the thermal resistance is decreased linearly according to equation 5.8 in order to reduce the reactor temperature and hence mitigate the dehydration of the membrane. In an experimental setup, this could be achieved by controlling the flow rate of the coolant. A more practical alternative to controlling the thermal resistance of the reactor however, would be to control the temperature of the coolant or to define the reactor feed temperature as a function of the current density. Xing et al. (2014) showed for example that increasing the anode feed temperature in a H_2 PEM fuel cell at constant cathode feed temperature lead to a reduction in the cell performance at lower current densities but an increased performance at current densities of more than 4000 A/m^2 .

The difference in the limiting current density as a consequence of the modified thermal resistance is ca. 300 A/m^2 . Fundamentally however, this modified operational mode can be used to reach significantly higher current densities. It has to be considered though that at the reactant flow rates

in the experimental setup of Kuwertz *et al.* (2013), a current density of 10000 A/m² is equivalent to a conversion of 77%. Hence, at these high current densities, mass transfer effects might play a significant role and could possibly limit the current even though flooding and membrane dehydration are successfully avoided.

To prove that it is possible to utilize the insights about the effect of the thermal and water management on the performance of the electrochemical cell to reach significantly higher current densities, the mass transfer effects are circumvented by increasing the anode and cathode feed flow rate by 30% and by reducing the GDL thickness from 400 to 200 μm in the following simulation. This alone does not solve the flooding and dehydration challenge. However, combining the positive effects of a reduced membrane thickness of 120 μm, a tradeoff between higher reactant crossover and increased ohmic losses at very thin or very thick ionomers respectively, and a current density dependent thermal resistance

$$R_{mod} = 0.8 \frac{\text{K}}{\text{W}} \text{ for } j \leq 8000 \frac{\text{A}}{\text{m}^2} \quad (5.9)$$

$$R_{mod} = 0.8 - \frac{\left(i - 8000 \frac{\text{A}}{\text{m}^2}\right)}{15500 \frac{\text{AW}}{\text{Km}^2}} \text{ for } j > 8000 \frac{\text{A}}{\text{m}^2} \quad (5.10)$$

the polarization curve shown in Figure 5.24 can be obtained.

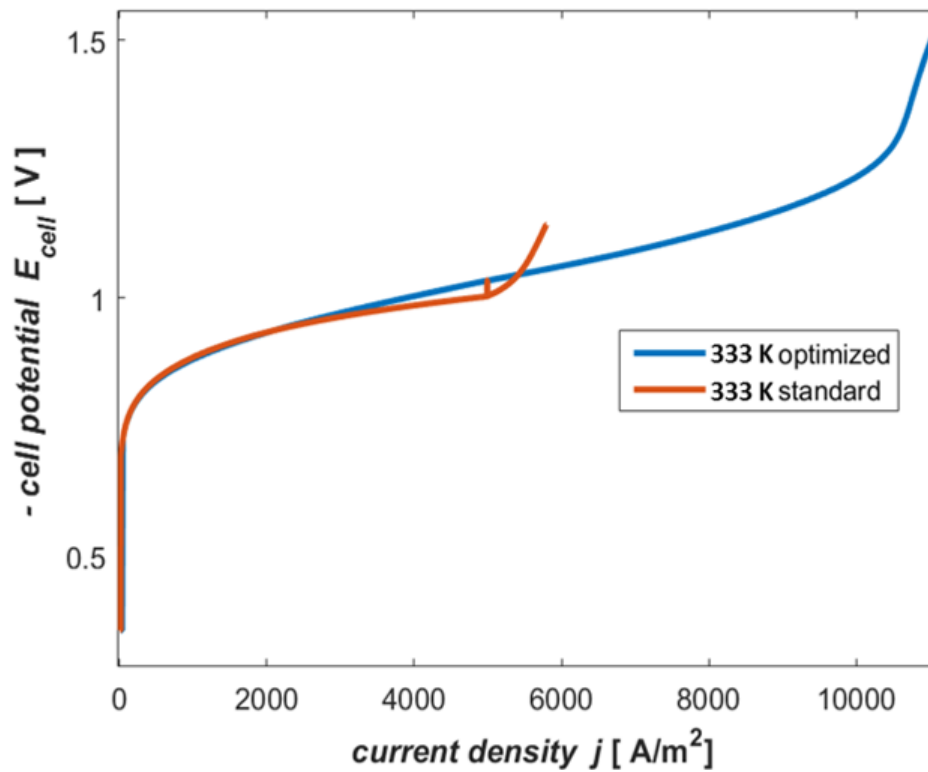


Fig. 5.24, Polarization curves simulated at 333 K with a constant thermal resistance of 0.294 K/W (red) and with a current density dependent thermal resistance according to equation 5.9 and 5.10 as well as a reduced membrane and GDL thickness combined with an increased feed flowrate (blue). Adopted from (Bechtel 2020a).

The limiting current is now more than 90% higher than in the simulation with the standard thermal resistance, which is also included in Figure 5.24 for reasons of comparability. Interestingly, neither flooding nor membrane dehydration is now at cause for the limiting behavior at ca. 11000 A/m² but rather a third mechanism; the kinetic limitation of the HClOR as discussed in detail in chapter 5.1.

This becomes clear when looking at the anode overpotential and the membrane potential losses in Figure 5.25 compared to Figure 5.20, where membrane dehydration was shown to cause the limiting behavior.

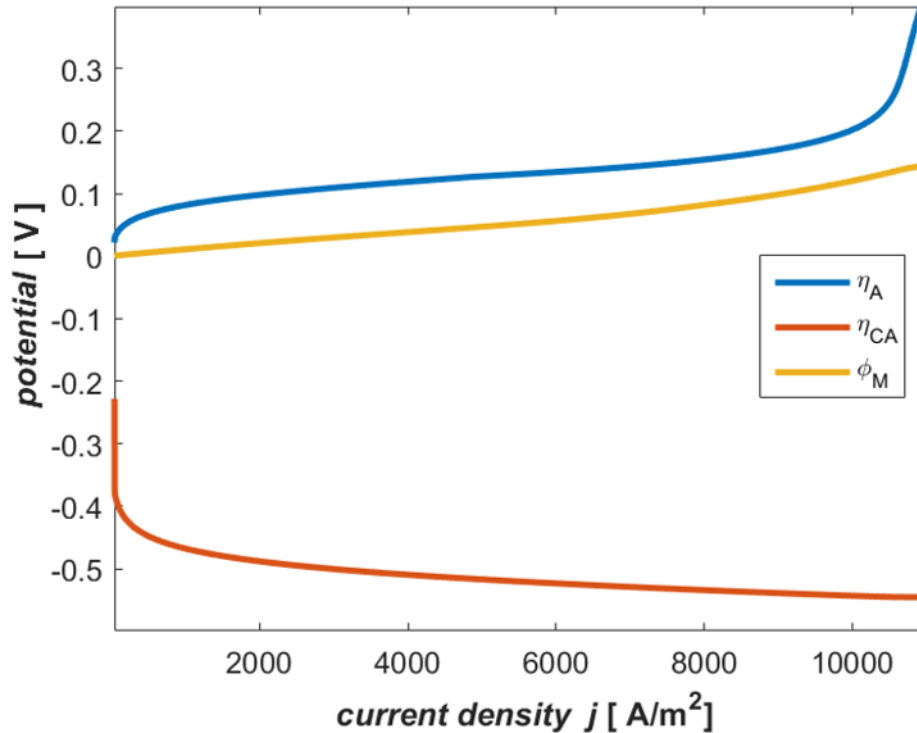


Fig. 5.25, Anode and cathode overpotentials as well as the potential loss in the membrane as a function of the current density for the simulation at 333 K employing the optimized reactor operation strategy. Adopted from (Bechtel 2020a).

The membrane potential now does not exceed 150 mV and is significantly smaller than the anode overpotential that becomes dominant at a current density of 10500 A/m². Furthermore, the cathode overpotential remains almost constant at these high current densities, underlining that also flooding is successfully avoided. The strong increase in the anode overpotential is caused by the surface coverage of the anode catalyst reaching its saturation value, as can be extracted from Figure 5.26 and as it was already shown to be the case in the half-cell simulations of the HClOR in chapter 5.1 (please see Fig. 5.2).

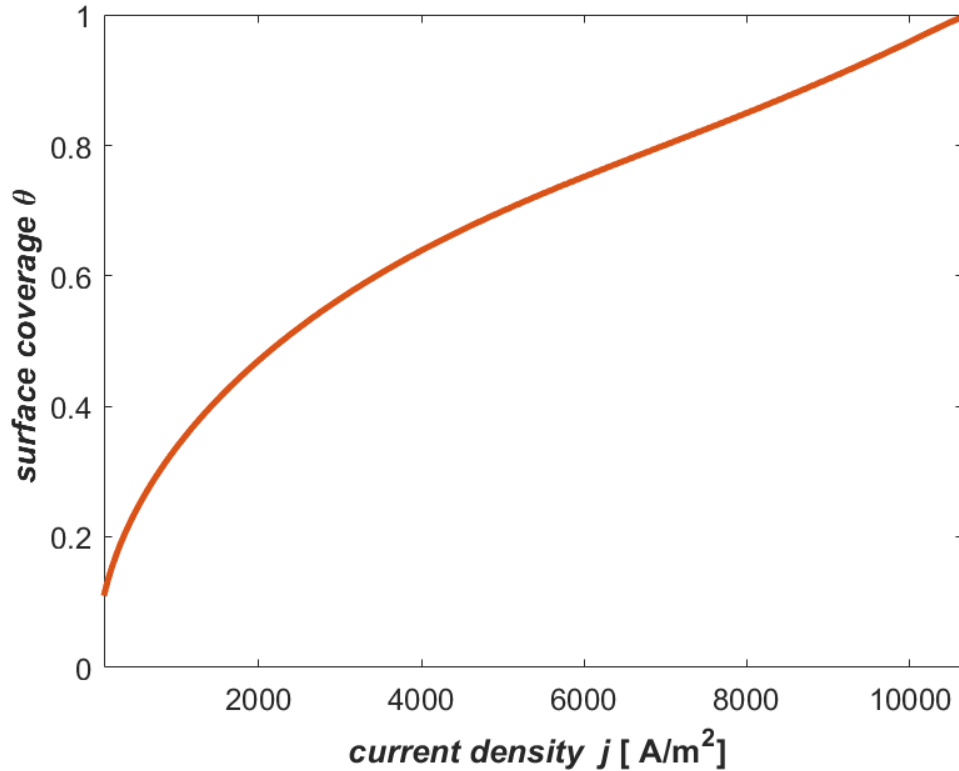


Fig. 5.26, Catalyst surface coverage as a function of the current density for the simulation at 333 K employing the optimized reactor operation strategy. Adopted from (Bechtel 2020a).

At this point, higher overpotentials do not accelerate the reaction any further because the purely chemical Tafel step in the microkinetic reaction mechanism of the HClOR is limiting the overall reaction rate. While at current densities below $10000 A/m^2$ membrane dehydration and flooding of the cCL are the main concern for the overall reactor performance, the kinetic limitation of the HClOR, which so far has only been observed in the half-cell experiments of Martínez (2015) but not the full-cell investigations by Kuwertz *et al.* (2013) due to the low experimentally achieved current densities, does become relevant at higher current densities. As shown in chapter 5.1.5, this can be mitigated by an increase in the catalyst loading so that theoretically even higher current densities than the ones reached in Figure 5.24 can be achieved. This final investigation highlights that under certain conditions not only structural and operational aspects that directly concern the water and energy balance of the full cell, but also the catalyst structure of the aCL have to be considered to avoid a kinetic limitation of the HClOR.

Please note that the reaction limited current density in the experiments of Martínez (2015) at a reactor temperature of 333 K is lower (ca. $10000 A/m^2$) than the one displayed in Figure 5.24. This

is due to the fact in their experiments, only small increases in the reactor temperature are to be expected (please see chapter 3.2.6). As Figure 5.21 b) shows, this is not the case in the setup of Kuwertz *et al.* (2013), mainly due to the significantly higher conversion and the absence of a liquid electrolyte circulating through the anode chamber. Hence, the elevated reactor temperature leads to an increased rate constant and reaction limited current density of the HClOR.

Lastly, the role of mass transfer at these high current densities is investigated to justify the reduction of the GDL thickness and the increase of the reactant flowrate in the last discussed scenario. Furthermore, this serves to determine, if further measures are necessary to prevent the mass transfer from impeding the reactor performance significantly, when operation at higher current densities than the so far experimentally achieved ones are desired. Figure 5.27 displays the partial pressures of O₂ and HCl over the dimensionless GDL length on the cathode and anode side respectively at a current density of 4000 A/m² and 11000 A/m² for the last simulation employing the optimized reactor operation strategy.

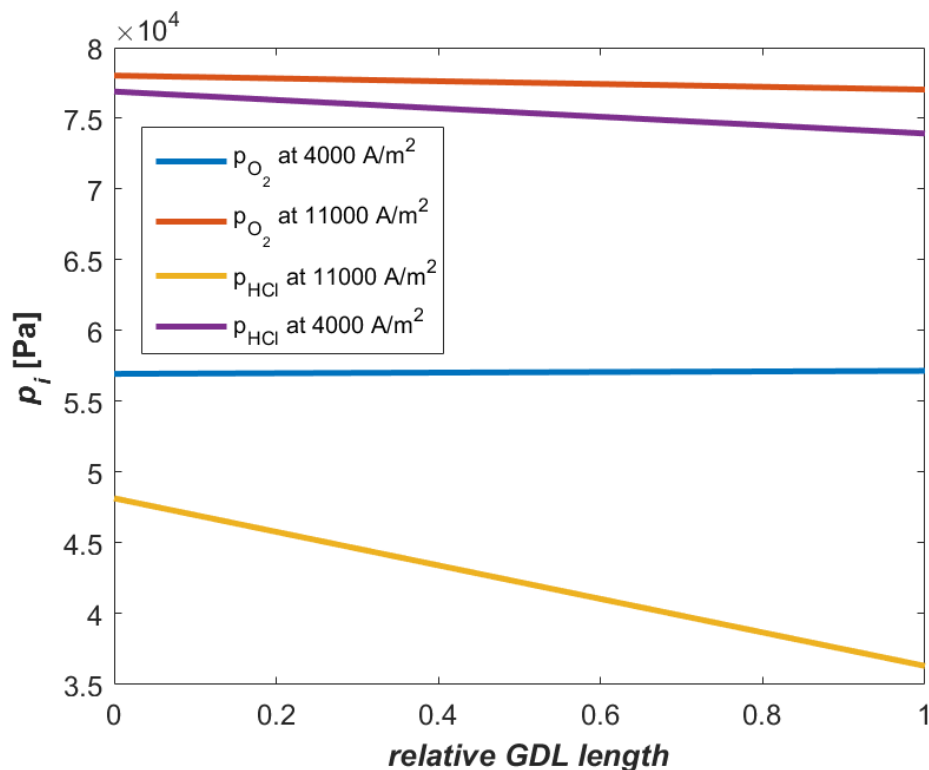


Fig. 5.27, Partial pressures of O₂ and HCl as a function of the relative GDL length at current densities of 4000 and 11000 A/m² for the simulation employing the optimized reactor operation strategy. Adopted from (Bechtel 2020a).

Due to the increased flowrate and the stoichiometry of the reaction, the gradient of the O₂ partial pressure remains negligibly small in both cases. At 4000 A/m² the gradient is even slightly positive, which is due to the total pressure increasing in x-direction (please see Figure 3.1) at low current densities and hence low saturation levels as a consequence of the ORR stoichiometry. At the anode, the gradient of HCl is small at current densities lower than 4000 A/m², which corresponds to the current density range that Kuwertz *et al.* (2013) reached in their experiments. However, at 11000 A/m², mass transfer within the GDL seems to play an important, although not yet limiting, role as can be deduced from the distinct gradient in the HCl partial pressure. Since the anode and cathode feed flow rate were increased by 30% in this simulation, the mass transfer resistance can be expected to be even more significant when employing the standard flow rate. Therefore, while the effect of mass transfer in the GDL is negligible under the conditions in the experiments of Kuwertz *et al.* (2013) with current densities below ca. 4000 A/m², a reduction of the GDL and membrane thickness as well as an adjustment of the reactant flow rates should be considered in future experiments if operation at higher current densities is desired.

Finally, it should be noted that at these high conversions a 1-D model as employed in the present work cannot be quantitatively predictive. The objective of this investigation was to understand the physical mechanisms involved in the phenomena observed in the simulated and experimental polarization curves, how geometrical and operational parameters influence these physical mechanisms and to eventually use that knowledge to propose strategies that allow for operating the reactor at significantly higher current densities than before. For this reason, the focus was laid on a detailed modeling of the physicochemical processes in direction of the sandwich coordinate, as delineated in chapter 3.1. In future work, these qualitative insights can be transformed into more quantitative predictions of the reactor performance by considering the coordinate along the channel and by including a discretized energy balance that is able to account for internal temperature gradients. Since the simulation time at the current resolution and level of detail in regards to the considered physicochemical mechanisms is already up to six hours, and since the focus of this work is not to obtain a best fit to experimental polarization curves, the consideration of 2D and 3D effects is however out of the scope of the present work.

5.3.4 Experimental investigation of the HCl gas-phase electrolysis employing an ODC

In the following, the above discussed insights are validated by experimental investigations using the cyclone full-cell introduced in chapter 4.2. Since the model predicts flooding to be at cause for the limiting behavior at low temperatures, a higher HCl flowrate per cell area than in the experiments of Kuwertz *et al.* (2013) was chosen in the experiments of this work. This leads to higher water concentration gradients between anode and cathode due to fast convective removal of water through the anode outlet stream, which increases the water flux through the membrane and hence aids in removing water from the cathode helping to avoid flooding of the cCL.

Furthermore, no cooling is provided to the reactor to induce a moderate temperature increase in the reactor at higher current densities, which also proved to be beneficial for delaying flooding of the cathode towards higher current densities. Due to the highly insulating material of the cell, an increase in the reactor temperature appears indeed likely. However, because of the small cell area and high reactant flowrates, the temperature increase is not expected to be significant enough to cause membrane dehydration, as it was shown to occur at high reactor temperatures and conversions as well as insufficient cooling in the previous chapter. Furthermore, two different membrane thicknesses were investigated, as a reduction of the membrane thickness was shown to result in higher limiting current densities in chapter 5.3.3. Lastly, since chloride ion poisoning of the platinum based cathode catalyst was proven to occur in chapter 5.2, a Rh_xS_y based catalyst was employed additionally for the first time. Besides validating the numerical model, the experiments hence also serve to investigate whether these adjustments in the flowrate, membrane thickness, thermal management and the catalyst system indeed lead to the predicted increase in the limiting current densities to more than 5000 A/m^2 , as necessary for an industrial application of the process.

Figure 5.28a displays polarization data of two subsequent measurements employing the MEA provided by Clausthal based on Pt/C as a cathode catalyst and a Nafion 117 membrane (please see chapter 4.3), while Figure 5.28b provides the same data for an MEA employing the Rh_xS_y cathode catalyst and a Nafion 1100 membrane. Additionally, Figure 5.28b contains the experimental results from Kuwertz *et al.* (2013), who however used thinner Nafion 117 membranes, for the same temperature as a benchmark.

While the anode catalyst is Pt/C with an identical loading in both cases, the Nafion loading of the MEAs prepared at TU Clausthal is higher. The reason for choosing a higher Nafion loading are insights from the previous chapter suggesting that this has a positive impact on the limiting current density of the HClOR due to an increase in the ECSA. However, at the intermediate current densities investigated in these experiments, the HClOR is far from being reaction limited so that the higher loading can rather be expected to have a slightly negative impact on the cell potential due to an increased mass transfer resistance. Furthermore, the uncertainties in the catalyst loading of the MEAs from TU Clausthal is estimated to be 30% as a consequence of the small active area and the MEA preparation procedure. Both effects offer an explanation as to why the cell potentials in the measurements depicted in Figure 5.28a are higher than the ones in (Kuwertz 2013) even though they have the same platinum and Nafion loading on the cathode side and the same platinum loading on the anode side.

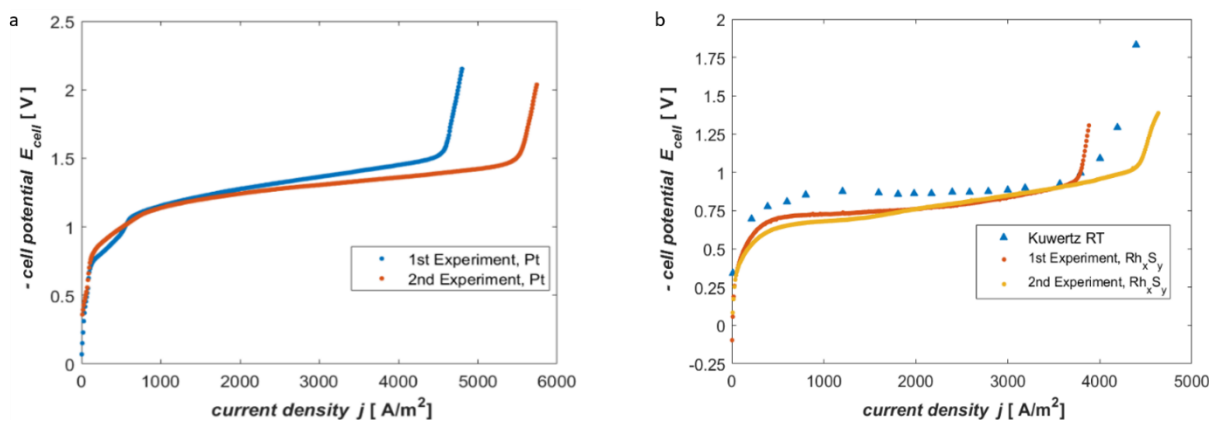


Fig. 5.28, Experimental polarization curves measured at RT employing the platinum based cathode catalyst from TU Clausthal on a Nafion 117 membrane a) and the Rh_xS_y based cathode catalyst by De Nora together with a Nafion 1110 membrane. The anode catalyst is platinum in both cases and the two experiments depicted in each figure are carried out directly after each other.

Three major conclusions can be drawn from Figure 5.28a and 5.28b regarding the performance of Rh_xS_y as a cathode catalyst, the causes of the observed limiting current density and, lastly, the impact of these results on the industrial applicability of the HCl gas-phase electrolysis.

The first conclusion is that the OCV is closer to the thermodynamic value and the kinetic overpotential is significantly lower when employing the Rh_xS_y catalyst. At a current density of 1000 A/m^2 , the cell potential is ca -0.64 V for the Rh_xS_y based MEA, -1.15 V for the Pt based

MEA and -0.83 V in the measurements of Kuwertz *et al.* (2013). Moreover, the absolute OCVs and cell potentials measured with the Rh_xS_y system (second experiment) are lower than any values recorded by Kuwertz *et al.* (2013) up to a current density of 4500 A/m², including their measurements at higher temperatures, despite the fact that the membrane employed in the present Rh_xS_y experiments is 43% thicker, leading to increased ohmic losses. This again confirms the hypothesis of chapter 5.2 that chloride ion poisoning of the cathode catalyst due to HCl and Cl₂ crossover has a significant impact on the ORR kinetics on Pt in the gas-phase electrolysis of HCl. While the performance of Rh_xS_y compared to Pt based catalysts for the ORR in the presence of hydrochloric acid has already been investigated, e.g. by Gullá *et al.* (2007), who employed a rotating disc electrode equipped with both catalysts immersed in hydrochloric acid, this is the first time that the performance of Rh_xS_y as a catalyst material has been experimentally evaluated in the frame of the gas-phase electrolysis of HCl employing an ODC. Interestingly, in the work of Gulla *et al.* (2007), the Pt/C based catalyst performed similar to or even better than the investigated Rh_xS_y catalysts. The results presented in Figure 5.27b however indicate that the Rh_xS_y catalyst clearly outperforms the platinum based one, which is an additional advantage to its higher durability, so that Rh_xS_y seems to be a well-suited system to be employed in an industrial application of HCl gas-phase electrolysis. A detailed comparison of the Rh_xS_y catalyst employed in the present work with the one in literature is not possible as its exact composition and synthesis is confidential.

The second major conclusion concerns the causes of the experimentally observed and simulated limiting behavior and the thermal management of the reactor as discussed in the previous chapter. The two different graphs in Figure 5.28a and 5.28b correspond to measurements taken directly subsequent to each other. The thermal sensors in the oxygen outlet stream showed an increase of ca. 2 K from the start of the first measurement to the end of the second measurement in both cases. Based on the scan rate of 0.5 mA/s and the cell area of 2.27 cm², each measurement takes approximately 40-50 minutes. As a consequence of the high flowrate per cell area in the present experiment and the geometry of the cyclone flow cell as well as the highly insulating materials it is constructed of, temperatures at the MEA can be expected to be even higher than in the cathode reactor outlet stream. The fact that this experimentally observed temperature increase in the second measurements leads to clearly higher limiting current densities for both catalyst systems, supports the hypothesis of flooding as cause for the limiting behavior at low feed temperatures (please see chapter 5.3.1) and the significance of the thermal management as predicted by the numerical

model. More so, comparing the limiting current densities of Figure 5.28a and 5.28b also underlines that decreasing the membrane thickness indeed leads to higher limiting current densities as predicted in chapter 5.3.3, again pointing towards flooding as cause for the limiting behavior. This is confirmed by a last experiment with the same Rh_xS_y catalyst but now employing a Nafion 115 membrane, which again slightly increases the limiting current density as displayed in Figure 5.29.

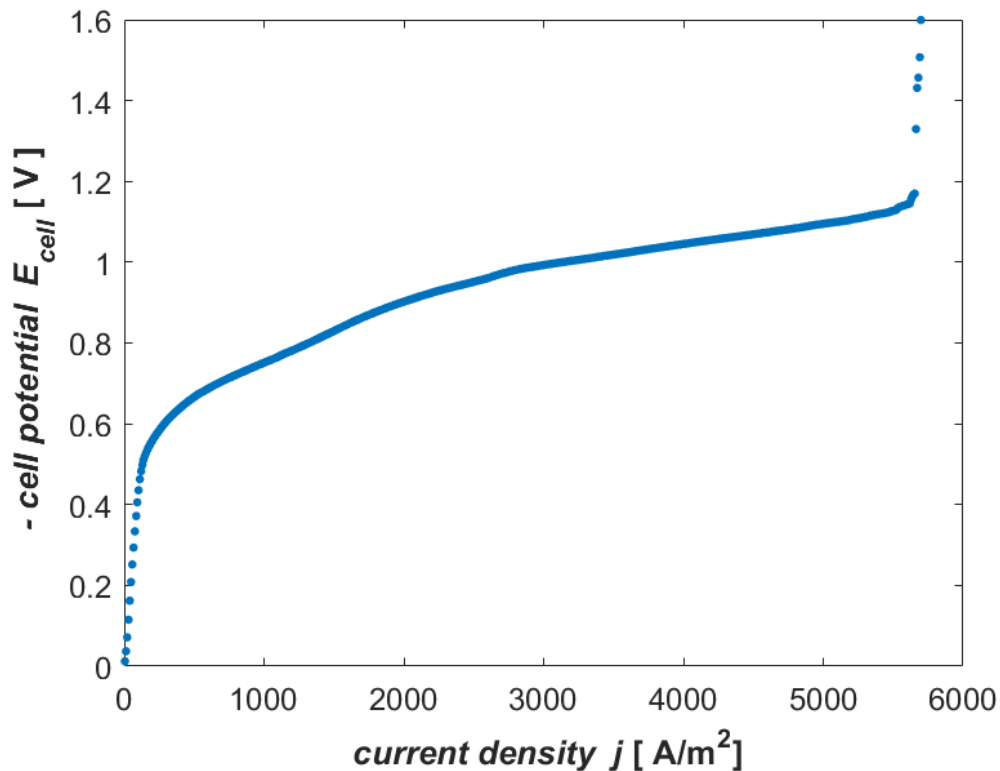


Fig. 5.29, Experimental polarization curves measured at RT employing the Rh_xS_y based cathode catalyst by De Nora and a Nafion 115 membrane.

Please note that in this experiment no second run was performed. Hence, as in Figure 5.28a and 5.28b, a second run would be expected to exhibit even higher current densities due to the increased reactor temperature. Interestingly, the slope in the ohmic regime is markedly steeper than in Figure 5.28b, even though the membrane is thinner. This might be due to the differences in the membrane water content, although before each measurement, the humidified oxygen stream was fed through the cathode chamber of the reactor for ca. 45 minutes to allow for a comparable membrane water uptake.

This leads to the third major conclusion. The limiting current densities in Figure 5.29 and in Figure 5.28a for the second measurement are now 5800 A/m^2 , which not only exceeds the limiting current density of ca. 4300 A/m^2 in the measurements of Kuwertz *et al.* (2013) at room temperature by 33%, but also the ones they measured at higher temperatures. As can be extracted from Figure 5.29, the cell potential at 5000 A/m^2 is 1.09 V, which is ca 300 mV lower than the one of the Bayer UHDENORA liquid-phase reactor at the same current density (Kuwertz 2013, Martínez 2015). It can hence be concluded that the detailed analysis of the physicochemical phenomena occurring in the gas-phase electrolyzer employing the developed numerical model and experimental setup indeed allowed for successfully increasing the limiting current density to an industrially relevant level, while maintaining a significantly lower cell potential compared to the Bayer UHDENORA reactor. This, together with the successful application of a Rh_xS_y based catalyst, is an important step towards the realization of the HCl gas-phase electrolysis on an industrial scale.

While adjustments in the cathode humidification, reactant feed temperatures and other parameters discussed earlier in this work are very likely to further positively affect the performance of the reactor, it should be noted that the cell area in the investigated reactor is comparatively small. In the future, challenges that come with larger cell sizes should hence be tackled by the same combined experimental and theoretical approach, now extending the numerical model to consider 2D and possibly 3D effects complemented by further experimental investigations employing larger reactors.

5.3.5 Summary of the full-cell investigations

In this chapter, simulation results employing the developed 1-D multiphase physics-based model of the HCl gas-phase oxidation were validated with experimental data from Kuwertz *et al.* (2013) and further complimented by own experimental investigations. The analysis of the polarization curves demonstrated that the limiting current densities observed in both simulation and experiment are mainly a consequence of two opposing mechanisms, namely flooding of the cathode catalyst layer and dehydration of the membrane and anode catalyst layer. Which one of these mechanisms dominates, strongly depends on the thermal management of the cell. Based on a qualitative

comparison and analysis of the experimental and simulated polarization curves it can be stated that the likely cause for the limiting behavior in the experiments of Kuwertz *et al.* (2013) is flooding. However, at the highest temperature of 333 K, the effects of membrane dehydration are shown to already significantly impact the reactor performance and slight changes in the operating conditions are able to provoke the dehydration of the membrane under otherwise identical conditions. Hence, due to the lack of precise geometrical data about the reactor employed by Kuwertz *et al.* (2013), a clear discrimination between flooding and membrane dehydration is not possible for the highest investigated temperature of 333 K.

The insights on the physicochemical mechanisms causing the limiting behavior allowed for systematically adjusting operating conditions and geometrical parameters in the reactor model in a way that lead to a simulated increase in the limiting current density by more than 90%. This was achieved by defining the thermal resistance of the reactor as a function of the current density, avoiding both too high humidification levels resulting in flooding and too low humidification levels facilitating membrane dehydration. Interestingly, at the so achieved current densities of more than 10000 A/m², a third phenomenon, the rate determining recombination step of two PtCl species forming chlorine becomes a limiting factor as well, which was so far only observed in the half-cell investigations of the HClOR. Moreover, at these current densities, mass-transfer effects were shown to have a considerable, yet not limiting effect on the reactor performance. In future investigations, the discussed optimizations should therefore come hand in hand with thinner GDLs as well increased anode catalyst loadings to avoid a reaction limitation of the HClOR.

Lastly, various model based predictions were experimentally validated. Also, by adjustments in the operating conditions and the MEA based on the above-mentioned insights, industrially feasible current densities of more than 5000 A/m² at a cell potential of 1.09 V could be achieved for the first time. Both the increase in the limiting current density but also the reduction in the cell potential not only translate into significantly lower operating expenses and investment costs, but also generally enhance the feasibility of the HCl gas-phase oxidation on an industrial scale, which is an important step in making the chlorine industry more energy efficient.

In future investigations, the potential for a more efficient reactor operation should be maximized by a rigorous optimization of the above discussed structural and operational parameters, taking into account possible constraints given by the overall industrial process structure. Furthermore, the

presented model as a basis for this optimization should be extended to include effects like the reactant depletion and water accumulation along the channel, crossover of reactant species and temperature gradients within the reactor, again supported by according experiments employing a larger reactor and higher conversions.

6 Conclusions

The aim of this thesis is to advance the HCl gas-phase electrolysis employing an ODC on its path from a pure reactor concept towards an industrially feasible process and to furthermore gain a deeper understanding of the physical mechanisms occurring within the electrolyzer, which lead to the limiting behaviors as well as the severe performance losses in the ORR observed in the half- and full-cell experiments of the previous literature.

In the first part of the work, three novel processes, based on the gas-phase reactor and three different strategies for the separation of unreacted HCl from the desired product Cl₂ are proposed and benchmarked against the Bayer UHDENORA process by means of an exergy analysis supplied with data from detailed flowsheet simulations of all four processes. In the first of these processes, named ELECTRA-DIST, the separation of these gases is achieved by means of a low-temperature distillation unit, while the second process, ELECTRA-ABS, combines an absorption, extraction and desorption step and the last variant, ELECTRA-IL, is based on the absorption and subsequent desorption of HCl in an ionic liquid.

It is shown that the exergetic advantage of the gas-phase electrolyzer over the state-of-the-art liquid-phase reactor can not only be maintained but even extended on the overall process level and that already intermediate single pass and overall conversions of HCl are exergetically feasible, reducing the complexity of the reactor design and operation.

Since all three novel process variants are shown to be comparably efficient, the selection of a candidate in a real industrial application can be made based on other site-specific criteria, as each of the processes display distinct advantages and disadvantages. The most important decision criteria relate to the humidity of the anode outlet stream of the reactor, the relevance of high conversions, the heat integration within the production site and the availability of a low temperature cooling system.

Lastly, the exergy analysis shows the electrochemical reactor to be responsible for 88-95% of the overall exergy demand in the three process variants. Hence, significant further improvements in the efficiency of these processes can only originate in optimizations of the reactor rather than the separation steps.

Hence, the second part of the work focuses on the electrochemical gas-phase reactor itself. A 1D non-isothermal two-phase agglomerate model with a focus on the rigorous modeling of mass transfer, the HClOR reaction kinetics and the water household is presented.

To allow for a precise modeling of mass transfer, a novel approach for fitting Lennard-Jones parameters, on which the Chapman Enskog equations for calculating the three transport coefficients (binary diffusion coefficients, viscosities and thermal conductivities) rely, is developed and implemented into the numerical reactor model. It is shown that fitting Lennard-Jones parameters towards experimental data of only one transport property, as commonly done in the scientific literature, does not necessarily result in a parameter set that is able to describe all three transport properties with sufficient accuracy as well. Rather it is demonstrated that only fitting towards all three transport properties simultaneously yields a subset of parameters that is able to predict all three transport properties with an accuracy well within the uncertainty of the underlying experimental data. Additionally, a modified Eucken correction for the estimation of thermal conductivities of gases is proposed. Applying the approach to seven industrially relevant gas species shows excellent agreement between calculated and experimental values for all three transport coefficients, clearly outperforming the classical fitting procedure employed in the previous scientific literature. In conclusion, the proposed parameter fitting procedure poses an inexpensive and simple method that can be extended to any gas for which experimental data is available.

The numerical reactor model is furthermore complemented by a model for estimating the crossover of HCl and Cl₂ from the anode to the cathode to shed light on the role of chloride ion poisoning in the poor performance of the ODC employed in the gas-phase reactor. In addition to these two numerical models, an experimental setup is developed allowing for investigations of the HClOR, ORR and the full-cell combining both. This enables a combined theoretical and experimental investigation of the electrochemical reactor with the following major findings.

Firstly, the limiting behavior previously observed in half-cell measurements of the HCl gas-phase oxidation is proven to be a purely kinetic limitation, instead of being induced by slow mass transfer or membrane dehydration as assumed in earlier literature. This kinetic limitation is caused by the purely chemical Tafel step of the Heyrovski-Tafel mechanism eventually becoming rate limiting due to a saturation of the catalyst surface with Cl · species, at which point a further increase in the

cell potential does not accelerate the reaction any further. Based on these insights, the first rate expression for the HClOR able to emulate this limiting behavior is proposed. Building on this, it is concluded that a higher Nafion and catalyst loading in the aCL in an attempt to increase the amount of active sites would be a promising reactor optimization strategy with significant potential for energetic and financial savings in an industrial application of the process.

These insights are experimentally validated by demonstrating that under otherwise identical conditions, the limiting current densities are significantly influenced by the potential history, likely due to the potential dependent competition between chloride adsorption and oxide formation on the platinum catalyst. Lastly, a shoulder is observed in these experimental polarization curves that could be an indication for the presence of at least two $\text{Cl}\cdot$ surface species differing in their adsorption strength and rate constant for the subsequent Tafel step forming Cl_2 . This hypothesis is supported by simulations with the numerical reactor model also showing a comparable shoulder upon adding a second surface species.

The second major finding concerns the crossover of HCl and Cl_2 and its impact on the performance of the ORR. Both, $\text{HCl}_{(\text{aq})}$ and Cl_2 crossover are shown to occur under the conditions of the HCl gas-phase oxidation employing an ODC as well as in the Bayer UHDENORA liquid-phase reactor, by again employing a combined experimental and theoretical approach. Furthermore, the crossover of $\text{HCl}_{(\text{aq})}$ clearly dominates the corresponding Cl_2 flux. More importantly, it is verified that this crossover significantly impedes the ORR on platinum-based catalysts within minutes of operation, explaining the poor performance of the ODC in the previous experimental literature on the HCl gas-phase oxidation and underlining the importance of investigating different catalyst materials for the industrial applicability of this reactor concept. Lastly, simulations indicate that crossover in the gas-phase reactor can be reduced by operation at lower current densities and increased cathode humidification, while in the liquid-phase reactor of the Bayer UHDENORA process, operation at higher current densities is concluded to be beneficial.

The last major findings concern the full-cell setup combining the HClOR and ORR. The numerical reactor model indicates that the limiting behavior observed in previous literature is a consequence of two opposing mechanisms, namely flooding of the cathode catalyst layer and dehydration of the membrane and anode catalyst layer. Which one of these mechanisms dominates, strongly depends on the water and thermal management of the cell. This is due to the highly exothermal

dissociation reaction of HCl in water as well as the overpotential of the reactor, which is markedly higher than in classical H₂ PEM fuel cells, both leading to a significant heat dissipation. For this reason, already slight changes in the operating conditions are able to provoke a change from flooding to membrane dehydration as the cause for the observed limiting behavior under otherwise identical conditions. The insights on the physicochemical mechanisms causing the limiting behavior allow for systematically adjusting operating conditions and geometrical parameters in the reactor model in a way that lead to a simulated increase in the limiting current density by more than 90%. This is mainly achieved by employing a current density depending thermal resistance and therefore avoiding both too high humidification levels resulting in flooding and too low humidification levels facilitating membrane dehydration. It can hence be concluded that isothermal reactor operation is not necessarily desirable, but that the significant heat dissipation should rather be utilized in a controlled manner to allow for enhanced reactor performance.

These insights obtained from the numerical reactor model are validated experimentally. Also, based on the previous learnings on HCl and Cl₂ crossover, a Rh_xSy based cathode catalyst is employed for the first time in the investigation of the HCl gas-phase electrolysis, which leads to significantly lower activation overpotentials. It can be derived that the investigation of alternative catalyst materials is not only crucial from a material-stability point of view, but also leads to an increased reactor performance. By adjusting the operating conditions based on the insights from the reactor simulations, industrially feasible current densities of more than 5000 A/m² at a cell potential of 1.09 V are experimentally achieved for the first time, which is indispensable for an industrial realization of the process.

In conclusion, the gas-phase electrolysis of HCl in its current state indeed appears to be a feasible and energy efficient alternative to the Bayer UHDENORA process with the potential to markedly reduce the energy demand of the industrial chlorine production, which, due to the significance of this sector, would be an important contribution to reaching the 2050 climate goals.

7 Outlook

In the following, remaining open questions about the overall process as well as the electrolyzer itself are discussed, aiming both at a better understanding of the HCl gas-phase electrolysis from a scientific point of view but also on further advancing its applicability in a real industrial setting.

Two interesting questions on the overall process level are, whether the gas-phase electrolysis of HCl is not only exergetically more efficient but also more sustainable and economically attractive. To this end, first steps of a life cycle analysis have been undertaken already that indicate that the lower energy demand and higher possible single pass conversions indeed make the novel processes more sustainable than the Bayer UHDENORA process in various impact categories like human toxicity, fossil depletion and climate change. Since these investigations are at a very preliminary state, further research should be carried out to validate and quantify these results. Complementary to that, the investment and operating costs of all process variants should be estimated, so that a comparison between the novel processes and the state-of-the-art can be made in all three categories; sustainability, energy efficiency and costs.

Ultimately, an optimization of the three novel processes based on both the numerical reactor model as well as models for the remaining units and their interconnection with respect to cost, sustainability and exergy demand would certainly be beneficial in case of an industrial application of the process. Moreover, since there is a strong interaction between the reactor and process level, changes in the reactor operation, affecting for example the humidity in the anode or the reactor temperature, impact the efficiency and design of the overall process as well. Hence, also further investigations and optimizations of the electrochemical reactor itself, as discussed in the following, always have to be seen in the context of the overall process and should proceed such an optimization on the process level.

Future research on the gas-phase reactor should continue to follow the combined experimental and theoretical approach employed in this thesis. One of the most crucial next steps is the development of a larger reactor. Due to the significant volume of HCl emerging from the production of isocyanates, the membranes used in the Bayer UHDENORA process have a size of ca. 2.5 m². The final step in assessing the industrial applicability of the here proposed processes is hence to prove

the feasibility of the gas-phase reactor employing membrane sizes of at least the same order of magnitude. This upscaling will likely be accompanied by various challenges in the water and thermal management arising from the absence of a liquid electrolyte, as it is present in the Bayer UHDENORA liquid-phase reactor. Furthermore, while Rh_xS_y is successfully employed as a cathode catalyst in the experiments of the present work, future studies should also focus on the investigation of anode catalyst materials that are more stable in the chemically aggressive environment of the gas-phase reactor, like ruthenium oxide. Especially with larger reactors, further experimental confirmation and location of flooding and dehydration, e.g. by means of integrated humidity sensors and thermocouples or neutron imaging amongst other methods (Lapicque 2012), would be of interest for the continued development of reactor optimization strategies.

To assist in these developments, the numerical reactor and crossover model should be further developed as well. To be able to accurately emulate the water household and polytropic behavior at high conversions, the model should hence be stepwise extended to a pseudo 2D model, considering the along the channel coordinate, and eventually a full 2D or 3D model, including the so far lumped energy balance. Furthermore, uncertainties in the model that mostly stem from the effect of gaseous HCl on membrane properties like the water diffusion coefficient or equilibrium water content, should be reduced by the experimental investigation of these effects and their subsequent integration into the model.

On a more microscopic level, the kinetics of the HClOR and ORR on suitable catalyst materials under realistic conditions present in the gas-phase reactor pose another interesting field of research. This includes the investigation of the surface species involved in the HClOR as well as the potential history dependence of their surface coverage, which is shown in this thesis to play a significant role in achieving higher limiting current densities. Moreover, the ORR was shown to be strongly impeded by the crossover of $\text{HCl}_{(\text{aq})}$. A combination of the crossover model and the overall reactor model seems hence promising for a more accurate and holistic depiction of the physicochemical processes occurring within the gas-phase reactor. However, this is only feasible, if the influence of chloride anions on the ORR can be understood more quantitatively, so that the reactor model is able to emulate the effect of $\text{HCl}_{(\text{aq})}$ crossover on the reactor performance.

Another challenge would be the operation of the reactor at elevated pressures so that the enormous amount of dissipated heat can be utilized for the generation of low pressure steam at a temperature

of ca. 430 K. Operating the reactor at this temperature would not only increase the practical usability of the dissipated heat but also decrease the exergy demand of the overall process by another 40% (assuming equivalent cell potentials), which would make the gas-phase electrolysis an interesting alternative not only to the Bayer UHDENORA process but also the Deacon-like processes, especially since higher overall conversions can be achieved.

Lastly, future investigations of a new reactor concept, the alkaline electrolyzer, are motivated in the following. As shown in this thesis, the three major aspects that mainly influence the performance of the HCl gas-phase electrolyzer are the water household, the thermal management and chloride ion poisoning of the (platinum based) cathode catalyst. While various strategies to control and mitigate all three aspects are successfully developed in this work, the alkaline reactor might offer an intrinsic solution to these challenges.

As shown in the reaction scheme (eq. 7.1 to 7.3), the reaction product water is now emerging at the anode and consumed at the cathode, resolving the challenge of water accumulation in the cCL with increasing current densities. Secondly, the ORR is significantly less sluggish at high pH compared to the acidic milieu of the PEM electrolyzer, and silver, a commonly used catalysts in an alkaline fuel cell and also in the here presented alkaline electrolyzer, is not only cheaper than Pt and Rh_xS_y, but also not prone to chloride ion poisoning. Lastly, the thermal management of the cell becomes easier due to the convective heat removal via the electrolyte stream flowing through the cell, whose temperature and flowrate can be controlled (please see chapter 4.2).

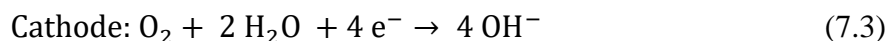
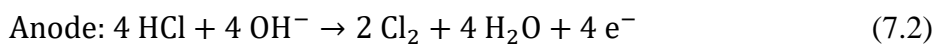
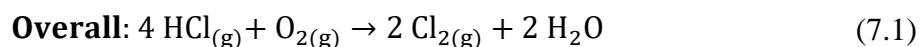


Figure 7.1 displays polarization data from a first experiment with a prototype of the alkaline fuel cell, as introduced in chapter 4.2. Please note that these are merely preliminary measurements intended to motivate future research on this reactor concept and to identify first challenges that need to be addressed.

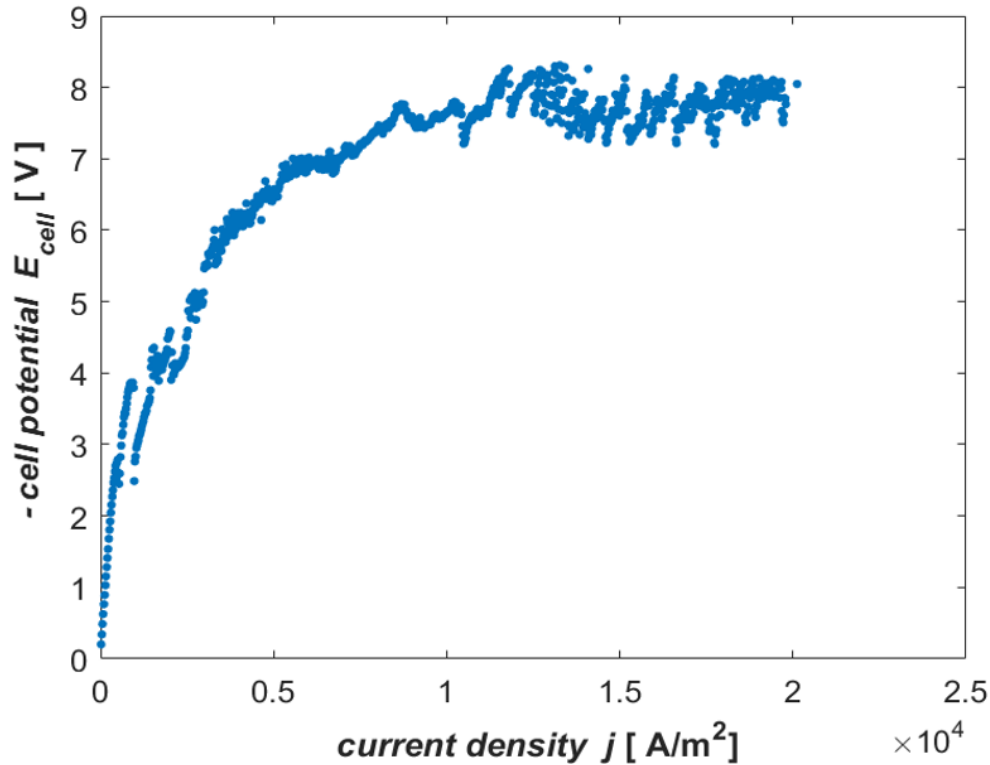


Fig. 7.1, Polarization data of the alkaline electrolyzer at RT employing 20wt% NaOH in water as the electrolyte.

During the experiment, significant amounts of NaOH flowing through the gap between both catalyst layers leaked into the anode chamber of the reactor due to insufficient sealing, which lead to the unwanted formation of brine. Furthermore, the convective flux of NaOH through the aGDE and into the aGC likely reduced the concentration of chloride ions in the aCL. Hence, it is well possible that oxygen evolution is taking place and is responsible for a significant fraction of the measured current density. The OER is known to be sluggish on platinum catalysts (Reier 2012) and even though the reaction is more facile on ruthenium oxide (Stoerzinger 2017), which is contained in the aGDE as well, the kinetics of the HClOR are significantly faster, as shown in chapter 5.1. Hence the low concentration of chloride ions as well as the sluggish OER and the significant ohmic resistance of ca. 4 Ohm (Artemov 2015) in the 3 mm electrolyte filled gap between both GDEs likely explain the observed significant overpotentials.

Therefore, while the theoretical concept of the alkaline electrolyzer seems promising as it offers solutions to the greatest challenges of the PEM electrolyzer, future studies should focus on developing a strategy for sealing off the anode compartment and lowering the ohmic resistance in

the electrolyte gap by reducing its width. Only then it can be evaluated whether the alkaline electrolyzer is a feasible alternative to the PEM electrolyzer.

Appendix

A1 Phase equilibrium in the extraction step of the ELECTRA-ABS process

At phase equilibrium, the chemical potential and fugacity $f_{i,l}$ of a substance i is the same in each phase l . Neglecting the Poyinting correction factor, the following equation can be formulated.

$$f_{i,l} = \gamma_{i,l} x_{i,l} p_{i,sat} \varphi_{i,sat} \quad (\text{A.1})$$

Here, $\gamma_{i,l}$ is the activity coefficient of substance i in phase l , $x_{i,l}$ its molar fraction, $p_{i,sat}$ the saturation pressure of the pure component and $\varphi_{i,sat}$ the according fugacity coefficient, which is not a function of the composition of the mixture, since it is a property of the respective pure component. Additionally, at low concentrations of the dissolved gas, Henry's law is a good approximation for the saturation pressure, leading to

$$f_{i,l} \sim \gamma_{i,l} x_{i,l} H_{i,l} \quad (\text{A.2})$$

For small concentrations of the absorbed gas, the activity coefficient is approximately one. Consequently, the mole fraction of a component in each phase is inversely proportional to its Henry constant under equilibrium conditions.

$$\frac{x_{Cl_2,water}}{x_{Cl_2,octane}} = \frac{\frac{\dot{n}_{Cl_2,water}}{\dot{n}_{Cl_2,water} + \dot{n}_{water}}}{\frac{\dot{n}_{Cl_2,octane}}{\dot{n}_{Cl_2,octane} + \dot{n}_{octane}}} = \frac{H_{Cl_2,octane}}{H_{Cl_2,water}} \equiv K_{LLE} \quad (\text{A.3})$$

In equation A.3, $\dot{n}_{Cl_2,water}$ and $\dot{n}_{Cl_2,octane}$ are the molar equilibrium fluxes of Cl_2 in the water and octane stream leaving the extraction unit. The molar flux of pure water and octane fed into the extraction unit is defined as \dot{n}_{water} and \dot{n}_{octane} , respectively. Figure A.1 visualizes the different fluxes entering and leaving the extraction unit.

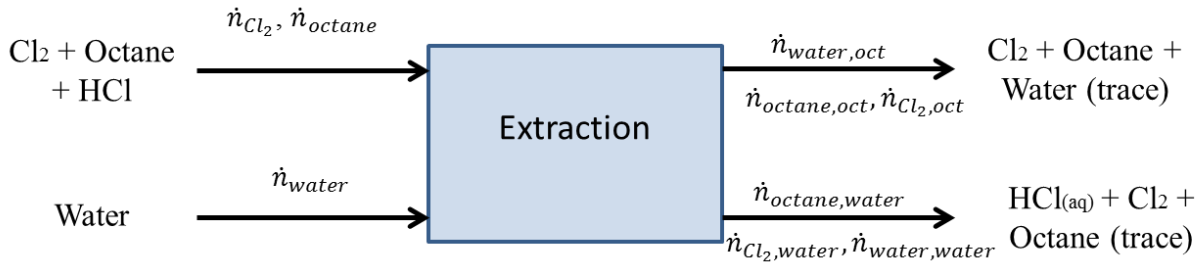


Fig. A.1, Visualization of the extraction process. Adopted from (Bechtel 2018a) with permission from John Wiley and Sons.

The small amount of HCl present in the octane outlet stream was neglected in this balance. The equilibrium calculations consider that the Henry constant of Cl_2 in water $H_{\text{Cl}_2, \text{water}}$ is influenced by the presence of HCl, which transfers into the aqueous phase during the extraction step. Alkan *et al.* (2005) investigated the dependence of the chlorine solubility in hydrochloric acid as a function of the acid concentration. However, they only employed concentrations of up to 7 M, which are surpassed in the simulations with a single pass conversion of 60% and a total conversion of 80%. Since the experimental data of Alkan *et al.* (2005) shows a linear trend for concentrations greater than 1 M, a linear fit was created for extrapolating the Cl_2 solubility at higher hydrochloric acid concentrations for temperatures of 293 K and 303 K, as displayed in Figure A.2. The solubility at 298.15 K was then approximated by linear interpolation between these two temperatures.

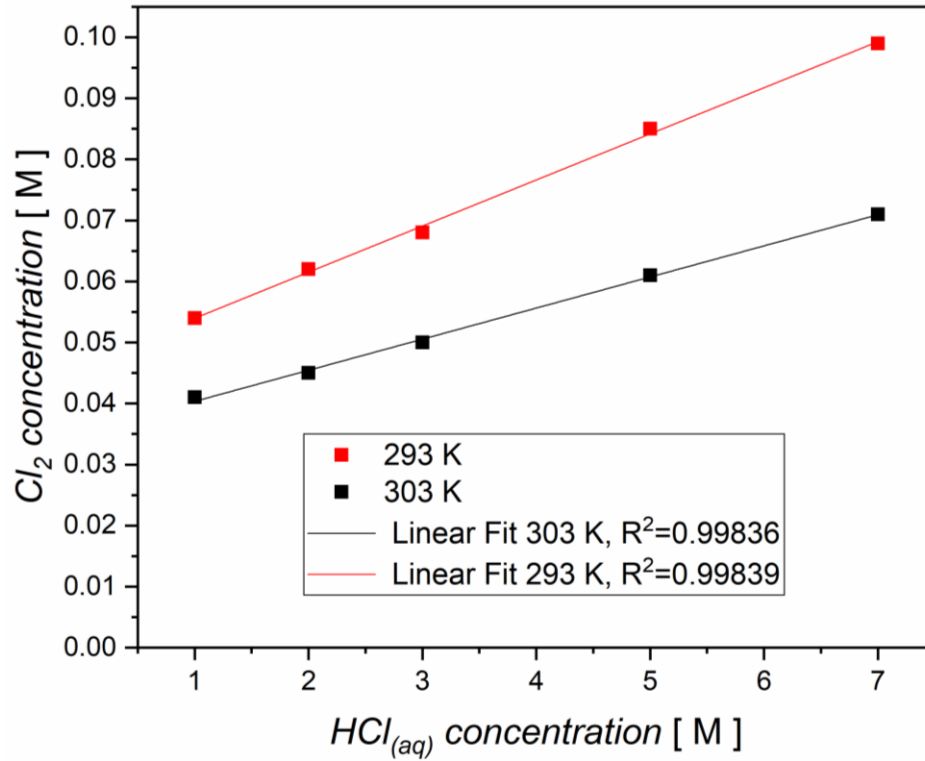


Fig. A.2, Linear fit to the data from Alkan *et al.* (2005) for extrapolating the chlorine solubility beyond hydrochloric acid concentrations of 7 M. Adopted from (Bechtel 2018a) with permission from John Wiley and Sons.

Lastly, the equilibrium mole fractions of water and octane in the water-rich and the octane-rich phase were extracted from Mańczyński *et al.* (2003). It is assumed that the presence of Cl₂ and HCl has no significant impact on the miscibility of octane and water, which seems to be a justifiable approximation due to the comparably large amount of water and octane. Based on the balance condition that the molar flux of Cl₂ entering and leaving the unit is equivalent, the distribution of Cl₂ between the two outlet streams of the extraction unit can be determined from equation A.3, yielding

$$\dot{n}_{Cl_2,water} = -\frac{\dot{n}_{Cl_2}(1 - K_{LLE}) + \dot{n}_{octane} + K_{LLE}\dot{n}_{water}}{2(K_{LLE} - 1)} + \sqrt{\frac{\left(-\frac{\dot{n}_{Cl_2}(1 - K_{LLE}) + \dot{n}_{octane} + K_{LLE}\dot{n}_{water}}{2(K_{LLE} - 1)}\right)^2}{4} + \frac{K_{LLE}\dot{n}_{water}\dot{n}_{Cl_2}}{K_{LLE} - 1}} \quad (A.4)$$

Since the molar flux of Cl_2 transferred into the aqueous phase is small, a simplified solution can be obtained that only differs by 0.5% from the above accurate solution at the present conditions:

$$\dot{n}_{\text{Cl}_2, \text{water}} \approx \frac{K_{LLE} \dot{n}_{\text{Cl}_2} \dot{n}_{\text{water}}}{\dot{n}_{\text{octane}} + \dot{n}_{\text{Cl}_2}} \quad (\text{A.5})$$

From the octane-water solubility data by Mańczyński *et al.* (2003) follows

$$\begin{aligned} \frac{\dot{n}_{\text{water, water}}}{\dot{n}_{\text{octane, water}}} &= \frac{\dot{n}_{\text{water}} - \dot{n}_{\text{water, oct}}}{\dot{n}_{\text{water, oct}}} = \frac{x_{\text{water, water}}}{x_{\text{octane, water}}} = \frac{1 - 9,96 \cdot 10^{-8}}{9,96 \cdot 10^{-8}} \\ &= 1.004 \cdot 10^7 \end{aligned} \quad (\text{A.6})$$

for the water-rich phase and

$$\frac{\dot{n}_{\text{octane, oct}}}{\dot{n}_{\text{water, oct}}} = \frac{\dot{n}_{\text{octane}} - \dot{n}_{\text{octane, water}}}{\dot{n}_{\text{water, oct}}} = \frac{x_{\text{octane, oct}}}{x_{\text{water, oct}}} = \frac{1 - 5 \cdot 10^{-4}}{5 \cdot 10^{-4}} = 1999 \quad (\text{A.7})$$

for the octane-rich phase. The amount of water and octane in each phase can then be calculated using equations A.6 and A.7.

A2 Exergy analysis

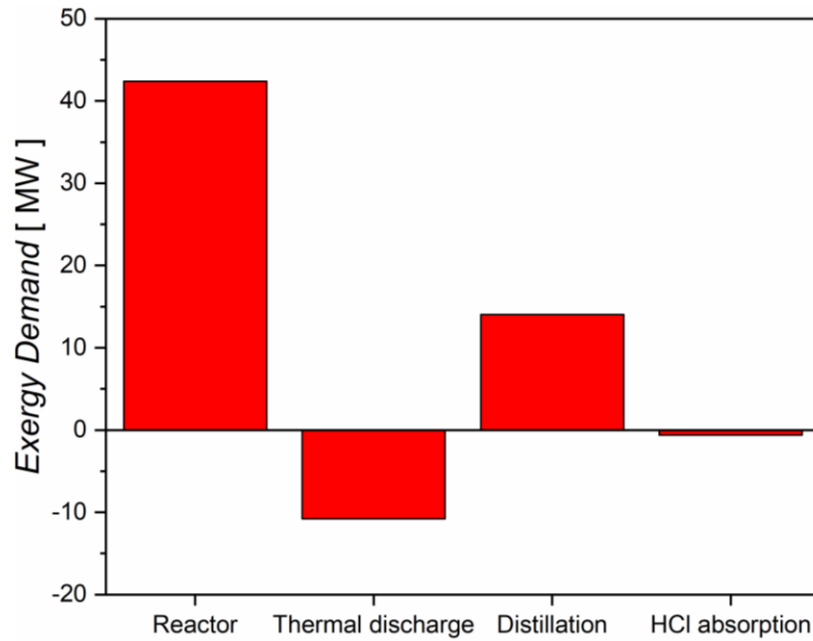


Fig. A.3, Exergy demand of the reactor, distillation column, absorption column and the sum of all heat exchangers in the state-of-the-art Bayer UHDENORA process. Negative values represent exergy streams leaving the system. Adopted from (Bechtel 2018a) with permission from John Wiley and Sons.

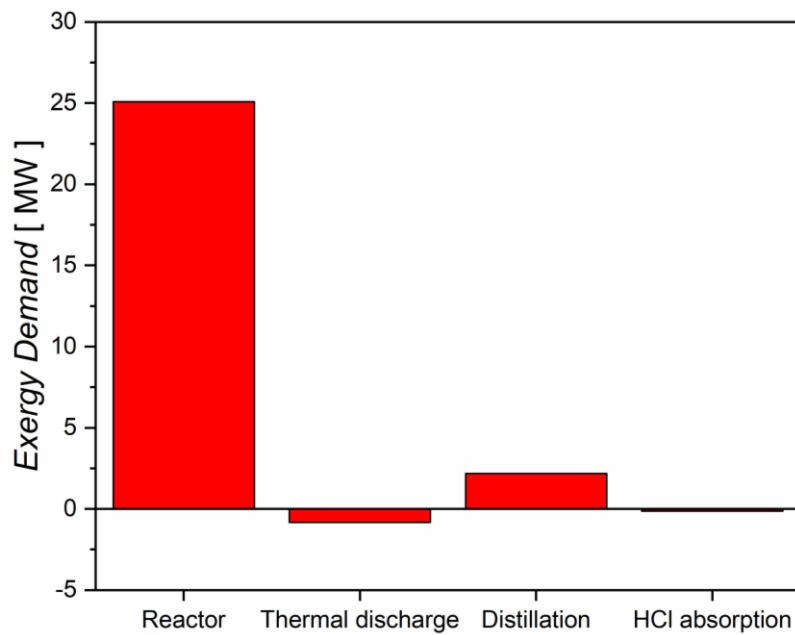


Fig. A.4, Exergy demand of the reactor, distillation column, absorption column and the sum of all heat exchangers in the ELECTRA-DIST process with a single pass conversion of 80%. Negative values represent exergy streams leaving the system. Adopted from (Bechtel 2018a) with permission from John Wiley and Sons.

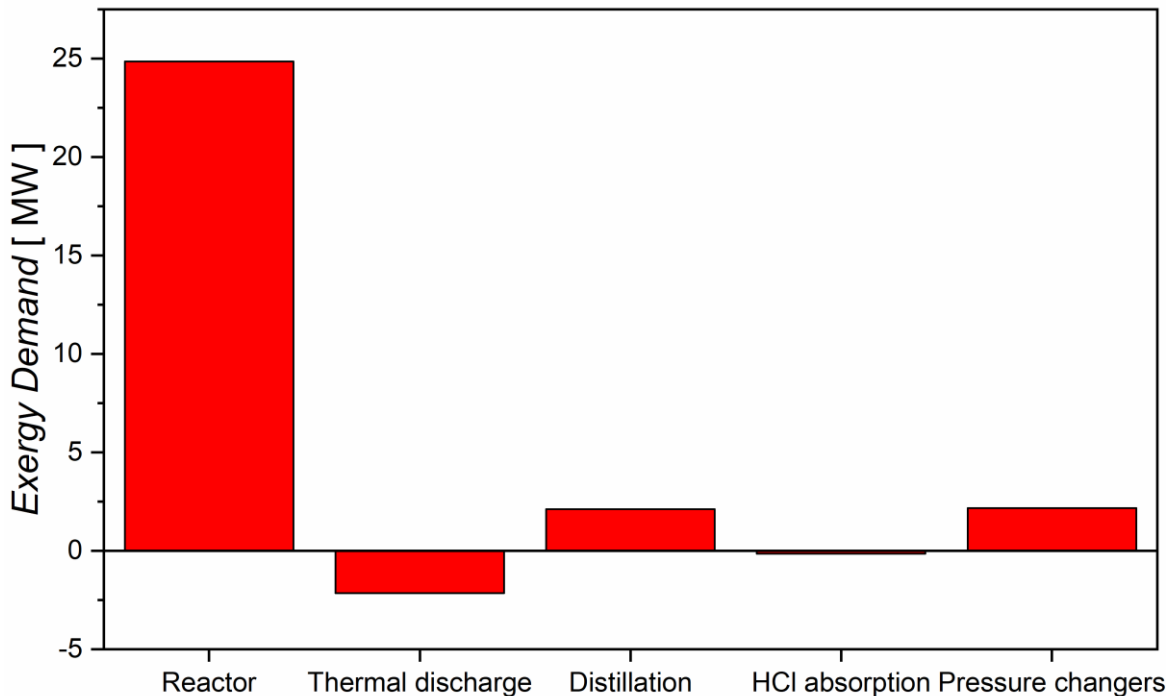


Fig. A.5, Exergy demand of the reactor, distillation column, absorption column, pressure changers and the sum of all heat exchangers in the ELECTRA-ABS process with a single pass conversion of 80%. Negative values represent exergy streams leaving the system. Adopted from (Bechtel 2018a) with permission from John Wiley and Sons.

A3 Diffusion coefficient of water in Nafion

Motupally *et al.* (2002) investigated the transport of water through a Nafion membrane in the presence of hydrochloric acid. They derived equation 3.26 for the Fickian diffusion coefficient of water within the membrane based on self-diffusion coefficient data from Zawodzinski *et al.* (1991) as well as measurements by Balko *et al.* (1981), who determined the water content of a Nafion membrane in contact with hydrochloric acid in dependence of the acid concentration. Motupally *et al.* (2002) assumed a linear relationship for the derivation of equation 3.26, which is however only valid for high acid concentrations, while there is a strongly exponential dependence observable at low concentrations (Balko 1981). Since the cathode in the experiments of Motupally *et al.* (2002) and Martínez (2015) is filled with pure water and diluted sulfuric acid respectively, this assumption is questionable. Also, it is not trivial which concentration to employ in this equation due to the fact that there is no hydrochloric acid present on the cathode side of the reactor investigated by Martínez (2015) and Motupally *et al.* (2002). Furthermore, instead of the factor of

$2.5 \cdot 10^{-7}$ in equation 3.26, as taken from Motupally *et al.* (2002), the authors used a factor of $1.96 \cdot 10^{-7}$ in the otherwise identical equation in one of their earlier publications (Motupally 1999). It is therefore not entirely clear which equation the authors used to obtain their results in (Motupally 2002) and where this difference originates in. For these reasons, equation 3.25 proposed by Fuller (1992) was employed for calculating the Fickian diffusion coefficient of water in Nafion in the reactor model of the present work.

A4 Vapor-liquid equilibrium of HCl/H₂O and activity coefficients of aqueous hydrochloric acid

As stated in the model assumptions, a vapor-liquid equilibrium between HCl in its gaseous and its dissolved state is presupposed at the surface of the agglomerates within the aCL. Since there is no sufficient experimental data available for the absorption of gaseous HCl in Nafion, the agglomerate is assumed to be homogenous, similarly to the treatment of the membrane. The polymer and Pt/C catalyst are assumed to not influence the VLE, and hence simply reduce the volume concentration of water and the absorbed HCl_(aq). It is furthermore assumed that the volume of the agglomerate is not changing significantly with its water content, an assumption that is also made in various other models (Sun 2005, Kulikovsky 2000).

In reality, interactions between Nafion and HCl are expected to reduce the equilibrium concentration of HCl_(aq) in Nafion. In the numerical crossover model introduced in chapter 3.3, a partitioning factor for the absorption of hydrochloric acid in Nafion was multiplied with the equilibrium concentration of HCl in pure water to account for this effect. This appears to be a reasonable approximation, however, in future research it should be investigated, whether this partitioning factor is indeed also applicable for the absorption of gaseous HCl into the ionomer, since it was originally determined for Nafion in contact with hydrochloric acid. For now, the partitioning factor is hence not included into the numerical reactor model and only considered in the crossover model developed with A. Crothers, which should be considered when merging both models in future investigations.

Based on this treatment, experimental VLE data of HCl and H₂O was employed to calculate the concentration of hydrochloric acid within the catalyst agglomerates. To this end, fit functions were generated to correlate the equilibrium mole fraction of chloride anions to the HCl partial pressure based on experimental data from (Green 2018) for temperatures of 298, 313, 323, 333, 343, 353 and 363 K.

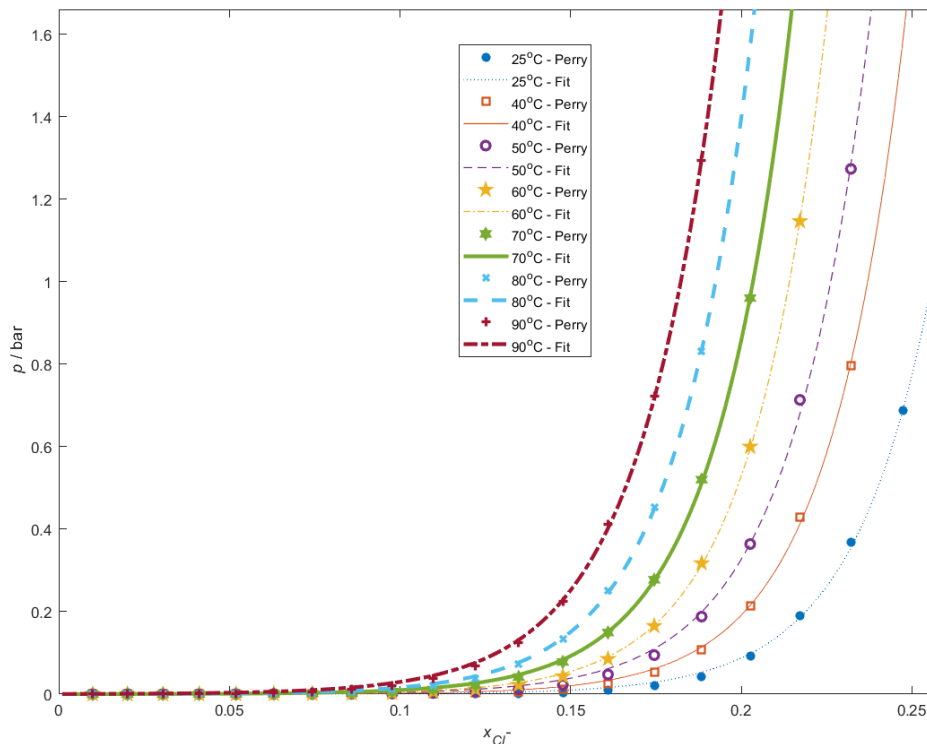


Fig. A.6, Experimental equilibrium data of chloride-ion mole fractions in water as a function of the HCl partial pressure from Perry's Chemical Engineer's Handbook (Green 2008) in comparison to the here developed fit functions. Due to the low pK_a of HCl, practically all dissolved HCl is dissociated into protons and chloride anions. Adopted from (Bechtel 2019b) with permission from Elsevier.

In the isothermal half-cell simulations, these fit functions can be directly employed in the numerical reactor model.

$$x = \frac{\ln\left(\frac{P}{A}\right)}{B} \quad (\text{A.8})$$

Table A.1, Fit parameters for determining the mole fraction of chloride anions in solution as a function of the HCl partial pressure for temperatures between 298 and 363 K.

<i>Temperature / K</i>	<i>A</i>	<i>B</i>
298	$3.923 \cdot 10^{-5}$	39.3
313	$2.555 \cdot 10^{-5}$	44.62
323	$6.469 \cdot 10^{-5}$	42.64
333	$6.297 \cdot 10^{-5}$	45.18
343	0.0001164	44.53
353	0.0001895	44.53
363	0.0004165	42.71

For the non-isothermal full-cell simulations, a single fit function describing the mole fraction as a function of both the temperature and HCl partial pressure was developed using the *polyfitn* tool in Matlab 2015b.

$$\begin{aligned}
 x_{Cl^-}(p_{HCl}, T) = & 0.12748p_{HCl}^3 - 2.19 \cdot 10^{-5}p_{HCl}^2T - 0.28021p_{HCl}^2 + 4.99 \\
 & \cdot 10^{-7}p_{HCl}T^2 - 0.0003090p_{HCl}T + 0.287p_{HCl} \\
 & + 1.177 \cdot 10^{-7}T^3 - 0.000115T^2 + 0.0362T - 3.51 \quad (A.9)
 \end{aligned}$$

Here, the temperature is given in units of Kelvin and the pressure in units of atm. The mean deviation between equation A.9 and the fit function for discrete temperatures values (eq. A.8) is 0.62%, while the maximum deviation is 2.5%. For correlating the activity coefficient of chloride anions in water with their mole fraction, a similar procedure was followed, employing experimental data from Cerquetti *et al.* (1968).

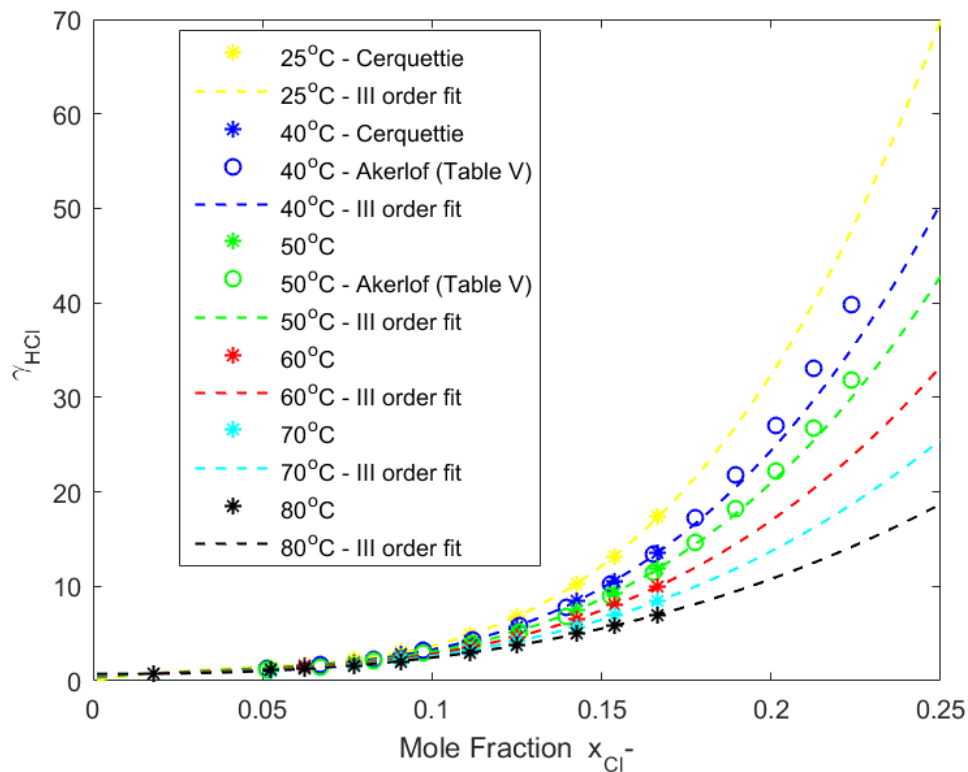


Fig. A.7, Experimental data (Cerquetti 1968, Åkerlöf 1938) of the of chloride-anion activity coefficient as a function of the mole fraction in the aqueous solution in comparison to the fit functions proposed in the present work. Adopted from (Bechtel 2019b) with permission from Elsevier.

For obtaining the data presented in Figure A.7, the molal activity data (Cerquetti 1968) was first converted to a molar activity coefficient as described in (Bart 2001). Åkerlöf and Teare (1938) determined molal activity coefficients for higher concentrations than Cerquetti *et al.* (1968) at temperatures of 313 and 323 K. Hence, their data was not included in the fitting procedure but used to validate that the proposed fit functions (eq. A.10) are also physically reasonable outside the concentration interval investigated by Cerquetti *et al.* (1968).

$$\gamma_{HCl} = ax^3 + bx^2 + cx + d \quad (\text{A.10})$$

Table A.2, Fit parameters for determining the activity coefficient of chloride anions in solution as a function of the chloride anion mole fraction for temperatures between 298 and 353 K.

<i>Temperature / K</i>	<i>a * 10⁻³</i>	<i>b * 10⁻³</i>	<i>c * 10⁻³</i>	<i>d * 10⁻³</i>
298	7.3605	-0.9597	0.05955	-0.000008781
313	4.6909	-0.50294	0.033168	0.003307
323	3.84237	-0.392108	0.027594	0.00038994
333	2.56144	-0.176891	0.015011	0.00054907
343	1.503888	0.0049432	0.0041049	0.00066799
353	0.69572202	0.12150502	-0.0020027	0.00074803

No sufficiently accurate single fit function could be generated for the activity coefficient γ_{HCl} as a function of the temperature and mole fraction. In the reactor model, the temperature dependence of the activity coefficient is hence accounted for by linearly interpolating between the fit functions given in equation A.10.

A5 The HClOR rate constant as a function of the water content and temperature

As Zhu *et al.* (2019) showed, the electrochemically active surface area (ECSA) is a function of the water content in the catalyst layer. Hence, the ECSA of the aCL at any given water content is determined relative to its ECSA at full hydration according to the following fit function

$$\frac{ECSA(\lambda)}{ECSA(\lambda = 14)} = ECSA_{rel} = [\log(0.9\lambda - 0.21)]^{0.23} \quad (A.11)$$

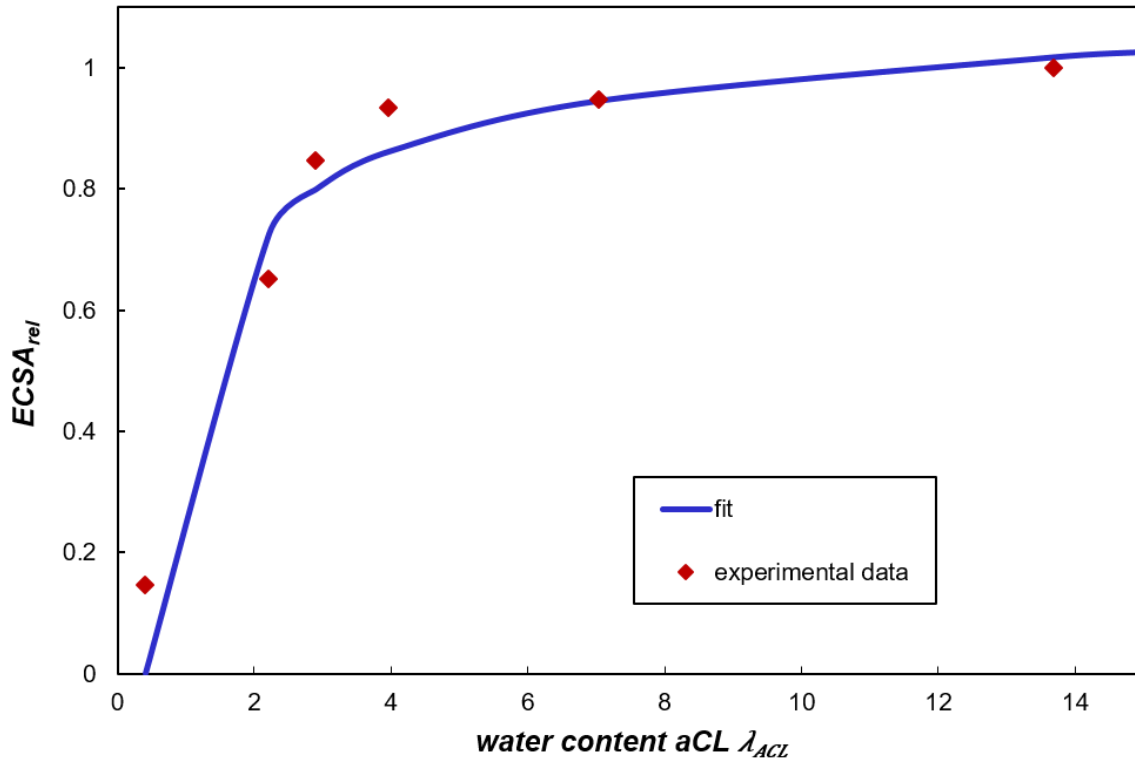


Fig. A.8, Experimental data of Zhu *et al.* (2019) in comparison to the fit of the relative ECSA as a function of the water content in the aCL. The maximum relative experimental ECSA value at a water content of ca. 14 is defined as 1. Adopted from (Bechtel 2020a).

The aCL water content in the simulations of the HClOR half-cell, where the ECSA was kept constant due to sufficient hydration, assumed a value of 4 at the reaction limited current density in both the 313 and 333 K simulations. Hence, in the full-cell model, the rate constant of the HClOR $k_{A,full-cell}$ can be calculated based on the above fit function and the rate constant k_A determined according to equation 3.43.

$$k_{A,full-cell} = 0.89k_A \frac{ECSA_{rel}(\lambda)}{ECSA_{rel}(\lambda = 4)} \quad (A.12)$$

The factor of 0.89 accounts for different Nafion loadings in the half-cell and full-cell simulations as explained in chapter 3.2.7. For determining the temperature dependence of the rate constant k_A , the limiting current densities from the experimental work of Martínez (2015) at the investigated temperatures of 298, 313, 323 and 333 K were converted to rate constants according to equation 3.43.

Subsequently, the following fit function was developed.

$$k_A(T) = 32.188 e^{0.01788T} \quad (\text{A.13})$$

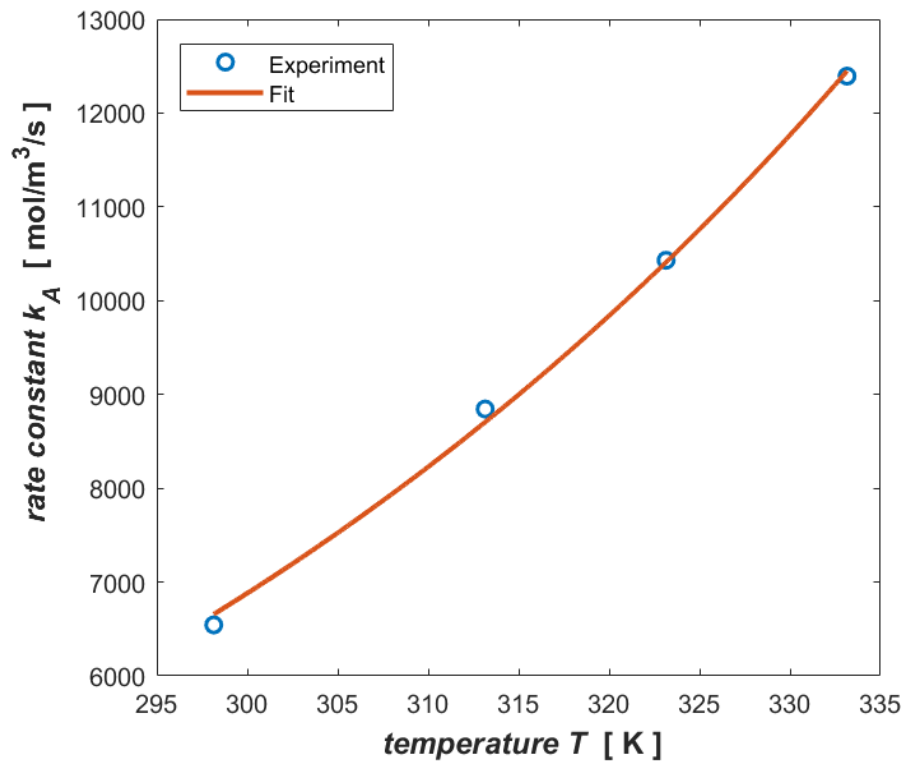


Fig. A.9, Rate constant of the HClOR as a function of the temperature derived from experimental data from Martínez (2015) (blue circles) and the fit function given in equation A.13 (red line).

A6 Experimental setup



Fig. A.10, Photography of the experimental setup including pumps (1) for supplying the electrolyte stored in vessel (2) to the reactor and the NaOH solution with indigo carmine (by Alfa Aesar) as indicator stored in vessel (3) to the neutralization column (4). The flow rate of gases is controlled by 2 MFCs (5) and the oxygen feed stream is humidified by a gas bubbler (6). The thermostat (7) and the heating tubes (8) around the feed gas tubes allow for controlling the temperature of the electrolyte and the reactor feed gases respectively. The reactor is placed in the oven (9) on the back of the picture.

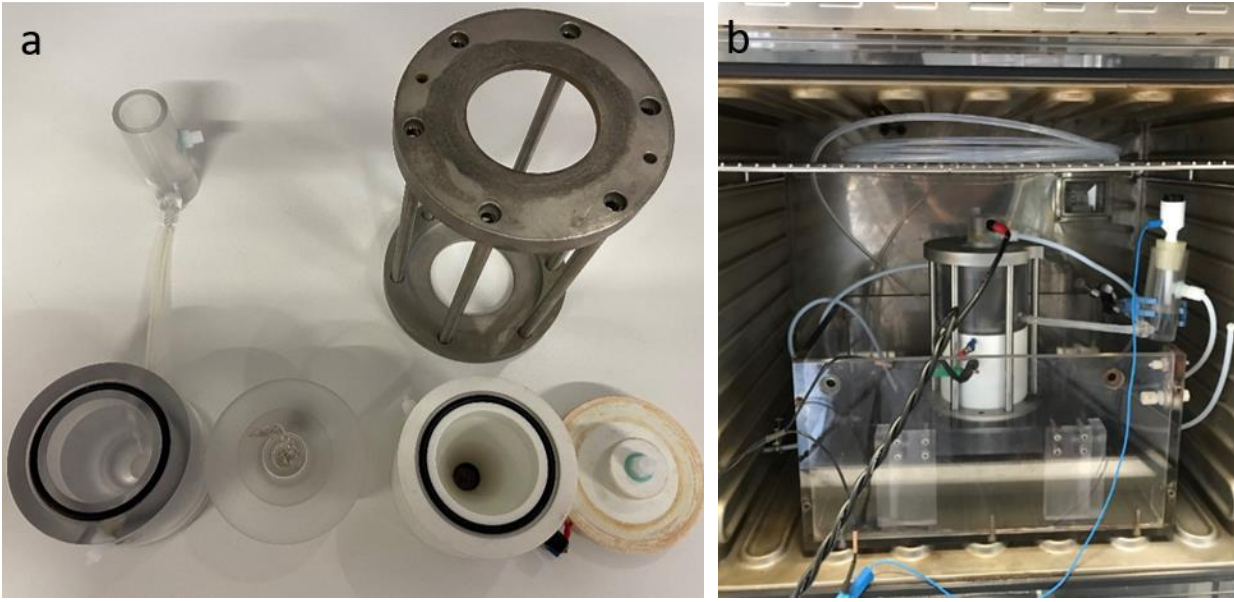


Fig. A.11, Photography of the half-cell dismantled a) and placed in the oven b).

The reactor is oriented in a way that the liquid filled compartment is up so that the liquid electrolyte presses the MEA on the titanium support which is connected to the current collector. This is necessary to ensure sufficient contact. Hence, to be precise, gravity poses an additional driving force for the transport of water through the membrane that is so far not considered in the numerical reactor model.

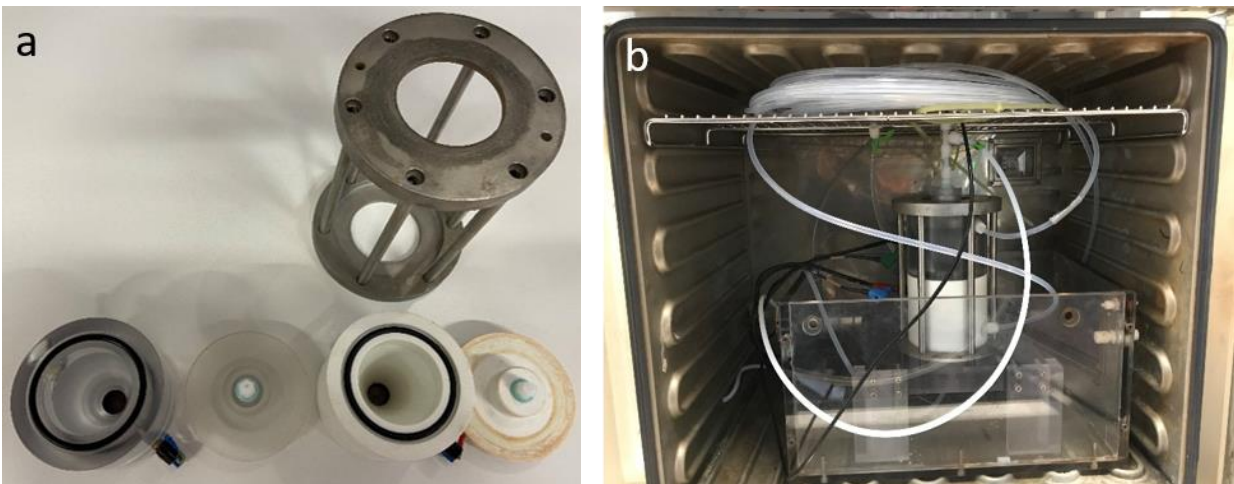


Fig. A.12, Photography of the full-cell dismantled a) and placed in the oven b).

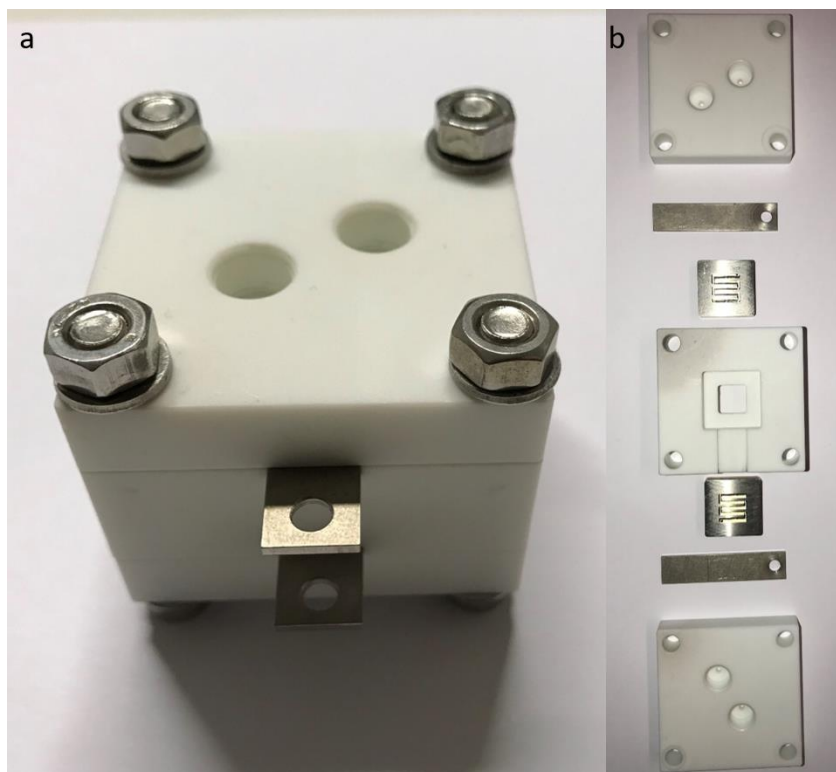


Fig. A.13, Photography of the assembled (a) and disassembled (b) alkaline full-cell.

A7 Kinetic versus mass transfer limitations in the gas-phase oxidation of HCl

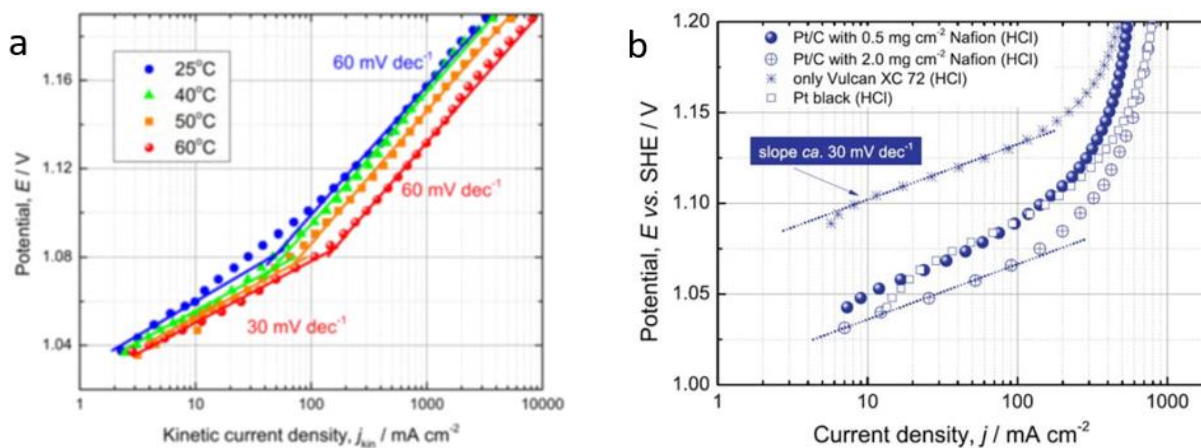


Fig. A.14, Tafel plot from the work of Martínez (2015) (with permission from I. G. Martínez) corrected for apparent mass transfer resistances a) in comparison to an uncorrected Tafel plot from Martínez (2014) (with permission from Elsevier and I. G. Martínez), employing different catalyst materials and loadings b).

A8 Relevance of the OER in competition to the HClOR

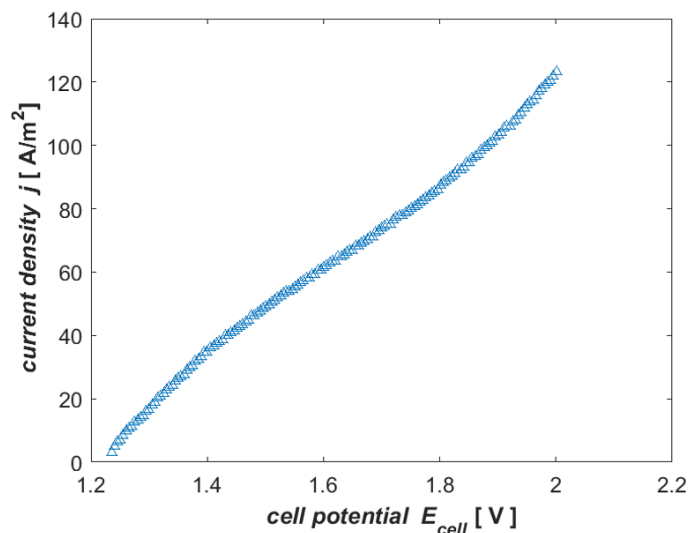


Fig. A.15, Polarization curve recorded under the same conditions under which the data displayed in Figure 5.6 was obtained, except for the HCl feed being replaced by pure N_2 in order to determine whether there is a significant contribution of the OER to the current density in Figure 5.6.

A9 Influence of the starting potential on the limiting current density in HClOR linear sweep voltammetry experiments

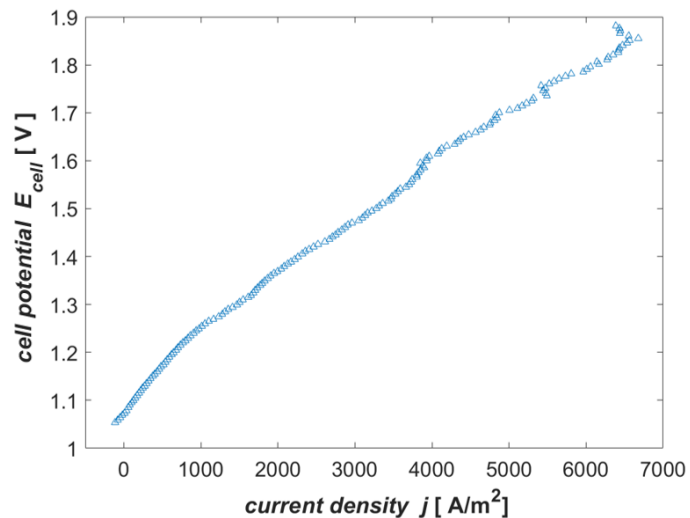


Fig. A.16, Polarization curve recorded under the same conditions under which the data displayed in Figure 5.6 was obtained, except for the starting potential now being 1.05 V.

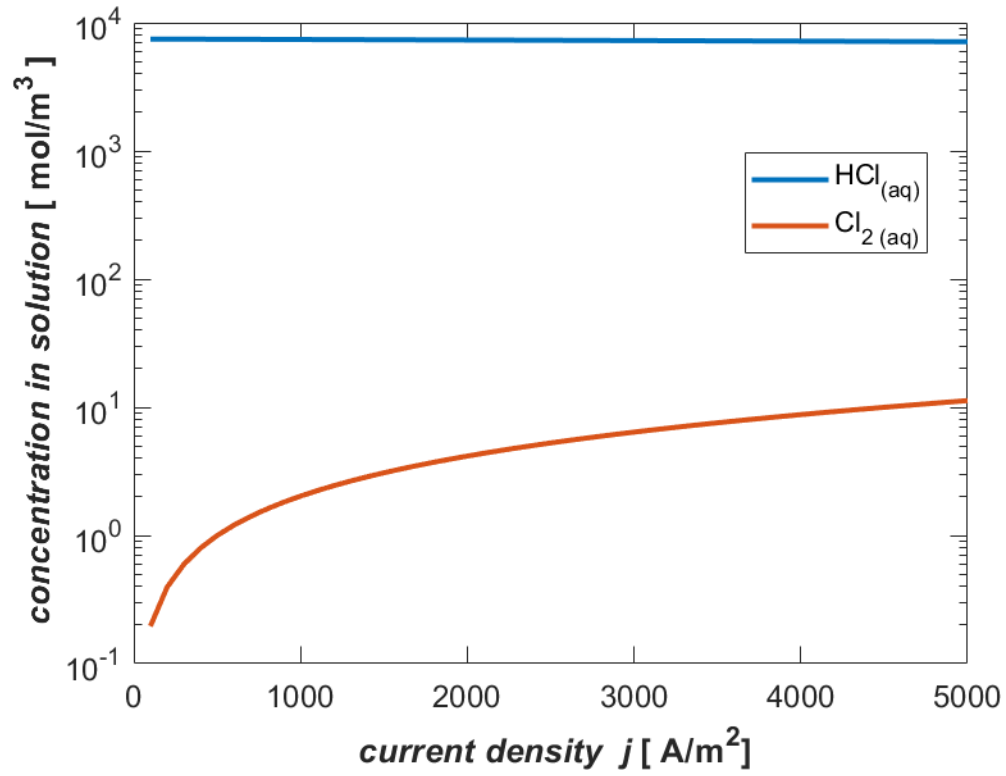
A10 Crossover of HCl and Cl₂

Fig. A.17, equilibrium concentrations of HCl_(aq) and Cl₂(aq) in an aqueous solution based on current density dependent partial pressure data obtained from the full-cell simulation at 333 K employing the standard thermal resistance.

List of Figures

Fig. 1.1, Scheme for the utilization of renewable energy sources for recycling HCl to Cl ₂	5
Fig. 1.2, Scheme of the three gas phase reactors.	8
Fig. 1.3, Working principle and components of the gas phase reactor.	9
Fig. 2.1, Process flow scheme of the Bayer UHDENORA state-of-the-art process.....	26
Fig. 2.2, Process flow scheme of the ELECTRA-DIST process.	29
Fig. 2.3, Process flow scheme of the ELECTRA-ABS process.	33
Fig. 2.4, Process design methodology consisting of a three step IL screening procedure and the flowsheet simulation.	36
Fig. 2.5, Infinite dilution thermodynamic properties of the IL candidates.	38
Fig. 2.6, Process flow scheme of the IL process.....	39
Fig. 2.7, Exergy demand of different unit operations of the ELECTRA-IL and Bayer UHDENORA process.....	44
Fig. 2.8, Additional exergy demand and condenser temperature in dependence of the operating pressure of the distillation column in the ELECTRA-DIST process.....	48
Fig. 2.9, Sankey diagram for the ELECTRA-DIST process.....	51
Fig. 2.10, Specific total exergy demand of the ELECTRA-DIST, ELECTRA-ABS and the state-of-the-art process	53
Fig. 3.1, Modeling domains of the numerical reactor model.....	61
Fig. 3.2, Saturation within the GDL as a function of the capillary pressure	72
Fig. 3.3, Saturation within the CL as a function of the capillary pressure.....	73
Fig. 3.4, Relative difference between experimental and calculated binary diffusion coefficients as a function of the LJ parameters.....	98
Fig. 3.5, Subsets that lead to a deviation between experimental and calculated transport properties of NH ₃ below the experimental uncertainty.....	100
Fig. 3.6, Comparison of the experimentally determined viscosity of nitrous oxide with calculated values using the CE equations.	109
Fig. 3.7, Comparison of the experimentally determined binary diffusion coefficient of nitrous oxide in nitrogen with calculated values using the CE equations.....	109
Fig. 3.8, Comparison of the experimentally determined thermal conductivity of nitrous oxide with the calculated values based on the CE equations.....	110
Fig. 3.9, Comparison of experimentally determined and calculated thermal conductivities of HCl, N ₂ and O ₂	113
Fig. 3.10, Comparison of experimentally determined and calculated binary diffusion coefficients of N ₂ -He and N ₂ -HCl mixtures.	114
Fig. 3.11, Comparison of experimentally determined and calculated viscosities of HCl, N ₂ and O ₂	114
Fig. 3.12, Comparison of different approaches for the correction of the thermal conductivity.	116

Fig. 4.1, Experimental setup for the half-cell investigations of the HClOR and ORR.....	119
Fig. 4.2, Exploded view of the cyclone flow half-cell.....	121
Fig. 4.3, Experimental setup for the full-cell investigations.....	122
Fig. 4.4, Exploded view of the cyclone flow full-cell.....	123
Fig. 4.5, Exploded view of the alkaline electrolyzer.....	122
Fig. 4.6, Scheme of the thermal bonding procedure for the three different MEAs.....	126
Fig. 5.1, Simulation results obtained with the presented model compared to experimental polarization data from Martínez (2015) at 313 K and 333 K.....	131
Fig. 5.2, Catalyst surface coverage as a function of the current density at 333 K.....	132
Fig. 5.3, Mole fractions of HCl, Cl ₂ and H ₂ O over the normalized thickness of the aGDL.....	133
Fig. 5.4, Effectiveness factor for agglomerates with two different radii.....	135
Fig. 5.5, Simulated polarization curves for the standard loading and an increased loading corresponding to a doubling of the ECSA.....	138
Fig. 5.6, Experimental polarization data for a starting potential of 0.8 V and 0.4 V.....	141
Fig. 5.7, Simulated polarization curve assuming the presence of two different Cl ⁻ surface species.....	145
Fig. 5.8, Cyclic voltammograms of the Pt/C WE with sulfuric and hydrochloric acid circulating through the CE chamber referenced versus RHE.....	150
Fig. 5.9, Chronoamperometry at 0.6 V vs RHE with the sulfuric acid stream flowing through the CE chamber being exchanged with hydrochloric acid after 600 s.....	151
Fig. 5.10, Fluxes of Cl ⁻ and Cl ₂ through the membrane in the liquid phase reactor as a function of the current density.....	153
Fig. 5.11, Contributions of diffusion, osmotic-driven convection, electroosmotic-driven convection and migration to the overall flux of a) Cl ⁻ and b) Cl ₂ through the membrane in the liquid-phase reactor as a function of the current density.....	154
Fig. 5.12, Fluxes of Cl ⁻ and Cl ₂ through the membrane in the gas phase reactor as a function of the current density.....	156
Fig. 5.13, Contributions of diffusion, osmotic-driven convection, electroosmotic-driven convection and migration to the overall flux of a) Cl ⁻ and b) Cl ₂ through the membrane in the gas-phase reactor as a function of the current density.....	157
Fig. 5.14, Fluxes of Cl ⁻ and Cl ₂ through the membrane in the gas-phase reactor as a function of the current density for three different water contents at the M cCL interface.....	158
Fig. 5.15, Fluxes of Cl ⁻ and Cl ₂ through the membrane in the gas phase reactor as a function of the effective diffusion coefficients.....	159
Fig. 5.16, Simulated polarization curves at 313, 323 and 333 K.....	161
Fig. 5.17, Water content in the aCL and cCL at 313 and 333 K as a function of the current density.....	163
Fig. 5.18, Water crossover through the membrane as a function of the current density for the 313, 323 and 333 K simulation.....	164

Fig. 5.19, Polarization curves employing a thermal resistance of 0.8 K/W and temperatures of 313 and 333 K.....	166
Fig. 5.20, Anode and cathode overpotential as well as the potential loss in the membrane as a function of the current density for the 313 and 333 K simulation employing a thermal resistance of 0.8 K/W.	167
Fig. 5.21, aCL and cCL water content employing an increased thermal resistance of 0.8 K/W a) and reactor temperature for the standard and the increased thermal resistance b) as a function of the current density.....	168
Fig. 5.22, Polarization curves for three different membrane thicknesses employing the standard thermal resistance.....	171
Fig. 5.23, Polarization curves employing a constant thermal resistance of 0.8 K/W as well as a current density dependent thermal resistance.	174
Fig. 5.24, Polarization curves for the standard and an optimized reactor operation.....	176
Fig. 5.25, Anode and cathode overpotentials as well as the potential loss in the membrane as a function of the current density for the simulation at 333 K employing the optimized reactor operation strategy.....	177
Fig. 5.26, Catalyst surface coverage as a function of the current density for the simulation at 333 K employing the optimized reactor operation strategy.....	178
Fig. 5.27, Partial pressures of O ₂ and HCl as a function of the relative GDL length at current densities of 4000 and 11000 A/m ² employing the optimized reactor operation strategy.	179
Fig. 5.28, Experimental polarization curves measured at RT employing the platinum based cathode catalyst by Clausthal on a Nafion 117 membrane a) and the Rh _x S _y based cathode catalyst by De Nora with a Nafion 1110 membrane.....	182
Fig. 5.29, Experimental polarization curves measured at RT employing the Rh _x S _y based cathode catalyst by De Nora and a Nafion 115 membrane.	184
Fig. 7.1, Polarization data of the alkaline electrolyzer at RT employing 20w% NaOH as an electrolyte.....	195
Fig. A.1, Visualization of the extraction process.....	198
Fig. A.2, Solubility of Cl ₂ in hydrochloric acid.....	199
Fig. A.3, Exergy demand of the reactor, distillation column, absorption column and the sum of all heat exchangers in the state-of-the-art Bayer UHDENORA process.	201
Fig. A.4, Exergy demand of the reactor, distillation column, absorption column and the sum of all heat exchangers in the ELECTRA-DIST process with a single pass conversion of 80 %.	201
Fig. A.5, Exergy demand of the reactor, distillation column, absorption column, pressure changers and the sum of all heat exchangers in the ELECTRA-ABS process with a single pass conversion of 80 %.....	202
Fig. A.6, Chloride equilibrium mole fractions in water as a function of the HCl partial pressure.	204

Fig. A.7, Chloride anion activity coefficient as a function of the mole fraction in the aqueous solution.....	206
Fig. A.8, Relative ECSA as a function of the water content in the aCL.	208
Fig. A.9, Rate constant of the HClOR as a function of temperature.	209
Fig. A.10, Photography of the experimental setup.	210
Fig. A.11, Photography of the half-cell.	211
Fig. A.12, Photography of the full-cell.	211
Fig. A.13, Photography of the alkaline full-cell.	212
Fig. A.14, mass transfer corrected and uncorrected Tafel plots from Martínez (2015).	212
Fig. A.15, Significance of the OER in the investigations of the HClOR	213
Fig. A.16, Experimental polarization data for a starting potential of 1.05 V.	213
Fig. A.17, Equilibrium concentrations of $\text{HCl}_{(\text{aq})}$ and $\text{Cl}_{2(\text{aq})}$ in an aqueous solution based on current density dependent partial pressure data of both species obtained from the full-cell simulation at 333 K employing the standard thermal resistance.	214

List of Tables

Table 2.1, Conditions for the flowsheet simulations and exergy analysis.....	20
Table 2.2, Technical data and process conditions of the Bayer UHDENORA process.	24
Table 2.3, Total exergy consumption of the six analyzed process configurations.	41
Table 3.1, Governing equations of the numerical reactor model.....	63
Table 3.2, Boundary conditions of the numerical reactor model.....	64
Table 3.3, Model parameters implemented in the reactor simulation.....	86
Table 3.4, Parameters for the numerical crossover model.....	94
Table 3.5, Values for the LJ parameters, δ , and for the modified Eucken correction factors obtained with the here proposed fitting procedure.	108
Table 3.6, Values for the mean and maximum relative deviation between the calculated and experimentally determined transport properties for all seven investigated species.....	111
Table A.1, Fit parameters for determining the mole fraction of chloride anions in solution as a function of the HCl partial pressure.....	204
Table A.2, Fit parameters for determining the activity coefficient of chloride anions in solution as a function of the chloride anion mole fraction.....	207

References

- Abdollahi-Demneha, F., Moosaviana, M. A., Omidkhahb, M. R., Bahmanyara, H. 2011. "Calculating exergy in flowsheeting simulators: A HYSYS implementation." *Energy* 36: 5320-5327.
- Afshar, R., Murad, S., Saxena, S. C. 1981. "Thermal conductivity of gaseous ammonia in the temperature range 358-925 K." *Chem. Eng. Commun.* 10: 1-11.
- Åkerlöf, G., Teare, J. 1938. "A note on the density of aqueous solutions of hydrochloric acid." *J. Am. Chem. Soc.* 60: 1226-1228.
- Alkan, M., Oktay, M., Kocakerimc, M. M., Çopurc, M. 2005. "Solubility of chlorine in aqueous hydrochloric acid solutions." *J. Hazard. Mater.* 119: 13-18.
- Ando, H., Uchida, Y., Kohei, S., Knapp, C., Omoto, N., Kinoshita, M. 2010. *Trends and Views in the Development of Technologies for Chlorine Production from Hydrogen Chloride*. R&D Report, SUMITOMO KAGAKU, Vol. 2, Sumitomo Chemical Co., Ltd.
- Andrew, S. P. S. 1955. "A simple method of measuring gaseous diffusion coefficients." *Chem. Eng. Sci.* 4: 269-272.
- Arruda, T. M., Shyam, B., Ziegelbauer, J. M., Mukerjee, S., Ramaker, D. E. 2008. "Investigation into the competitive and site-specific nature of anion adsorption on Pt using in situ X-ray absorption spectroscopy." *J. Phys. Chem. C* 112: 18087-18097.
- Artemov, V. G., Volkov, A. A., Sysoev, N. N. 2015. "Conductivity of aqueous HCl, NaOH and NaCl solutions: Is water just a substrate?" *EPL* 109: 26002.
- Aspen. 2001. *Aspen Physical Property System 11.1*. Product Manual, Bedford: Aspen Technology.
- Atyabi, S. A., Afshari, E., Wongwiset, S., Yan, W. M., Hadjadj, A., Shadloo, M. S. 2019. "Effects of assembly pressure on PEM fuel cell performance by taking into accounts electrical and thermal contact resistances." *Energy* 179: 490-501.
- Balko, E. N., McElroy, J. F., LaConti, A. B. 1981. "Halogen acid electrolysis in solid polymer electrolyte cells." *Int. J. Hydrogen Energ.* 6: 577-587.
- Ball, M., Wietschel, M. 2009. "The future of hydrogen – opportunities and challenges." *Int. J. Hydrogen Energ.* 34: 615–627.
- Balliet, R. J., Newman, J. 2011. "Cold start of a polymer-electrolyte fuel cell I. Development of a two-dimensional model." *J. Electrochem. Soc.* 158: B927-B938.

- Barret, S. 2016. "Dutch partners deliver first 2 MW PEMFC plant in China." *Fuel Cell Bull.* 11: 13. Accessed 13.06.2020. <http://www.renewableenergyfocus.com/view/45502/dutch-partners-deliver-first-2-mw-pem-fuel-cell-plant-in-china/>.
- Bart, H. J., 2001. "Reactive Extraction." In *Heat and mass transfer*, by Mewes, D., Mayinger, F. Berlin, Heidelberg: Springer.
- Barton, S. C. 2005. "Oxygen transport in composite mediated biocathodes." *Electrochim. Acta* 50: 2145-2153.
- Barua, A. K. 1959. "Thermal conductivity and Eucken type correction for binary mixtures of N₂ with some rare gases." *Physica* 25: 1275-1286.
- Baschuk, J. J., Li, X. 2000. "Modelling of polymer electrolyte membrane fuel cells with variable degrees of water flooding." *J. Power Sources* 86: 181-196.
- BASF. 2017. *MDI capacity increases at BASF Verbund site in Antwerp, Belgium*. Accessed 11.06.2020. <https://www.basf.com/global/en/media/news-releases/2017/01/p-17-110.html>.
- Baturina, O., Epshteyn, A., Northrup, P., Swider-Lyons, K. 2011. "Insights into PEMFC performance degradation from HCl in air." *J. Electrochem. Soc.* 158: B1198-B1205.
- Bazzanella, A. M., Ausfelder, F. 2017. *Low carbon energy and feedstock for the European chemical industry*. Technology study Dechema, Frankfurt: DECHEMA Gesellschaft für Chemische Technik und Biotechnologie e.V.
- Bechtel, S. 2014. *Untersuchungen und Optimierungen an Modellen zur Berechnung von Transportkoeffizienten und deren Einbindung in die Ammoniak-Oxidation*. Bachelorthesis, Technical University of Darmstadt.
- Bechtel, S., Vidaković-Koch, T., Sundmacher, K., Max Planck Gesellschaft zur Förderung der Wissenschaften e.V. 2017. A method and an apparatus for separating chlorine gas from a gaseous anode outlet stream of an electrochemical reactor. Patent WO2019/105955 A2.
- Bechtel, S., Vidaković-Koch, T., Sundmacher, K. 2018a. "Novel process for the exergetically efficient recycling of chlorine by gas-phase electrolysis of hydrogen chloride." *Chem. Eng. J.* 346: 535–548.
- Bechtel, S., Song, Z., Zhou, T., Vidaković-Koch, T., Sundmacher, K. 2018b. "Integrated process and ionic liquid design by combining flowsheet simulation with quantum-chemical solvent screening." *Comput. Aided Chem. Eng.* 44: 2167-2172.
- Bechtel, S., Vidaković-Koch, T., Sundmacher, K. 2019a. "Energy-efficient gas-phase electrolysis of hydrogen chloride." *Chem. Ing. Tech.* 91: 1–15.

- Bechtel, S., Sorrentino, A., Vidaković-Koch, T., Weber, A. Z., Sundmacher, K. 2019b. "Electrochemical gas-phase oxidation of hydrogen chloride to chlorine: model-based analysis of transport and reaction mechanisms." *Electrochim. Acta* 324: 134780.
- Bechtel, S., Vidaković-Koch, T., Weber, A. Z., Sundmacher, K. 2020a. "Model-based analysis of the limiting mechanisms in the gas-phase oxidation of HCl employing an oxygen depolarized cathode." *J. Electrochem. Soc.* 167: 013537.
- Bechtel, S., Bayer, B., Vidaković-Koch, T., Wisser, A., Vogel, H., Sundmacher, K. 2020b. "Precise determination of LJ parameters and Eucken correction factors for a more accurate modeling of transport properties in gases." *Heat Mass Transfer*.
- Bechtel, S., Crothers, A. R., Weber, A. Z., Kunz, U., Turek, T., Vidaković-Koch, T., Sundmacher, K. 2020c. "Advances in the HCl gas-phase electrolysis employing an oxygen-depolarized cathode." *Electrochim. Acta*, submitted on 11.08.2020.
- Beers, K. M., Hallinan Jr, D. T., Wang, X., Pople, J. A., Balsara, N. P. 2011. "Counterion condensation in Nafion." *Macromolecules* 44: 8866-8870.
- Bernardi, D. M., Verbrugge, M. W. 1992. "A mathematical model of the solid-polymer-electrolyte fuel cell." *J. Electrochem. Soc.* 139: 2477.
- Berning, T., Djilali, N. 2003. "A three-dimensional, multi-phase, multicomponent model of the cathode and anode of a PEM fuel cell." *J. Electrochem. Soc.* 150: A1598-A1607.
- Bird, R. B., Stewart, W. E., Lightfoot, E. N. 2006. *Transport phenomena*. Revised 2nd Edition. Hoboken: Wiley.
- Boulamanti, A., Moya, J. A. 2017. *Energy efficiency and GHG emissions: Prospective scenarios for the chemical and petrochemical industry*. JRC Science for policy report, Petten: Joint Research Centre , European Commission.
- Brain, T. J. S. 1967. "New thermal conductivity measurements for argon, nitrogen and steam." *Int. J. Heat Mass Transfer* 10: 737-744.
- Brokaw, R. S. 1969. "Predicting transport properties of dilute gases." *Ind. Eng. Chem. Process Des. Dev.* 8: 240-253.
- Carlson, E. C. 1996. "Don't gamble with physical properties for simulations." *Chem. Eng. Prog.* October: 35-46.
- Cerquetti, A., Longhi, P., Mussini, T. 1968. "Thermodynamics of aqueous hydrochloric acid from the E.M.F.'s of hydrogen-chlorine cells." *J. Chem. Eng.* 13: 458-461.

- Chakravarthy, V. S., Shah, R. K., Venkatarathnam, G. 2011. "A review of refrigeration methods in the temperature range 4–300 K." *J. Thermal Sci. Eng. Appl.* 3: 020801.
- Chapman, S., Cowling, T. G. 1970. *The mathematical theory of non-uniform gases*. 3rd Edition. Cambridge: Cambridge University Press.
- Chen, S., Kucernak, A. 2004. "Electrocatalysis under conditions of high mass transport: investigation of hydrogen oxidation on single submicron Pt particles supported on carbon." *J. Phys. Chem. B* 37: 13984–13994.
- Clayden, J. Greeves, N., Warren, S. 2012. *Organic chemistry*. 2nd Edition. Oxford: Oxford University Press.
- Clegg, S. L., Wexler, A. S. 2011. "Densities and apparent molar volumes of atmospherically important electrolyte solutions. 1. The solutes H₂SO₄, HNO₃, HCl, Na₂SO₄, NaNO₃, NaCl, (NH₄)₂SO₄, NH₄NO₃, and NH₄Cl from 0 to 50°C." *J. Phys. Chem. A* 115: 3393-3460.
- Clements, A. 2010. *The essential chemical industry*. 5th Edition. New York: University of York, Chemical Industry Education Centre.
- Coker, A. K. 2007. *Ludwig's applied process design for chemical and petrochemical plants*. 4th Edition. Burlington: Gulf Professional Publishing.
- Conway, B. E., Novak, D. M. 1979. "Electrocatalytic effect of the oxide film at Pt anodes on Cl recombination kinetics in chlorine evolution." *J. Electroanal. Chem.* 99: 133-156.
- Crothers, A. R., Darling, R. M., Kusoglu, A., Radke, C. J., Weber, A. Z. 2020. "Theory of multicomponent phenomena in cation-exchange membranes: Part II. Transport model and validation." *J. Electrochem. Soc.* 167: 013548.
- Crusius, J. P., Hellmann, R., Castro-Palacio, J. C., Vesovic, V. 2018. "Ab initio intermolecular potential energy surface for the CO₂—N₂ system and related thermophysical properties." *J. Chem. Phys.* 148: 214306.
- Crusius, J. P., Hellmann, R., Hassel, E., Bich, E. 2015. "Ab initio inter-molecular potential energy surface and thermophysical properties of nitrous oxide." *J. Chem. Phys.* 142: 244307.
- Darling, R. M., Weber, A. Z., Tucker, M. C., Perry, M. L. 2016. "The influence of electric field on crossover in redox-flow batteries." *J. Electrochem. Soc.* 163: A5014-A5022.
- De Groot, J. J., Kestin, J., Sookiazian, H. 1974. "Instrument to measure the thermal conductivity of gases." *Physica* 75: 454-482.
- Drioli, E., Giorno, L. 2017. *Comprehensive membrane science and engineering*. 2nd Edition. Amsterdam: Elsevier.

- Dullien, F. 1979. *Porous media fluid transport and pore structure*. 1st Edition. Cambridge: Academic Press.
- Dutta, S., Shimpalee, S., Van Zee, J. W. 2000. "Three-dimensional numerical simulation of straight channel PEM fuel cells." *J. Appl. Electrochem.* 30: 135-146.
- Eames, D. J, Newman, J. 1995. "Electrochemical conversion of anhydrous HCl to Cl₂ using a solid-polymer-electrolyte electrolysis cell." *J. Electrochem. Soc.* 142: 3619-3625.
- Edwards, J. E. 2008. *Process modeling selection of thermodynamic methods*. Technical Report, Teesside: P & I Design Ltd.
- Eikerling, M., Kharkats, Y. I., Kornyshev, A. A., Volkovich, Y. M. 1998. "Phenomenological theory of electro-osmotic effect and water management in polymer electrolyte proton-conducting membranes." *J. Electrochem. Soc.* 145: 2684.
- Eikerling, M., Kornyshev, A. A. 1999. "Electrochemical impedance of the cathode catalyst layer in polymer electrolyte fuel cells." *J. Electroanal. Chem.* 475: 107-123.
- Ellis, C. S., J. N. Holsen. 1969. "Diffusion coefficients for He-N₂ and N₂-CO₂ at elevated temperatures." *Ind. Eng. Chem. Res.* 8: 787-791.
- Epting, W. K., Litster, S. 2012. "Effects of an agglomerate size distribution on the PEFC agglomerate model." *Int. J. Hydrog. Energy* 37: 8505-8511.
- Eucken, A. 1913. "Über das Wärmeleitvermögen, die spezifische Wärme und die innere Reibung der Gase." *Phys. Z* 14: 324-332.
- Faita, G., Fiori, G., Nidola, A. 1970. "Anodic discharge of chloride ions on Pt-Ir alloy electrodes." *J. Electrochem. Soc.* 117: 1333-1335.
- Fan, J. 2002. "A generalized soft-sphere model for Monte Carlo simulation." *Phys. Fluids* 14: 4399-4405.
- Farahipour, R., Mehrkesh, A., Karunanithi, A. T. 2016. "A systematic screening methodology towards exploration of ionic liquids for CO₂ capture processes." *Chem. Eng. Sci.* 145: 126-132.
- Foster, E. G., Royal Dutch Shell Plc. 1982. Process for recovery of chlorine from hydrogen chloride. United States Patent US 4394367 A.
- Freire, F. J., Kaiser, B. A., Felix, V. M., Mah, D. T., Trainham, J. A., Law, C. G., Newman, J. S., University of South Carolina. 1993. Production of isocyanate using chlorine recycle. United States Patent US Patent US6010612 A.

- Fuller, T. F. 1992. *Solid-polymer-electrolyte fuel cells*. PhD Thesis, University of California Berkeley.
- Fuller, T. F., Newman, J. 1993. "Water and thermal management in solid-polymer-electrolyte fuel cells." *J. Electrochem. Soc.* 140: 1218.
- Gasteiger, H. A., Yan, S. G. 2004. "Dependence of PEM fuel cell performance on catalyst loading." *J. Power Sources* 127: 162-171.
- Gestermann, F., Schneider, J., Dummersdorf, H., Haerle, H., Minz, F., Waldmann, H., Bayer AG. 1995. Process for working up the reaction gases in the oxidation of HCl to chlorine . Germany Patent DE19535716A1.
- Gileadi, E. 1993. *Electrode kinetics for chemists, engineers and materials scientists*. New York: Wiley-VCH.
- Gilman, S. 1964. "Studies of anion adsorption on platinum by the multipulse potentiodynamic (m.p.p.) method. II. Chloride and phosphate desorption and equilibrium surface concentrations at constant potential." *J. Phys. Chem.* 68: 2112-2119.
- Gostick, J. T., Ioannidis, M. A., Fowler, M. W., Pritzker, M. D. 2009. "Wettability and capillary behavior of fibrous gas diffusion media for polymer electrolyte membrane fuel cells." *J. Power Sources* 194: 433-444.
- Gotoh, S., Manner, M., Sorensen, J. P., Stewart, W. E. 1974. "Binary diffusion coefficients of low-density gases. I. Measurements by modified Loschmidt method." *J. Chem. Eng. Data* 19: 169-171.
- Gottesfeld, S., Zawodzinski, T. A. 1997. "Polymer Electrolyte Fuel Cells." *Advances in electrochemical science and engineering*, by Alkire, R. C., Gerischer, H., Kolb, D.M., Tobias, C.W. Weinheim: Wiley-VCH Verlag.
- Green, D. W., Southard, M. Z. 2018. *Perry's chemical engineer's handbook*. 9th Edition. New York: McGraw-Hill Education.
- Guerrini, E., Consonni, V. Trasatti, S. 2005. "Surface and electrocatalytic properties of well-defined and vicinal RuO₂ single crystal faces. ." *J. Solid State Electrochem.* 9: 320–329.
- Gullá, A. F., Gancs, L., Allen, R. J., Mukerjee, S. 2007. "Carbon-supported low-loading rhodium sulfide electrocatalysts for oxygen depolarized cathode applications." *Appl. Catal. A Gen.* 326: 227-235.
- Hagemeyer, C., Volpe, A. F. 2018. *Modern applications of high throughput R&D in heterogeneous catalysis*. Schardscha: Bentham Science Publishers.

- Hanley, H. J. M., Klein, M. 1970. "M-6-8 potential function." *J. Chem. Phys.* 50.
- Harvey, D., Pharoah, J. G., Karan, K. 2008. "A comparison of different approaches to modelling the PEMFC catalyst layer." *J. Power Sources* 179: 209–219.
- Hellmann, R. 2018. "Reference values for the second virial coefficient and three dilute gas transport properties of ethane from a state-of-the-art intermolecular potential energy surface." *J. Chem. Eng. Data* 63: 470-481.
- Hellmann, R., Bich, E., Vogel, E., Vesovic, V. 2014. "Intermolecular potential energy surface and thermophysical properties of the CH₄–N₂ system." *J. Chem. Phys.* 141: 224301.
- Hirschfelder, J. O. 1957. "Heat conductivity in polyatomic or electronically excited gases. II." *J. Chem. Phys.* 26: 282-285.
- Hirschfelder, J. O., Curtiss, C. F., Bird, R. B. 1954. *The molecular theory of gases and liquids*. New York: Wiley.
- Hongsirikarna, K., Goodwin, J. G., Greenway, S., Creager, S. 2010. "Effect of cations (Na⁺, Ca²⁺, Fe³⁺) on the conductivity of a Nafion membrane." 195: 7213-7220.
- Huang, Y., Dong, H., Zhang, X., Li, C., Zhang, S. 2013. "New fragment contribution-corresponding states method for physicochemical properties prediction of ionic liquids." *AIChE J.* 59: 1348-1359.
- Hudak, E. M., Kumsa, D. W., Martin, H. B., Mortimer, J. T. 2017. "Electron transfer processes occurring on platinum neural stimulating electrodes: calculated charge-storage capacities are inaccessible during applied stimulation." *J. Neural Eng.* 14: 046012.
- Huheey, J. E., Keiter, E. A., Keiter, R. L., Medhi, O. K. 2006. *Inorganic chemistry: Principles of structure and reactivity*. Pearson Education India.
- Hwang, J. J., Chen, P. Y. 2006. "Heat/mass transfer in porous electrodes of fuel cells." *Int. J. Heat Mass Transf.* 49: 2315–2327.
- Istomin, V. A., Kustova, E. V., Mekhonoshina, M. A. 2014. "Validity of Eucken formula and Stokes' viscosity relation in high-temperature electronically excited gases." *AIP Conf. Proc.* (American Institute of Physics) 1628: 1229-1236.
- Itean, E. C., Glueck, A. R., Svehla, R. A. 1961. "Collision integrals for a modified Stockmeyer potential." NASA technical note D-481.
- Iwanaga, K., Seki, K., Hibi, T., Issoh, K., Suzuta, T., Nakada, M., Mori, Y., Abe, T. 2004. *The Development of Improved Hydrogen Chloride Oxidation Process*. R&D Report, SUMITOMO KAGAKU I, Sumitomo Chemical Co., Ltd.

- Ji, M., Wei, Z. 2009. "A review of water management in polymer electrolyte membrane fuel cells." *Energies* 2: 1057-1106.
- Johnston, H. L., McCloskey, K. E. 1940. "Viscosities of several common gases between 90 K and room temperature." *J. Phys. Chem.* 44: 1038-1058.
- Jörissen, J. 2014. "Chlorine and caustic technology, overview and traditional processes." In *Encyclopedia of applied electrochemistry*, by G., Ota, K., Savinell, R.F. Kreysa. New York: Springer Science+Business.
- KB Roller Tech Kopierwalzen GmbH. *Fluoro-elastomers (FPM, FKM)*. Accessed 16.06.2020. <https://www.kbrt.de/en/applications/fluoro-elastomers-fpm-fkm/>.
- Kee, R. J., Coltrin, M. E., Glarborg, P. 2003. *Chemically reacting flow: Theory & practice*. New York: Wiley.
- Kestin, J., Wakeham, W. A. 1979. "The viscosity of three polar gases." *Ber. Bunsen Phys. Chem.* 83: 573–576.
- Kestin, J., Wang, H. E. 1960. "The viscosity of superheated steam up to 270°C." *Physica* 26: 575-584.
- Kim, S. U., Monroe, C. W. 2014. "High-accuracy calculations of sixteen collision integrals for Lennard-Jones (12–6) gases and their interpolation to parameterize neon, argon, and krypton." *J. Comput. Phys.* 273: 358-373.
- Kodým, R., Fíla, V., Šnita, D., Bouzek, K. 2016. "Poisson–Nernst–Planck model of multiple ion transport across an ion-selective membrane under conditions close to chlor-alkali electrolysis." *J. Appl. Electrochem.* 46: 679-694.
- Krewer, U., Vidakovic-Koch, T., Rihko-Struckmann, L. 2011. "Electrochemical oxidation of carbon-containing fuels and their dynamics in low-temperature fuel cells." *ChemPhysChem* 12: 2518-2544.
- Krishna, R., Wesselingh, J. 1997. "Review article number 50 – The Maxwell-Stefan approach to mass transfer." *Chem. Eng. Sci.* 52: 861.
- Krishtalik, L. I. 1981. "Kinetics and mechanism of anodic chlorine and oxygen evolution reactions on transition metal oxide electrodes." *Electrochim. Acta* 26: 329-337.
- Kubannek, F., Krewer, U. 2016. "A cyclone flow cell for quantitative analysis of kinetics at porous electrodes by differential electrochemical mass spectrometry." *Electrochim. Acta* 210: 862-873.

- Kulikovsky, A. A. 2000. "Kulikovsky, A. A. (2000). Two-dimensional numerical modelling of a direct methanol fuel cell." *J. Appl. Electrochem.* 30: 1005-1014.
- Kusoglu, A., Kwong, A., Clark, K. T., Gunterman, H. P., Weber, A. Z. 2012. "Water uptake of fuel-cell catalyst layers." 159: F530.
- Kusoglu, A., Weber, A. Z. 2017. "New insights into perfluorinated sulfonic-acid ionomers." *Chem. Rev.* 117: 987-1104.
- Kuwertz, R., Aoun, N., Turek, T., Kunz, U. 2016a. "Influence of PTFE content in gas diffusion layers used for gas-phase hydrogen chloride electrolysis with oxygen depolarized cathode." *J. Electrochem. Soc.* 163: F988-F997.
- Kuwertz, R., Martinez, I. G., Vidaković-Koch, T., Sundmacher, K., Turek, T., Kunz, U. 2016b. "Material development and process optimization for gasphase hydrogen chloride electrolysis with oxygen depolarized cathode." *J. Appl. Electrochem.* 46: 755-767.
- Kuwertz, R. 2016c. *Energy-efficient chlorine production by gas-phase hydrogen chloride electrolysis with oxygen depolarized cathode.* PhD Thesis, Technische Universität Clausthal.
- Kuwertz, R., Martinez, I. G., Vidaković-Koch, T., Sundmacher, K., Turek, T., Kunz, U. 2013. "Energy-efficient chlorine production by gas-phase HCl electrolysis with oxygen depolarized cathode." *Electrochem. Commun.* 34: 320-322.
- Lapicque, F., Didierjean, S., Bonnet, C., Conteau, D., Lottin, O. 2012. "Chapter 12 - Experimental monitoring techniques for polymer electrolyte membrane fuel cells." In *Polymer Electrolyte Membrane and Direct Methanol Fuel Cell Technology - Fundamentals and Performance of Low Temperature Fuel Cells*, by Roth, C. Hartnig C., 368-401. Sawston: Woodhead Publishing.
- Lax, E. 1967. *Taschenbuch fuer Chemiker und Physiker - Bd.1: Makroskopische physikalisch-chemische Eigenschaften.* 3rd Edition. Berlin: Springer.
- Lazzús, J. A. 2012. "A group contribution method to predict the melting point of ionic liquids." *Fluid Phase Equilibr.* 313: 1-6.
- Le Neindre, B. 1972. "Contribution à l'étude expérimentale de la conductivité thermique de quelques fluides à haute température et à haute pression." 15: 1-24.
- Lei, Z., Chen, B., Koo, Y., MacFarlane, D. R. 2017. "Introduction: Ionic Liquids." *Chem. Rev.* 117: 6633–6635.

- Linstrom, P. J., Mallard, W. G. 2018. *NIST Chemistry WebBook, NIST Standard Reference Database Number 69*. Gaithersburg MD: National Institute of Standards and Technology. Accessed 05.05.2017. doi:<https://doi.org/10.18434/T4D303>.
- Luo, Z., Chang, Z., Zhang, Y., Liu, Z., Li, J 2010. "Electro-osmotic drag coefficient and proton conductivity in Nafion membrane for PEMFC." *Chem. Rev.* 35: 3120-3124.
- Mańczyński, A., Góral, M., Wiśniewska-Gocłowska, B., Skrzecz, A., Shaw, D. 2003. "Mutual solubilities of water and alkanes." *Monatsh. Chem.* 134: 633–653.
- Makharia, R., Mathias, M. F., Baker, D. R. 2005. "Measurement of catalyst layer electrolyte resistance in PEFCs using electrochemical impedance spectroscopy." *J. Electrochem. Soc.* 152: A970.
- Mallakpour S., Dinari, M. 2012. "Ionic liquids as green solvents: Progress and prospects." In *Green Solvents II*, by Inamuddin D. Mohammad A. Dordrecht: Springer.
- Marquardt, W. 1996. "Trends in computer-aided process modeling." *Comput. Chem. Eng.* 20: 591-609.
- Marrero, T. R., Mason, E. A. 1972. "Gaseous diffusion coefficients." *J. Phys. Chem. Ref. Data* 1: 3-118.
- Martínez, I. G., Vidaković-Koch, T., Kuwertz, R., Kunz, U., Turek, T., Sundmacher, K. 2014. "Analysis of a novel chlorine recycling process based on anhydrous HCl oxidation." *Electrochim. Acta* 123: 387-394.
- Martínez, I. G., Vidaković-Koch, T., Kuwertz, R., Kunz, U., Turek, T., Sundmacher, K. 2013. "The kinetics of hydrogen chloride oxidation." *J. Serb. Chem. Soc.* 78: 2115-2130.
- Martínez, I. G. 2015. *Hydrogen chloride electrolysis in a polymer-electrolyte-membrane reactor with oxygen-depolarized cathode*. PhD Thesis, Otto-von-Guericke-University Magdeburg.
- Mason, E. A., Monchick, L. 1962a. "Transport properties of polar gas." *J. Chem. Phys.* 36: 2746–275.
- Mason, E. A., Monchick, L. 1962b. "Heat conductivity of polyatomic and polar gases." *J. Chem. Phys.* 36: 1622-1639.
- Matsunaga, N., Hori, M., Nagashima, A. 1994. "Measurements of the mutual diffusion coefficients of gases by the Taylor method." *Trans. JSME B* 60: 504-507.
- McGee, H. A. 1991. *Molecular Engineering*. New York: McGraw-Hill.
- Merchant Research. 2015. *Toluene diisocyanate (TDI): 2015 world market outlook and forecast up to 2019*. Market Report, Birmingham: Merchant Research and Consulting Ltd.

- Mian, A. A., Coates, J., Cordiner, J. B. 1969. "Binary gaseous diffusion coefficients of N₂-HCl, Ar-HBr and N₂-HBr systems as a function of temperature." *Can. J. Chem. Eng.* 47: 499-502.
- Monchick, L., Mason, E. A. 1961. "Transport properties of polar gases." *J. Chem. Phys.* 35: 1676-1697.
- Moran, M. J., Shapiro, H. N., Boettner, D. D., Bailey, M. B. 2010. *Fundamentals of engineering thermodynamics*. 7th Edition. Hoboken: John Wiley & Sons.
- Morris, J. C. 1946. "The Mechanism of the hydrolysis of chlorine." *J. Am. Chem. Soc.* 68: 1692-1694.
- Morrison, R. T., Boyd, R. N. 1983. *Organic Chemistry*. Boston: Allyn and Bacon.
- Motupally, S., Becker, A. J., Weidner, J. W. 1999. "Effect of operating conditions on water transport in PEM anhydrous electrolyzers." Edited by R. F., Scanlon, S. L., Fenton, J. M., Weidner, J. Savinell. *Tutorials in electrochemical engineering-mathematical modeling: Proceedings of the international symposium of the Electrochemical Society*. The Electrochemical Society. 280-295.
- Motupally, S., Becker, A. J., Weidner, J. W. 2002. "Water transport in polymer electrolyte membrane electrolyzers used to recycle anhydrous HCl: I. Characterization of diffusion and electro-osmotic drag." *J. Electrochem. Soc.* 149: D69-D71.
- Motupally, S., Mah, D. T., Freire, F. J., Weidner, J. W. 1998. "Recycling chlorine from hydrogen chloride, a new and economical electrolytic process." (Electrochem Soc. Interface).
- Mukherjee, M., Bonnet, C., Lopicque, F. 2020. "Estimation of through-plane and in-plane gas permeability across gas diffusion layers (GDLs): Comparison with equivalent permeability in bipolar plates and relation to fuel cell performance." *Int. J. Hydrog. Energy* 45: 13428-13440.
- Müller, P., Müller-Dolezal, H., Stoltz, R., Söll, H. 2014. *Houben-Weyl methods of organic chemistry Vol. VIII: Peroxides, carbonic acid derivatives, carboxylic acids, carboxylic acid derivatives*. 4th Edition. New York: Thieme.
- Nelson, E. T. 1956. "The measurement of vapour diffusivities in coal-gas and some common gases." *J. Appl. Chem.* 6: 286-292.
- Newman, J. S., Thomas-Alyea, K. E. 2004. *Electrochemical systems*. 3rd Edition. Hoboken: Wiley John + Sons.

- Neyerlin, K. C., Gu, W., Jorne, J., Gasteiger, H. A. 2006. "Determination of catalyst unique parameters for the oxygen reduction reaction in a PEMFC." *J. Electrochem. Soc.* 153: 955-1963.
- Nguyen, T. V., White, R. E. 1993. "A water and heat management model for proton-exchange-membrane fuel cells." *J. Electrochem. Soc.* 140: 2178.
- Novak, D. M., Conway, B. E. 1981. "Competitive adsorption and state of charge of halide ions in monolayer oxide film growth processes at Pt anodes." *J. Chem. Soc.* 77: 2341-2359.
- Ochi, S., Kamishima, O., Mizusaki, J., Kawamura, J. 2009. "Investigation of proton diffusion in Nafion® 117 membrane by electrical conductivity and NMR." *Solid State Ion.* 180: 580-584.
- Ooms, P., Bulan, A., Covestro Deutschland AG. 2010. Method for manufacturing diaryl carbonates and polycarbonates. Patent EP2371807A1.
- Paduszyński, K., Domańska, U. 2014. "Viscosity of ionic liquids: an extensive database and a new group contribution model based on a feed-forward artificial neural network." *J. Chem. Inf. Model.* 54: 1311-1324.
- Paidar, M., Fateev, V., Bouzek, K. 2016. "Membrane electrolysis—History, current status and perspective." *Electrochim. Acta* 209: 737-756.
- Pant, L. M., Gerhardt, M. R., Macauley, N., Mukundan, R., Borup, R. L., Weber, A. Z. 2019. "Along-the-channel modeling and analysis of PEFCs at low stoichiometry: Development of a 1 + 2D model." *Electrochim. Acta* 326: 134963.
- Pavlišič, A., Jovanovič, P., Šelih, V. S., Šala, M., Hodnik, N., Hočevar, S., Gaberšček, M. 2014. "The influence of chloride impurities on Pt/C fuel cell catalyst corrosion." *Chem. Commun.* 50: 3732-3734.
- Pérez-Ramírez, J., Mondelli, C., Schmidt, T., Schlüter, O. F. K., Wolf, A., Mleczko, L., Dreier, T. 2011. "Sustainable chlorine recycling via catalysed HCl oxidation: From fundamentals to implementation." *Energy Environ. Sci.* 4: 4786-4799.
- Perry, R. H., Green, D. W., Maloney, J. O. 1997. *Perry's chemical engineers' handbook*. 7th Edition. New York: McGraw-Hill.
- Powell, R. W., Tye, R. P. 1961. "The thermal and electrical conductivity of titanium and its alloys." *J. Less Common Met.* 3: 226-233.
- Price, D. M., Jarratt, M. 2002. "Thermal conductivity of PTFE and PTFE composites." *Thermochim. Acta* 392: 231-236.

- Priyantha, N., Malavipathirana, S. 1996. "Effect of chloride ions on the electrochemical behavior of platinum surfaces." *J. Natn. Sci. Coun. Sri Lanka* 24: 237-246.
- Promislow, K., Stockie, J. M. 2001. "Adiabatic relaxation of convective-diffusive gas transport in a porous fuel cell electrode." *SIAM J. Appl. Math.* 62: 180-205.
- Querol, E., Gonzalez-Regueral, B., Perez-Benedito, J. L. 2013. *Practical approach to exergy and thermoeconomic analyses of industrial processes*. Berlin: Springer.
- Reid, R. C., Prausnitz, J. M., Poling, B. E. 1987. *The properties of gases and liquids*. 4th Edition. New York: McGraw-Hill.
- Reier, T., Oezaslan, M., Strasser, P. 2012. "Electrocatalytic oxygen evolution reaction (OER) on Ru, Ir, and Pt catalysts: A comparative study of nanoparticles and bulk materials." *ACS Catal.* 2: 1765-1772.
- Rohan, S. 2015. *Chlorine market by application (EDC/ PVC, C1 & C2 aromatics, inorganic chemicals, organic chemicals, chlorinated intermediates, isocyanates, propylene oxide, pulp & paper, textiles, water treatment, others), by region - trends & forecasts to 2019*. Market report, Hadapsar: MarketsAndMarkets.
- Schäfer, K. 1943. "Über das Verhältnis der Wärmeleitfähigkeit und Viskosität von Dipolgasen." *Z. physik. Chem. (B)* 53: 149.
- Schley, P., Jaeschke, M., Küchenmeister, C., Vogel, E. 2004. "Viscosity measurements and predictions for natural gas." *Int. J. Thermophys.* 25: 1623-1652.
- Schmidt, T. J., Paulus, U. A., Gasteiger, H. A., Behm, R. J. 2001. "The oxygen reduction reaction on a Pt/carbon fuel cell catalyst in the presence of chloride anions." *J. Electroanal. Chem.* 508: 41-47.
- Secanell, M., Karan, K., Suleman, A., Djilali, N. 2008. "Optimal design of ultralow-platinum PEMFC anode electrodes." *J. Electrochem. Soc.* 155: B125-B134.
- Seitsonen A. P., Hofmann J. P., Over H., 2010. "Deacon Process over RuO₂ and TiO₂-Supported RuO₂." In *High Performance Computing in Science and Engineering, Garching/Munich 2009*, by Wagner S., Steinmetz M., Bode A., Müller M. Berlin, Heidelberg: Springer.
- Sethuraman, V. A., Lakshmanan, B., Weidner, J. W. 2009. "Quantifying desorption and rearrangement rates of carbon monoxide on a PEM fuel cell electrode." *Electrochim. Acta* 54: 5492-5499.
- Siegel, N. P., Ellis, M. W., Nelson, D. J., Von Spakovsky, M. R. 2004. "A two-dimensional computational model of a PEMFC with liquid water transport." *J. Power Sources* 128: 173-184.

- Slade, S., Campbell, S. A., Ralph, T. R., Walsh, F. C. 2002. "Ionic conductivity of an extruded Nafion 1100 EW series of membranes." *J. Electrochem. Soc.* 149: A1556-A1564.
- Song, Z., Zhou, T., Qi, Z., Sundmacher, K. 2017. "Systematic method for screening ionic liquids as extraction solvents exemplified by an extractive desulfurization process." *ACS Sustain. Chem. Eng.* 5: 3382-3389.
- Sonnenschein, M. F. 2015. *Polyurethanes: Science, technology, markets, and trends*. 1st Edition. Hoboken: Wiley & Sons, Inc.
- Sönnichsen, N. 2020. *Prices of electricity for the industry in Germany from 2008 to 2018*, Statista. Accessed 19.06.2020. <https://www.statista.com/statistics/595803/electricity-industry-price-germany/>.
- Sorrentino, A., Vidaković-Koch, T., Hanke-Rauschenbach, R., Sundmacher, K. 2017. "Concentration-alternating frequency response: A new method for studying polymer electrolyte membrane fuel cell dynamics." *Electrochim. Acta* 243: 53–64.
- Spingler, F. B., Phillips, A., Schuler, T., Tucker, M. C., Weber, A. Z. 2017. "Spingler, F. B., Phillips, A., Schuler, T., Tucker, M. C., Weber, A. Z. (2017). Investigating fuel-cell transport limitations using hydrogen limiting current." *Int. J. Hydrog. Energy* 42: 13960-13969.
- Springer, T. E., Zawodzinski, T. A., Gottesfeld, S. 1991. "Polymer electrolyte fuel cell model." *J. Electrochem. Soc.* 138: 2334.
- Srivastava, B. N., Srivastava, R. C. 1959. "Thermal conductivity and Eucken correction for diatomic gases and binary gas mixtures." *J. Chem. Phys.* 30: 1200-1205.
- Stanic, V., Braun, J., Hoberecht, M. 2003. "Durability of membrane electrode assemblies (MEAs) in PEM fuel cells operated on pure hydrogen and oxygen." *1st International Energy Conversion Engineering Conference (IECEC)*. 5965.
- Stockie, J. M., Promislow, K., Wetton, B. R. 2003. "A finite volume method for multicomponent gas transport in a porous fuel cell electrode." *Int. J. Numer. Methods Fluids* 41: 577-599.
- Stoerzinger, K. A., Rao, R. R., Wang, X. R., Hong, W. T., Rouleau, C. M., Shao-Horn, Y. 2017. "The role of Ru redox in pH-dependent oxygen evolution on rutile ruthenium dioxide surfaces." *Chem* 2: 668-675.
- Stübler, N., Hickmann, T., Ziegmann, G. 2012. "Electrical and mechanical properties of graphite-based polymer composites for bipolar plates in pem fuel cells." *15th European Conference on Composite Materials*. Venice: European Society for Composite Materials.

- Sun, W., Peppley, B. A., Karan, K. 2005. "An improved two-dimensional agglomerate cathode model to study the influence of catalyst layer structural parameters." *Electrochim. Acta* 50: 3359-3374.
- Sundmacher, K. 1999. "Cyclone flow cell for the investigation of gas-diffusion electrodes." *J. Appl. Electrochem.* 29: 919–926.
- Szargut, J. 2005. *Exergy Method: Technical and ecological applications*. 18th Edition. Southampton UK: WIT Press.
- Tang, Z., Svoboda, R., Lawton, J. S., Aaron, D. S., Papandrew, A. B., Zawodzinski, T. A. 2013. "Composition and conductivity of membranes equilibrated with solutions of sulfuric acid and vanadyl sulfate." *J. Electrochem. Soc.* 160: F1040-F1047.
- Thyssenkrupp. 2012. *Hydrochloric acid electrolysis*. Company Brochure, Dortmund: ThyssenKrupp Uhde GmbH.
- Ticianelli, E. A., Derouin, C. R., Srinivasan, S. 1988. "Localization of platinum in low catalyst loading electrodes to attain high power densities in SPE fuel cells." *J. Electroanal. Chem. Interfacial Electrochem.* 251: 275–295.
- Tilak, B. V. 1979. "Kinetics of chlorine evolution—A comparative study." *J. Electrochem. Soc.* 126: 1343–1348.
- Trainham, J. A., Law, G. C., Newman, J. S., Keating, K. B., Eames, D. J., Du Pont de Nemours and Co. 1993. Electrochemical conversion of anhydrous hydrogen halide to halogen gas using a cation-transporting membrane. United States Patent US5411641A.
- Tremblay, D., Watanasiri, S., Song, Y., Chen, C. 2012. *Benefits of multi-solvent NRTL models in Aspen Plus*. Bedford: Aspen Technology.
- Um, S., Wang, C. Y., Chen, K. S. 2000. "Computational fluid dynamics modeling of proton exchange membrane fuel cells." *J. Electrochem. Soc.* 147: 4485.
- Ventura, S. P. M., Silva, F. A., Quental, M. V., Mondal, D., Freire, M. G., Coutinho, J. A. P. 2017. "Ionic-liquid-mediated extraction and separation processes for bioactive compounds: Past, Present, and future trends." *Chem. Rev.* 117: 6984–7052.
- Vidaković-Koch, T., Hanke-Rauschenbach, R., Martínez, I. G., Sundmacher, K. 2017. "Catalyst layer modeling." In *Springer Handbook of Electrochemical Energy*, by C., Swider-Lyons, K. Breitkopf, 259-286. Berlin: Springer.
- Vidaković-Koch, T., Martinez I. G., Kuwertz, R., Kunz, U., Turek, T., Sundmacher, K. 2012. "Electrochemical membrane reactors for sustainable chlorine recycling." *Membranes* 2: 510-528.

- Vie, P. J. S., Kjelstrup, S. 2004. "Thermal conductivities from temperature profiles in the polymer electrolyte fuel cell." *Electrochim. Acta* 49: 1069–1077.
- Villada, C., Bonk, A., Bauer, T., Bolívar, F. 2018. "High-temperature stability of nitrate/nitrite molten salt mixtures under different atmospheres." *Appl. Energy* 226: 107-115.
- Vos, J. G., Koper, M. T. M. 2018. "Measurement of competition between oxygen evolution and chlorine evolution using rotating ring-disk electrode voltammetry." *J. Electroanal. Chem.* 819: 260-268.
- Wang, C. Y. 2004. "Fundamental models for fuel cell engineering." *Chem. Rev.* 104: 4727-4766.
- Wang, C. Y., Cheng, P. 1996. "A multiphase mixture model for multiphase, multicomponent transport in capillary porous." *Int. J. Heat Mass Transfer* 39: 3607-3618.
- Wang, C. Y., Cheng, P. 1997. "Multiphase flow and heat transfer in porous media." *Adv. Heat Transfer* 30: 93-196.
- Wang, M., Guo, H., Ma, C. 2006. "Temperature distribution on the MEA surface of a PEMFC with serpentine channel flow bed." *J. Power Sources* 157: 181–187.
- Wang, Y., Chen, K. S., Mishler, J., Cho, S. C., Adroher, X. C. 2011. "A review of polymer electrolyte membrane fuel cells: Technology, applications, and needs on fundamental research." *Appl. Energy* 88: 981-1007.
- Wang, Z. H., Wang, C. Y., Chen, K. S. 2001. "Two-phase flow and transport in the air cathode of proton exchange membrane fuel cells " *J. Power Sources* 94: 40-50.
- Weast, R. C. 1978. *CRC handbook of chemistry and physics*. 58th Edition. Boca Raton: CRC Press.
- Weber, A. Z., Borup, R. L., Darling, R. M., Das, P. K., Dursch, T. J., Gu, W., *et al.* 2014. "A critical review of modeling transport phenomena in polymer-electrolyte fuel cells." *J. Electrochem. Soc.* 161: F1254-F1299.
- Weber, A. Z., Newman, J. 2004a. "Modeling transport in polymer-electrolyte fuel cells." *Chem. Rev.* 104: 4679-4726.
- Weber, A. Z., Darling, R. M., Newman, J. 2004b. "Modeling two-phase behavior in PEFCs." *J. Electrochem. Soc.* 51: A1715-A1727.
- Weber, A. Z., Newman, J. 2004c. "Transport in polymer-electrolyte membranes: II. Mathematical model." *J. Electrochem. Soc.* 151: A311-A325.
- Weber, R., Kintrup, J., Bulan, A., Kamper, F., Covestro Deutschland. 2006. Processes for the production of chlorine from hydrogen chloride and oxygen. United States Patent US20080029404A1.

- West, A. C., Fuller, T. F. 1996. "Influence of rib spacing in proton-exchange membrane electrode assemblies." *J. Appl. Electrochem.* 26: 557-565.
- Wijngaarden, R. I., Westerterp, K. R., Kronberg, A., Bos, A. N. R. 2008. *Industrial catalysis: Optimizing catalysts and processes*. Weinheim: Wiley-VCH.
- Wilhelm, E., Battino, R., Wilcok, R. J. 1977. "Low-pressure solubility of gases in liquid water." *Chem. Rev.* 77: 219-262.
- Wilkinson, M., Blanco, M., Gu, E., Martin, J. J., Wilkinson, D. P., Zhang, J. J., Wang, H. 2006. "In situ experimental technique for measurement of temperature and current distribution in proton exchange membrane fuel cells." *Electrochem. Solid St.* 9: A507-A511.
- Wu, H. 2016. "A review of recent development: Transport and performance modeling." *Appl. Energy* 165: 81–106.
- Wu, H., Berg, P., Li, Y. 2010. "Steady and unsteady 3D non-isothermal modeling of PEM fuel cells with the effect of non-equilibrium phase transfer." *Appl. Energy* 87: 2778–2784.
- Xing, L., Liu, X., Alaje, T., Kumar, R., Mamlouk, M., Scott, K. 2014. "A two-phase flow and non-isothermal agglomerate model for a proton exchange membrane (PEM) fuel cell." *Energy* 73: 618–634.
- Xing, L., Mamlouk, M., Scott, K. 2013. "A two dimensional agglomerate model for a proton exchange membrane fuel cell, Energy." *Energy* 61: 196–210.
- Yaws, C. L. 2009. *Transport Properties of Chemicals and Hydrocarbons*. 1st Edition. Norwich: William Andrew.
- Yee, L. F., Abdullah, P., Ata, S., Abdullah, A., Ishak, B., Nidzham, K. 2008. "Chlorination and chloramines formation." *Malaysian J. Anal. Sci.* 12: 528 - 535.
- Yeo, R. S., McBreen, J. 1979. "Transport properties of Nafion membranes in electrochemically regenerative hydrogen/halogen cells." *J. Electrochem. Soc.* 126: 1682–1687.
- Yi, J. S., Nguyen, T. V. 1998. "An along-the-channel model for proton exchange membrane fuel cells." *J. Electrochem. Soc.* 145: 1149.
- Yi, J. S., Nguyen, T. V. 1999. "Multicomponent transport in porous electrodes of proton exchange membrane fuel cells using the interdigitated gas distributors." *J. Electrochem. Soc.* 146: 38.
- Young, C. L. 1983. *Solubility data series: Sulfur dioxide, chlorine, fluorine and chlorine oxides*. 1st Edition. Vol. 12. Oxford: Pergamon Press.

- Zawodzinski, T. A., Neeman, M., Sillerud, L. O., Gottesfeld, S. 1991. "Determination of water diffusion coefficients in perfluorosulfonate ionomeric membranes." *J. Phys. Chem.* 95: 6040-6044.
- Zawodzinski, T. A., Springer, T. E., Davey, J., Jestel, R., Lopez, C., Valerio, J., Gottesfeld, S. 1993a. "A comparative study of water uptake by and transport through ionomeric fuel cell membranes." *J. Electrochem. Soc.* 140: 1981.
- Zawodzinski, T. A., Derouin, C., Radzinski, S., Sherman, R. J., Smith, V. T., Springer, T. E., Gottesfeld S. 1993b. "Water-uptake by and transport through Nafion® 117 membranes." *J. Electrochem. Soc.* 140: 1041-1047.
- Zenyuk, I. V., Das, P. K., Weber, A. Z. 2016. "Understanding impacts of catalyst-layer thickness on fuel-cell performance via mathematical modeling." *J. Electrochem. Soc.* 163: F691.
- Zhang, G., Guo, L., Ma, L., Liu, H. 2010. "Simultaneous measurement of current and temperature distributions in a proton exchange membrane fuel cell." *J. Power Sources* 195: 3597-3604.
- Zhang, J. L., Xie, Z., Zhang, J. J., Tanga, Y. H., Song, C. J., Nasvessin, T., Shi, Z. Q., Song, D. T., Wang, H. J., Wilkinson, D. P., Liu, Z. S., Holdcroft, S. 2006. "High temperature PEM fuel cells." *J. Power Sources* 160: 872–891.
- Zhang, J., Tang, Y., Song, C., Zhang, J., Wang, H. 2006. "PEM fuel cell open circuit voltage (OCV) in the temperature range of 23°C to 120°C." *J. Power Sources* 163: 532–537.
- Zhao, Y., Gu, S., Gong, K., Zheng, J., Wang, J., Yan, Y. 2017a. "Low-voltage gaseous HCl electrolysis with an iron redox-mediated cathode for chlorine regeneration." *Angew. Chem. Int. Ed.* 56: 10735-10739.
- Zhao, Y., Gu, S., Gong, K., Zheng, J., Wang, J., Yan, Y. 2017b. "Iodine redox-mediated electrolysis for energy-efficient chlorine regeneration from gaseous HCl." *J. Electrochem. Soc.* 164: E138-E143.
- Zhao, Yongsheng, Gani, R., Afzal, R. M., Zhang, X., Zhang, S. 2017. "Ionic liquids for absorption and separation of gases: An extensive database and a systematic screening method." *AIChE J.* 63: 1353-1367.
- Zhavrin, Y. I., Kosov, V. N., Poyarkov, I. V., Asembaeva, M. K., Fedorenko, O. V., Nysanbaeva A. T. 2013. "Temperature dependences of the effective diffusion coefficients of the components of three-component gas systems, used in the synthesis of ammonia." *J. Eng. Phys. Thermophy.* 86: 676–680.
- Zhu, M., Xie, X, Wu, K., Najmi, A., Jiao, K. 2019. "Experimental investigation of the effect of membrane water content on PEM fuel cell cold start." *Energy Procedia* 158: 1724–1729.

Publications

Journal Publications and Patents

Bechtel, S., Vidaković-Koch, T., Sundmacher, K., Max Planck Gesellschaft zur Förderung der Wissenschaften e.V. 2017. A method and an apparatus for separating chlorine gas from a gaseous anode outlet stream of an electrochemical reactor. *Patent WO2019/105955 A2*.

Simon Bechtel developed the three separation processes published in this patent and was responsible for the scientific and organizational part of the patenting process.

Bechtel, S., Vidaković-Koch, T., Sundmacher, K. 2018. "Novel process for the exergetically efficient recycling of chlorine by gas-phase electrolysis of hydrogen chloride." *Chem. Eng. J.* 346: 535–548.

Simon Bechtel developed the processes, carried out the flow sheet simulations and exergy analysis and wrote the manuscript.

Bechtel, S., Vidaković-Koch, T., Sundmacher, K. 2019. "Energy-efficient gas-phase electrolysis of hydrogen chloride." *Chem. Ing. Tech.* 91: 1–15.

Simon Bechtel wrote this review article.

Bechtel, S., Sorrentino, A., Vidaković-Koch, T., Weber, A. Z., Sundmacher, K. 2019. "Electrochemical gas-phase oxidation of hydrogen chloride to chlorine: Model-based analysis of transport and reaction mechanisms." *Electrochim. Acta* 324: 134780.

Simon Bechtel developed the numerical model, carried out the simulations and wrote the manuscript. The coding structure of an earlier simplified H₂ PEM fuel cell model by A. Sorrentino was employed in the development of the reactor model. Furthermore, Simon Bechtel wrote the manuscript.

Bechtel, S., Vidaković-Koch, T., Weber, A. Z., Sundmacher, K. 2020. "Model-based analysis of the limiting mechanisms in the gas-phase oxidation of HCl employing an oxygen depolarized cathode." *J. Electrochem. Soc.* 167: 013537.

Simon Bechtel developed the model, carried out the simulations and wrote the manuscript.

Bechtel, S., Bayer, B., Vidaković-Koch, T., Wisser, A., Vogel, H., Sundmacher, K. 2020. "Precise determination of LJ parameters and Eucken correction factors for a more accurate modeling of transport properties in gases." *Heat Mass Transfer*.

Simon Bechtel developed and implemented the method published in this article and wrote the manuscript.

Bechtel, S., Crothers, A. R., Weber, A. Z., Kunz, U., Turek, T., Vidaković-Koch, T., Sundmacher, K. 2020. "Advances in the HCl gas-phase electrolysis employing an oxygen-depolarized cathode." *Electrochim. Acta*, submitted on 11.08.2020.

Simon Bechtel carried out all experiments, built the experimental setup, helped in creating the numerical crossover model, interpreted the simulation results, carried out the half-cell simulation investigating the kinetic limitation and wrote the manuscript.

Conference proceedings published in a peer reviewed Journal

Bechtel, S., Song, Z., Zhou, T., Vidaković-Koch, T., Sundmacher, K. 2018. "Integrated process and ionic liquid design by combining flowsheet simulation with quantum-chemical solvent screening." Proceedings of the 13th International Symposium on Process Systems Engineering – PSE 2018 July 1-5, 2018, San Diego, California, *Comput. Aided Chem. Eng.* 44: 2167-2172.

Simon Bechtel carried out the first and fourth step in the proposed ionic liquid screening procedure corresponding to the screening for chemical stability and the final flowsheet simulations as well as the exergy analysis and wrote the manuscript.

Conference talks and posters

Bechtel, S., Song, Z., Zhou, T., Vidaković-Koch, T., Sundmacher, K. "Integrated process and ionic liquid design by combining flowsheet simulation with quantum-chemical solvent screening." Process Systems Engineering – PSE 2018, San Diego, USA. (Oral presentation).

Bechtel, S., Vidaković-Koch, T., Sundmacher, K. " Non-isothermal multiphase model of the HCl gas-phase oxidation employing an ODC." 70th Annual Meeting of the International Society of Electrochemistry 2019, Durban, South Africa. (Oral presentation).

Bechtel, S., Vidaković-Koch, T., Weber, A. Z., Sundmacher, K. "Model-based analysis of the limiting mechanisms in the gas-phase oxidation of HCl employing an oxygen depolarized cathode." GDE Symposium 2019, Magdeburg, Germany. (Poster presentation)